Whole-mantle tomography of Southeast Asia: New insight into plumes and slabs

Genti Toyokuni[1], Dapeng Zhao[1], and Kenkichi Kurata[1]

[1]Tohoku University

November 24, 2022

Abstract

We present detailed 3-D images of whole mantle P-wave velocity structure beneath Southeast Asia and surrounding regions. The results are obtained by applying an updated global tomographic method to invert ~8 million P, pP, PP, PcP, and Pdiff arrival times from 23,587 earthquakes recorded at 14,136 stations distributed all over the world. Our tomographic model reveals a continuous, thin low-velocity (low-V) zone from the surface to the core-mantle boundary beneath the Hainan hotspot, which may reflect the Hainan plume that exists in the whole mantle. Beneath the Australian slab that has subducted into the lower mantle, a strong low-V anomaly is detected, which may reflect subslab hot mantle upwelling (SHMU) due to return flow of the slab subduction. Our model also shows the distinct shape of subducted slabs in the upper mantle and slab remnants in the lower mantle. In particular, a hole in the subducting Australian slab is revealed at depths of 280–430 km beneath eastern Java. The low-V anomaly in the mantle wedge above the Australian slab is connected with the SHMU through the slab hole, suggesting that mixture of the island arc magma and the SHMU may have caused huge eruptions of the Tambora and Rinjani volcanoes in eastern Java.

Whole-mantle tomography of Southeast Asia: New insight into plumes and slabs

Genti Toyokuni[1*], Dapeng Zhao[1], and Kenkichi Kurata[1]

[1] Department of Geophysics, Graduate School of Science, Tohoku University, Sendai 980-8578, Japan

Submitted to ***Journal of Geophysical Research: Solid Earth*** in February 2022

*Corresponding author:

Genti Toyokuni

E-mail: toyokuni@tohoku.ac.jp

ORCID ID: 0000-0003-3786-207X

Key Points:

- A novel high-resolution P-wave tomographic model of the entire mantle beneath Southeast Asia is obtained.
- The model reveals a continuous whole-mantle plume beneath the Hainan hotspot rising from the core-mantle boundary.
- A strong low-velocity anomaly exists beneath the Australian slab, which may reflect subduction-induced hot mantle upwelling.

Abstract

We present detailed 3-D images of whole mantle P-wave velocity structure beneath Southeast Asia and surrounding regions. The results are obtained by applying an updated global tomographic method to invert ~8 million P, pP, PP, PcP, and Pdiff arrival times from 23,587 earthquakes recorded at 14,136 stations distributed all over the world. Our tomographic model reveals a continuous, thin low-velocity (low-V) zone from the surface to the core-mantle boundary beneath the Hainan hotspot, which may reflect the Hainan plume that exists in the whole mantle. Beneath the Australian slab that has subducted into the lower mantle, a strong low-V anomaly is detected, which may reflect subslab hot mantle upwelling (SHMU) due to return flow of the slab subduction. Our model also shows the distinct shape of subducted slabs in the upper mantle and slab remnants in the lower mantle. In particular, a hole in the subducting Australian slab is revealed at depths of 280–430 km beneath eastern Java. The low-V anomaly in the mantle wedge above the Australian slab is connected with the SHMU through the slab hole, suggesting that mixture of the island arc magma and the SHMU may have caused huge eruptions of the Tambora and Rinjani volcanoes in eastern Java.

Plain Language Summary

Southeast Asia is surrounded by plate subduction zones, and very intense seismic and volcanic activities have been occurring there. Volcanic activity originating from the deep Earth, represented by the Hainan hotspot, also takes place. It is known that seafloor spreading and subduction have been repeated in the past, and the relationship between the slabs subducted deeply into the mantle and the plate movement on the surface is an important key to understanding the evolution history of this region. In this study, we apply an updated method of seismic tomography to investigate the whole mantle 3-D P-wave velocity structure beneath SE

Asia. For the first time, a continuous whole-mantle plume is revealed beneath the Hainan hotspot with its root at the core-mantle boundary. Hot mantle upwellings above and below the subducting Australian slab are connected through a slab hole at depths of 280–430 km beneath eastern Java. The mixture of those hot mantle materials might have caused huge eruptions of the Tambora and Rinjani volcanoes in eastern Java.

1. Introduction

Southeast (SE) Asia and its surrounding regions exhibit very complex structure and tectonics, where the Sunda Plate, Eurasian Plate, Philippine Sea Plate, Indian Plate, Australian Plate, and several small plates are interacting with each other (Figure 1). The Sunda Plate located in the center of the region constitutes land areas such as the Indochina Peninsula, Malay Peninsula, Indonesian islands (Sumatra, Java, Borneo, etc.), the Philippines, and broad oceanic areas such as the Sunda Shelf, the South China Sea (SCS), the Sulu Sea, and the Celebes Sea. The Sunda Plate is surrounded by well-developed subduction zones. Trenches of particular note are the Sunda Trench where the Indian Plate and the Australian Plate are subducting beneath the Sunda Plate from the west and the south, respectively, the Philippine Trench where the Philippine Sea Plate subducts beneath the Sunda Plate from the east, and the Manila Trench where the Sunda Plate subducts beneath the Philippine Sea Plate from the west.

Seismic activity in this region is extremely high, and many large earthquakes have occurred at depths < 100 km along the Sunda Trench and the Philippine Trench (Figure S1). In particular, the 2004 Sumatra–Andaman earthquake (Mw 9.1) that occurred on December 26, 2004 caused 230,000 deaths due to the strong ground motion and tsunami. Deep-focus earthquakes also occurred actively, and the June 17, 1996 earthquake off Maumere, Indonesia, recorded Mw 7.9 despite its focal depth of 587 km. Activity of arc volcanoes making up the volcanic front is also high in this region. For example, the Tambora volcano on Sumbawa Island, east of Java, caused the world's largest volcanic eruption in the recorded history on April 5, 1815, which resulted in "the year without a summer." Furthermore, there are hotspot volcanoes on Hainan Island in the northern part of the SCS, and inland volcanic activity is also high around the Indochina Peninsula (Figure 1).

The tectonic evolution of SE Asia after 350 Ma can be summarized as four-stage separation of continental slivers from the Gondwana continent on the southern side, and their accretion to the Eurasia continent on the northern side (Metcalfe, 2005; Müller et al., 2019). At the first stage (the Devonian, 350 Ma), continental slivers consisted of North China, South China, Tarim, Indochina, East Malaya, and West Sumatra were separated from Gondwana and drifted northwards, resulted in opening of the Paleo-Tethys on the southern side. At the second stage (the Lower Permian, 270 Ma), continental slivers consisted of Sibumasu and Qiangtang drifted northwards, resulted in opening of the Meso-Tethys on the southern side and closure of the Paleo-Tethys on the northern side by the Late Triassic. At the third stage (the Late Triassic, 200 Ma), continental slivers consisted of Lhasa, West Burma, West Sulawesi, etc. drifted northwards, resulted in opening of the Ceno-Tethys on the southern side and closure of the Meso-Tethys on the northern side by the Early Cretaceous. At the fourth stage (the Late Jurassic, 140 Ma), the Indian subcontinent drifted northwards, resulted in opening of the Indian Ocean on the southern side and closure of the Ceno-Tethys on the northern side by the Eocene. At 40 Ma, the Indian subcontinent began to collide with the Eurasian continent, the SCS expanded, and the Sunda Plate rotated clockwise. Through these histories, from the east, the Izanagi Plate subducted until 60 Ma, followed by subduction of the Pacific Plate, the Paleo-South China Sea Plate, and the Philippine Sea Plate, etc.

Seismic tomography is a powerful tool to obtain detailed 3-D images of the subsurface structure. Tomographic studies targeting SE Asia have been actively made, but most of them focused on the upper mantle structure (Filippova & Solovey, 2021; Hua et al., 2022; Huang et al., 2015; Lebedev & Nolet, 2003; Legendre et al., 2015; Li & van der Hilst, 2010; Li et al., 2006; Shi et al., 2020; Wehner et al., 2021; Wei et al., 2012; Widiyantoro et al., 2011; Zenonos et al., 2019). The lower mantle structure beneath SE Asia has been mainly studied by global seismic tomography (e.g., Hall & Spakman, 2015). The following is an overview of the structural features obtained by previous tomographic studies regarding the upper and lower mantle beneath this area. More detailed reviews can be found in Zhao (2015) and Hall & Spakman (2015).

Regarding the upper mantle structure, detailed studies have been conducted by mainly using P-wave velocity (Vp) regional tomography (Hua et al., 2022; Huang et al., 2015; Li & van der Hilst, 2010; Li et al., 2006; Shi et al., 2020; Wei et al., 2012; Widiyantoro et al., 2011; Zenonos et al., 2019). Regional tomographic studies using surface-wave and *S*-wave data have been also conducted, but the resolution of the obtained S-wave velocity (Vs) models is lower than that of the Vp models (Filippova & Solovey, 2021; Lebedev & Nolet, 2003; Legendre et al., 2015; Zenonos et al., 2019). Recently, Wehner et al. (2021) determined a 3-D Vs model under SE Asia using full waveform tomography. To date, very few studies have revealed the detailed upper mantle structure using global tomography (Pesicek et al., 2008; Zhao et al., 2021). There are also some studies combining the tomographic results with tectonic reconstruction models or mantle convection simulation (Hafkenscheid et al., 2001; Hall & Spakman, 2015; Jolivet et al., 2018; Spakman & Hall, 2010; Yang et al., 2016; Zahirovic et al., 2016).

A common feature of the upper mantle tomography is that the subducting slabs are clearly imaged as high-velocity (high-V) zones where intermediate-depth and deep earthquakes occurred.

The Indo-Australian slab subducting from the Sunda Trench has been investigated in detail at depths ≤ 660 km. Of particular interest are the bending of the slab beneath northern Sumatra (Hall & Spakman, 2015; Pesicek et al., 2008) and the presence of a slab hole with a diameter of ~400 km at 250–500 km depths beneath eastern Java (Hall & Spakman, 2015; Wehner et al., 2021; Widiyantoro et al., 2011; Zenonos et al., 2019). Huang et al. (2015) conducted Vp anisotropic tomography and suggested the existence of 3-D mantle flow through the slab hole, but they showed that the slab hole was located between Sumatra and Java. Wehner et al. (2021) mentioned the relationship of the slab hole with the nearby Tambora volcano, but they did not discuss about its eruption mechanism. Other characteristic slab structures include a spoon-shaped bended slab beneath the Banda Sea (Spakman & Hall, 2010), and the Sangihe and Halmahera slabs that sink subparallel to each other with a north-south strike beneath the Molucca Sea (Hall & Spakman, 2015; Huang et al., 2015). The continental lithosphere of the Sunda Plate surrounded by these subduction systems is generally imaged as low-velocity (low-V) zones in all tomographic models.

Many global tomography models have been used to investigate the lower mantle structure beneath SE Asia (e.g., Amaru, 2007; Burdick et al., 2017; Fukao & Obayashi, 2013; Hosseini, 2016; Hosseini et al., 2020; Lu et al., 2019; Obayashi et al., 2013; Simmons et al., 2010, 2012; Zhao, 2004; Zhao et al., 2013). However, the spatial resolution of these models is generally > ~500 km, which is inferior to that of regional tomography. Zhao et al. (2021) applied a global tomography method with spatial resolution comparable to that of regional tomography to South China–Indochina–SCS areas, but their model does not cover most of SE Asia.

A common feature of the lower mantle tomography is the existence of a high-V body beneath the Sunda Shelf–Borneo–Philippines at depths ~900–1400 km. This body is identified as slab remnants subducted in the Paleogene by studies combined with plate reconstructions (Hall & Spakman, 2015; Replumaz et al., 2004), but no study has been made to investigate the correspondence between the detailed slab shape and the time-dependent position of the subduction zones. Most of the tomographic studies have revealed a hot mantle plume beneath the Hainan hotspot rising from the lower mantle. However, the continuity of this plume in the lower mantle is unclear in the existing models, and the depth at which the plume began to rise is controversial (e.g., Hua et al., 2022; Huang et al., 2015; Yan et al., 2018; Zhao et al., 2021).

As outlined above, SE Asia has grown through repeating subductions and formations of various tectonic plates, and contains important clues to elucidate subduction dynamics and evolution of the Earth. However, previous studies using high-resolution seismic tomography had focused mainly on the upper mantle structure, and very few studies focused on the detailed whole-mantle structure beneath SE Asia. The purpose of this work is to obtain a high-resolution 3-D Vp model of the whole mantle, from the lithosphere to the core-mantle boundary (CMB), beneath entire SE Asia using an updated global tomography method, so as to improve our understanding of the deep structure and mantle dynamics of this region, in particular, the subducting slabs and upwelling mantle plumes.

2. Method

Global tomography is a method to image 3-D seismic velocity structure of the whole Earth by inverting a great number of travel-time data of earthquakes recorded at seismic stations distributed all over the world (Zhao, 2015). In this work, we use the global tomography method proposed by Zhao (2004) and updated by Zhao et al. (2013, 2017). Zhao et al. (1992) and Zhao (2004) developed a method that can trace seismic rays for an Earth model with 3-D velocity variations and complex shapes of velocity boundaries (such as the Moho, 410 and 660 km discontinuities). The unknown parameters to be inverted are velocity perturbations from an initial 1-D model at 3-D grid nodes that are arranged along the latitude and longitude lines. Zhao et al. (2013) updated their tomographic code by adopting a so-called flexible grid that is independent of the latitude and longitude so that the 3-D mantle structure beneath the polar regions can be also imaged well. Zhao et al. (2017) further proposed a multiscale grid approach that adopts the 3-D flexible grid for the whole globe but reduces the grid interval beneath a target region. This multiscale global tomography method is able to investigate the whole mantle 3-D structure beneath the target area with high resolution comparable to that of regional tomography. Zhao et al. (2017) applied this updated method to the Izu-Bonin area to investigate the detailed geometry and structure of the subducted Pacific slab in and around the source zone of the 2015 Bonin deep earthquake (M7.9, focal depth ~680 km). This method was further applied to image the whole-mantle structure beneath Greenland and its surroundings (Toyokuni et al., 2020) and the South China–Indochina–SCS region (Zhao et al., 2021).

Here we apply this multiscale tomographic method (Zhao et al., 2017) to SE Asia. The absolute travel-time residuals from the ith event to the jth station (t_{ij}) is defined as

$$t_{ij} = T_{ij}{}^{\mathrm{OBS}} - T_{ij}{}^{\mathrm{CAL}} \tag{1}$$

where $T_{ij}{}^{\mathrm{OBS}}$ and $T_{ij}{}^{\mathrm{CAL}}$ are the observed and calculated (theoretical) arrival times, respectively. $T_{ij}{}^{\mathrm{CAL}}$ is calculated by using a 3-D ray tracing technique that combines the pseudo-bending scheme (Um & Thurber, 1987) and Snell's law (Zhao et al., 1992). The initial 1-D model is the IASP91 Earth model (Kennett & Engdahl, 1991). We conduct the tomographic inversions using the LSQR algorithm (Paige & Saunders, 1982) with damping and smoothing regularizations. The optimal values of the damping parameter ($\lambda_d = 15$) and smoothing parameters ($\lambda_{sv} = 1.05 \times 10^{-2}$ and $\lambda_{sh} = 9 \times 10^{-3}$ for the vertical and horizontal directions, respectively) are found from trade-off curves that are constructed by conducting many inversions with various pairs of the damping and smoothing parameters, following the previous studies (Toyokuni et al., 2020; Zhao et al., 2017, 2021).

The target region spans the latitudinal range of [–20°, 25°], longitudinal range of [90°, 140°], and depth range of [0 to 2889 km] (from the surface to CMB). The horizontal grid interval is set to be fine as 55.6 km inside the target area (a great-circle distance of 0.5° on the surface) and to be coarse as 222.2 km outside the target area (a great-circle distance 2.0° on the surface) (Figure 2a). The grid meshes are placed at the following depths inside the target volume:15, 32.5, 50, 75, 100, 140, 180, 220, 260, 300, 340, 380, 420, 460, 500, 575, 650, 725, 800, 875, 950, 1025, 1100, 1200, 1300, 1400, 1500, 1600, 1700, 1800, 1900, 2000, 2100, 2200, 2300, 2425, 2550, 2675, and 2800 km, and outside the target volume: 15, 50, 100, 180, 260, 340, 420, 500, 650, 800, 950, 1100, 1300, 1500, 1700, 1900, 2100, 2300, 2550, and 2800 km (Figure 2b). The number of horizontal grid nodes at each depth is shown in Table S1.

3. Data

The data used in this study are arrival times of not only direct P waves, but also four types of later phases, i.e., pP, PP, PcP, and Pdiff (Figure S2). The data are obtained from the International Seismological Centre (ISC) website (http://www.isc.ac.uk/) and further selected for analysis. (1) The data from 1964 to 2016 in the ISC-EHB catalog (http://www.isc.ac.uk/isc-ehb/) are downloaded, and only the earthquakes containing P, pP, and PP arrival times are extracted. We note that the ISC-EHB catalog does not contain PcP and Pdiff arrival times. The number of extracted earthquakes is 170,435. (2) The data from 2002 to 2012 in the reviewed ISC catalog (http://www.isc.ac.uk/iscbulletin/) are downloaded, and only the earthquakes containing PcP and Pdiff arrival times are extracted. The number of extracted earthquakes is 72,191. (3) To homogenize the hypocentral distribution of 242,626 earthquakes, which are the sum of the data (1) and (2), the entire crust and mantle are divided into small cubic blocks, and in each block only one earthquake with the largest number of arrival times is extracted. The number of earthquakes in the study volume is enhanced by adopting a smaller block size of 0.8° (horizontal) × 10 km (depth) inside the target volume, and a larger block size of 1.5° (horizontal) × 20 km (depth) outside the target volume. The data with travel-time residuals exceeding ±5 s are not used in the tomographic inversion. The number of earthquakes finally used is 23,587, and the total number of arrival time data is 7,762,801, consisting of 7,200,864 P, 246,856 pP, 207,728 PP, 70,253 PcP, 37,100 Pdiff arrival times, which were recorded at 14,136 seismic stations (Figure 3). The number of earthquakes and stations inside the target volume is 11,344 and 656, respectively (Figures S3 and S4). The focal depth range of the extracted earthquakes inside the study volume is 0–700 km.

The CPU time for one tomographic inversion of the selected data set is approximately 43 h and 23 min using our workstation computer Xeon E5-2660 v3 (2.6 GHz, 1 core). The root-mean-square (RMS) travel-time residual is 1.67 s for the initial 1-D Vp model, but it is reduced to 1.37 s for the final 3-D Vp model obtained by the inversion with the optimal damping and smoothing parameters as mentioned above.

4. Results

Figure S5 shows the seismic ray coverage in various depth layers. The density of ray path coverage varies throughout the study volume, which can be visualized by ray hit counts (HC), i.e., the number of rays sampling a grid node (Figures S6−S8). To illustrate the HC distribution, areas with HC < 50, 50 ≤ HC < 100, and HC ≥ 100 are shown in black, gray, and white, respectively. Robust results are expected in areas with a HC ≥ 50, and less reliable parts are masked in white in the tomographic images. Near the Earth's surface (depth ≤ 180 km), seismic rays do not crisscross well beneath the Pacific Ocean, SCS, and Indian Ocean. At greater depths, the ray density and crisscrossing beneath the Pacific Ocean and SCS improves, while the sparse rays beneath the Indian Ocean does not improve until the bottom of the mantle transition zone (MTZ, 410−660 km depths). In the lower mantle (depth > 660 km), rays crisscross well down to the CMB. The reference velocity model is optimized by subtracting the average velocity perturbation at each depth from the velocity anomalies obtained using IASP91 (Kennett & Engdahl, 1991) (Figure 4). Here we show our tomographic results as Vp perturbations from the optimized 1-D model (Figures 5−8), while the Vp images relative to the original IASP91 model are shown in Figures S9−S11.

The results are shown in map views in Figures 5 and 6. The corresponding HC distributions are shown in Figure S6. At a depth of 100 km, high-Vp bands along the Sunda, Manila, and Philippine Trenches, and subduction zone at the eastern end of the Banda Sea Plate are prominent, which clearly correspond to the subducting oceanic slabs. Almost the entire region beneath the northern Australian Craton is also imaged as a remarkable high-Vp zone. Spot-like high-Vp zones are visible at the boundary between the Indian and Australian Plates. As for low-Vp anomalies, a wide extent is observed inside the subduction zones such as beneath the Java Sea, Sulu Sea, Celebes Sea, Banda Sea, Sunda Shelf, and Borneo Island. Spot-like low-Vp zones are also visible at the southern end of the Yangtze Plate and beneath the joint of the Malay Peninsula. At depths of 250−400 km, the high-Vp bands corresponding to the subducting slabs move further behind the trenches as they subduct deeper. Beneath eastern Java, there is a prominent break (window) of the high-Vp band at depths > 280 km. The high-Vp zones beneath northern Australia and the boundary between the Indian and Australian Plates disappear with increasing depth. The low-Vp anomalies inside the subduction zones become less prominent at greater depths, but instead, other low-Vp zones appear outside the Sunda Trench. Especially, beneath the Timor Sea, a low-Vp band elongated in the east-west direction is remarkable. A low-Vp zone is visible at all depths beneath the northern end of the Sunda Plate, i.e., beneath southern Yangtze Plate−Hainan hotspot−Indochina Peninsula.

At depths of 430−520 km, high-Vp zones beneath the Andaman Sea, SCS, and the western end of the Caroline Plate are prominent. The break of the high-Vp band beneath eastern Java is still visible at depths of 430−460 km. A remarkable low-Vp anomaly appears beneath from southern SCS to Borneo, but it disappears with increasing depth. The low-Vp band outside the Sunda Trench is further expanded, and the low-Vp amplitudes become particularly remarkable at its southwestern part. The low-Vp zone beneath the northern end of the Sunda Plate is confined around Hainan Island. Spot-like low-Vp zones are also visible beneath the active volcanoes on the central Philippine Sea Plate. At depths of 550−650 km, a vast high-Vp zone appears beneath the Sunda Plate. Other high-Vp zones also widely exist beneath the Philippine Sea Plate and Australian Plate, so high-Vp amplitudes dominate almost the entire study area. On the other hand, low-Vp is only prominent at the vast crescent-shaped zone beneath the southwestern Sunda Trench. Other low-Vp features remain just as spot-like, for example, beneath Hainan Island.

At depths of 700−800 km, the high-Vp zones become less noticeable, and they remain only beneath the Malay Peninsula, Sumatra, Java, and the west of the Philippine Sea Plate. Instead, a vast low-Vp anomaly appears beneath Hainan−SCS−Sunda Shelf−Borneo. The crescent-shaped low-Vp zone beneath the southwestern Sunda Trench can be seen at all depths. At depths of

900−1400 km, a vast high-Vp zone appears beneath the Sunda shelf−Borneo−Philippines with the largest amplitudes at depths of 1000−1100 km. However, the high-Vp amplitudes gradually decrease at greater depths, and at a depth of 1400 km, only a slight trace remains beneath Borneo. The crescent-shaped low-Vp zone beneath the southwestern Sunda Trench is still visible at depths of 900−1000 km, but is subdivided into spot-like low-Vp zones at greater depths. Spot-like low-Vp zones are also visible beneath Hainan Island and its surrounding areas.

At depths of 1500−2400 km, both the high-Vp and low-Vp amplitudes become small, and only a few conspicuous features are visible. A weak high-Vp anomaly is found beneath the Philippine Sea Plate at depths of 1800−2000 km. Spot-like low-Vp zones exist beneath the southwest of the Sunda Trench only at depths of 1500−1600 km. A confined low-Vp anomaly exists beneath around Hainan Island at depths of 1500−2200 km, while it moves toward the southeast as the depth increases. At depths of 2600−2800 km, both the high-Vp and low-Vp amplitudes increase again, indicating that the structural heterogeneity is stronger at these depths compared to the shallower areas. A prominent high-Vp band exists beneath from the east of Borneo to the Philippine Sea Plate. On the other hand, a low-Vp band is remarkable beneath the Timor Sea. Spot-like low-Vp anomalies can be seen beneath the western margin of the Philippine Sea Plate and beneath the SCS on the CMB.

Vertical cross-sections of our Vp tomographic model and the corresponding HC distributions are shown in Figures 7−8 and Figures S7−S8, respectively. In Figure 7, the C-C' to I-I' sections are almost orthogonal to the Sunda subduction zone, and the Australian slab subducting northward from the Sunda Trench is clearly imaged. Among these, the D-D' to H-H' sections show that the slab penetrates the MTZ and sinks to a depth of ~1400 km in the lower mantle. In the G-G' and H-H' sections through the break in the high-Vp subducted Australian slab at depths of 280−460 km beneath eastern Java (Figure 5), no earthquakes have occurred inside the break, suggesting the existence of a hole in the slab. It is consistent with the characteristics of seismicity in other regions of the world, where earthquakes occur in the high-Vp zone, or at the boundary between high-Vp and low-Vp anomalies (Huang & Zhao, 2004; Mishra & Zhao, 2003; Toyokuni et al., 2021; Yang et al., 2022). The D-D' to I-I' sections clearly show low-Vp anomalies in the upper mantle extending toward the volcano located at the volcanic front of the Sunda subduction zone. In the J-J' to L-L' sections orthogonal to the boundary between the Australian and Timor Plates, the subducted Australian slab in the upper mantle can be clearly confirmed (e.g., I-I' section). In these sections, earthquakes occur continuously along the high-Vp slab subducting toward the MTZ. In addition, the J-J' and L-L' sections show the slab subduction at the boundary between the Sunda and Molucca Sea Plates, and at the boundary between the Bird's Head and Banda Sea Plates, respectively. In the M-M' to O-O' sections, a clear high-Vp zone can be confirmed from ~2000 km depth to the CMB beneath the southern part of the Philippine Sea Plate.

In Figure 7, the c-c' and d-d' sections passing through the Hainan hotspot show a clear plume-like low-Vp anomaly that rises from the CMB with the modulated low-Vp amplitudes depending on depths. In the f-f' to h-h' sections that are almost orthogonal to the Philippine Trench, the Philippine Sea slab subducting westward beneath the Sunda Plate is clearly imaged as high-Vp anomalies. Especially in the H-H' section, a high-Vp anomaly with the same slope, which seems to be another slab, can be seen in the lower mantle beneath the subducting Philippine Sea slab. This high-Vp zone seems to be sinking to the CMB while rolling back eastward. The K-K' section clearly shows the low-Vp anomaly beneath volcanoes constituting the volcanic front of the Sunda subduction zone and the high-Vp slab beneath it. In the M-M' to

O-O' sections, a prominent high-Vp anomaly exists beneath the Australian Craton at depths < ~400 km.

In Figure 8, the E-E' and F-F' sections passing through the Hainan hotspot clearly show strong low-Vp anomalies in the upper mantle. Especially in the E-E' section, the low-Vp conduit rising from the CMB is connected with the low-Vp anomaly in the upper mantle, which very likely indicate the Hainan mantle plume. The low-Vp amplitude of the conduit in the E-E' section decreases once at depths around 1000−2000 km, but the low-Vp amplitude in the F-F' section increases at the same depth. These features suggest that this low-Vp conduit rises vertically from the CMB, meanders to the southwest direction at a depth of ~2000 km, and then rises again to the upper mantle where it broadens beneath the Hainan hotspot and Indochina Peninsula.

In Figure 8, the G-G' section shows a high-Vp zone that corresponds to the Australian slab subducting from the Sunda Trench and sinking through the MTZ to a depth of ~1500 km. In the H-H' section, this high-Vp anomaly and another high-Vp zone corresponding to the Philippine Sea slab subducting from the Philippine Trench are combined to form a U-shaped high-Vp anomaly. Furthermore, in the I-I' section on the southeastern side, a thin high-Vp zone extending vertically from the bottom of the U-shaped anomaly toward the CMB is clearly imaged. The J-J' section shows a high-Vp pile deposited on the CMB.

5. Resolution tests

We performed three kinds of resolution tests, including the checkerboard resolution tests (CRTs) (Humphreys & Clayton, 1988; Zhao et al., 2017), restoring resolution tests (RRTs) (Zhao et al., 1992, 2017), and synthetic resolution tests (SRTs) (Toyokuni et al., 2020; Zhao et al., 2017), to evaluate the ray coverage and spatial resolution of our tomographic model. To conduct the CRTs, we construct an input velocity model that contains alternate positive (+3%) and negative (−3%) Vp anomalies assigned to the 3-D grid nodes. Two input models with different grid intervals (CRT1 and CRT2, Tables 1, S2, and S3) are prepared. To conduct the RRT, we highlight the patterns of the actual tomographic result to construct the RRT input Vp model, i.e., at the grid nodes with the Vp perturbation (dVp) > +0.6% in the real tomographic model, we set dVp = +1.5%, and at the grid nodes with dVp < −0.6% in the real tomographic model, we set dVp = −1.5% in the RRT input model (Table 1). Vp perturbations at the other grid nodes are set to zero. To conduct the SRTs, we construct input models with dVp = +1.5% representing the Australian slab, and dVp = −1.5% representing hot mantle upwelling above and beneath the slab and the Hainan mantle plume. Seven SRT input models with different combinations of the high-Vp slab and low-Vp anomalies are constructed (SRT1−SRT7, Table 1), which are prepared so as to confirm (1) the continuity of the Hainan mantle plume from the surface to CMB, and (2) the reliability of high-Vp Australian slab and a hole in it, low-Vp corner flow in the mantle wedge, low-Vp subslab hot mantle upwelling, and low-Vp corridor connecting the two low-Vp sections. Synthetic datasets for the CRT, RRT, and SRT are constructed by calculating theoretical travel times for each input model but with random errors added, which range between −0.2 and +0.2 s with a standard deviation of 0.1 s, representing the picking errors of the observed data. In the RRTs and SRTs, we use the same grid setting in the main computation (Section 2).

Main features of the test results are summarized in Figures 9 and 10; the complete test results are shown in the supporting information for the CRT1 (Figure S12−S14), CRT2 (Figure S15−S17), RRT (Figure S18−S22), SRT1 (Figure S23−S27), SRT2 (Figure S28−S32), SRT3

(Figure S33−S37), SRT4 (Figure S38−S42), SRT5 (Figure S43−S48), SRT6 (Figure S49−S52), and SRT7 (Figure S53−S57). Regarding the CRT results, the recovery rate is defined as follows:

$$RR_i\ (\%) = \frac{(\text{dVp at the } i\text{th node of the output model})}{(\text{dVp at the } i\text{th node of the input model})} \times 100 \tag{2}$$

On the map views of the CRT1 results (Figure S12), the output dVp patterns are biased to either high-Vp or low-Vp, and the resolution is obviously poor at shallow depths (15−140 km). As for the recovery rate, the black-to-grey areas with poor recovery are dominant beneath the Pacific Ocean, SCS, and Indian Ocean at depths of 15−140 km, whereas white areas are dominant in other parts from the Earth's surface to CMB. In the vertical cross-sections (Figures S13−S14), the depth extent of the areas with good resolution can be confirmed more clearly, displaying less severe pattern of reliability shown by the ray hit count (Figures S7−S8). The CRT2 results (Figures 9a and S15−S17) are slightly severe, and the black-to-grey areas with poor recovery can be seen beneath the Indian Ocean to a depth of 650 km, although the pattern shows almost the same reliability indicated by the ray hit count. The two CRT results show that the whole mantle beneath the study area except for the upper mantle (depths ≤ 660 km) beneath the Indian Ocean, and depths ≤ 140 km in other oceanic areas has a lateral resolution of 167 km and a depth resolution of 40−75 km in the upper mantle and 75−125 km in the lower mantle, which are comparable to the vertical grid interval. This is more than three times the resolution of the existing global tomography models (> 500 km). The regions with a hit count < 50 have low CRT recovery, which indicates that the regions not masked in white in the main tomographic results (Figures 5−8) have sufficient resolution.

In the output of RRTs (Figures 9b, 10a, and S18−S22), it can be seen that the pattern recovery is lower in the vicinity of the MTZ beneath the Indian Ocean. In other regions, we can see that the input patterns are generally recovered, although the input amplitudes tend to slightly decrease. In the output of SRTs (Figures 9c−9i, 10b−10f, and S23−S57), the features of the input models are reproduced very well, showing the robustness of the continuity of the Hainan plume from the surface to CMB, and the features around the hole in the Australian slab.

6. Discussion

6.1 Comparison with previous models

First we give an overview of our model by comparing with the previous models focusing on slab structures. Our novel Vp model clearly reveals subducted slabs as high-Vp bands at depths < ~800 km with the resolution comparable to the previous regional tomography (Figures 5, 6, and 11). The bending of the subducting Indo-Australian slab beneath northern Sumatra (Hall & Spakman, 2015; Pesicek et al., 2008) is confirmed at depths of 310−550 km (Figures 5, 11b, and 11c). However, our model shows another linear high-Vp band continuous from the south without bending, suggesting another slab subducted from the intersecting trench (Figures 11b−11e). A hole in the Australian slab beneath eastern Java, which was pointed out by many previous studies (Hall & Spakman, 2015; Wehner et al., 2021; Widiyantoro et al., 2011; Zenonos et al., 2019), is confirmed as a break in the high-Vp band at depths of 280–460 km, which is discussed in detail in Section 6.5 (Figures 11a and 11b). The spoon-shaped Banda slab is also revealed at depths of 250−600 km, with a flat-lying portion at a depth of ~600 km (Hall & Spakman, 2015; Spakman & Hall, 2010) (Figures 11a−11d). The Sangihe and Halmahera slabs beneath the Molucca Sea (Hall & Spakman, 2015) are clearly separated by a linear low-Vp band sandwiched between the high-Vp slabs at depths 250−800 km (Figure 11a and A-A' section in Figure 12). Vast high-Vp anomalies in the MTZ due to the slab stagnation (Hua et al., 2022; Huang et al., 2015) are also confirmed in our model (Figure 11d). In the lower mantle, a high-Vp body beneath Sunda Shelf−Borneo−Philippines at depths of 900−1400 km (e.g., Hall & Spakman, 2015) is clearly revealed in our model (Figures 6, 11g, and 11h).

Next we compare our model with the previous global tomography models. Ten P-wave tomographic models are used for the comparison, i.e., UU-P07 (Amaru, 2007), MITP08 (Li et al., 2008), GyPSuM-P (Simmons et al., 2010), LLNL_G3Dv3 (Simmons et al., 2012), GAP-P4 (Fukao & Obayashi, 2013; Obayashi et al., 2013), SPani-P (Tesoniero et al., 2015), Hosseini2016 (Hosseini, 2016), MITP_USA_2016MAY (Burdick et al., 2017), TX2019slab-P (Lu et al., 2019), and DETOX-P3 (Hosseini et al., 2020). These models were downloaded from the SubMachine website (http://www.earth.ox.ac.uk/~smachine/cgi/index.php) (Hosseini et al., 2018).

In Figures 13 and S58−S60 we compare these models with our model for four vertical cross-sections. Our model is shown in the upper left, and all these models are displayed using the same color scale. In Figure 13, passing through the Hainan hotspot, a low-Vp conduit elongated vertically from the CMB toward the Earth's surface shows up clearly in our model, which may be a hot mantle plume as pointed out by previous studies (e.g., Zhao et al., 2021). The Hainan plume in the lower mantle is also visible in Hosseini2016 and DETOX-P3, but only our model clearly shows the plume upwelling from the CMB. In other models, the low-Vp zone extends over a wide area near the surface other than right beneath the Hainan area, and the characteristics of the mantle plume are hard to see. In Figure S58 passing through Borneo and northern Australia, the Australian slab subducting from the south can be traced to a depth of ~1400 km, which is common to all models. On the other hand, only our model clearly images the low-Vp anomaly corresponding to hot mantle upwelling in the mantle wedge beneath volcanic fronts. In Figure S59 passing through Java, Borneo, and the Philippines, a U-shaped high-Vp zone that combines the Australian and Philippine Sea slabs appears in all models except for GyPSuM-P and SPani-P. However, in our model, the continuity between the U-shaped high-Vp zone and deeper high-Vp anomalies can be seen more clearly. In Figure S60 passing through Sulawesi, there are large discrepancies between models. Our model shows a high-Vp zone that might be associated with slab remnants at depths > ~1500 km in the lower mantle, but similar features can be seen only in DETOX-P3, Hosseini2016, LLNL_G3Dv3, MITP_USA_2016MAY, and TX2019slab-P. Because TX2019slab-P is a model for which subducting slabs are introduced as a priori information in the upper mantle, the similarity of the slab characteristics with this model indicates the validity of our model.

6.2 Comparison with plate reconstruction

Assuming vertical slab subduction and mantle viscosity at a specific value, the depth of a slab subducting from the trench is proportional to the subduction age. Therefore, a high-Vp anomaly in the tomographic images can be associated with the corresponding slab subduction, by comparing the tomography of a particular depth with the reconstructed plate position in a particular age. The relationship between the subduction age and slab depth differs depending on the study, but representative results by Lithgow-Bertelloni & Richards (1998) and Butterworth et al. (2014) are shown in Figure S61. Using these relationships, the latest plate reconstruction by Müller et al. (2019) is compared with the depth slices of our tomography. Figures 14 and S62 show the comparison using the age-depth relationship by Lithgow-Bertelloni & Richards (1998) and Butterworth et al. (2014), respectively.

The most distinctive feature of these comparisons is coincidence of the vast high-Vp body beneath Sunda Shelf−Borneo−Philippines at depths of 900−1400 km (e.g., Hall & Spakman, 2015) with the position of the “opposite subduction zone” where plates subduct from the two subparallel trenches facing each other. For example, in Figure 14, the high-Vp body seems located in a region sandwiched between two opposing trench axes at 33−75 Ma, and the area of the high-Vp body decreases as the times go back and this region narrows. Before 90 Ma, the opposite subduction zone collapses, and the high-Vp body synchronously disappears. Because the horizontal movement of the subducted slabs may be small in the opposite subduction zone, the assumption of vertical subduction seems to be reasonable. In Figure S62, location of the high-Vp body shows good agreement with the opposite subduction at 69−100 Ma, but at 108 Ma, the opposite subduction collapses and the high-Vp body disappears. Due to the difference in the age-depth relationship, the correspondence of ages and trench locations vary between the two comparisons. However, both comparisons commonly suggest that the high-Vp body is originated from the slab subducted from the opposite subduction zone < 100 Ma.

Since the internal structure of the high-Vp body was not resolved in the conventional tomography models, this body has been interpreted as a slab complex subducted from various subduction zones (Hall & Spakman, 2015). However, in our tomography model, the central part of high-Vp body at depths of 1150−1200 km is distributed in two lines (Figure 11h). This might be because the shapes of the two slabs subducted from the opposite subduction zone are relatively well preserved.

6.3 The Hainan mantle plume

Zhao et al. (2021) investigated the whole mantle structure beneath South China–Indochina–SCS and revealed a mantle plume rising from the lower mantle beneath the Hainan hotspot and the southeast Asia basalt province (SABP), although its low-Vp amplitude in the lower mantle was weak and the root of the plume was unclear. For the first time, our tomographic images clearly show that the mantle plume beneath these areas is continuous from the CMB to the surface (A-A' to D-D' sections in Figure 12).

Looking to the south of these areas, a vast high-Vp body exists beneath the Sunda Shelf–Borneo–Philippines at depths of 900–1400 km, which might be the deposition of subducted slabs (Section 6.2). However, no apparent high-Vp anomaly is visible at depths of 1500–2200 km, and the high-Vp zone becomes prominent again beneath Sulawesi–Philippines at depths > ~2400 km (B-B' and b-b' to d-d' sections in Figure 12). This implies that the slabs subducted beneath this area are polarized into those that have already fallen to the vicinity of the CMB and those that remain shallower than 1400-km depth.

In the map view of our tomography at 2800 km depth (Figure 6), a high-Vp zone beneath Sulawesi–Philippines is surrounded by low-Vp anomalies distributed beneath the SCS and Timor Sea. Therefore, the hot mantle plume that formed the Hainan hotspot and SABP might be driven by the downward mantle flow when the slabs currently lying on the CMB beneath Sulawesi–Philippines subducted, but now its power has weakened because the slab portions has completely fallen down to the CMB. A geochemical study pointed out that the ascending rate of the Hainan mantle plume is very slow (<1 cm/yr), and the supply of hot mantle materials is close to be depleted (Zou & Fan, 2010), which is in good agreement with the inference from our tomographic results.

6.4 Subslab hot mantle upwelling (SHMU)

Our tomography model shows that the Australian slab, imaged as a distinct high-Vp zone, is penetrating into the lower mantle through the MTZ. Another notable feature is the existence of a strong subslab low-Vp zone extending from the lower mantle toward the Indian Ocean and Timor Sea (a-a' to d-d' sections in Figure 15). Hereafter we call the low-Vp zone "subslab hot mantle upwelling (SHMU)", which may be return flow generated as the slab subducts into the lower mantle, and rises guided by the slab.

Recently, the importance of SHMU in the upper mantle that exists directly beneath the subducting slab has begun to be recognized (Fan & Zhao, 2021; Wang et al., 2020). For example, Fan & Zhao (2021) obtained detailed tomographic images of the upper mantle in the world's six subduction zones, and suggested a possibility that the occurrence of giant megathrust earthquakes (M > 8.5) was affected by the upper-mantle SHMU because it may change the shape of the slab due to its buoyancy. The SHMU revealed by this study seems more powerful comparable to a hot mantle plume because it rises from the lower mantle and has large low-Vp amplitudes. When such a powerful SHMU rises along the subducting slab and reaches beneath the oceanic plate outside the trench axis, the oceanic plate might be thinned by thermal erosion (a-a' section in Figure 12). As mentioned in Section 1, SE Asia has grown by the separation of continental slivers from the southern hemisphere and their movement to the northern hemisphere, which might be driven by SHMU in addition to normal mantle convection.

6.5 Slab hole beneath eastern Java

Our model shows a hole in the Australian slab beneath eastern Java at depths of 280–460 km (Figure 15). At depths of 310–400 km, low-Vp zones located inside and outside the subduction zone seem connected through the slab hole, suggesting the existence of 3-D mantle flow as pointed out by Huang et al. (2015). The reliability of these features is confirmed by seven SRTs (SRT1–SRT7) (Figures 9 and 10, also see Section 5). The existence of the slab hole is also supported by the lack of slab seismicity there (Hall & Spakman, 2015).

In our tomography, bending of the slab can be confirmed near the bottom end of the slab hole at a depth of 490 km (Figure 15). Because the slab hole is considered to have formed since ~8 Ma (Hall & Spakman, 2015), the age-depth relationship by Lithgow-Bertelloni & Richards (1998) can be applicable. Comparison of the plate reconstruction by Müller et al. (2019) with our tomography shows that the axis of the Sunda Trench disappears west of the slab bend at 10 Ma (Figure 14). Therefore, we can infer that the slab hole was formed because the slab was partially torn by a tectonic force such that shifts the trench axis at ~10 Ma. An alternative interpretation is that the slab hole was formed by subduction of seamounts (Hall & Spakman, 2015). Further research is needed regarding the origin of the slab hole.

There are two interesting features related to the slab hole. One is that the Tambora and Rinjani volcanoes, which are the only two in this region of 25 world's volcanoes that caused large volcanic eruptions during the past 2500 years (Sigl et al., 2015), are located just above the east edge of this slab hole (Figure 15). The other feature is that the strong SHMU rising from the lower mantle seems connected with the upper-mantle corner flow in the mantle wedge through the slab hole (Figure 16). Considering these features together, we can infer that the catastrophic volcanic eruptions specialized only in this area were driven by the supply of hot mantle materials from the deep mantle comparable to a hot plume. A prominent K-rich feature of the Tambora ignimbrites (De Maisonneuve & Bergal-Kuvikas, 2019) might support our interpretation, and further support from geological and geochemical studies is needed.

6.6 Structure of the D” layer

Our model shows a high-Vp band at depths of 2600–2800 km beneath from eastern Borneo to the Philippine Sea Plate, whereas a low-Vp band located subparallel to the high-Vp band is remarkable beneath the Timor Sea. Comparisons with plate reconstructions show that these bodies are located just beneath an ancient subduction zone that existed at ~200 Ma (Figures 14 and S62). A recent study suggests that high-V zones in the lower mantle and the D” layer (a 200-300 km thick layer above the CMB) reflect the subducted slabs, whereas (at least parts of) the low-V zones there may reflect the subducted oceanic crust materials (Jones et al., 2020). Therefore, the low-Vp band beneath the Timor Sea might reflect the reworked oceanic crust, where hot mantle upwelling could be born.

7. Conclusions

A detailed 3-D P-wave velocity (Vp) model of the whole mantle beneath SE Asia and surrounding areas is obtained by inverting a large number of high-quality P-wave arrival-time data recorded by seismic stations distributed all over the world. The 3-D Vp structure from the lithosphere to the CMB is effectively resolved. The novel tomographic model reveals the following new features.

(1) It has become clear for the first time that the hot mantle plume beneath the Hainan hotspot is rising from the CMB. This hot plume may have been generated as a return flow as the slab remnants beneath Sulawesi–Philippines fell down to the CMB. Currently, the Hainan mantle plume seems to have weakened because the slab remnants had almost completely dropped down to the CMB.

(2) A strong low-Vp anomaly is revealed beneath the Australian slab that has subducted into the lower mantle. The low-Vp anomaly may reflect hot mantle upwelling due to return flow of the slab subduction. We call it subslab hot mantle upwelling (SHMU). The SHMU confined to the upper mantle has been found in many subduction zones in the world, but the one in this area is unusual because it originates from the lower mantle and has large low-Vp amplitudes.

(3) The subducted slabs are revealed very clearly in both the upper and lower mantle. In particular, a hole in the subducting Australian slab is clearly identified at depths of 280–460 km beneath eastern Java. In and around the slab hole, 3-D mantle flow may exist. Corner flow in the mantle wedge and the SHMU might be mixed through this slab hole, causing large-scale volcanic eruptions in eastern Java.

Acknowledgments

We are grateful to Profs. Satoshi Miura and Toru Matsuzawa for helpful discussions. Discussions with Ms. Masyitha Retno Budiati and Dr. Tomomi Okada motivated us to study SE Asia. This work was partially supported by research grants from Japan Society for the Promotion of Science (Nos. 18K03794, 19H01996 and 23224012). The GMT (Wessel et al., 2013) and GPlates (Müller et al., 2018) software packages are used in this study. The arrival-time data are downloaded from the ISC (http://www.isc.ac.uk/). Part of the event data are also downloaded from the USGS (https://www.usgs.gov/). The SubMachine website (http://www.earth.ox.ac.uk/~smachine/cgi/index.php) (Hosseini et al., 2018) was accessed to generate vertical cross-sections of the global tomography models as shown in Figure 13. Archiving of data from this study is underway through Zenodo. Currently these data can be seen in Supporting Information for review purposes.

Author contributions

Conceptualization: Genti Toyokuni, Dapeng Zhao

Data curation: Genti Toyokuni

Formal analysis: Genti Toyokuni, Kenkichi Kurata

Methodology: Dapeng Zhao, Genti Toyokuni

Resources: Genti Toyokuni, Dapeng Zhao

Visualization: Genti Toyokuni, Kenkichi Kurata

Writing – original draft: Genti Toyokuni, Dapeng Zhao

Writing – review & editing: Genti Toyokuni, Dapeng Zhao, Kenkichi Kurata

References

Amaru, M. L. (2007). Global travel time tomography with 3-D reference models. Ph. D. Thesis, Utrecht University. http://dspace.library.uu.nl/bitstream/handle/1874/19338/index.htm;jsessionid=88B6AA4941C5E76FD65034D89D4065E0?sequence=17

Bird, P. (2003). An updated digital model of plate boundaries. *Geochemistry, Geophysics, Geosystems*, 4(4), 1027. https://doi.org/10.1029/2001GC000252

Burdick, S., Vernon, F. L., Martynov, V., Eakins, J., Cox, T., Tytell, J., Mulder, T., White, M. C., Astiz, L., Pavlis, G. L., & van der Hilst, R. D. (2017). Model update May 2016: Upper-mantle heterogeneity beneath North America from travel-time tomography with global and USArray data. *Seismological Research Letters*, 88(2A), 319–325. https://doi.org/10.1785/0220160186

Butterworth, N. P., Talsma, A. S., Müller, R. D., Seton, M., Bunge, H.-P., Schuberth, B. S. A., Shephard, G. E., & Heine, C. (2014). Geological, tomographic, kinematic and geodynamic constraints on the dynamics of sinking slabs. *Journal of Geodynamics*, 73, 1–13. https://doi.org/10.1016/j.jog.2013.10.006

De Maisonneuve, C. B. & Bergal-Kuvikas, O. (2020). Timing, magnitude and geochemistry of major Southeast Asian volcanic eruptions: identifying tephrochronologic markers. *Journal of Quaternary Science*, 35, 272–287. https://doi.org/10.1002/jqs.3181

Fan, J., & Zhao, D. (2021). Subslab heterogeneity and giant megathrust earthquakes. *Nature Geoscience*, 14, 349–353. https://doi.org/10.1038/s41561-021-00728-x

Filippova, A. I., & Solovey, O. A. (2021). Deep velocity structure of Southeast Asia from Rayleigh wave group velocities: 3D isotropic model of the S-wave velocity distribution in the upper mantle. *Geotectonics*, 55, 531–542. https://doi.org/10.1134/S0016852121040063

Fukao, Y., & Obayashi, M. (2013). Subducted slabs stagnant above, penetrating through, and trapped below the 660 km discontinuity. *Journal of Geophysical Research: Solid Earth*, 118, 5920–5938. https://doi.org/10.1002/2013JB010466

Hafkenscheid, E., Buiter, S. J. H., Wortel, M. J. R., Spakman, W., & Bijwaard, H. (2001). Modelling the seismic velocity structure beneath Indonesia: a comparison with tomography. *Tectonophysics*, 333(1–2), 35–46. https://doi.org/10.1016/S0040-1951(00)00265-1

Hall, R., & Spakman, W. (2015). Mantle structure and tectonic history of SE Asia. *Tectonophysics*, 658, 14–45. http://dx.doi.org/10.1016/j.tecto.2015.07.003

Hosseini, K. (2016). Global multiple-frequency seismic tomography using teleseismic and core-diffracted body waves. Ph. D. Thesis, Faculty of Geosciences, LMU München. https://doi.org/10.5282/edoc.19597

Hosseini, K., Matthews, K. J., Sigloch, K., Shephard, G. E., Domeier, M., & Tsekhmistrenko, M. (2018). SubMachine: Web-Based tools for exploring seismic tomography and other models of Earth's deep interior. *Geochemistry, Geophysics, Geosystems*, 19(5), 1464–1483. https://doi.org/10.1029/2018GC007431

Hosseini, K., Sigloch, K., Tsekhmistrenko, M., Zaheri, A., Nissen-Meyer, T., & Igel, H. (2020). Global mantle structure from multifrequency tomography using *P*, *PP* and *P*-diffracted waves. *Geophysical Journal International*, 220(1), 96–141. https://doi.org/10.1093/gji/ggz394

Hua, Y., Zhao, D., & Xu, Y.-G. (2022). Azimuthal anisotropy tomography of the Southeast Asia subduction system. *Journal of Geophysical Research: Solid Earth*, 127, e2021JB022854. https://doi.org/10.1029/2021JB022854

Huang, J., & Zhao, D. (2004). Crustal heterogeneity and seismotectonics of the region around Beijing, China. *Tectonophysics*, 385(1–4), 159–180. https://doi.org/10.1016/j.tecto.2004.04.024

Huang, Z., Zhao, D., & Wang, L. (2015). P wave tomography and anisotropy beneath Southeast Asia: Insight into mantle dynamics. *Journal of Geophysical Research: Solid Earth*, 120, 5154–5174. https://doi.org/10.1002/2015JB012098

Humphreys, E., & Clayton, R. W. (1988). Adaptation of back projection tomography to seismic travel time problems. *Journal of Geophysical Research*, 93(B2), 1073–1085. https://doi.org/10.1029/JB093iB02p01073

Jones, T. D., Maguire, R. R., van Keken, P. E., Ritsema, J., & Koelemeijer, P. (2020). Subducted oceanic crust as the origin of seismically slow lower-mantle structures. *Progress in Earth and Planetary Science*, 7, 17. https://doi.org/10.1186/s40645-020-00327-1

Jolivet, L., Faccenna, C., Becker, T., Tesauro, M., Sternai, P., & Bouilhol, P. (2018). Mantle flow and deforming continents: From India-Asia convergence to Pacific subduction. *Tectonics*, 37, 2887–2914. https://doi.org/10.1029/2018TC005036

Kennett, B. L. N., & Engdahl, E. R. (1991). Traveltimes for global earthquake location and phase identification. *Geophysical Journal International*, 105, 429–465. https://doi.org/10.1111/j.1365-246X.1991.tb06724.x

Lebedev, S., & Nolet, G. (2003). Upper mantle beneath Southeast Asia from S velocity tomography. *Journal of Geophysical Research: Solid Earth*, 108(B1), 2048. https://doi.org/10.1029/2000JB000073

Legendre, C. P., Zhao, L., & Chen, Q.-F. (2015). Upper-mantle shear-wave structure under East and Southeast Asia from Automated Multimode Inversion of waveforms. *Geophysical Journal International*, 203(1), 707–719. https://doi.org/10.1093/gji/ggv322

Li, C., & van der Hilst, R. D. (2010). Structure of the upper mantle and transition zone beneath Southeast Asia from traveltime tomography. *Journal of Geophysical Research: Solid Earth*, 115, B07308. https://doi.org/10.1029/2009JB006882

Li, C., van der Hilst, R. D., & Toksöz, M. N. (2006). Constraining P-wave velocity variations in the upper mantle beneath Southeast Asia. *Physics of the Earth and Planetary Interiors*, 154(2), 180–195. https://doi.org/10.1016/j.pepi.2005.09.008

Li, C., van der Hilst, R. D., Engdahl, E. R., & Burdick, S. (2008). A new global model for P wave speed variations in Earth's mantle. *Geochemistry Geophysics Geosystems*, 9(5), Q05018. https://doi.org/10.1029/2007GC001806

Lithgow-Bertelloni, C., & Richards, M. A. (1998). The dynamics of Cenozoic and Mesozoic plate motions. *Reviews of Geophysics*, 36(1), 27–78. https://doi.org/10.1029/97RG02282

Lu, C., Grand, S. P., Lai, H., & Garnero, E. J. (2019). TX2019slab: A new P and S tomography model incorporating subducting slabs. *Journal of Geophysical Research: Solid Earth*, 124, 11549–11567. https://doi.org/10.1029/2019JB017448

Metcalfe, I. (2005). Asia: south-east. In: Selley, R. C., Cocks, L. R. M., Plimer, I. R. (Eds.), *Encyclopedia of Geology*. Elsevier, Oxford, pp. 169–196. https://doi.org/10.1016/j.jseaes.2008.09.004

Mishra, O. P., & Zhao, D. (2003). Crack density, saturation rate and porosity at the 2001 Bhuj, India, earthquake hypocenter: A fluid driven earthquake? *Earth and Planetary Sciences Letters*, 212(3–4), 393-405. https://doi.org/10.1016/S0012-821X(03)00285-1

Müller, R. D., Cannon, J., Qin, X., Watson, R. J., Gurnis, M., Williams, S., Pfaffelmoser, T., Seton, M., Russell, S. H. J., & Zahirovic, S. (2018). GPlates: Building a virtual Earth through deep time. *Geochemistry*, *Geophysics*, *Geosystems*, 19, 2243–2261. https://doi.org/10.1029/2018GC007584

Müller, R. D., Zahirovic, S., Williams, S. E., Cannon, J., Seton, M., Bower, D. J., Tetley, M. G., Heine, C., Le Breton, E., Liu, S., Russell, S. H. J., Yang, T., Leonard, J., & Gurnis, M. (2019). A global plate model including lithospheric deformation along major rifts and orogens since the Triassic. *Tectonics*, 38, 1884–1907. https://doi.org/10.1029/2018TC005462

Obayashi, M., Yoshimitsu, J., Nolet, G., Fukao, Y., Shiobara, H., Sugioka, H., Miyamachi, H., & Gao, Y. (2013). Finite frequency whole mantle P wave tomography: Improvement of subducted slab images. *Geophysical Research Letters*, 40, 5652–5657. https://doi.org/10.1002/2013GL057401

Paige, C. C., & Saunders, M. A. (1982). LSQR, An algorithm for sparse linear equations and sparse least squares. *ACM Transactions on Mathematical Software (TOMS)*, 8(1), 43–71. https://doi.org/10.1145/355984.355989

Pesicek, J. D., Thurber, C. H., Widiyantoro, S., Engdahl, E. R., & DeShon, H. R. (2008). Complex slab subduction beneath northern Sumatra. *Geophysical Research Letters*, 35, L20303. https://doi.org/10.1029/2008GL035262

Replumaz, A., Kárason, H., van der Hilst, R. D., Besse, J., & Tapponnier, P. (2004). 4-D evolution of SE Asia's mantle from geological reconstructions and seismic tomography. *Earth and Planetary Science Letters*, 221(1–4), 103–115. https://doi.org/10.1016/S0012-821X(04)00070-6

Shi, H., Li, T., Zhang, R., Zhang, G., & Yang, H. (2020). Imaging of the upper mantle beneath Southeast Asia: Constrained by teleseismic P-wave tomography, *Remote Sensing*, 12(18), 2975. https://doi.org/10.3390/rs12182975

Sigl, M., Winstrup, M., McConnell, J. R., Welten, K. C., Plunkett, G., Ludlow, F., Büntgen, U., Caffee, M., Chellman, N., Dahl-Jensen, D., Fischer, H., Kipfstuhl, S., Kostick, C., Maselli, O. J., Mekhaldi, F., Mulvaney, R., Muscheler, R., Pasteris, D. R., Pilcher, J. R., Salzer, M., Schüpbach, S., Steffensen, Vinther, B. M., & Woodruff, T. E. (2015). Timing and climate forcing of volcanic eruptions for the past 2,500 years, *Nature*, 523, 54–5439. https://doi.org/10.1038/nature14565

Simmons, N. A., Forte, A. M., Boschi, L., & Grand, S. P. (2010). GyPSuM: A joint tomographic model of mantle density and seismic wave speeds. *Journal of Geophysical Research: Solid Earth*, 115, B12310. https://doi.org/10.1029/2010JB007631

Simmons, N. A., Myers, S. C., Johannesson, G., & Matzel, E. (2012). LLNL-G3Dv3: Global P wave tomography model for improved regional and teleseismic travel time prediction. *Journal of Geophysical Research: Solid Earth*, 117, B10302. https://doi.org/10.1029/2012JB009525

Spakman, W., & Hall, R. (2010). Surface deformation and slab–mantle interaction during Banda arc subduction rollback. *Nature Geoscience*, 3, 562–566. https://doi.org/10.1038/ngeo917

Tesoniero, A., Auer, L., Boschi, L., & Cammarano, F. (2015). Hydration of marginal basins and compositional variations within the continental lithospheric mantle inferred from a new global model of shear and compressional velocity. *Journal of Geophysical Research: Solid Earth*, 120, 7789–7813. https://doi.org/10.1002/2015JB012026

Toyokuni, G., Matsuno, T., & Zhao, D. (2020). *P* wave tomography beneath Greenland and surrounding regions: 2. Lower mantle. *Journal of Geophysical Research: Solid Earth*, 125, e2020JB019839. https://doi.org/10.1029/2020JB0198379

Toyokuni, G., Zhao, D., & Chen, K. H. (2021). Structural control on the 2018 and 2019 Hualien earthquakes in Taiwan. *Physics of the Earth and Planetary Interiors*, 312, 106673. https://doi.org/10.1016/j.pepi.2021.106673

Um, J., & Thurber, C. (1987). A fast algorithm for two-point seismic ray tracing. *Bulletin of the Seismological Society of America*, 77(3), 972–986.

Wang, X., Chen, Q.-F., Niu, F., Wei, S., Ning, J., Li, J., Wang, W., Buchen, J., & Liu, L. (2020). Distinct slab interfaces imaged within the mantle transition zone. *Nature Geoscience*, 13, 822–827. https://doi.org/10.1038/s41561-020-00653-5

Wehner, D., Blom, N., Rawlinson, N., Daryono, D., Boehm, C., Miller, M. S., Supendi, P., & Widiyantoro, S. (2021). SASSY21: A 3-D seismic structural model of the lithosphere and underlying mantle beneath Southeast Asia from multi-scale adjoint waveform tomography. https://doi.org/10.1002/essoar.10507767.1

Wei, W., Xu, J., Zhao, D., & Shi, Y. (2012). East Asia mantle tomography: New insight into plate subduction and intraplate volcanism. *Journal of Asian Earth Sciences*, 60, 88–103. https://doi.org/10.1016/j.jseaes.2012.08.001

Wessel, P., Smith, W. H. F., Scharroo, R., Luis, J., & Wobbe, F. (2013). Generic Mapping Tools: Improved Version Released. *Eos, Transactions, American Geophysical Union*, 94(45), 409. https://doi.org/10.1002/2013EO450001

Widiyantoro, S., Pesicek, J. D., & Thurber, C. H. (2011). Subducting slab structure below the eastern Sunda arc inferred from non-linear seismic tomographic imaging. *Geological Society, London, Special Publications*, 355, 139–155. https://doi.org/10.1144/SP355.7

Yang, T., Gurnis, M., & Zahirovic, S. (2016). Mantle-induced subsidence and compression in SE Asia since the early Miocene. *Geophysical Research Letters*, 43, 1901–1909. https://doi.org/10.1002/2016GL068050

Yang, Z., Zhao, D., Dong, Y., & Cheng, B. (2022). Crustal flow and fluids affected the 2021 M7.4 Maduo earthquake in Northeast Tibet. *Journal of Asian Earth Sciences*, 225, 105050. https://doi.org/10.1016/j.jseaes.2021.105050

Zahirovic, S., Flament, N., Müller, R. D., Seton, M., & Gurnis, M. (2016). Large fluctuations of shallow seas in low-lying Southeast Asia driven by mantle flow. *Geochemistry, Geophysics, Geosystems*, 17, 3589–3607. http://dx.doi.org/10.1002/2016GC006434

Zenonos, A., De Siena, L., Widiyantoro, S., & Rawlinson, N. (2019). P and S wave travel time tomography of the SE Asia-Australia collision zone. *Physics of the Earth and Planetary Interiors*, 293, 106267. https://doi.org/10.1016/j.pepi.2019.05.010

Zhao, D. (2015). *Multiscale Seismic Tomography*, 304 pp. Tokyo: Springer. https://doi.org/10.1007/978-4-431-55360-1

Zhao, D. (2004). Global tomographic images of mantle plumes and subducting slabs: insight into deep Earth dynamics. *Physics of the Earth and Planetary Interiors*, 146, 3–34. https://doi.org/10.1016/j.pepi.2003.07.032

Zhao, D., Fujisawa, M., & Toyokuni, G. (2017). Tomography of the subducting Pacific slab and the 2015 Bonin deepest earthquake (Mw 7.9). *Scientific Reports*, 7, 44487. https://doi.org/10.1038/srep44487

Zhao, D., Hasegawa, A., & Horiuchi, S. (1992). Tomographic imaging of P and S wave velocity structure beneath northeastern Japan. *Journal of Geophysical Research*, 97, 19909–19928. https://doi.org/10.1029/92JB00603

Zhao, D., Toyokuni, G., & Kurata, K. (2021). Deep mantle structure and origin of Cenozoic intraplate volcanoes in Indochina, Hainan and South China Sea. *Geophysical Journal International*, 225, 572–588. https://doi.org/10.1093/gji/ggaa605

Zhao, D., Yamamoto, Y., & Yanada, T. (2013). Global mantle heterogeneity and its influence on teleseismic regional tomography. *Gondwana Research*, 23, 595–616. https://doi.org/10.1016/j.gr.2012.08.004

Zou, H., & Fan, Q. (2010). U-Th isotopes in Hainan basalts: implications for sub-asthenospheric origin of EM2 mantle endmember and the dynamics of melting beneath Hainan Island. *Lithos*, 116, 145–152. https://doi.org/10.1016/j.lithos.2010.01.010

Table 1. Information on the 10 resolution tests performed by this study.

Name	Description of the initial model
CRT1	Checkerboard resolution test #1. Lateral grid interval is 278 km (a great circle distance of 2.5° on the surface) inside the study region, and 556 km (a great circle distance of 5° on the surface) in other regions (Table S2).
CRT2	Checkerboard resolution test #2. Lateral grid interval is 167 km (a great circle distance of 1.5° on the surface) inside the study region, and 334 km (a great circle distance of 3° on the surface) in other regions (Table S3).
RRT	Restoring resolution test. Highlights the pattern of actual tomographic results, containing high-V (+1.5%) and low-V (−1.5%).
SRT1	Synthetic resolution test #1. Input model contains the following structures: (1) Subducting Australian slab with high-V (+1.5%) at depths of 15−725 km. (2) Hot mantle upwelling in the mantle wedge with low-V (−1.5%) at depths of 15−500 km. (3) Subslab hot mantle upwelling (SHMU) with low-V (−1.5%) at depths of 150−1500 km. (4) A hole in the Australian slab between depths 260−460 km and latitudes 110°−115° with no velocity perturbation. (5) A low-V (−1.5%) bridge elongated in the latitudinal direction with the width of 2° in the longitudinal direction between depths 260−460 km, connecting (2) and (3) through the slab hole (4). (6) A low-V (−1.5%) conduits with a radius of 222 km (a great circle distance of 2° on the surface) elongated between depths 15−2800 km beneath the Hainan hotspot.
SRT2	Synthetic resolution test #2. Input model is same as SRT1 but without (5).
SRT3	Synthetic resolution test #3. Input model is same as SRT1 but without (4) and (5).
SRT4	Synthetic resolution test #4. Input model is same as SRT1 but without (3) and (5).
SRT5	Synthetic resolution test #5. Input model is same as SRT1 but without (2) and (5).
SRT6	Synthetic resolution test #6. Input model is same as SRT1 but without (2), (3), and (5).
SRT7	Synthetic resolution test #7. Input model is same as SRT1 but without (2), (3), (4), and (5).

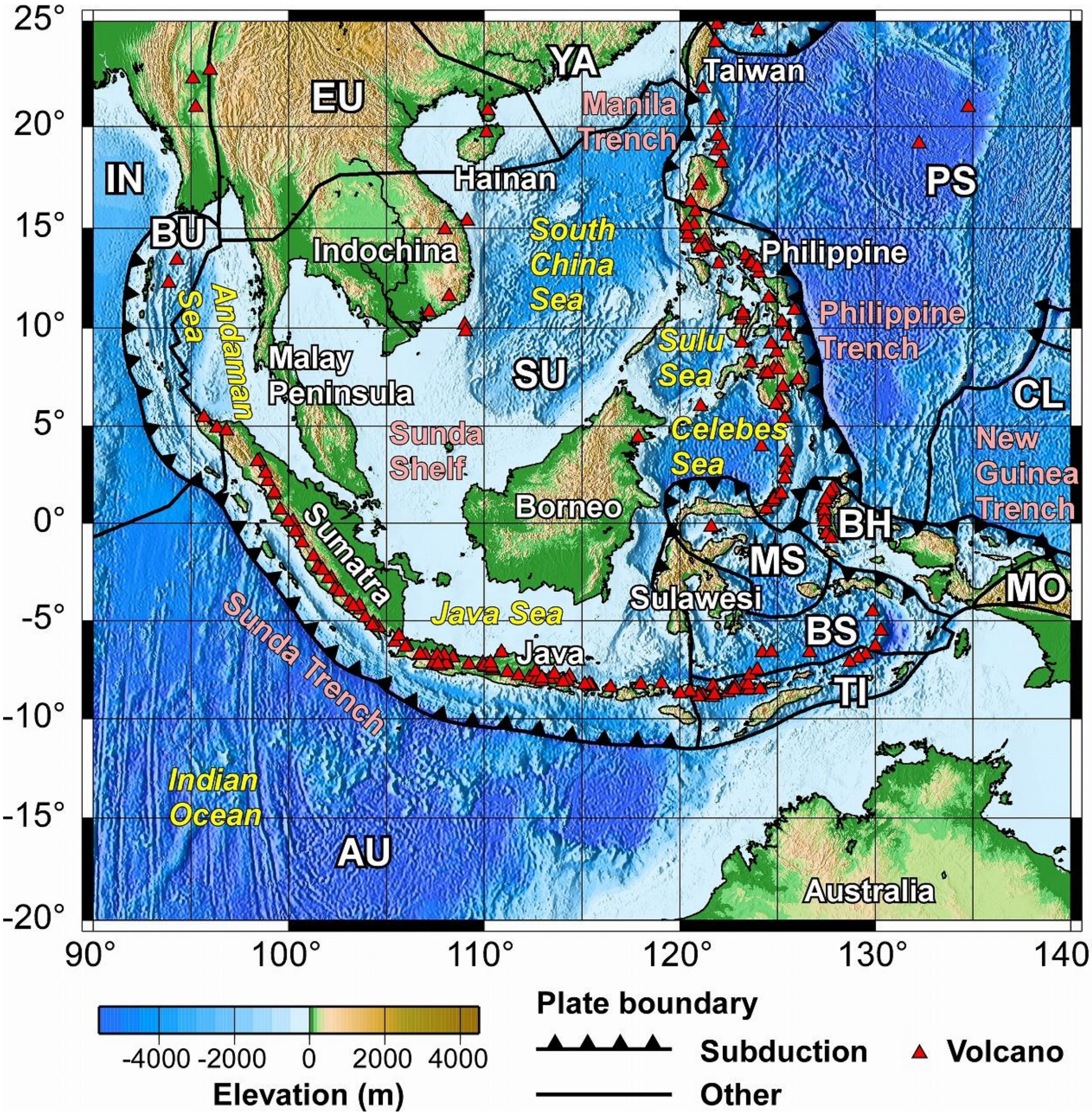

Figure 1. Map of our study region. The colors show the elevation whose scale is shown at the lower-left corner. The red triangles denote active volcanoes. The thick black lines denote plate boundaries (Bird, 2003), among which the jagged lines are subduction boundaries (trenches). AU = Australian Plate; BH = Bird's Head Plate; BS = Banda Sea Plate; BU = Burma Plate; CL =

Caroline Plate; EU = Eurasian Plate; IN = Indian Plate; MO = Maoke Plate; MS = Molucca Sea Plate; PS = Philippine Sea Plate; SU = Sunda Plate; TI = Timor Plate; YA = Yangtze Plate.

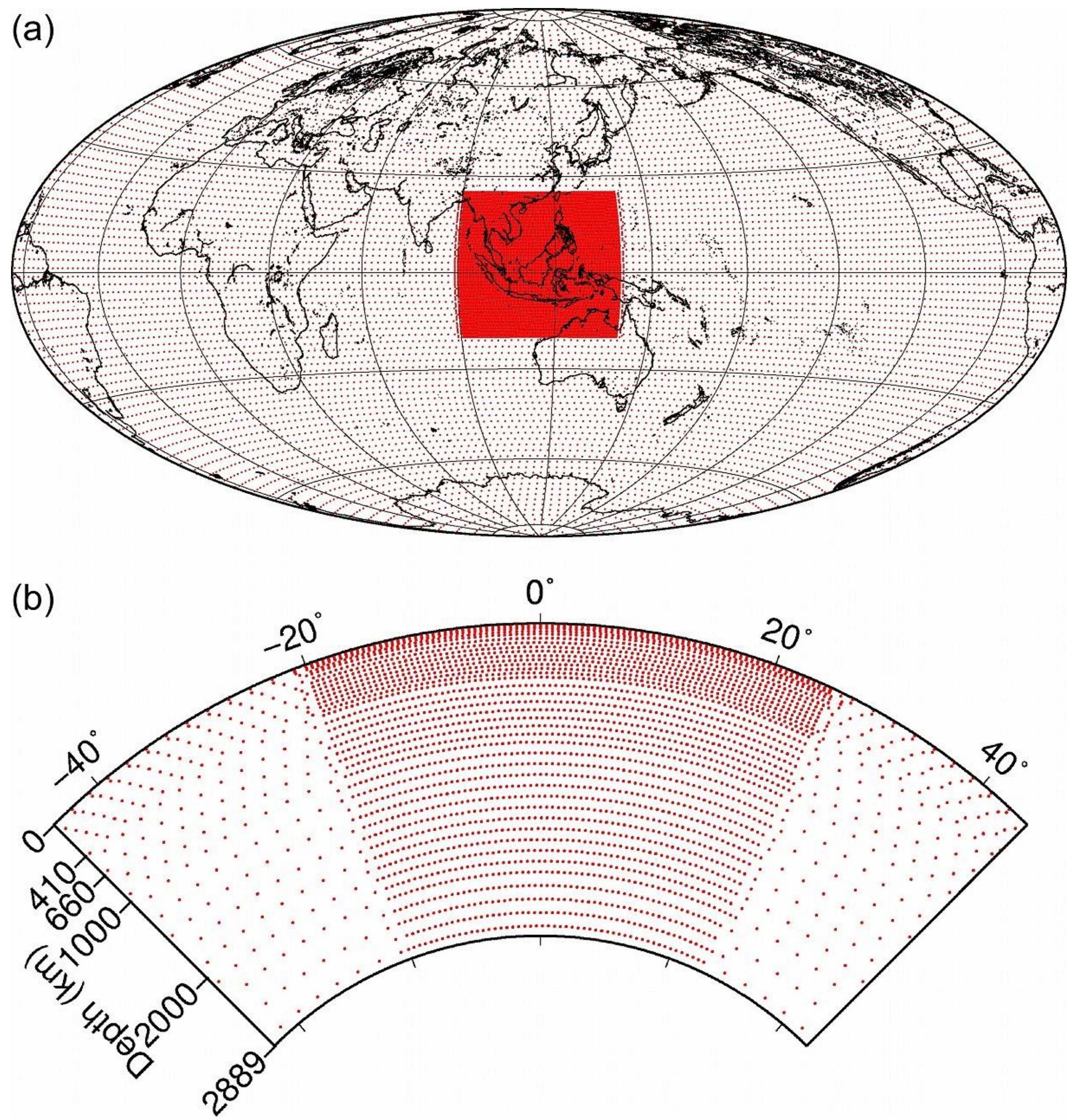

Figure 2. **(a)** Map view at a depth of 15 km and **(b)** N-S vertical cross-section along the longitude of 115° showing the 3-D grid nodes adopted for the tomographic inversion. In the

target area (the red box in (a)), a denser grid is arranged, whereas a coarser grid is set up in the surrounding crust and mantle of the Earth. The numbers atop (b) denote latitudes.

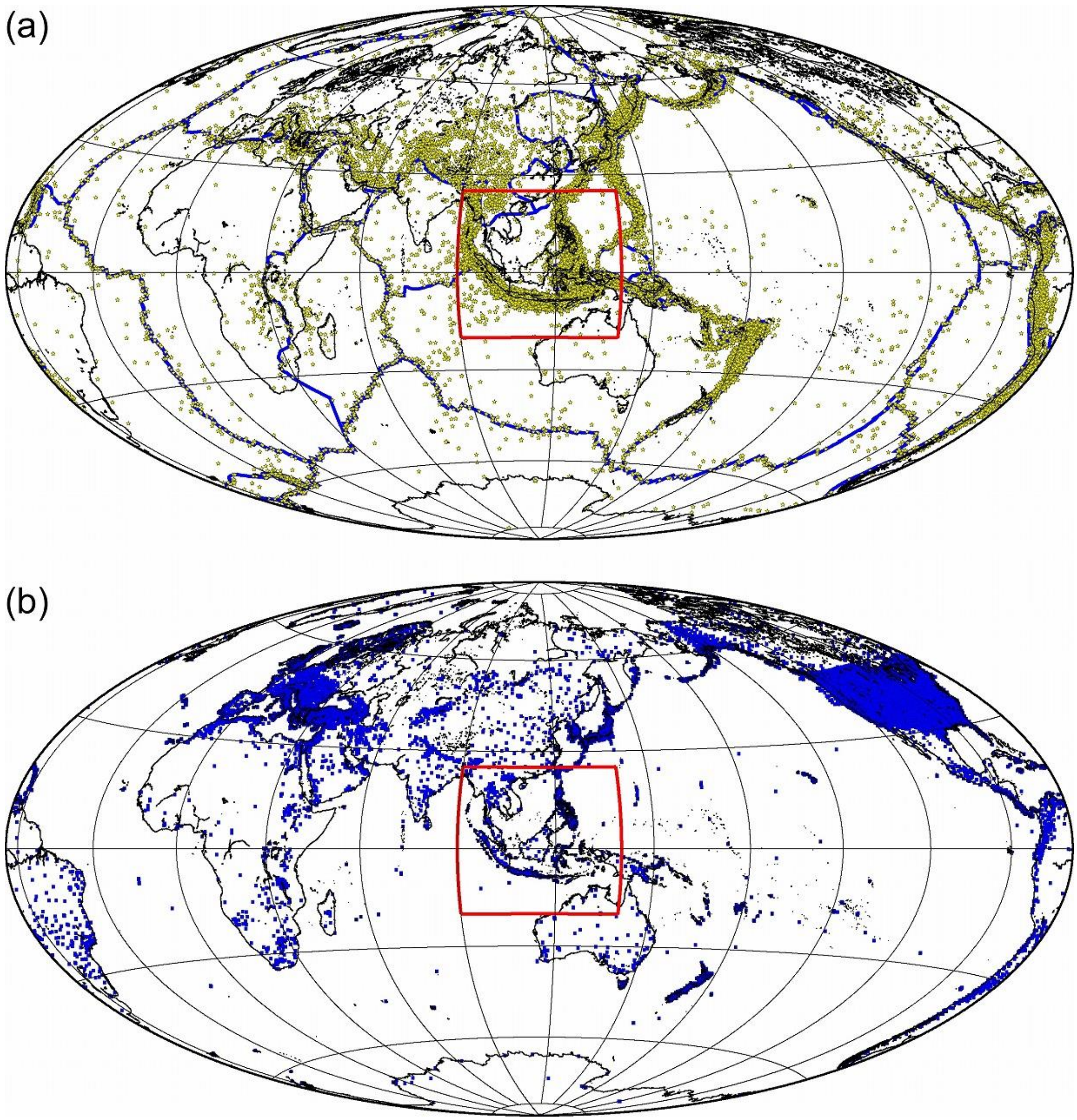

Figure 3. Distribution of 23,587 earthquakes **(a)** and 14,136 seismic stations **(b)** used in the tomographic inversion. The red box indicates the target area. The thick black lines denote plate boundaries.

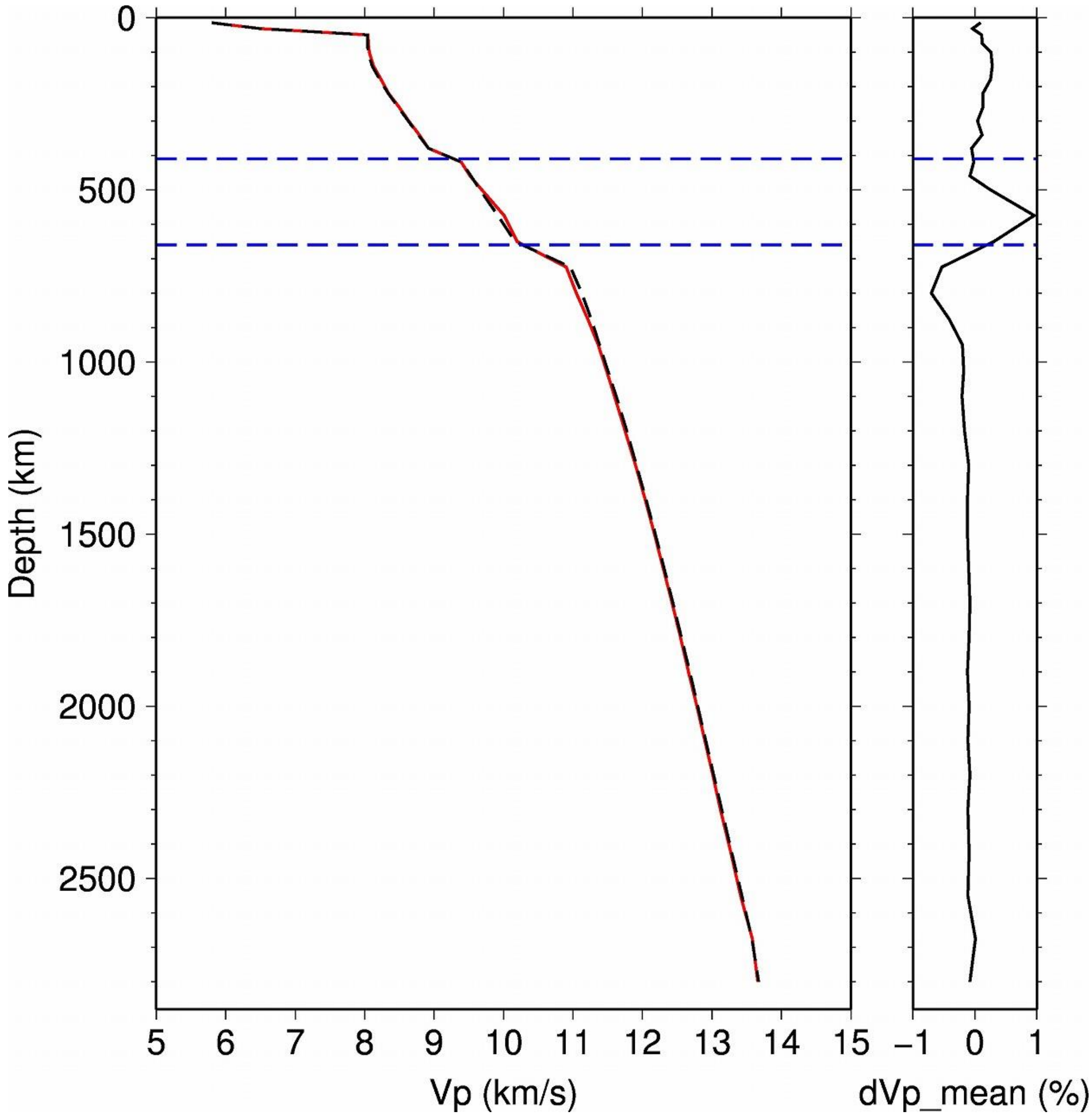

Figure 4. **(Left)** The starting 1-D P-wave velocity model (IASP91, Kennett & Engdahl, 1991) adopted for the tomographic inversions (black dotted line), and optimized 1-D P-wave velocity model after subtracting the average velocity anomaly of the tomographic results at each depth (red solid line). **(Right)** Depth distribution of the average velocity anomaly. The blue dotted lines denote 410 and 660 km indicating the range of the mantle transition zone.

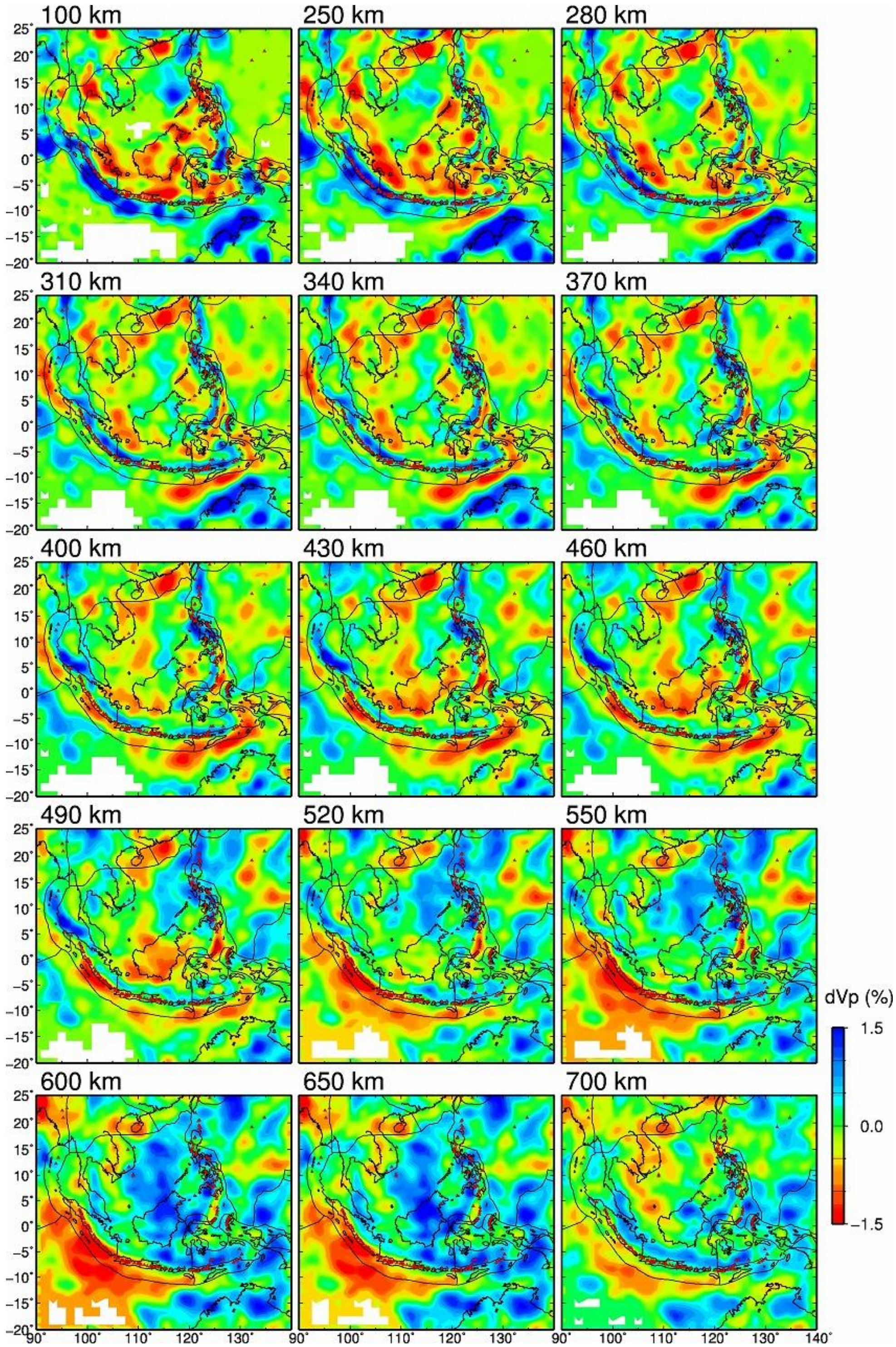

Figure 5. Map views of Vp tomography at depths of 100–700 km obtained by this study. The layer depth is shown at the upper-right corner of each map. The blue and red colors denote high

and low Vp perturbations, respectively, whose scale (in %) is shown on the right. Areas with hit counts < 50 are masked in white. The red triangles and thick black lines denote the active volcanoes and plate boundaries, respectively.

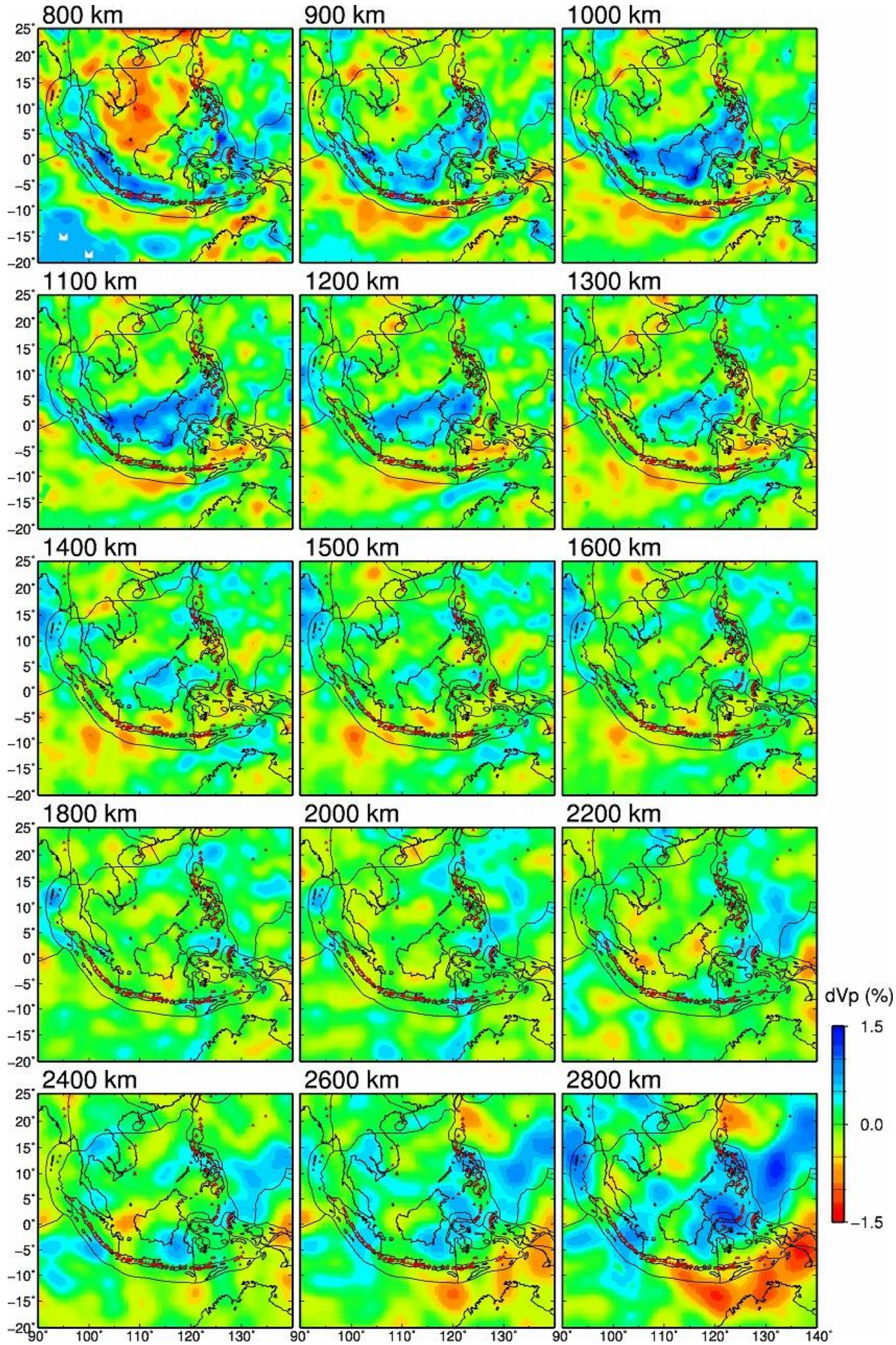

Figure 6. Same as Figure 5 but for Vp images at depths of 800–2800 km.

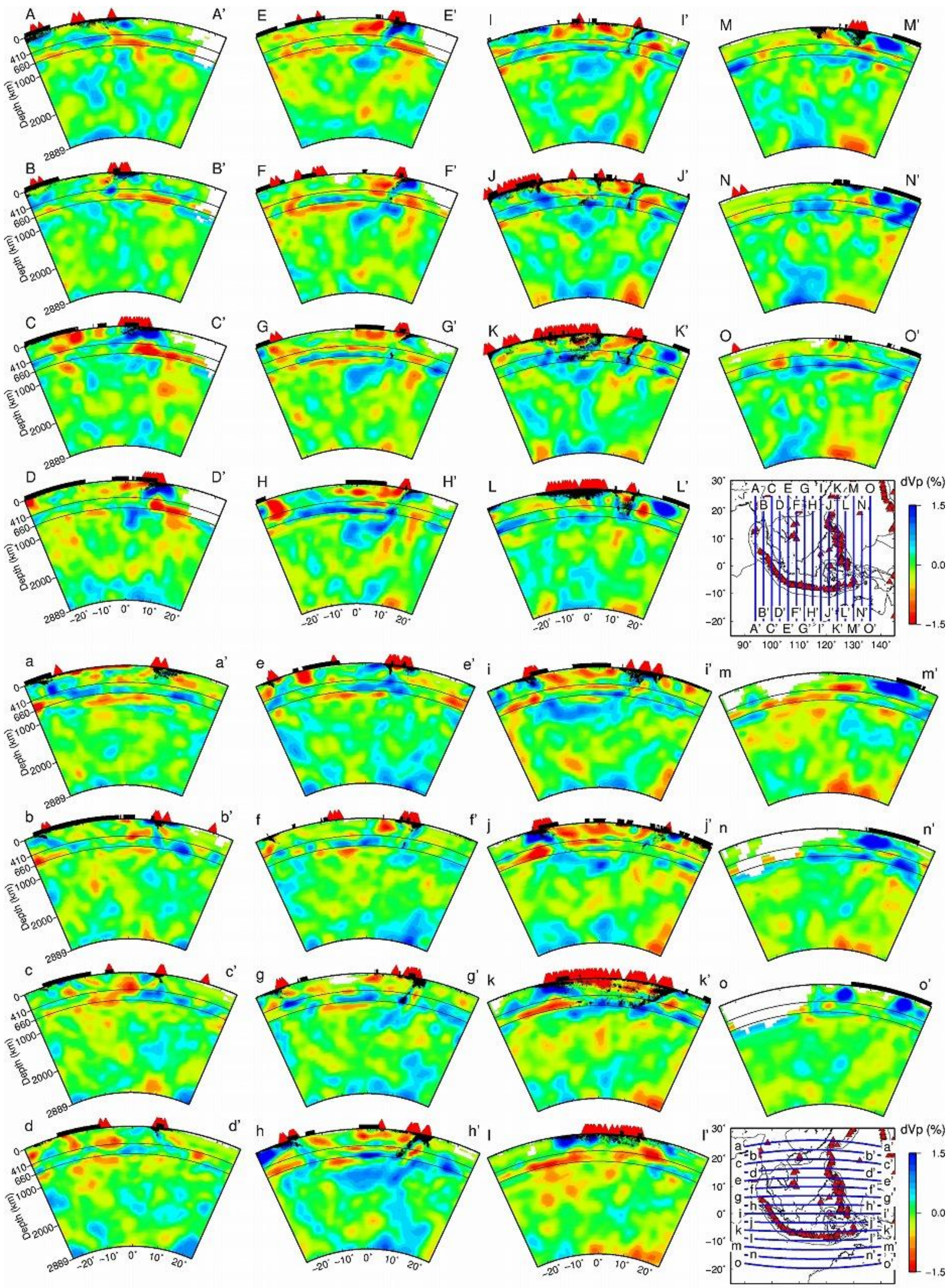

Figure 7. Vertical cross-sections of Vp tomography along **(top)** 15 profiles in the N-S direction (A-A' to O-O'), and **(bottom)** 15 profiles in the E-W direction (a-a' to o-o') as shown on the

inset map. The 410-km and 660-km discontinuities are shown in black solid lines. The thick black lines on the surface denote land areas. Other labels are the same as those in Figure 5.

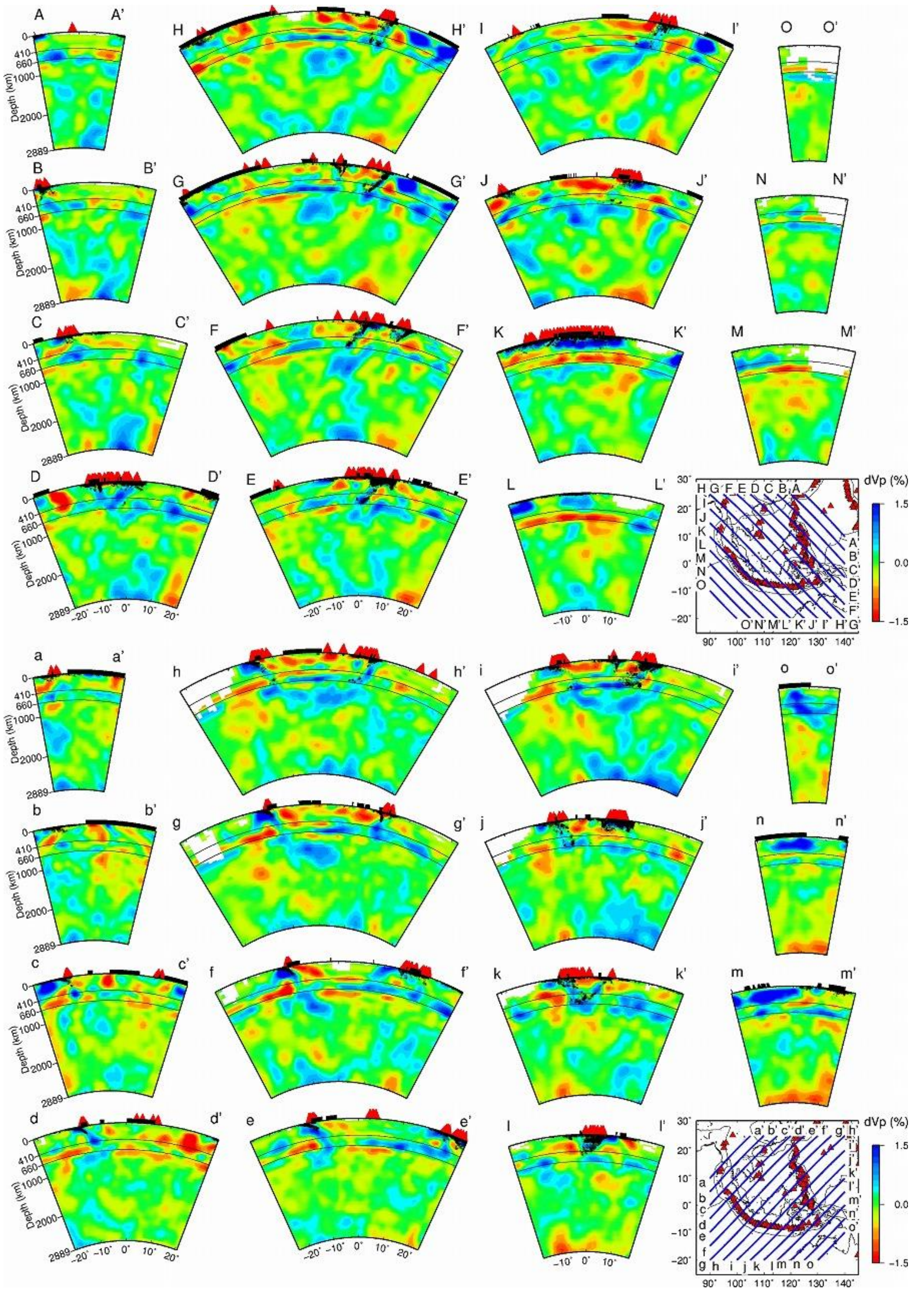

Figure 8. The same as Figure 7 but along **(top)** 15 profiles in the NW-SE direction (A-A' to O-O'), and **(bottom)** 15 profiles in the NE-SW direction (a-a' to o-o').

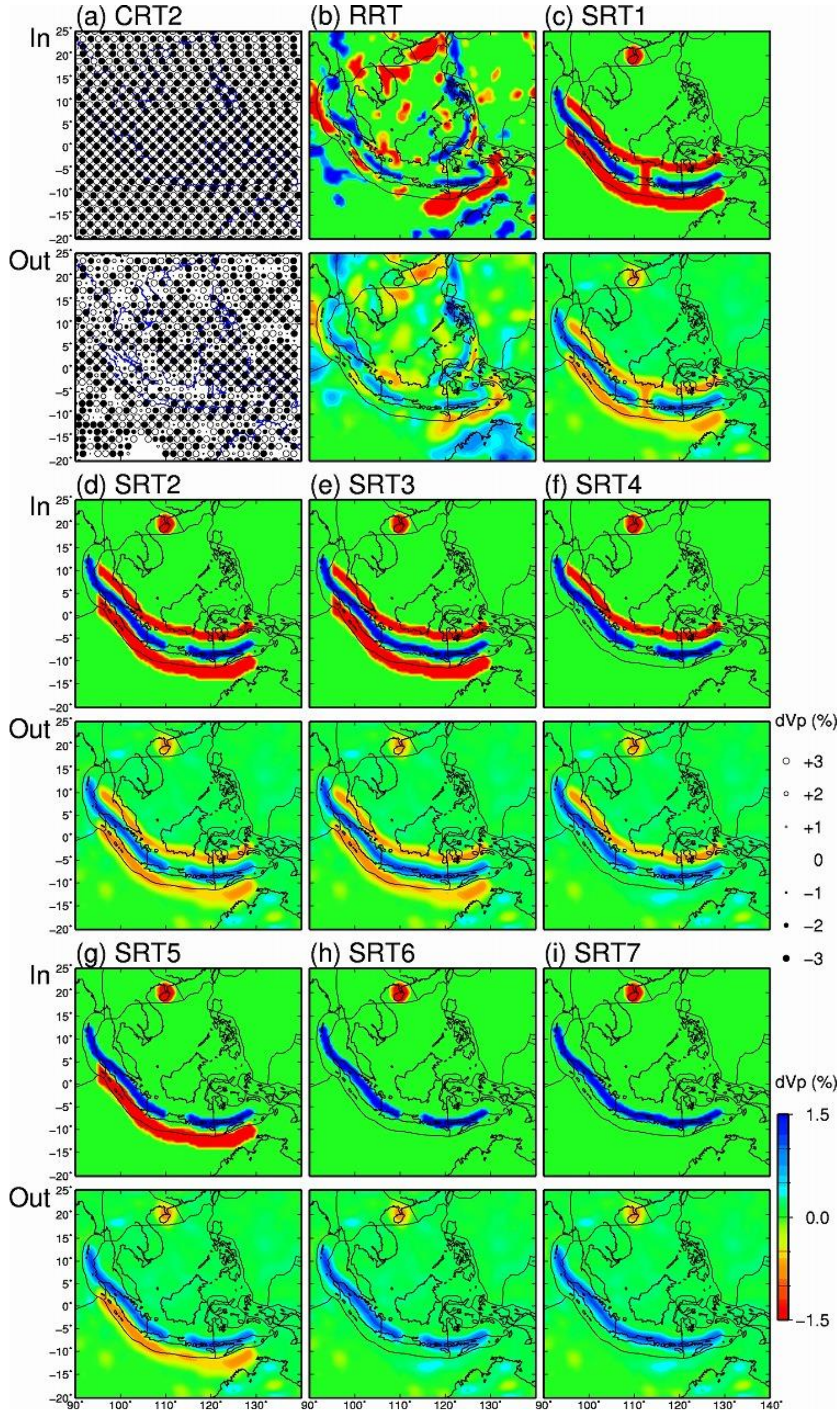

Figure 9. Summary of the resolution tests. Map view images at a depth of 380 km of the **(a)** CRT2, **(b)** RRT, **(c)** SRT1, **(d)** SRT2, **(e)** SRT3, **(f)** SRT4, **(g)** SRT5, **(h)** SRT6, and **(i)** SRT7.

The input (upper panel) and output (lower panel) models are shown for each test. The Vp perturbation scales (in %) are shown on the right.

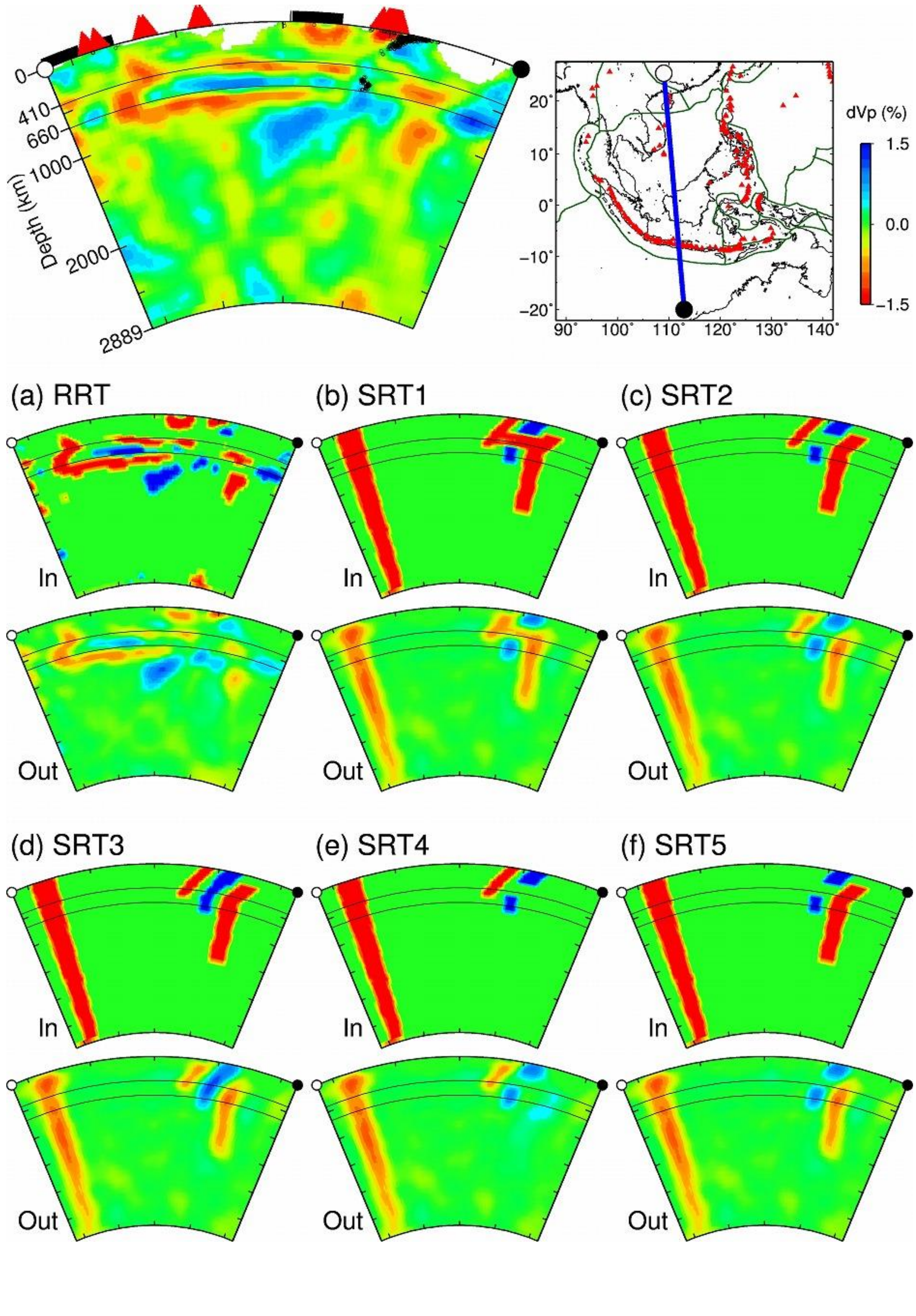

Figure 10. Summary of the resolution tests and comparison with the obtained real tomographic result (the upper-left panel). Vertical cross-sections through a hole in the Australian slab and the

Hainan hotspot for **(top)** actual tomography, **(a)** RRT, **(b)** SRT1, **(c)** SRT2, **(d)** SRT3, **(e)** SRT4, and **(f)** SRT5. The input (upper panel) and output (lower panel) models are shown for each test. The location of the cross-section and the Vp perturbation scale (in %) are shown at the top right. Other labels are the same as those in Figure 7.

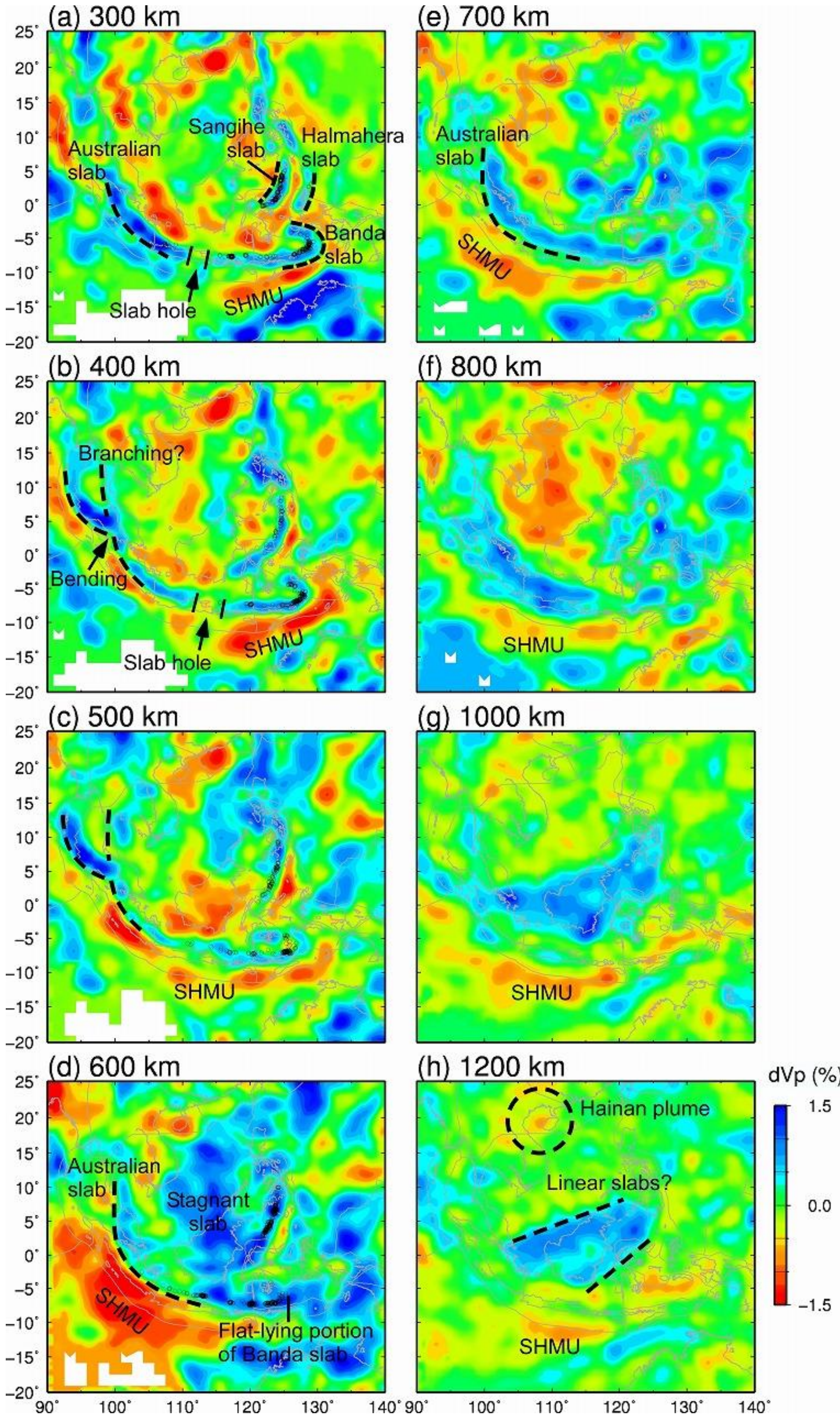

Figure 11. Summary and interpretation of Vp map views at depths of 300–1200 km. The Vp perturbation scale (in %) is shown on the right. The coastline and plate boundaries are shown in

gray to make the velocity images easier to see. The open circles denote local seismicity within a ±30-km depth range of each layer. SHMU = subslab hot mantle upwelling.

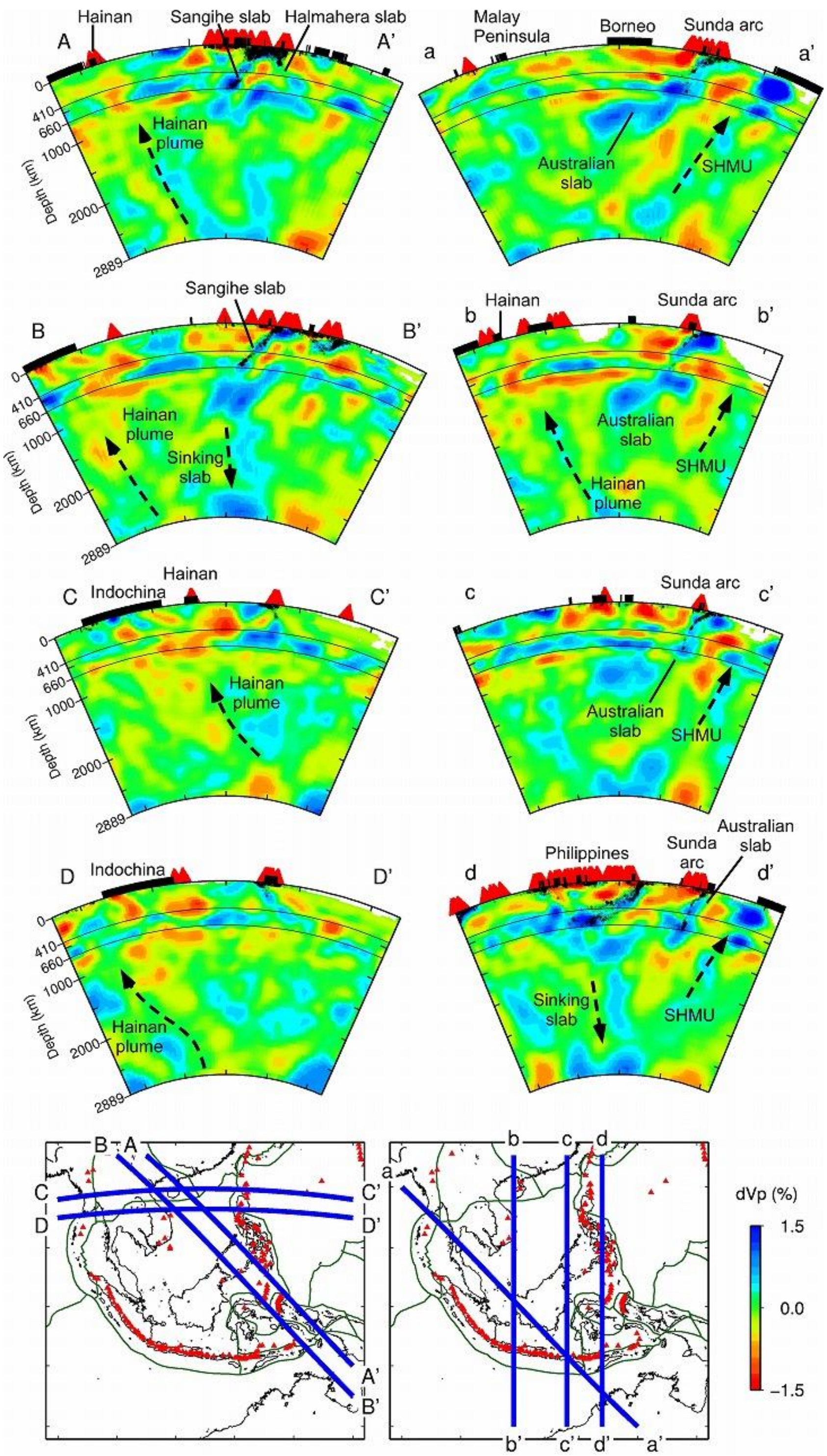

Figure 12. Summary and interpretation of Vp vertical cross-sections through **(left)** the Hainan hotspot and Indochina (A-A’ to D-D’), and **(right)** the Australian slab (a-a’ to d-d’), whose

locations are shown on the inset maps at the bottom. The Vp perturbation scale (in %) is shown on the right. Other labels are the same as those in Figure 7.

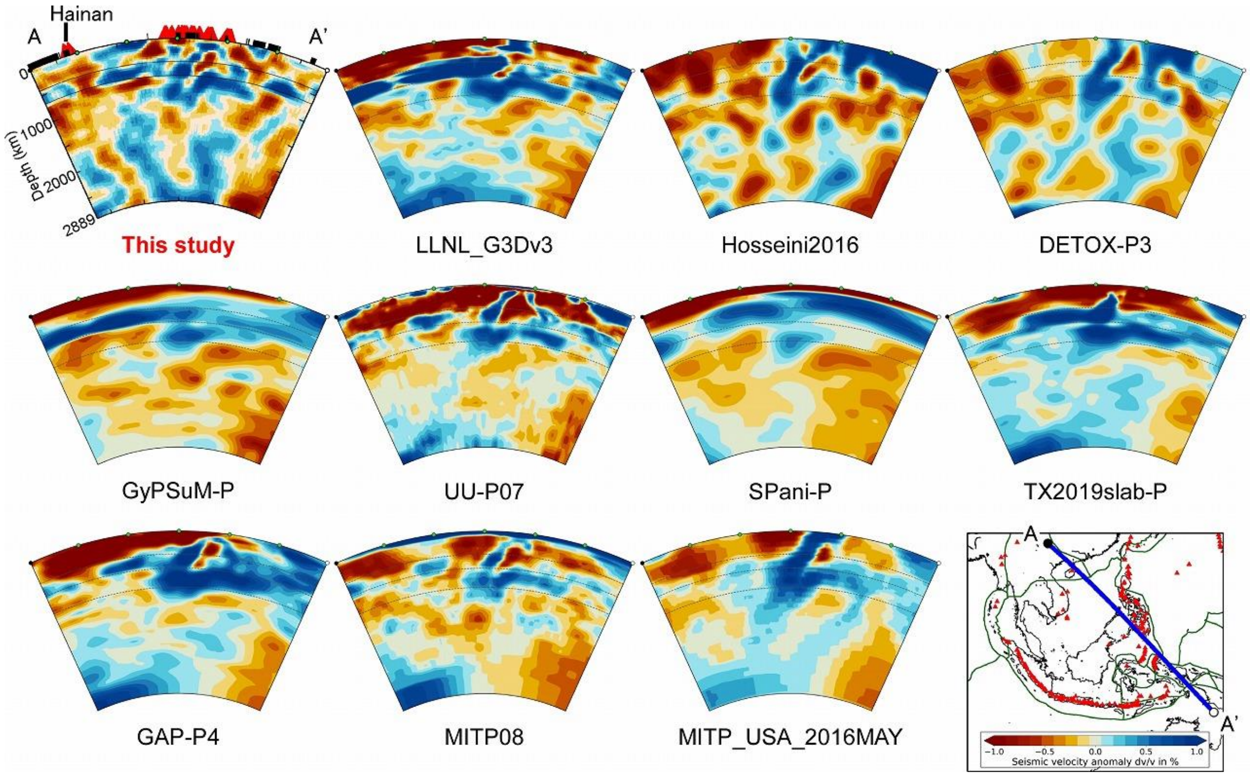

Figure 13. Comparison of a Vp vertical cross-section oriented in the NW-SE direction through the Hainan hotspot obtained by this study (upper left) with 10 existing models, i.e., UU-P07 (Amaru, 2007), MITP08 (Li et al., 2008), GyPSuM-P (Simmons et al., 2010), LLNL_G3Dv3 (Simmons et al., 2012), GAP-P4 (Fukao & Obayashi, 2013; Obayashi et al., 2013), SPani-P (Tesoniero et al., 2015), Hosseini2016 (Hosseini, 2016), MITP_USA_2016MAY (Burdick et al., 2017), TX2019slab-P (Lu et al., 2019), and DETOX-P3 (Hosseini et al., 2020). All figures are shown with the same color scale. The blue and red colors denote high and low Vp perturbations, respectively, whose scale (in %) is shown at the bottom of each panel.

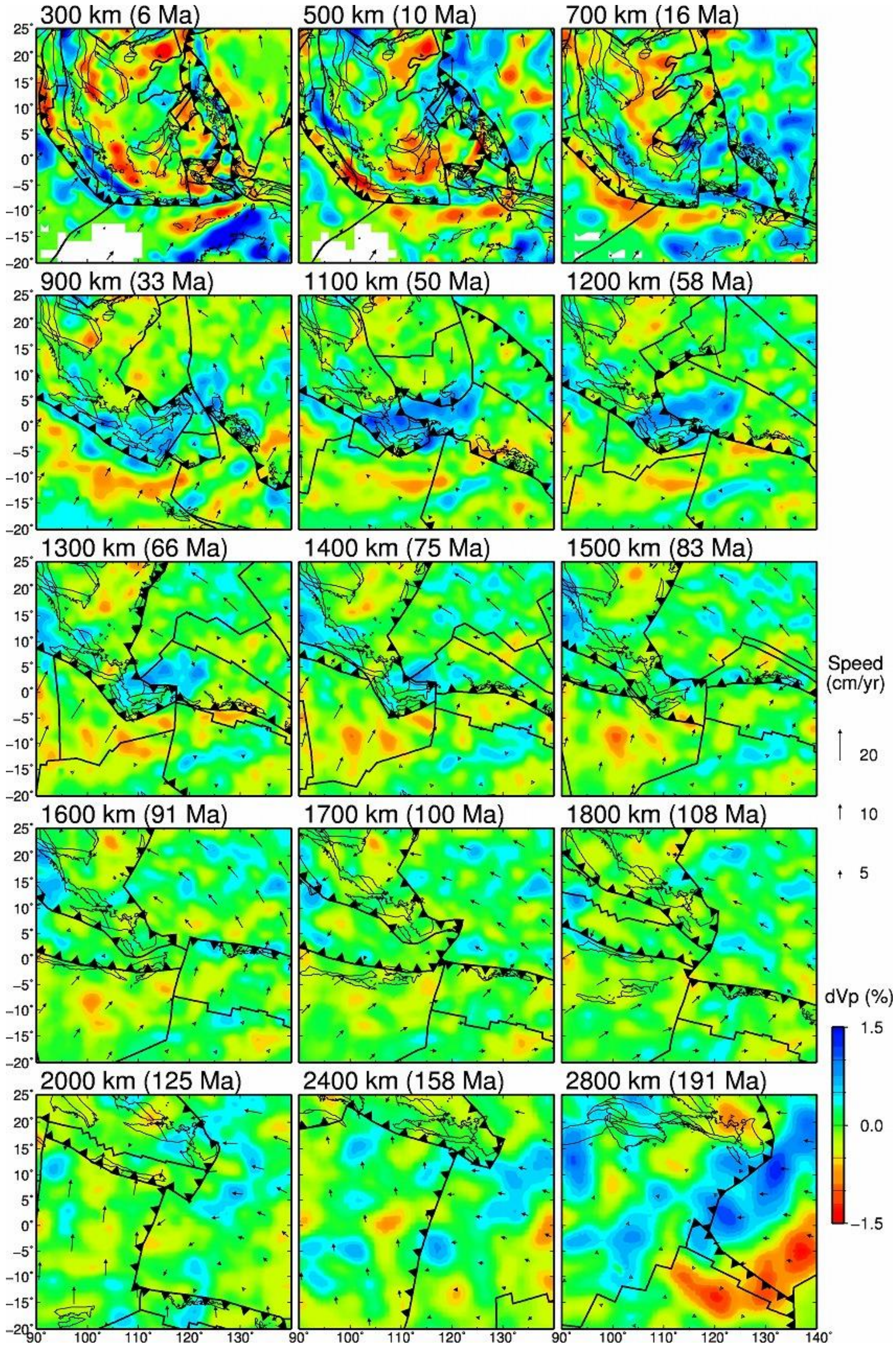

Figure 14. Comparison of Vp map views obtained by this study with plate reconstructions (Müller et al., 2019) using an age-depth relationship (Lithgow-Bertelloni & Richards, 1998). The

thin black lines denote geological blocks. The thick black lines denote plate boundaries, among which the jagged lines are subduction boundaries. Thin arrows denote absolute plate motion direction and speed, whose scale (in %) is shown on the right.

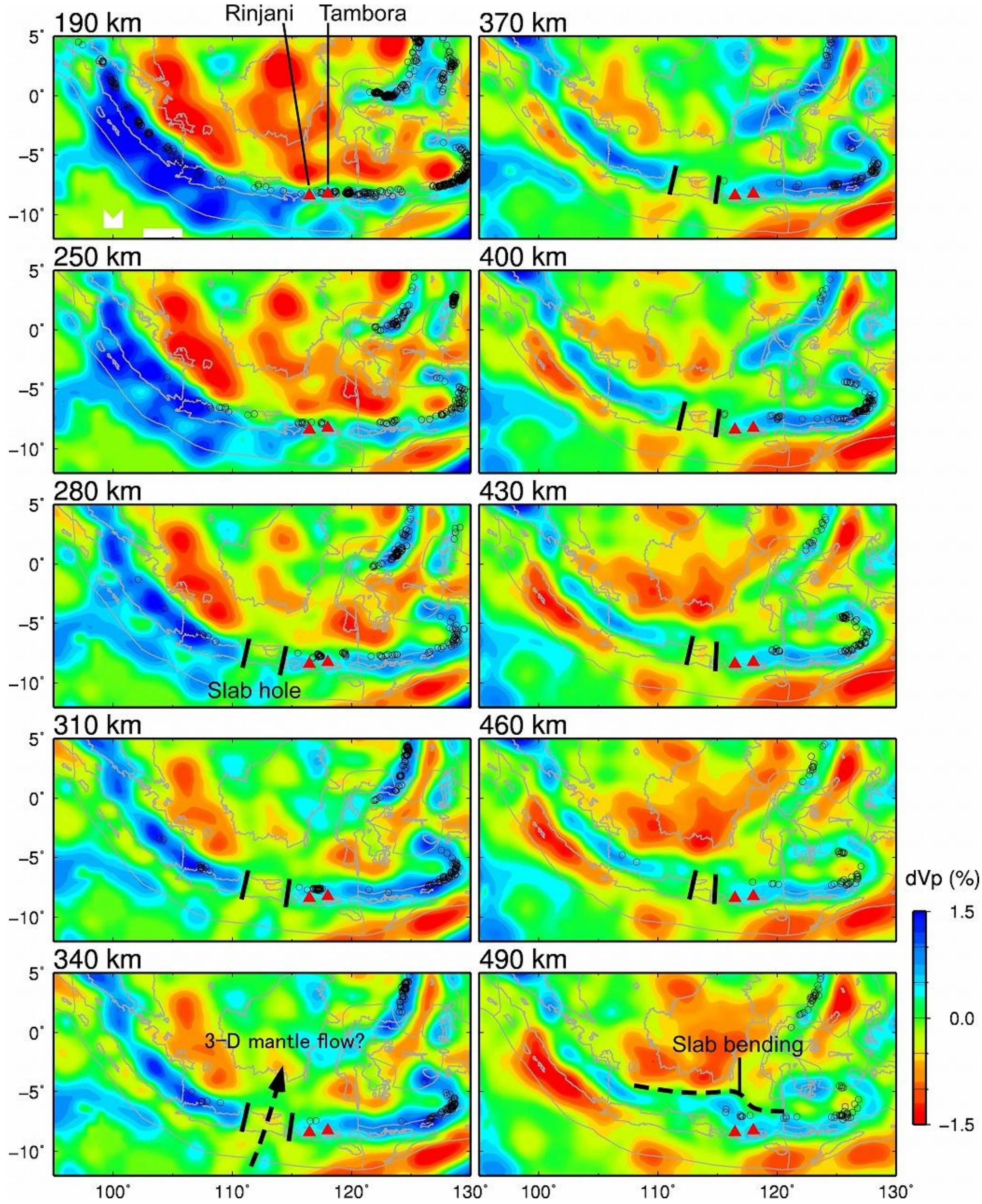

Figure 15. Enlarged map views of Vp tomography at depths of 190–490 km around the Australian slab. The layer depth is shown at the upper-right corner of each map. The blue and red

colors denote high and low Vp perturbations, respectively, whose scale (in %) is shown on the right. Areas with hit counts < 50 are masked in white. The identified hole in the Australian slab is indicated in-between the two black solid lines. The red triangles denote the Tambora and Rinjani volcanoes, which are only two located in this region of the 25 world's volcanoes that caused large volcanic eruptions during the past 2500 years (Sigl et al., 2015). The open circles denote local seismicity within a ±15-km depth range of each layer.

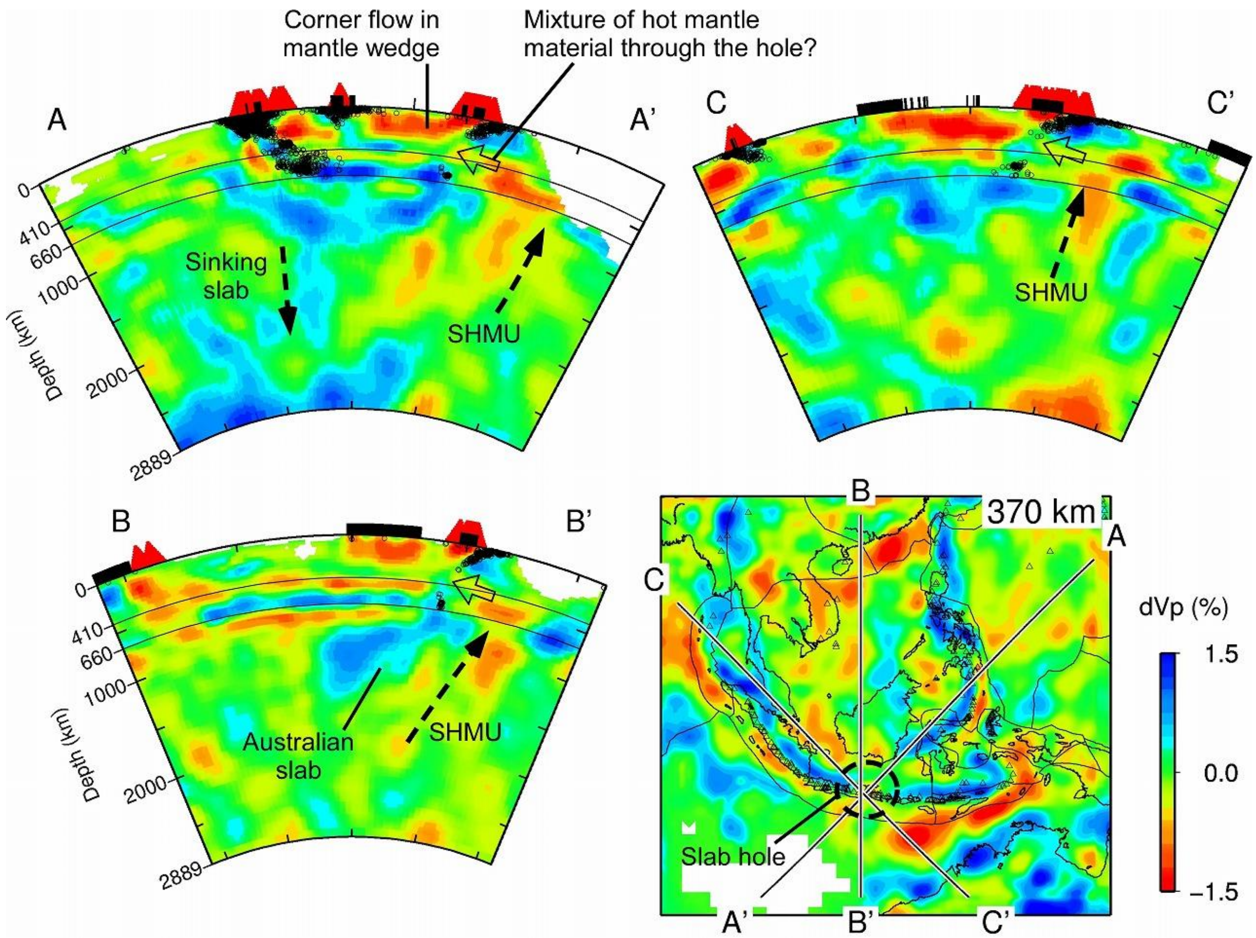

Figure 16. Vertical cross-sections (A-A' to C-C') and a map view (lower right) through the hole in the Australian slab beneath eastern Java. The red triangles denote active volcanoes within a ±222 km width of each section. The open circles denote local seismicity within a ±111 km width of each section. Locations of the profiles are shown on the map. The map view shows the tomography at a depth of 370 km.

Journal of Geophysical Research: Solid Earth

Supporting Information for

Whole-mantle tomography of Southeast Asia: New insight into plumes and slabs

Genti Toyokuni[1], Dapeng Zhao[1], and Kenkichi Kurata[1]

[1]Department of Geophysics, Graduate School of Science, Tohoku University, Sendai 980-8578, Japan

Contents of this file

- Figures S1 to S62
- Tables S1 to S3

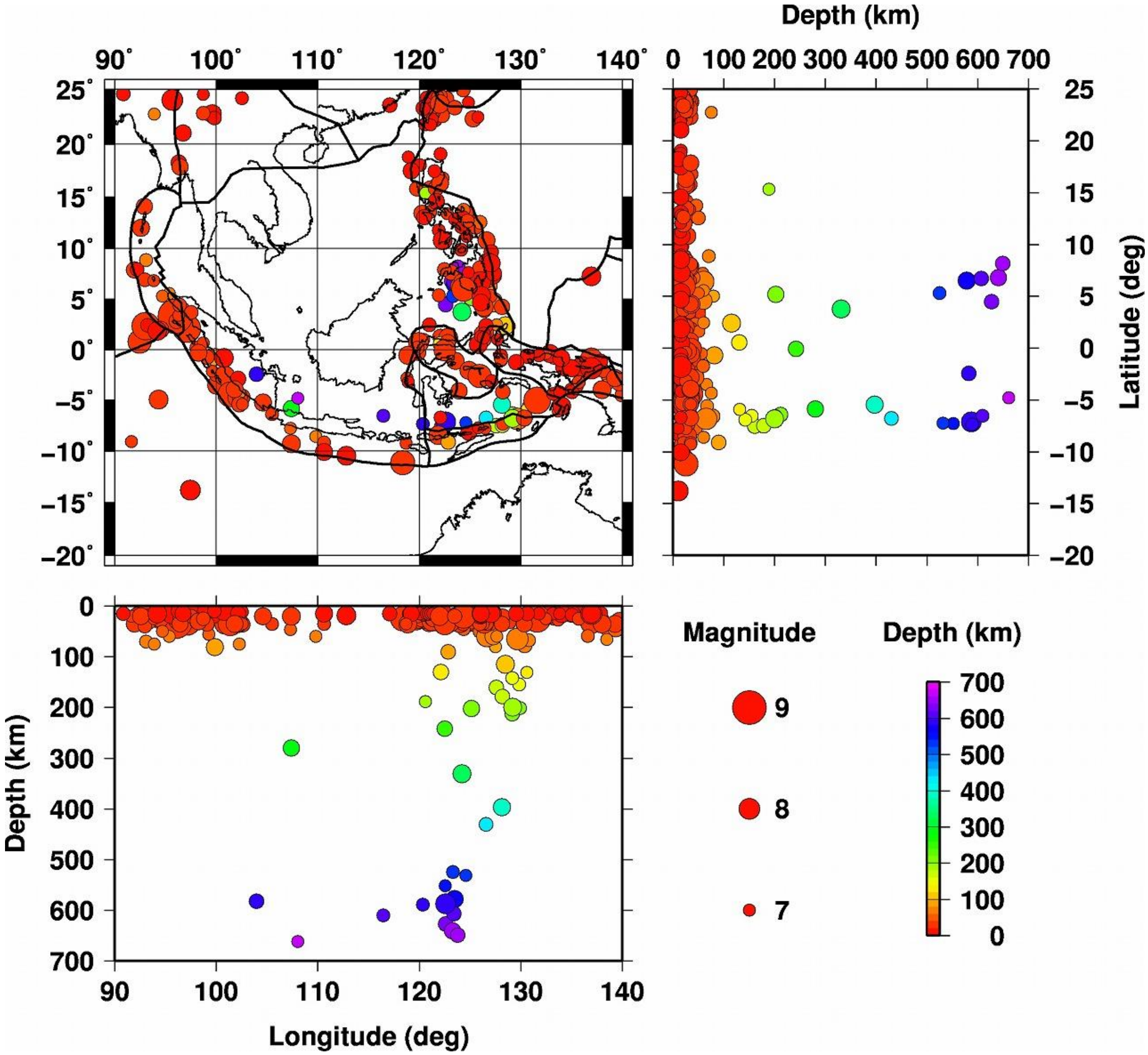

Figure S1. Hypocenter distribution of 287 large earthquakes (M ≥ 7) that occurred from January 1, 1900 to January 5, 2022 (https://earthquake.usgs.gov/). The circle size and color indicate the magnitude and focal depth, respectively, whose scales are shown in the lower right.

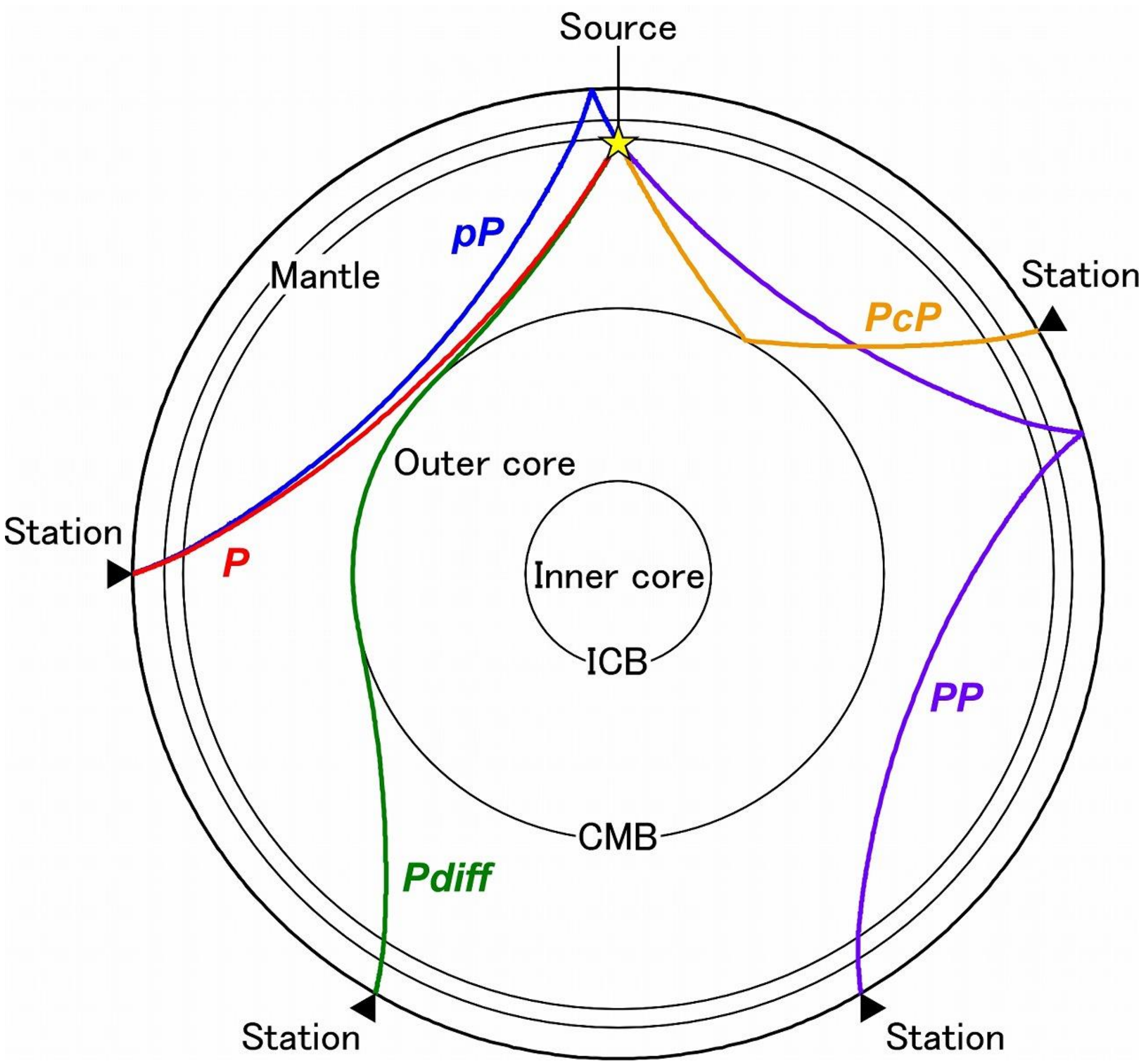

Figure S2. Schematic illustration of ray paths of P, pP, PP, PcP, and Pdiff waves. The star denotes a hypocenter. The reverse triangles denote seismic stations.

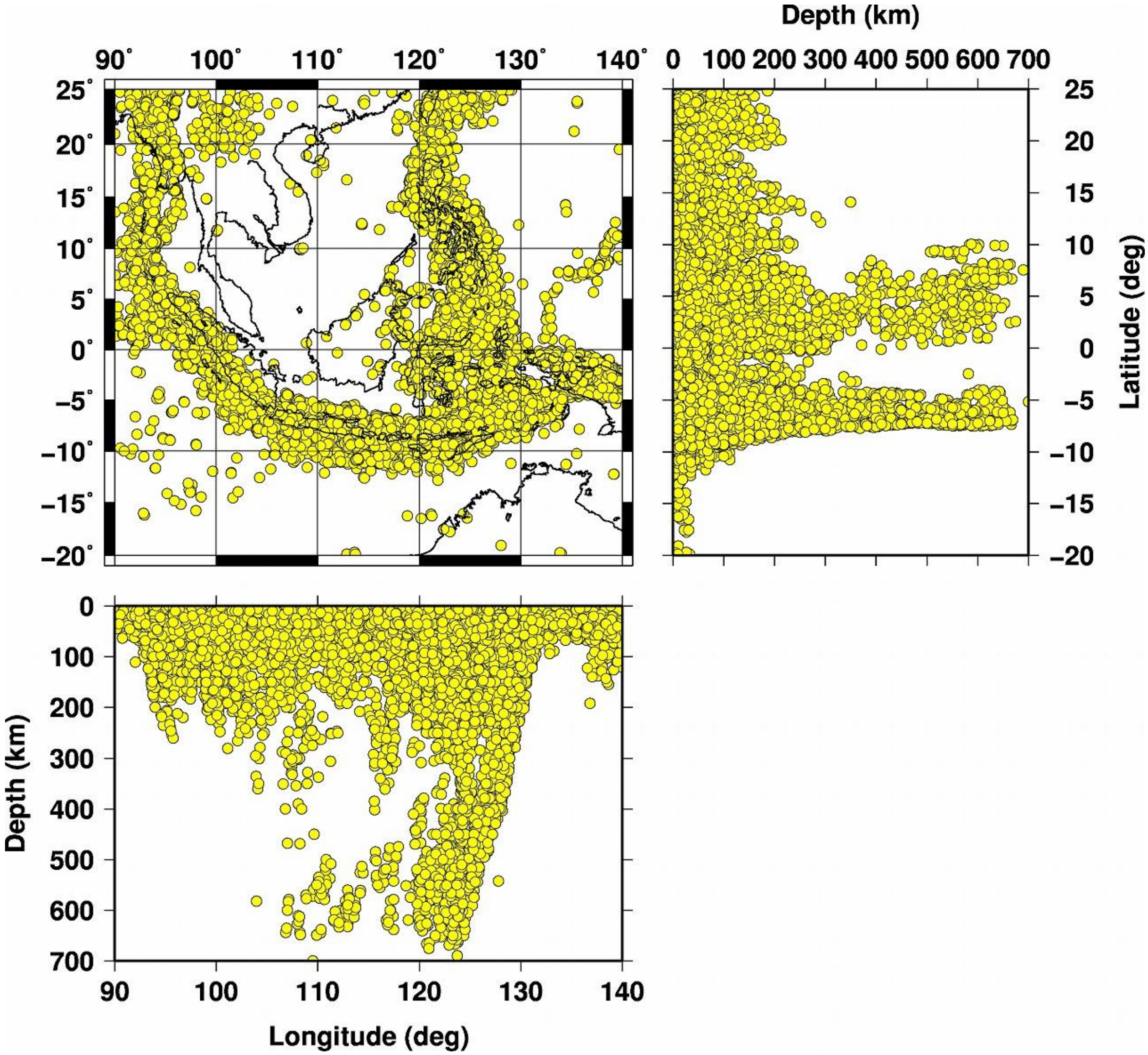

Figure S3. Distribution of 11,344 earthquakes inside the study volume, which are used in the tomographic inversion.

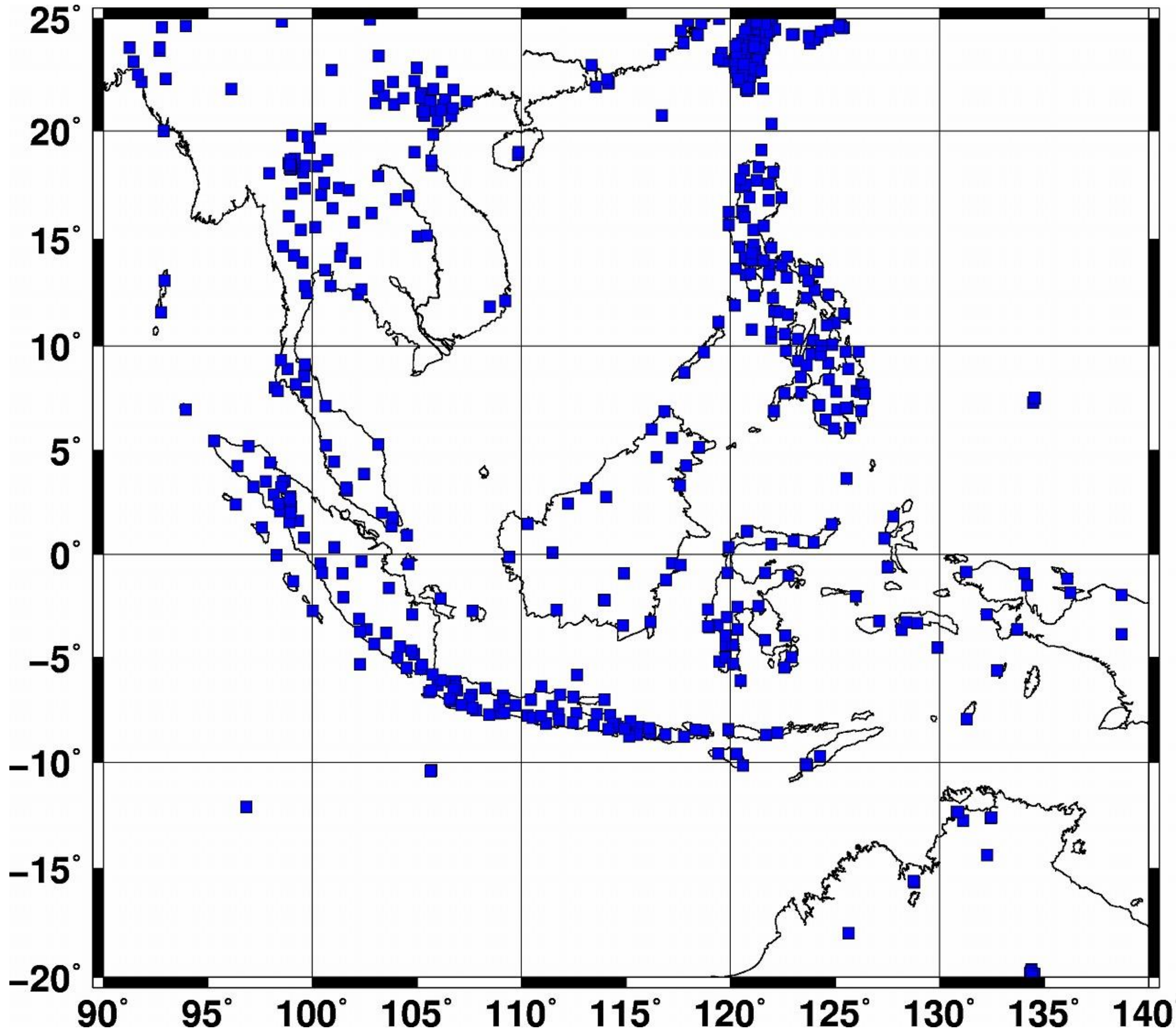

Figure S4. Distribution of 656 seismic stations inside the study region used in the tomographic inversion.

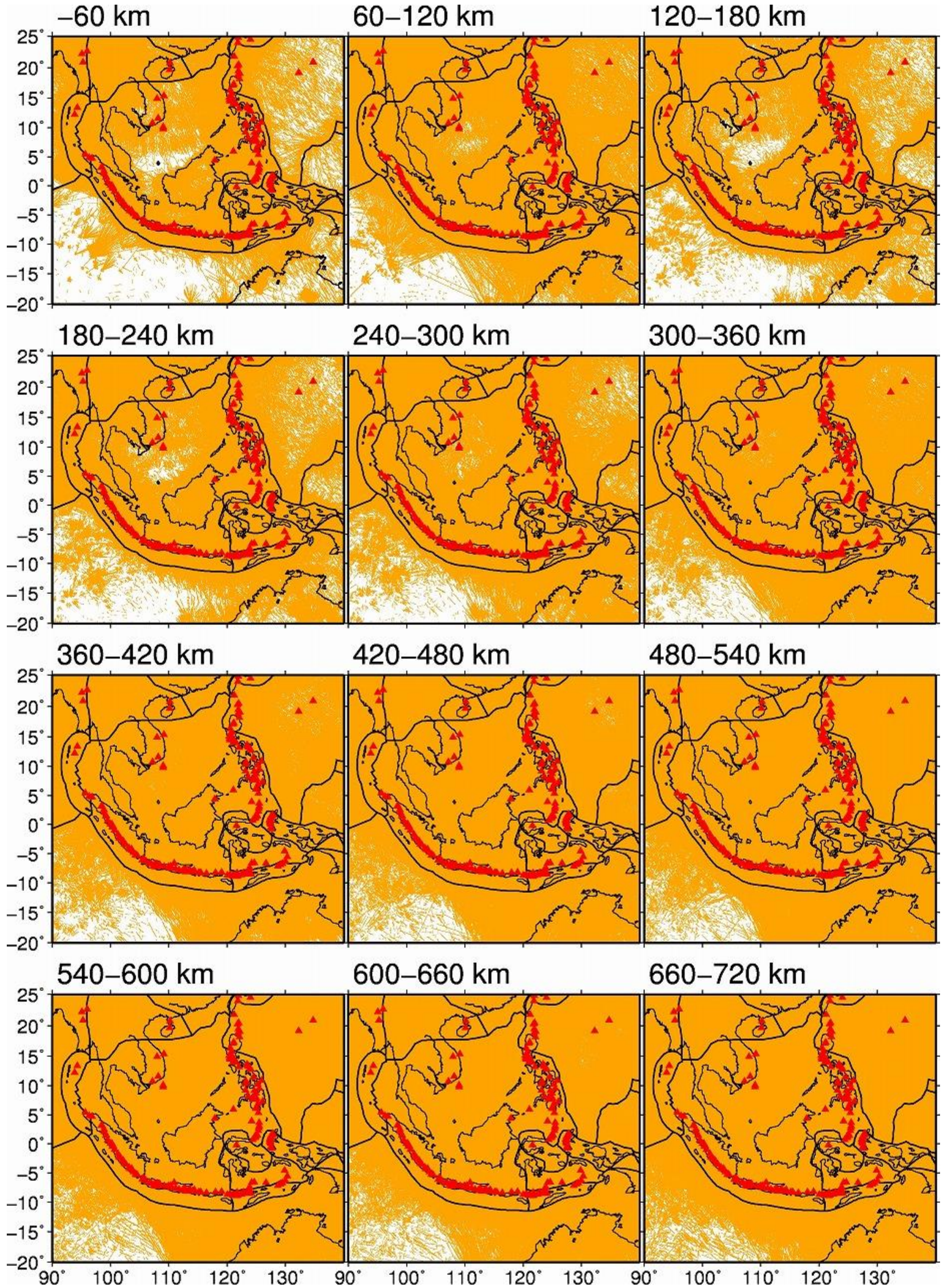

Figure S5. Distribution of seismic rays throughout the study volume. The layer depth range is shown at the upper-left corner of each panel.

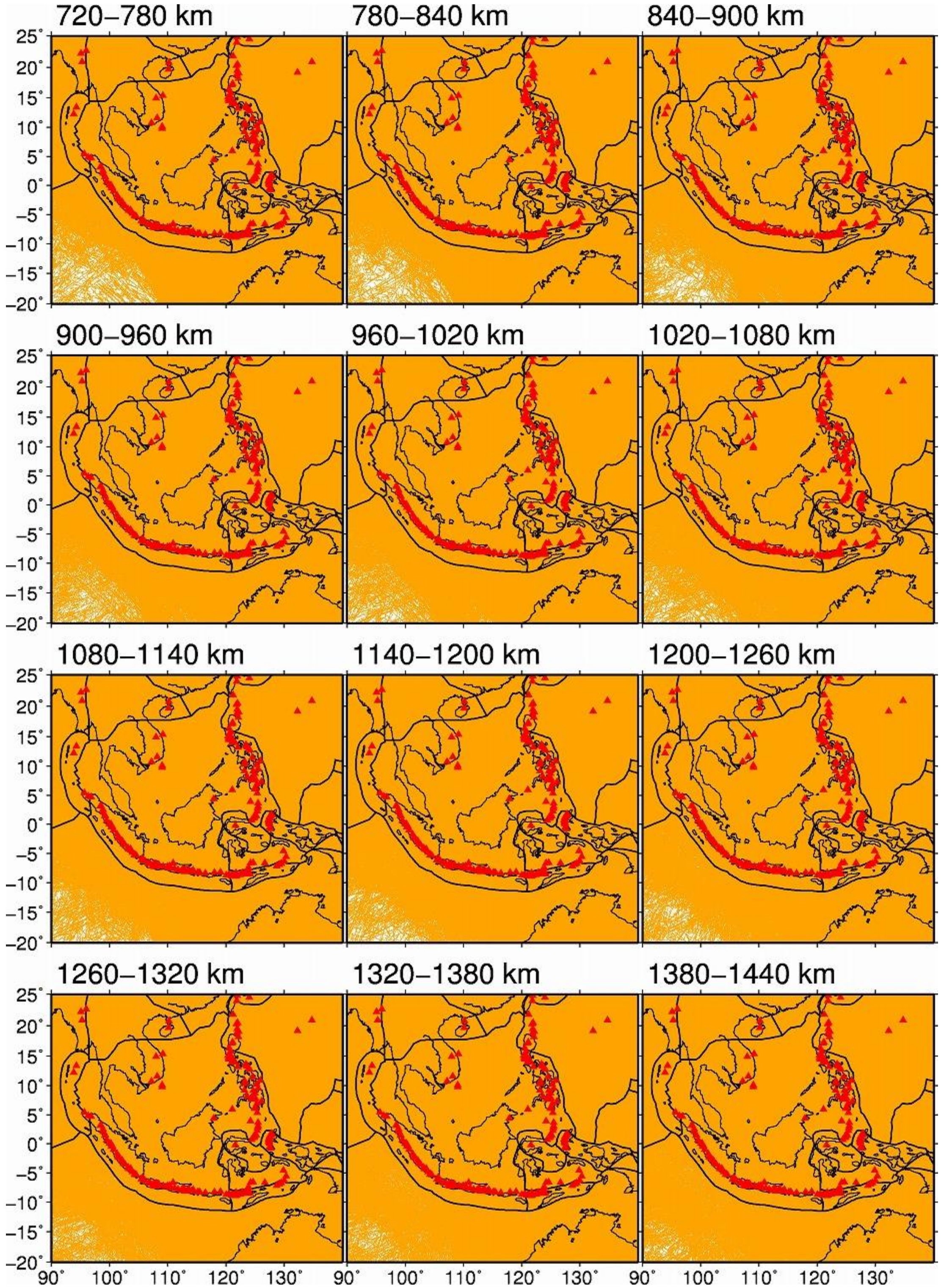

Figure S5. (continued).

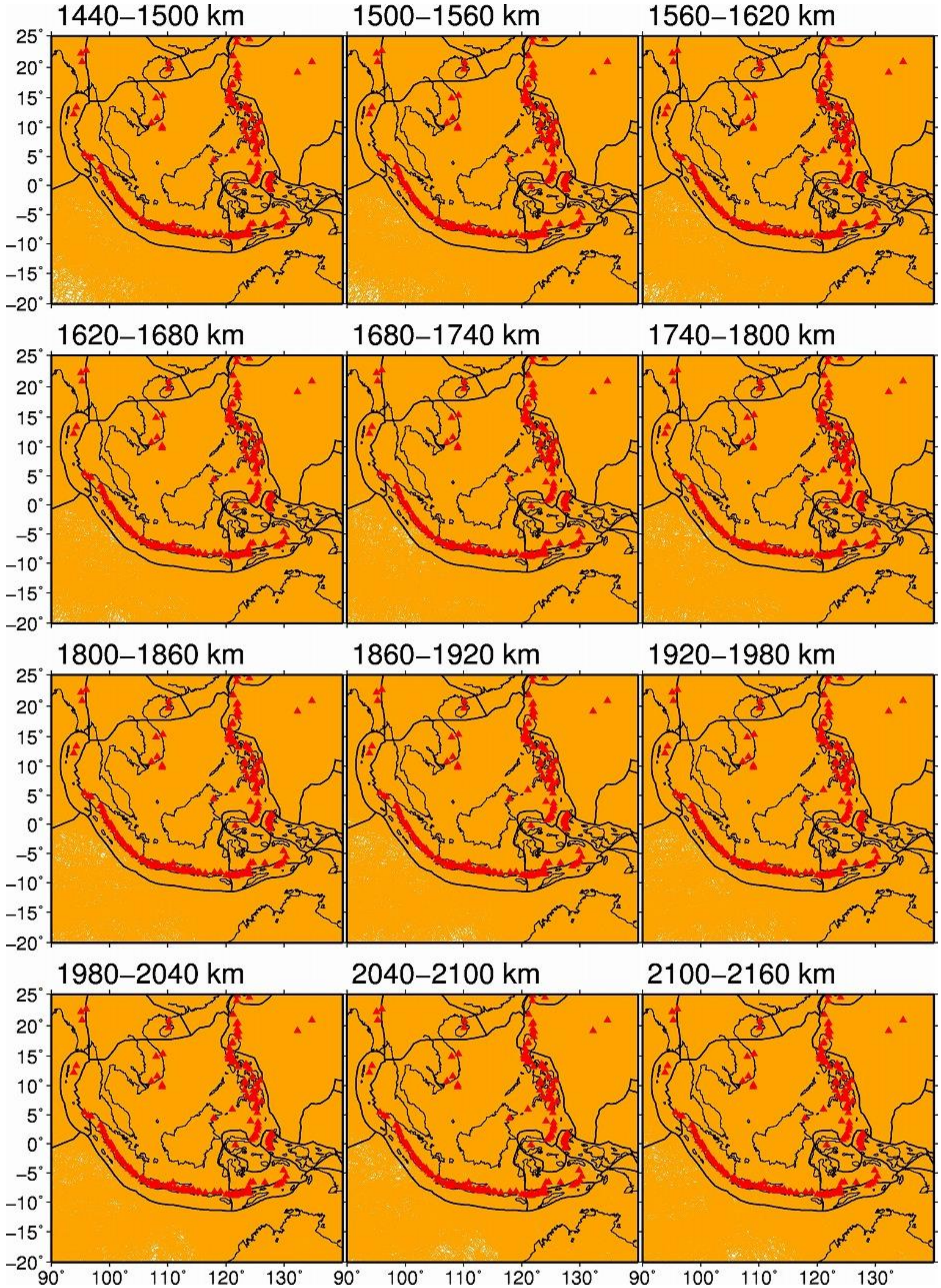

Figure S5. (continued).

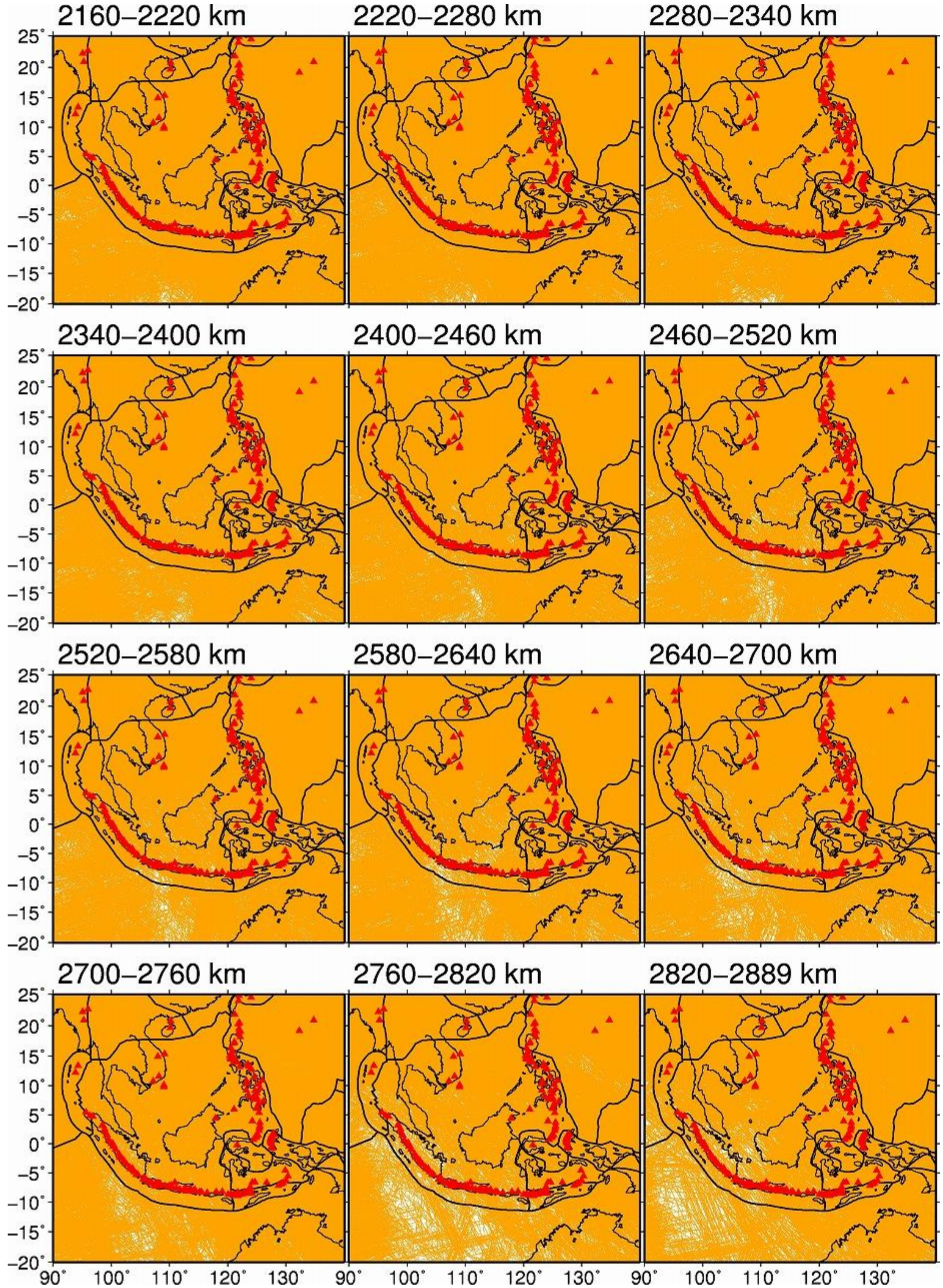

Figure S5. (continued).

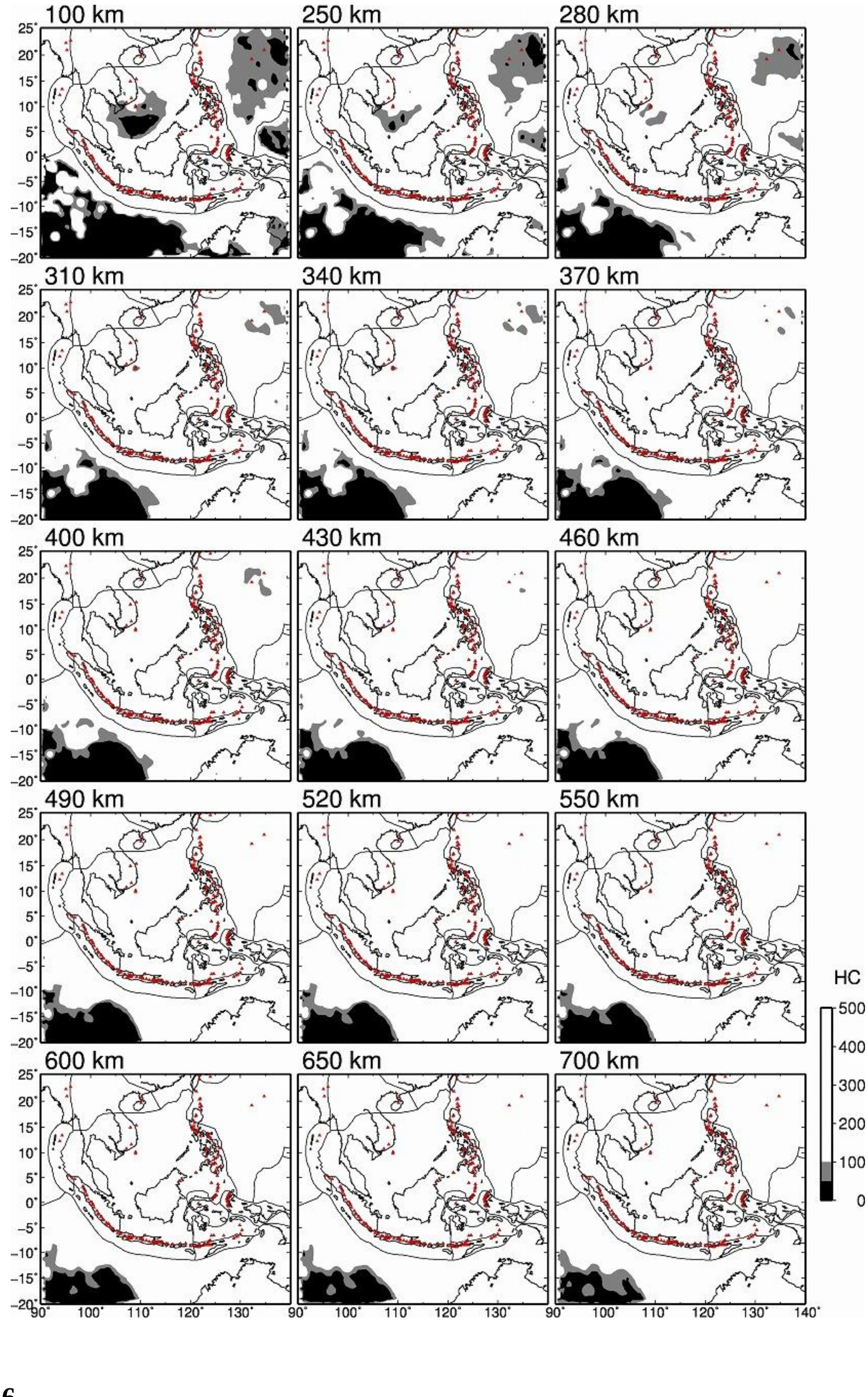
100 km
250 km
280 km
310 km
340 km
370 km
400 km
430 km
460 km
490 km
520 km
550 km
600 km
650 km
700 km
25˚
20˚
15˚
10˚
5˚
0˚
−5˚
−10˚
−15˚
−20˚
90˚
100˚
110˚
120˚
130˚
140˚
HC
500
400
300
200
100
0

Figure S6.

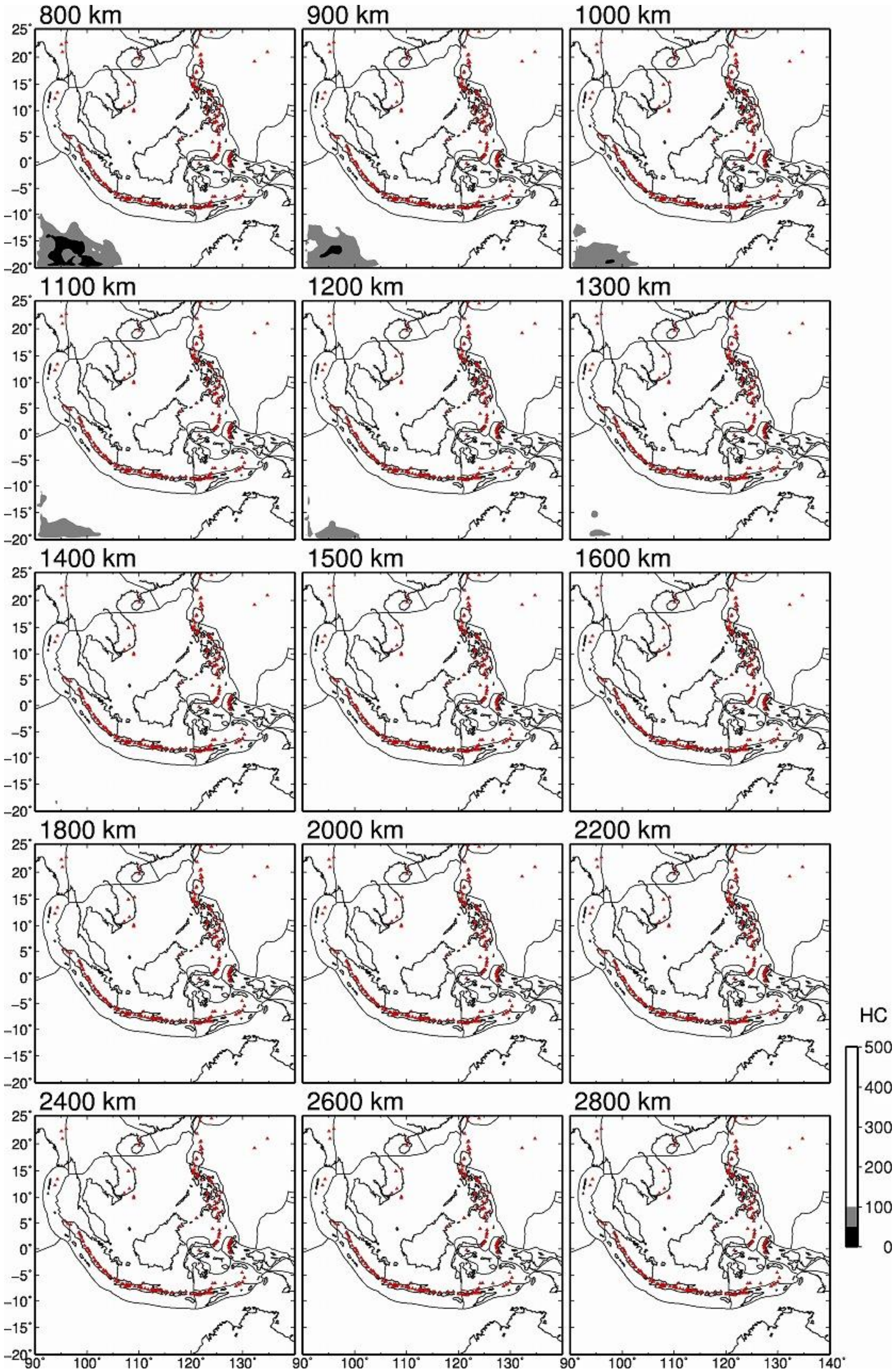

Figure S6. (continued).

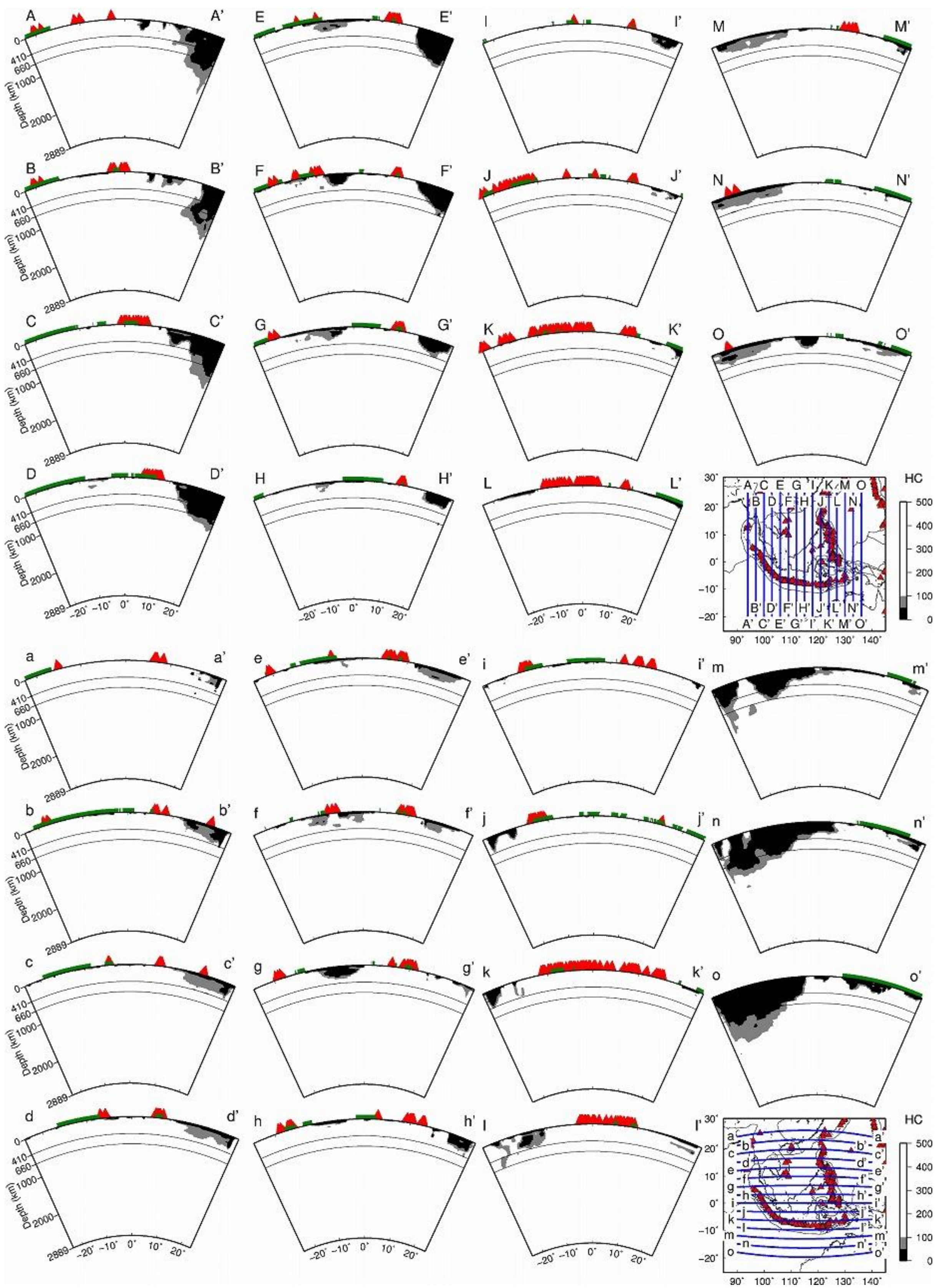
A A'
B B'
C C'
D D'
E E'
F F'
G G'
H H'
I I'
J J'
K K'
L L'
M M'
N N'
O O'
a a'
b b'
c c'
d d'
e e'
f f'
g g'
h h'
i i'
j j'
k k'
l l'
m m'
n n'
o o'
Depth (km)
0
410
660
1000
2000
2889
-20° -10° 0° 10° 20°
HC
500
400
300
200
100
0
90° 100° 110° 120° 130° 140°
30° 20° 10° 0° -10° -20°

Figure S7.

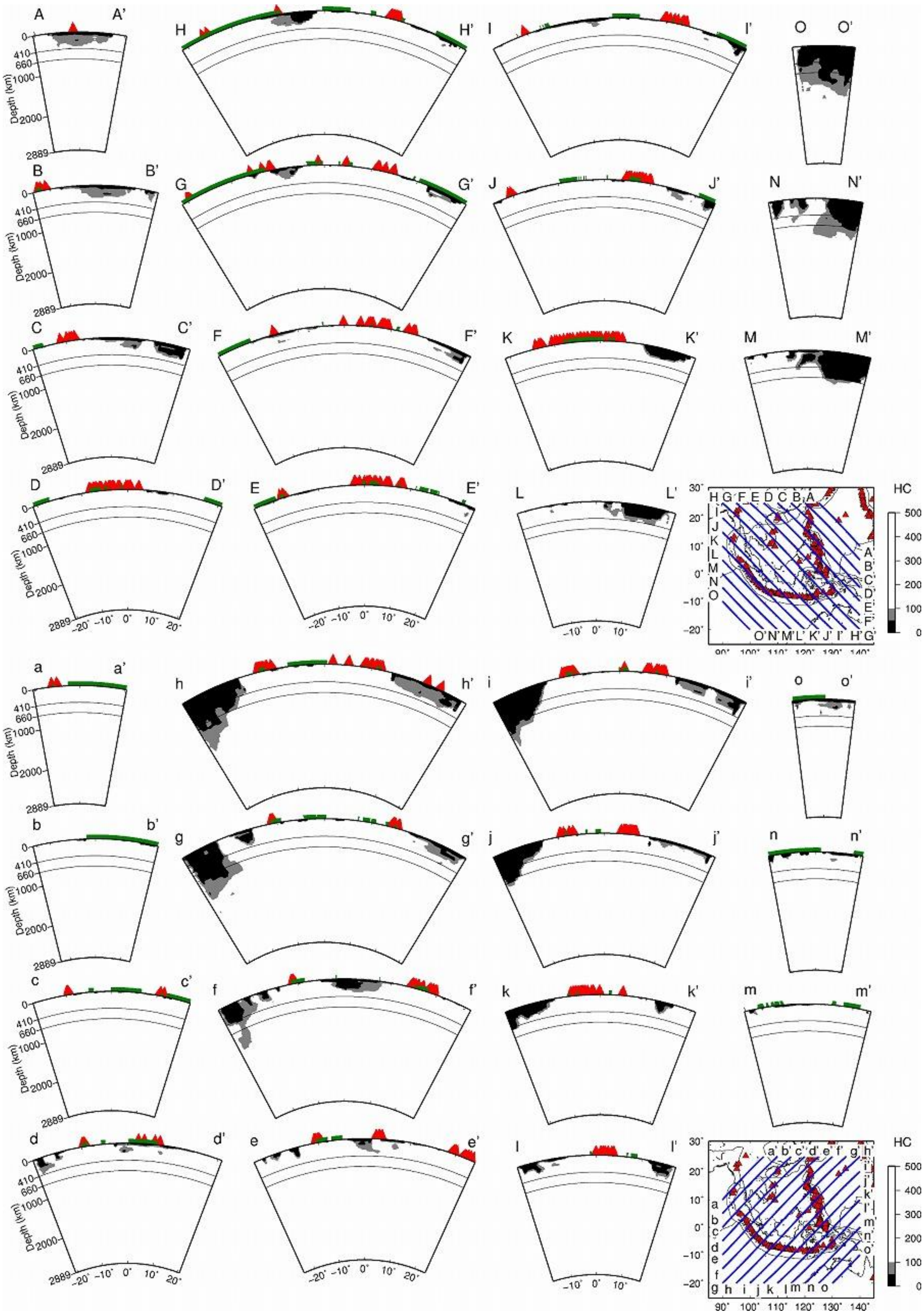

A
A'
B
B'
C
C'
D
D'
E
E'
F
F'
G
G'
H
H'
I
I'
J
J'
K
K'
L
L'
M
M'
N
N'
O
O'
Depth (km)
0
410
660
1000
2000
2889
-20˚ -10˚ 0˚ 10˚ 20˚
HC
500
400
300
200
100
0
30˚
20˚
10˚
0˚
-10˚
-20˚
90˚ 100˚ 110˚ 120˚ 130˚ 140˚
a
a'
b
b'
c
c'
d
d'
e
e'
f
f'
g
g'
h
h'
i
i'
j
j'
k
k'
l
l'
m
m'
n
n'
o
o'

55 **Figure S8.**

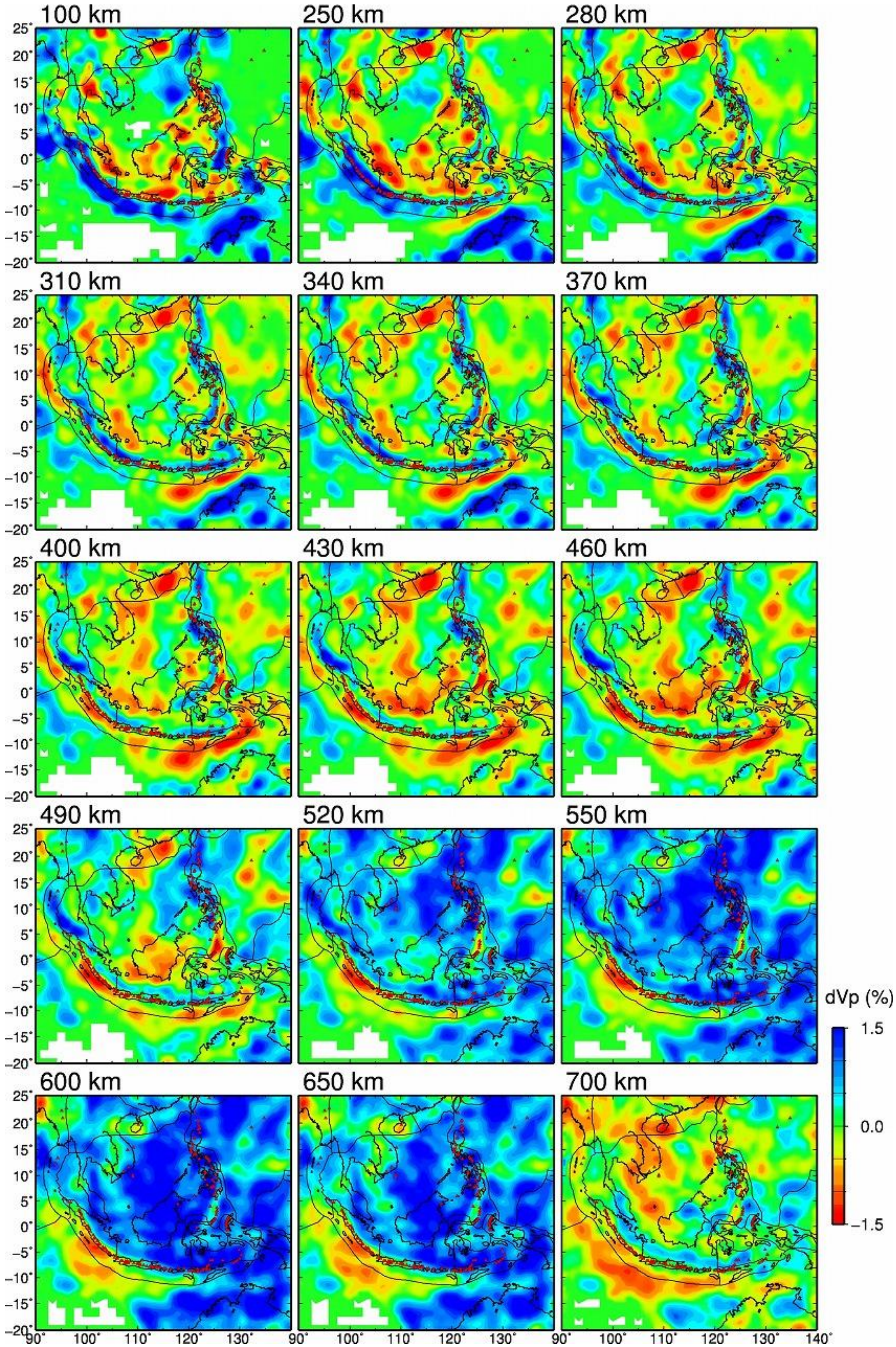
100 km
250 km
280 km
310 km
340 km
370 km
400 km
430 km
460 km
490 km
520 km
550 km
600 km
650 km
700 km
25°
20°
15°
10°
5°
0°
−5°
−10°
−15°
−20°
90°
100°
110°
120°
130°
140°
dVp (%)
1.5
0.0
−1.5

56 **Figure S9.**

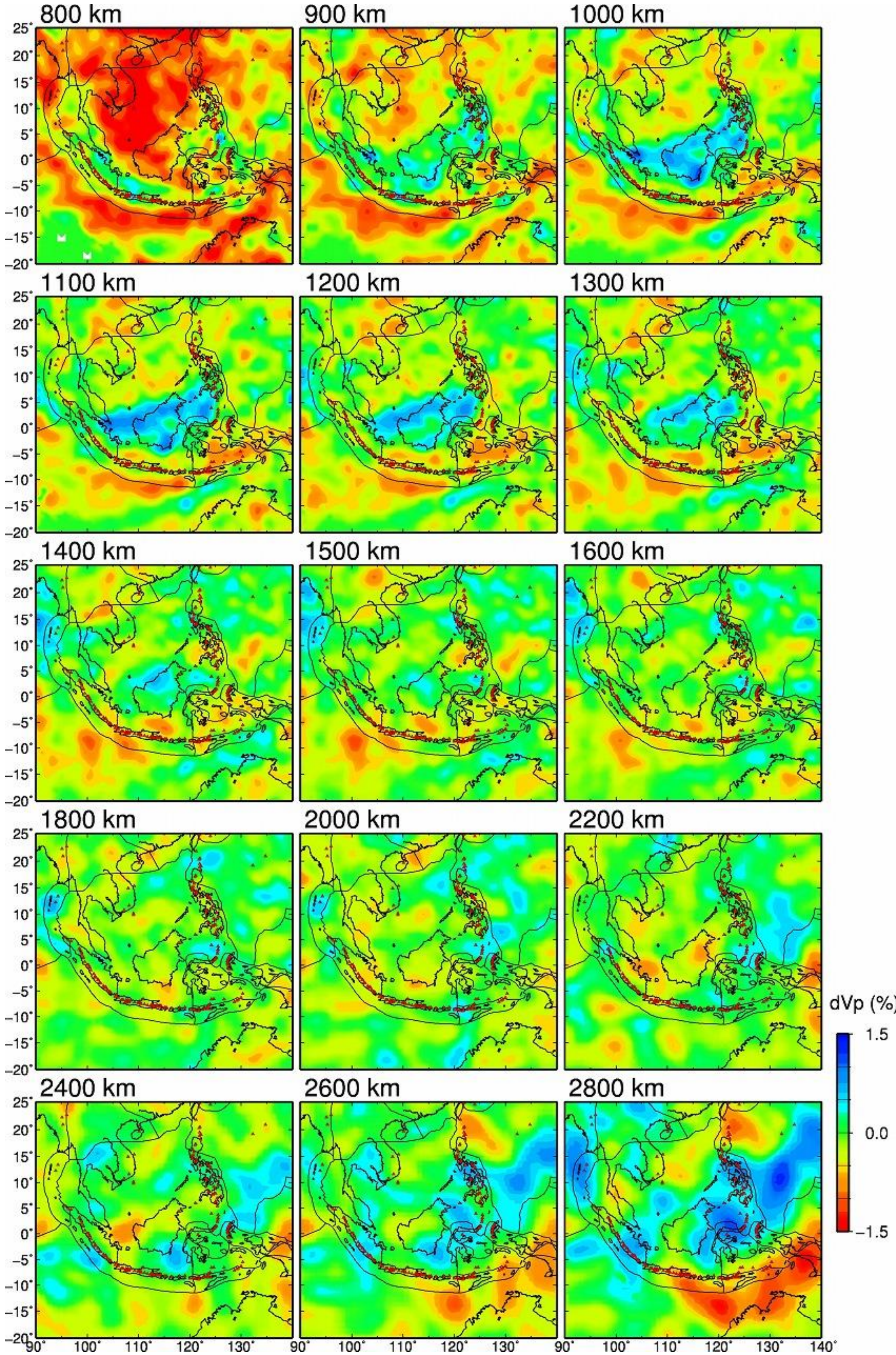

57 **Figure S9.** (continued).

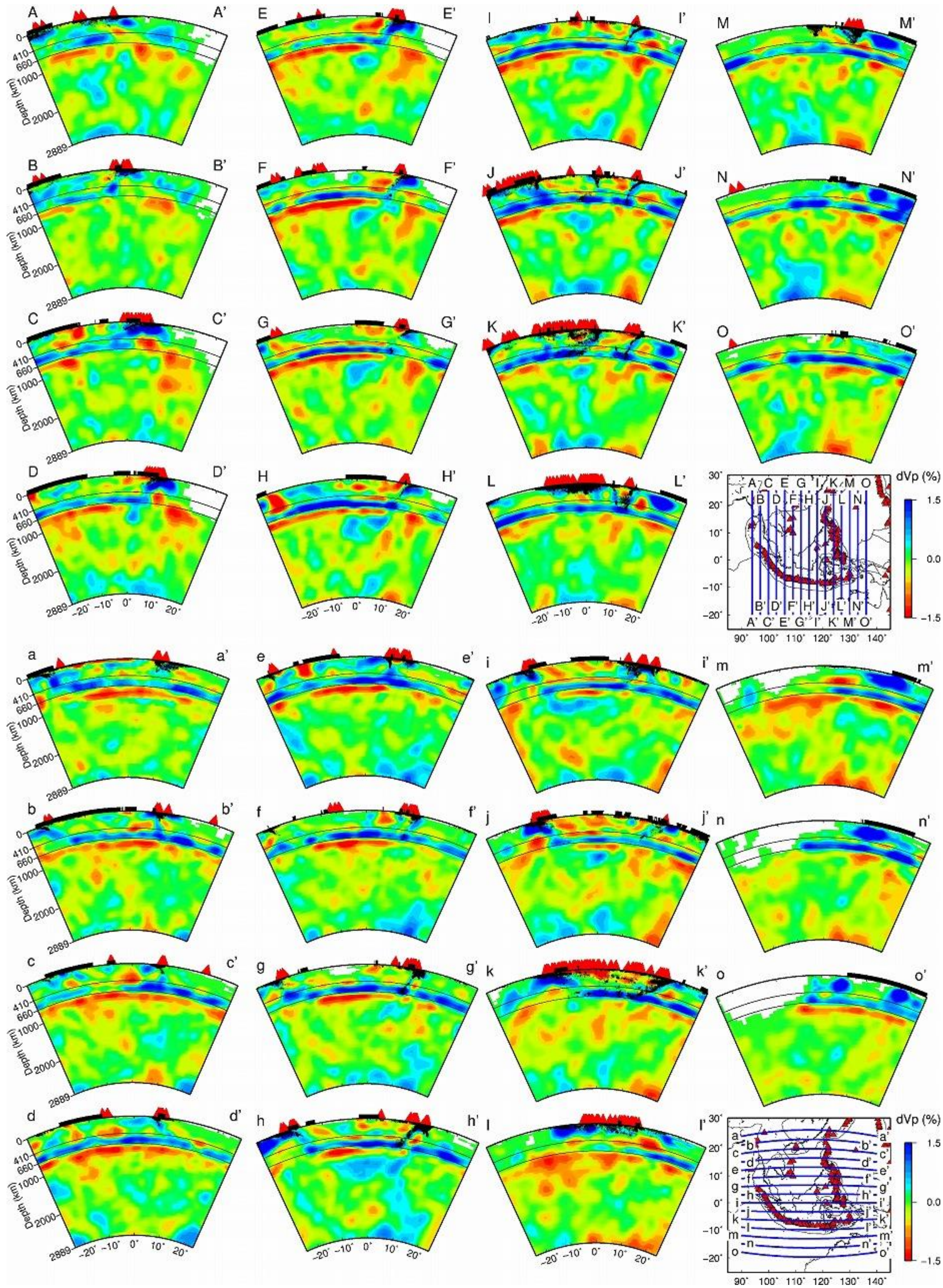

58 **Figure S10.**

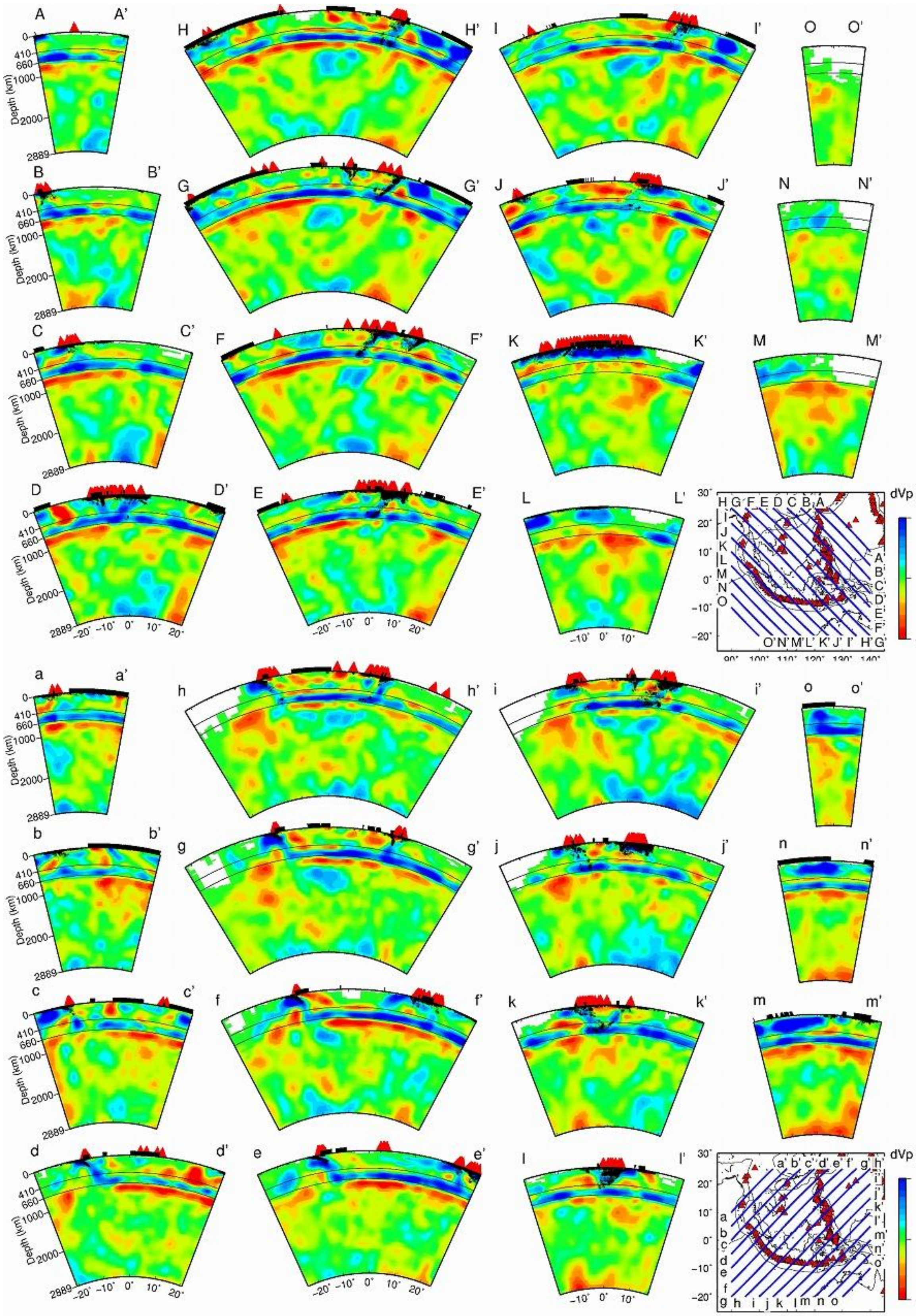

59 **Figure S11.**

Figure S6. Map view images of the ray hit count. The layer depth is shown at the lower-right corner of each map. The color scale is shown on the right. The areas in black color with hit count < 50 are masked in the resulting tomographic images.

Figure S7. Vertical cross-sections of the ray hit count along **(top)** 15 profiles in the N-S direction, and **(bottom)** 15 profiles in the E-W direction. Locations of the profiles are shown on the inset map. The 410-km and the 660-km discontinuities are shown in black solid lines. The thick green lines on the surface denote land areas. The red triangles denote active volcanoes. The thin black lines on the inset map denote the plate boundaries.

Figure S8. The same as Figure S7 but along **(top)** 15 profiles in the NW-SE direction, and **(bottom)** 15 profiles in the NE-SW direction.

Figure S9. The same as Figures 5 and 6 but before subtracting the average velocity anomalies at each depth (Figure 4) from the velocity anomalies obtained using IASP91 (Kennett & Engdahl, 1991).

Figure S10. The same as Figures 7 but before subtracting the average velocity anomalies at each depth (Figure 4) from the velocity anomalies obtained using IASP91 (Kennett & Engdahl, 1991).

Figure S11. The same as Figures 8 but before subtracting the average velocity anomalies at each depth (Figure 4) from the velocity anomalies obtained using IASP91 (Kennett & Engdahl, 1991).

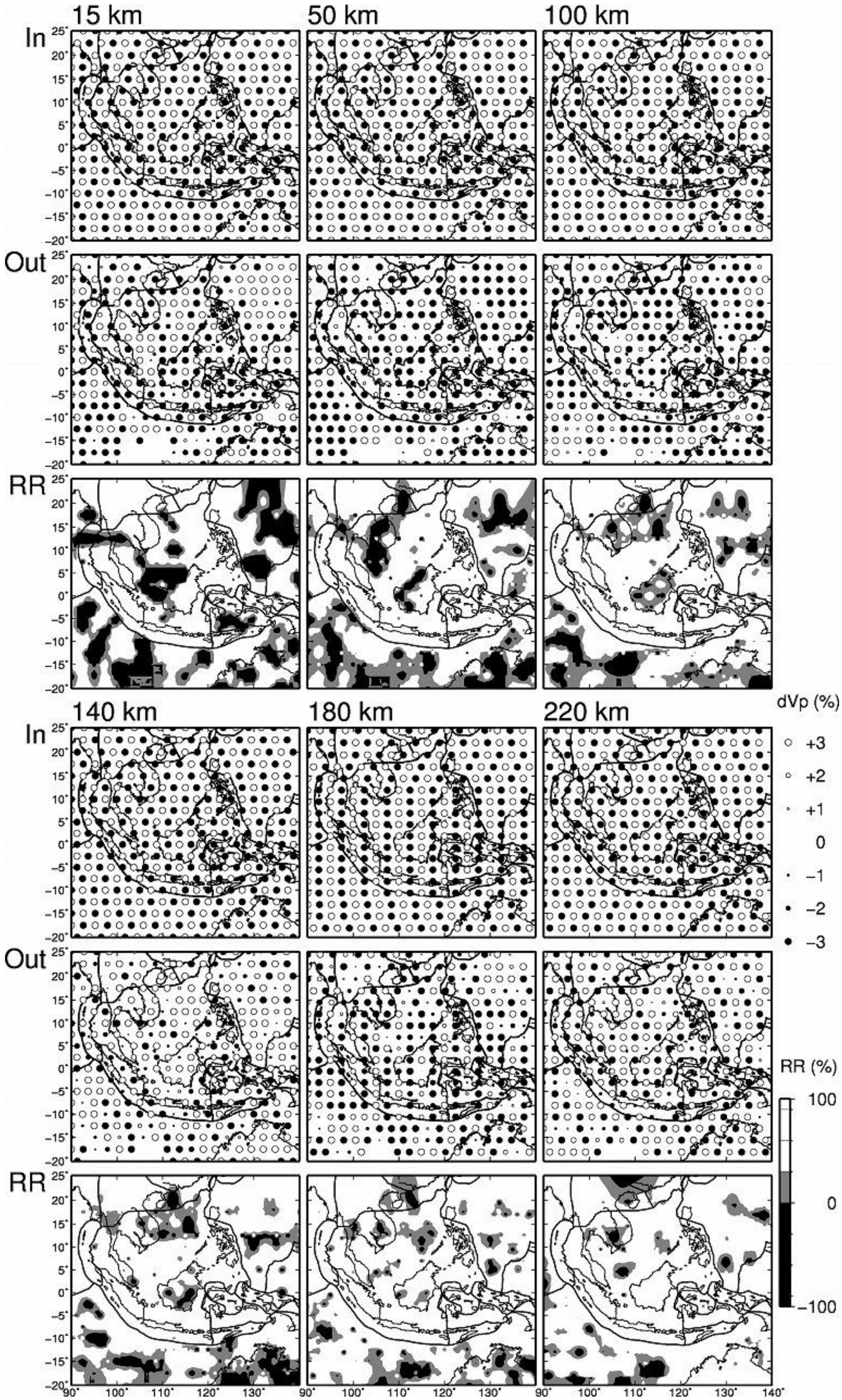

83 **Figure S12.**

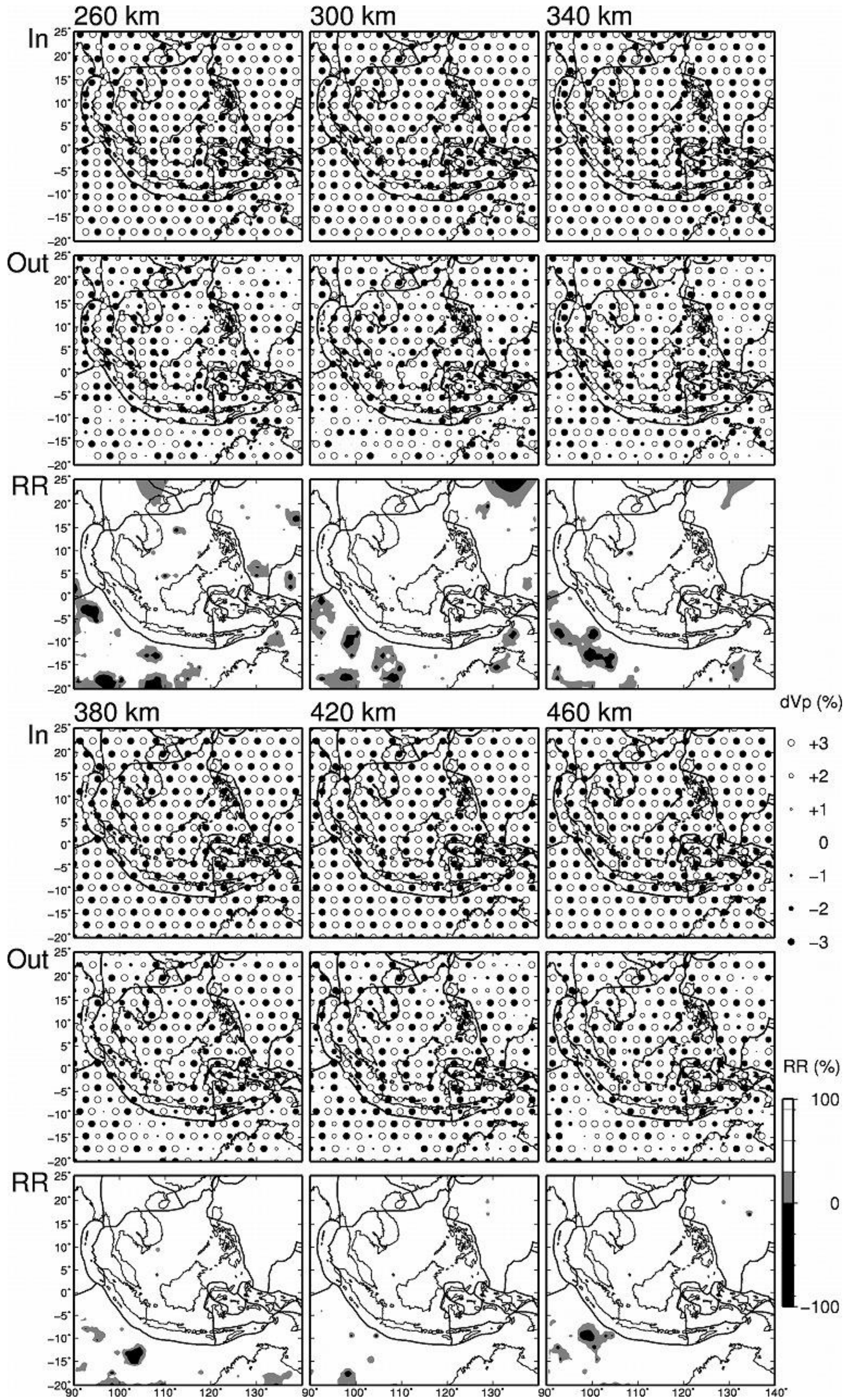

Figure S12. (continued).

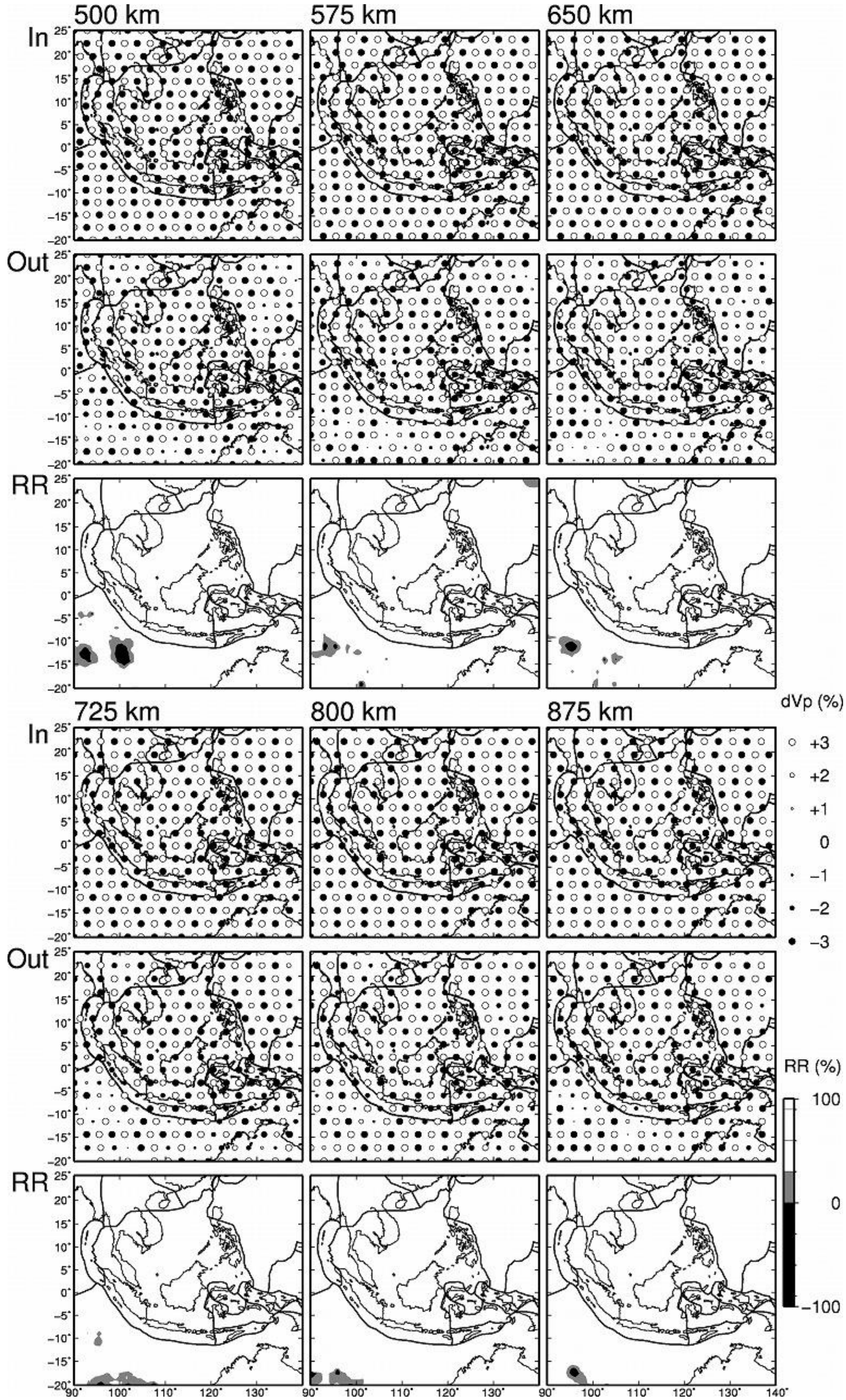

Figure S12. (continued).

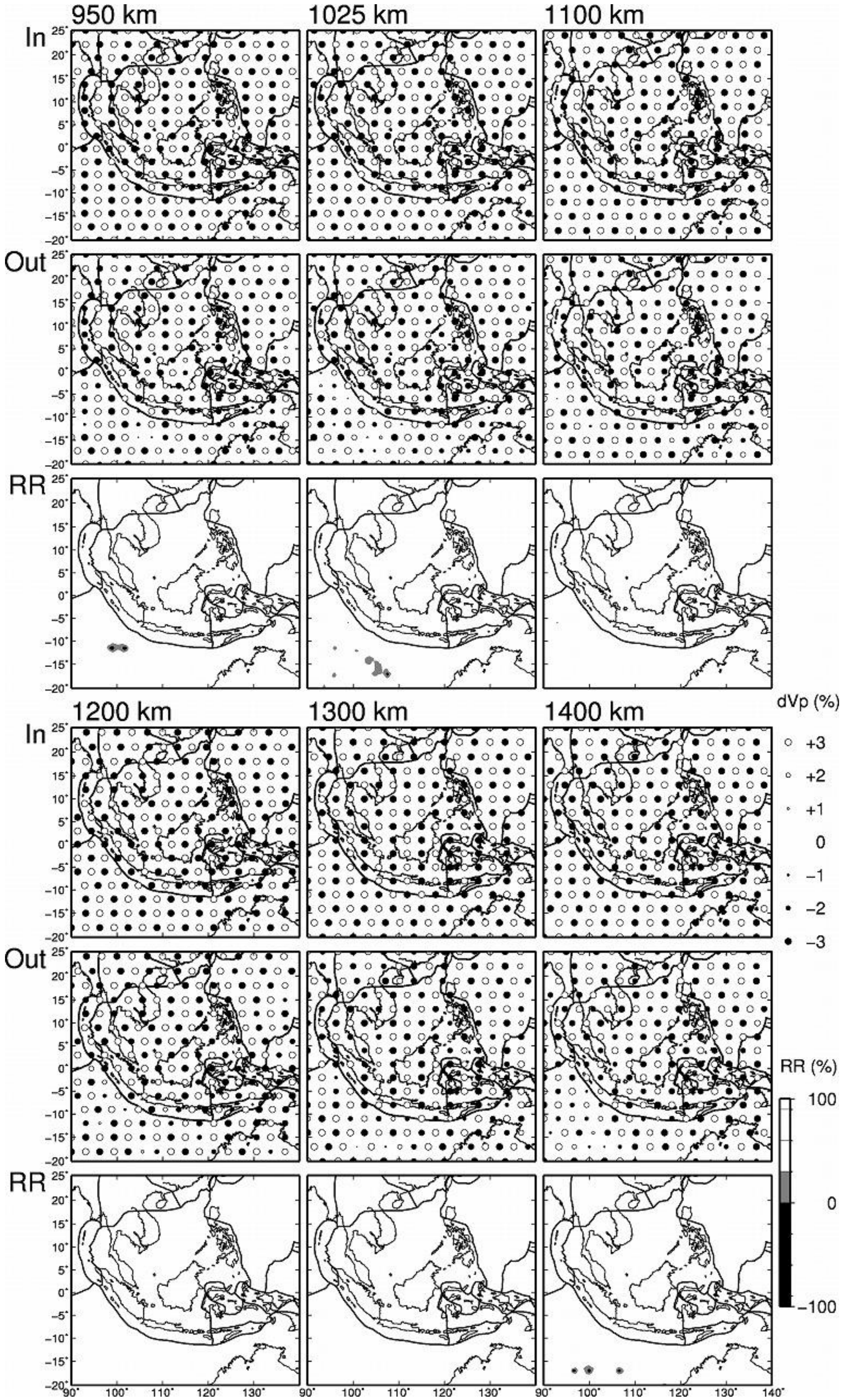

86 **Figure S12.** (continued).

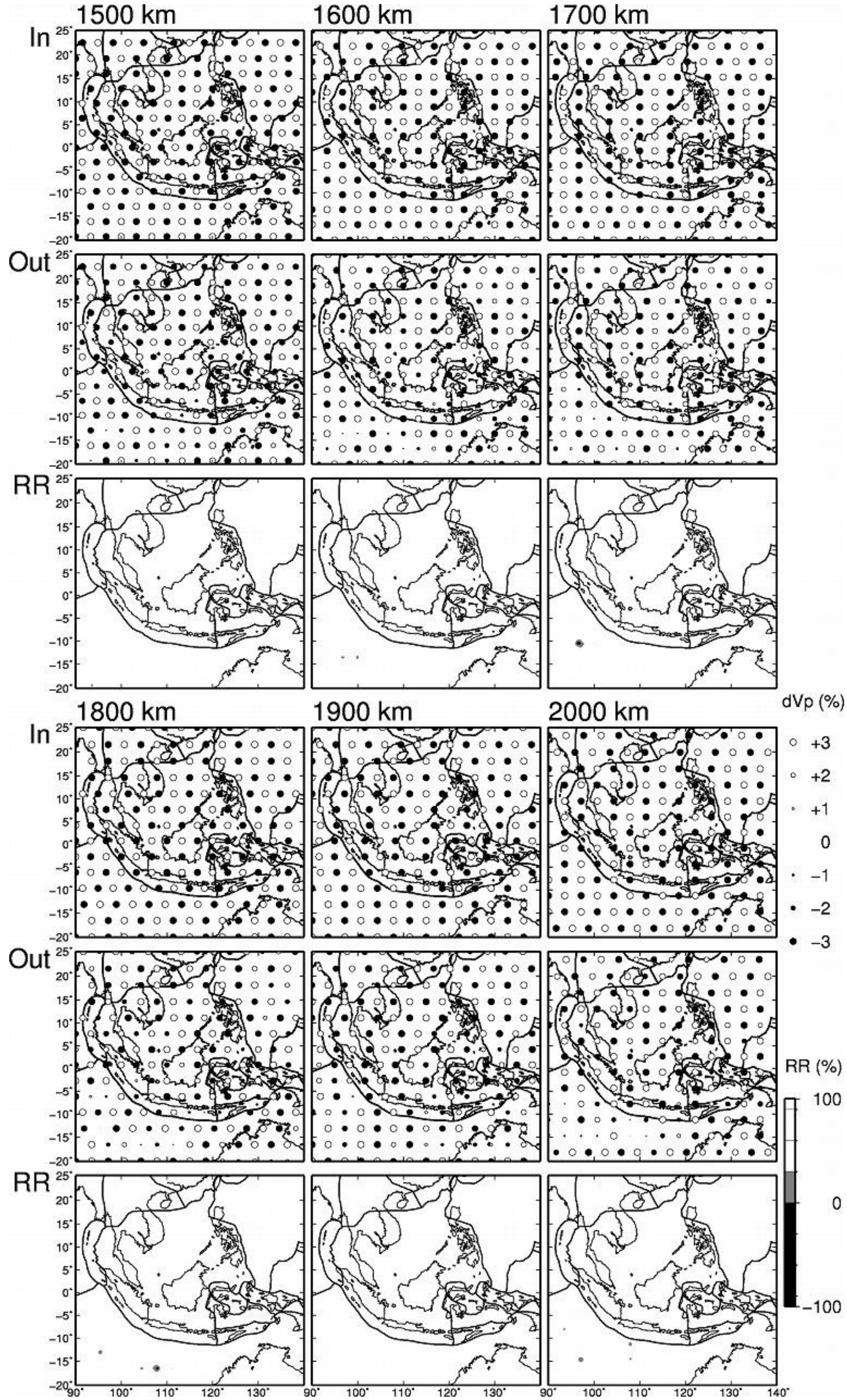

Figure S12. (continued).

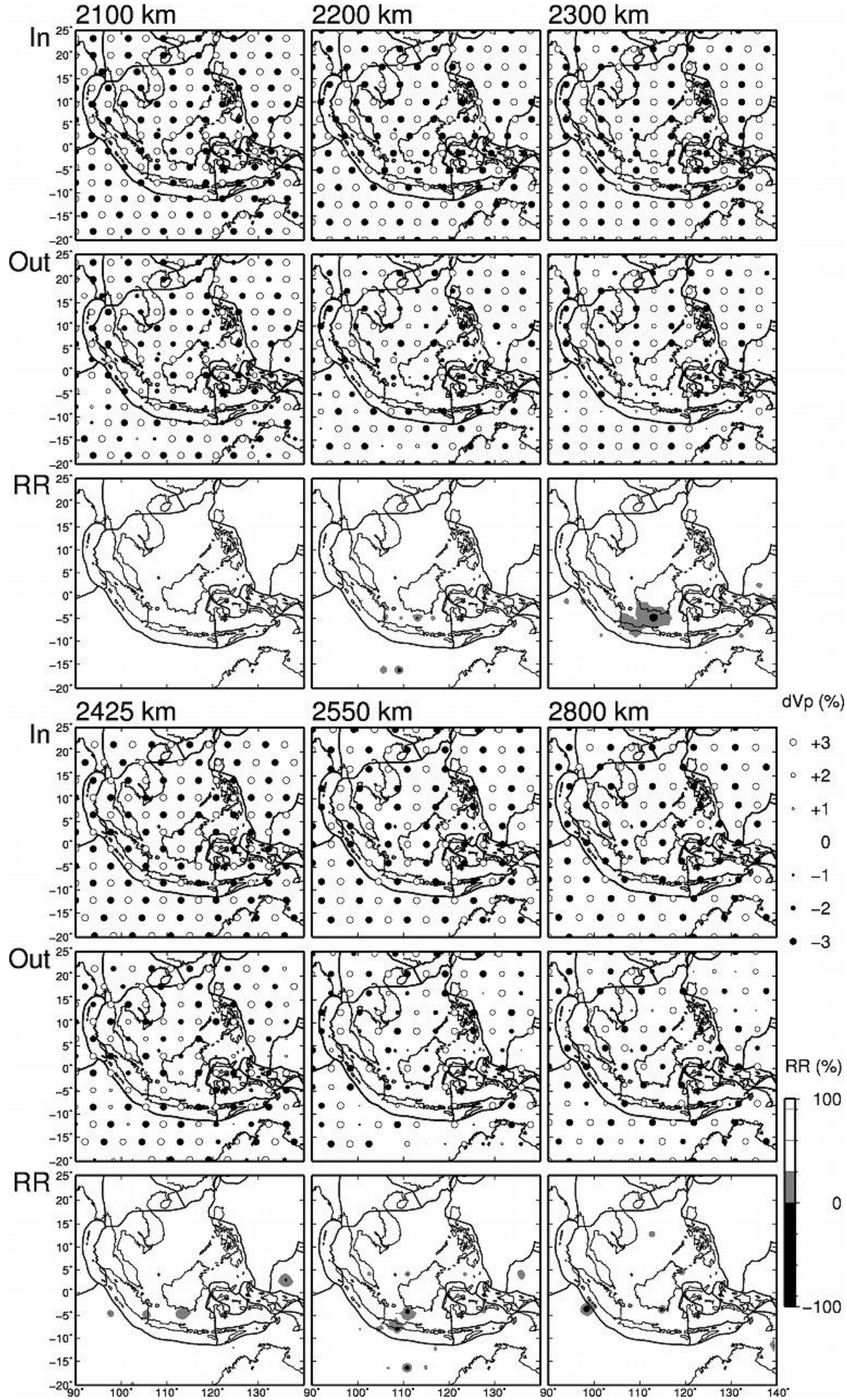

88 **Figure S12.** (continued).

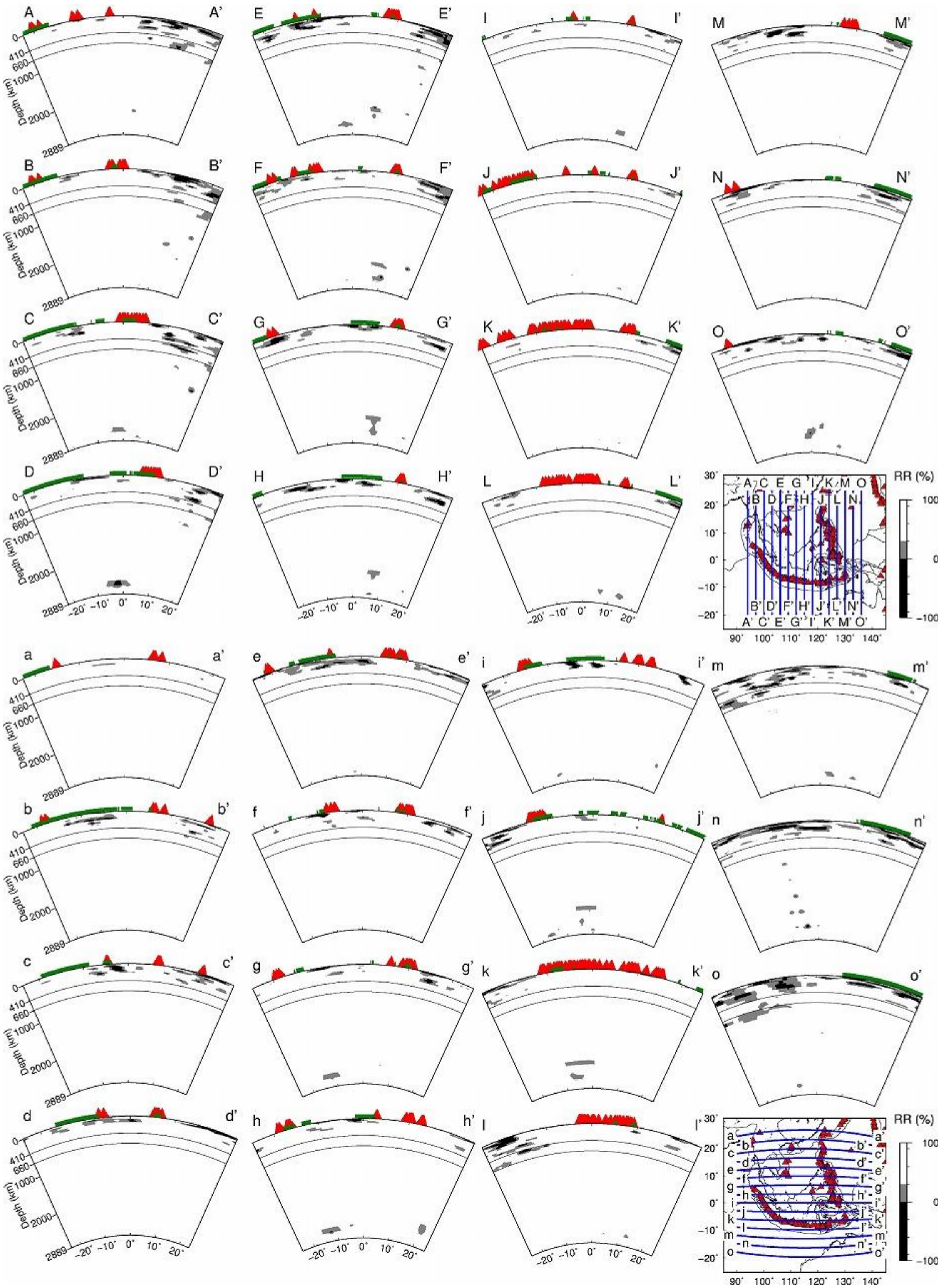
A A'
B B'
C C'
D D'
E E'
F F'
G G'
H H'
I I'
J J'
K K'
L L'
M M'
N N'
O O'
a a'
b b'
c c'
d d'
e e'
f f'
g g'
h h'
i i'
j j'
k k'
l l'
m m'
n n'
o o'
Depth (km)
0
410
660
1000
2000
2889
-20° -10° 0° 10° 20°
RR (%)
100
0
-100
30° 20° 10° 0° -10° -20°
90° 100° 110° 120° 130° 140°

Figure S13.

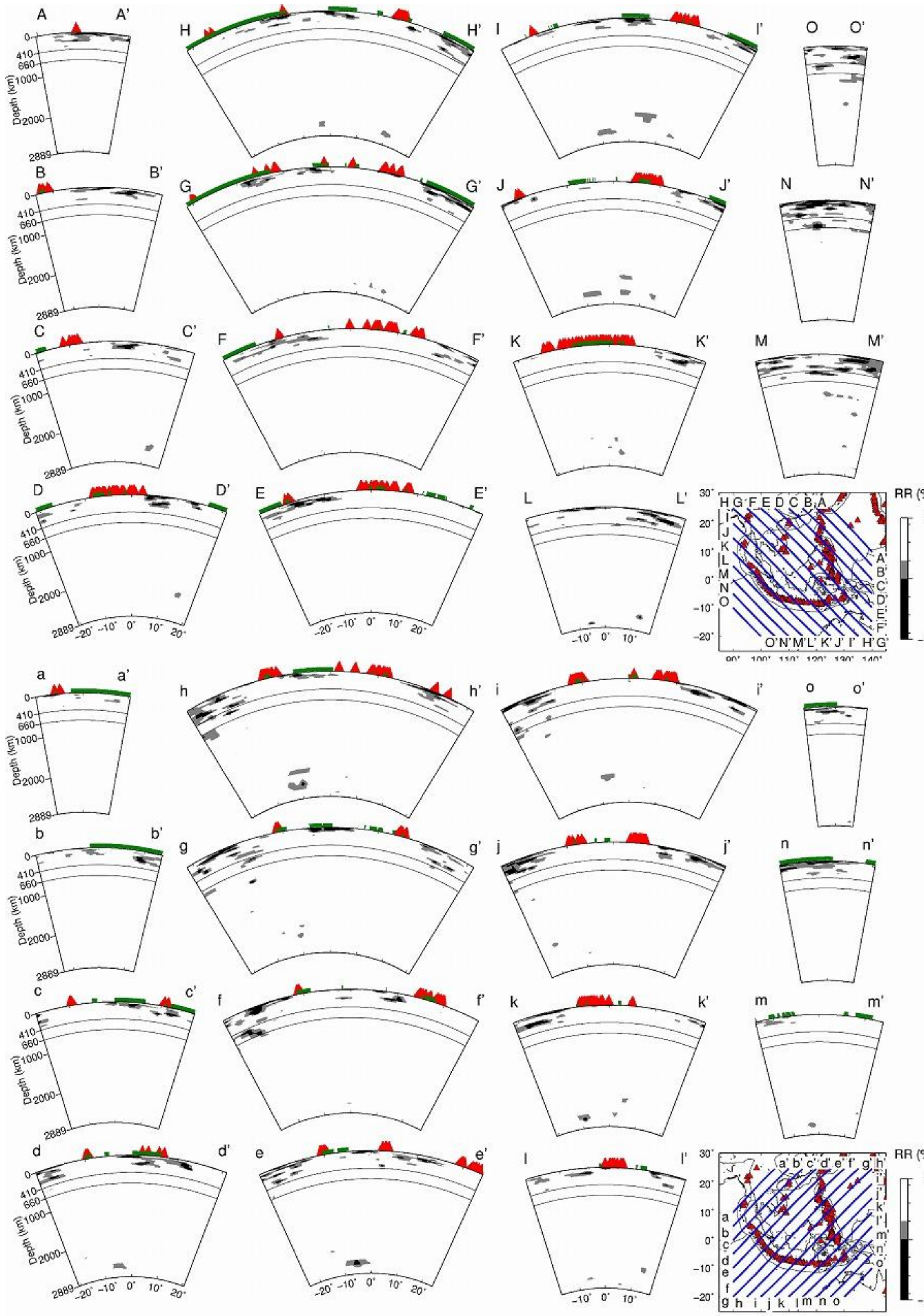

90 **Figure S14.**

Figure S12. Map views showing the input model (top panels), output results (middle panels) and the recovery rate (bottom panels) of the checkerboard resolution test with a lateral grid interval of 278 km (CRT1). The layer depth is shown at the upper-left corner of the top panels. The open and solid circles denote high and low Vp perturbations, respectively, whose scale is shown on the right. The color scale of the recovery rate (in %) is also shown on the right.

Figure S13. Vertical cross-sections of the recovery rate along **(top)** 15 profiles in the N-S direction, and **(bottom)** 15 profiles in the E-W direction, obtained by the checkerboard resolution test with a lateral grid interval of 278 km inside the study region (CRT1). Locations of the profiles are shown on the inset map. Other labels are the same as those in Figure S7.

Figure S14. The same as Figure S13 but along **(top)** 15 profiles in the NW-SE direction, and **(bottom)** 15 profiles in the NE-SW direction.

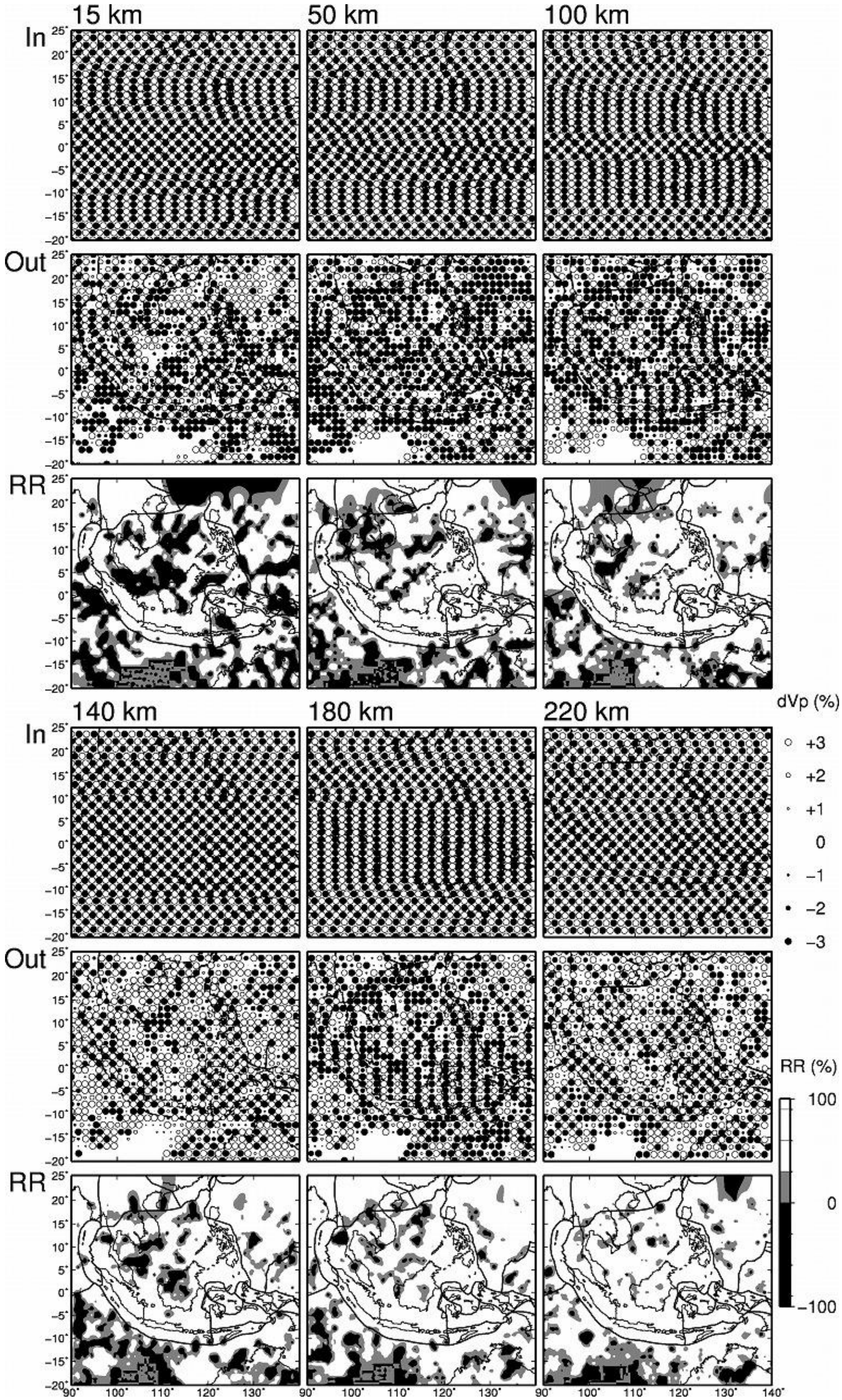

114 **Figure S15.**

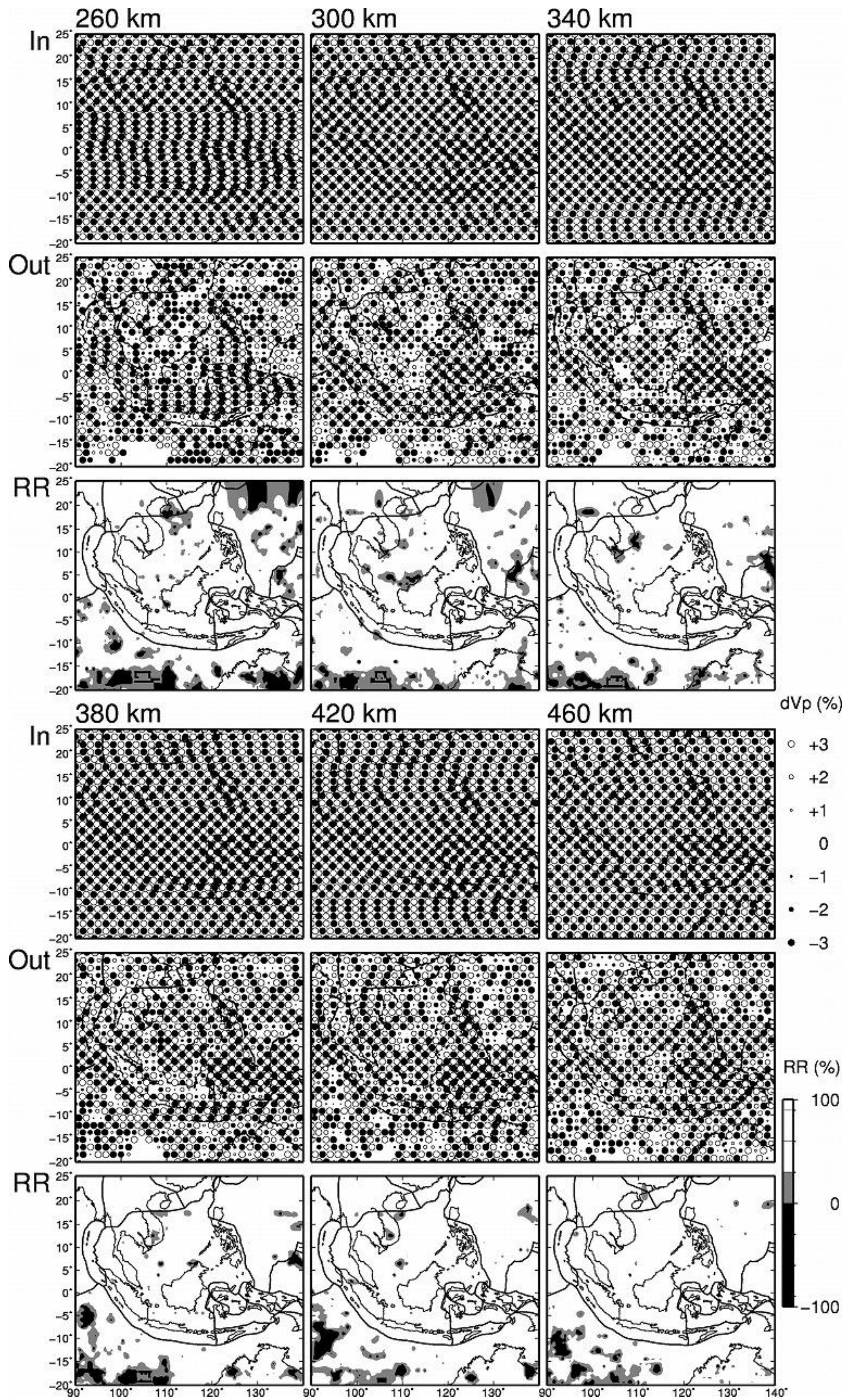

115 **Figure S15.** (continued).

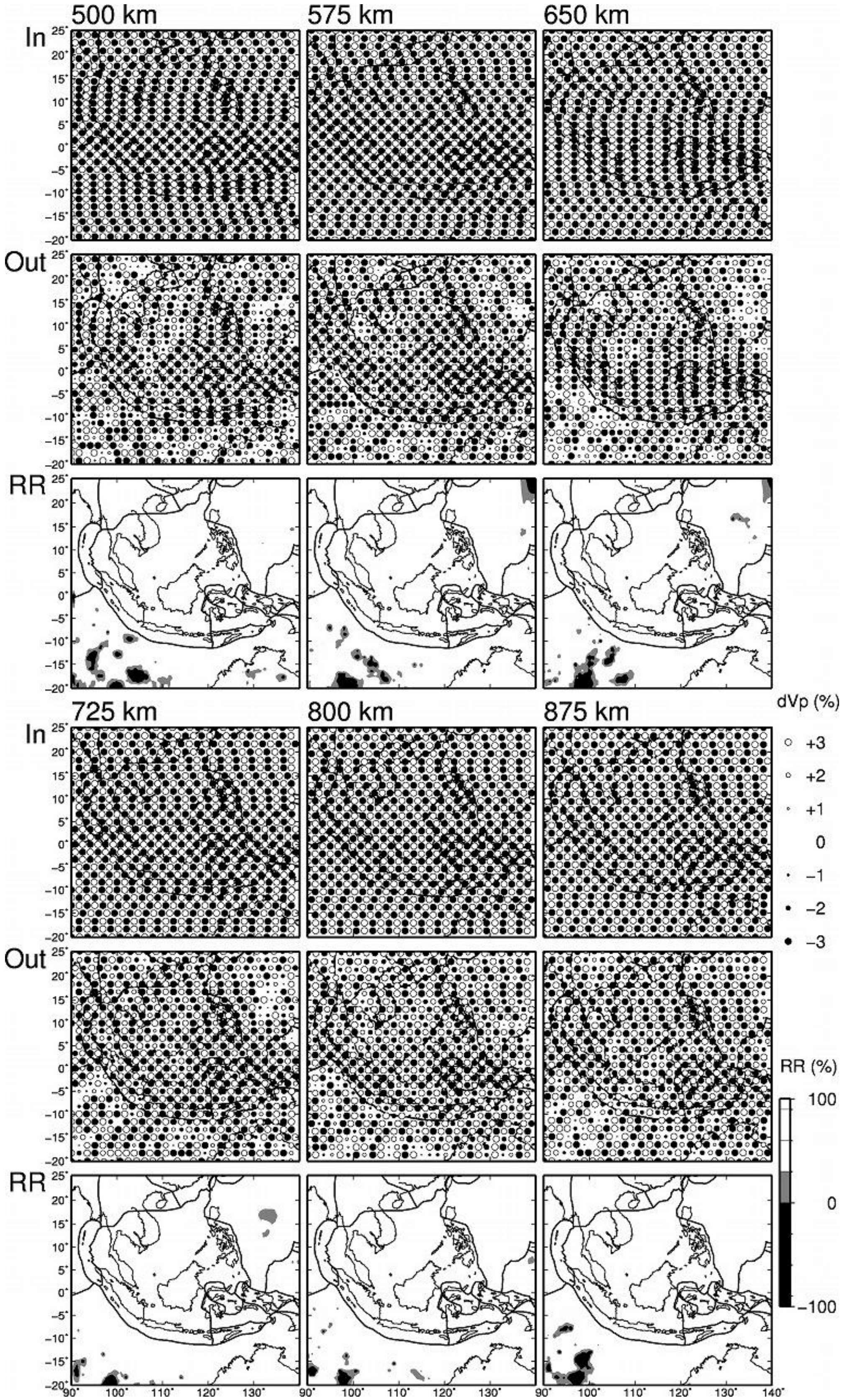

116 **Figure S15.** (continued).

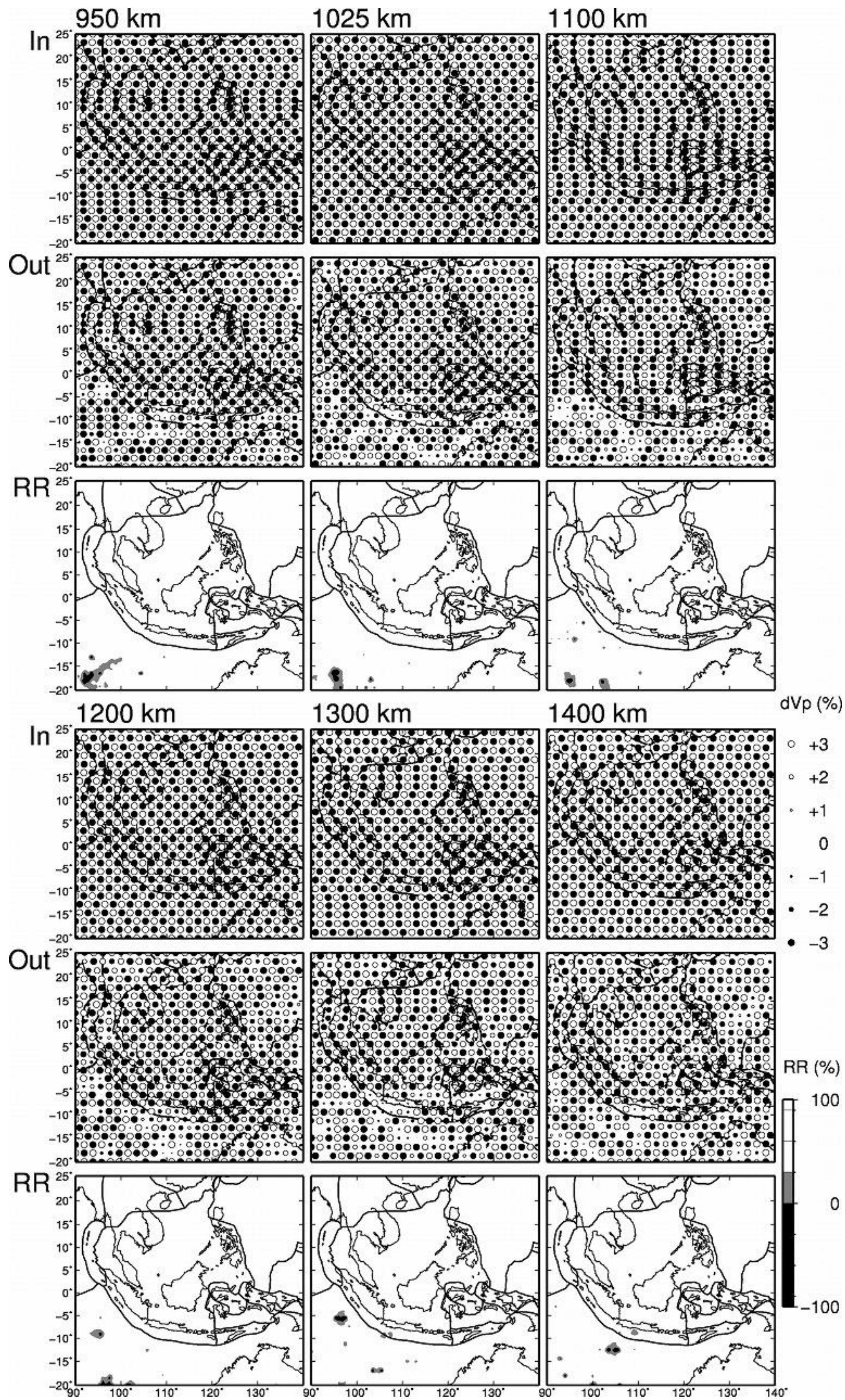

117 **Figure S15.** (continued).

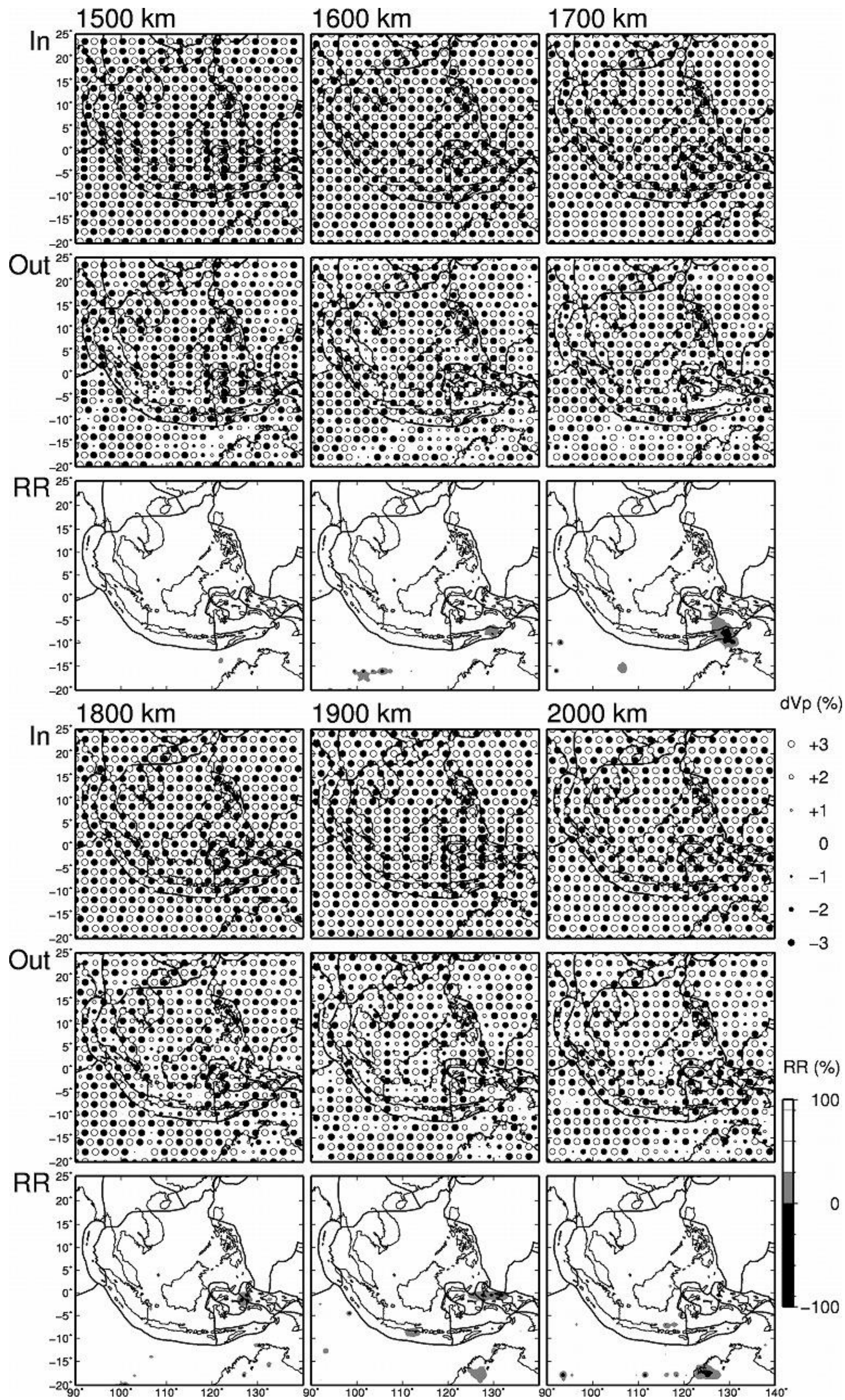

118 **Figure S15.** (continued).

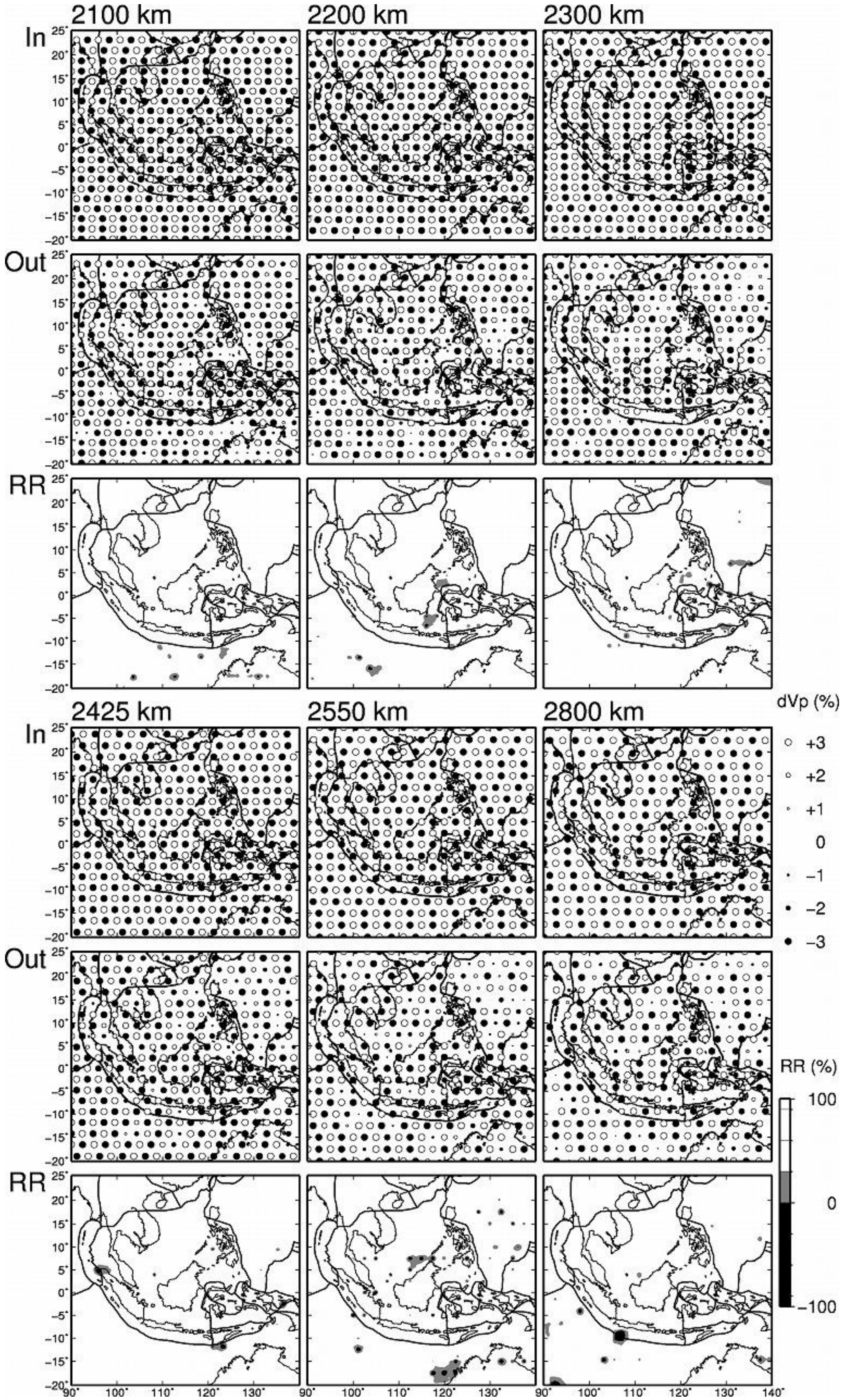

Figure S15. (continued).

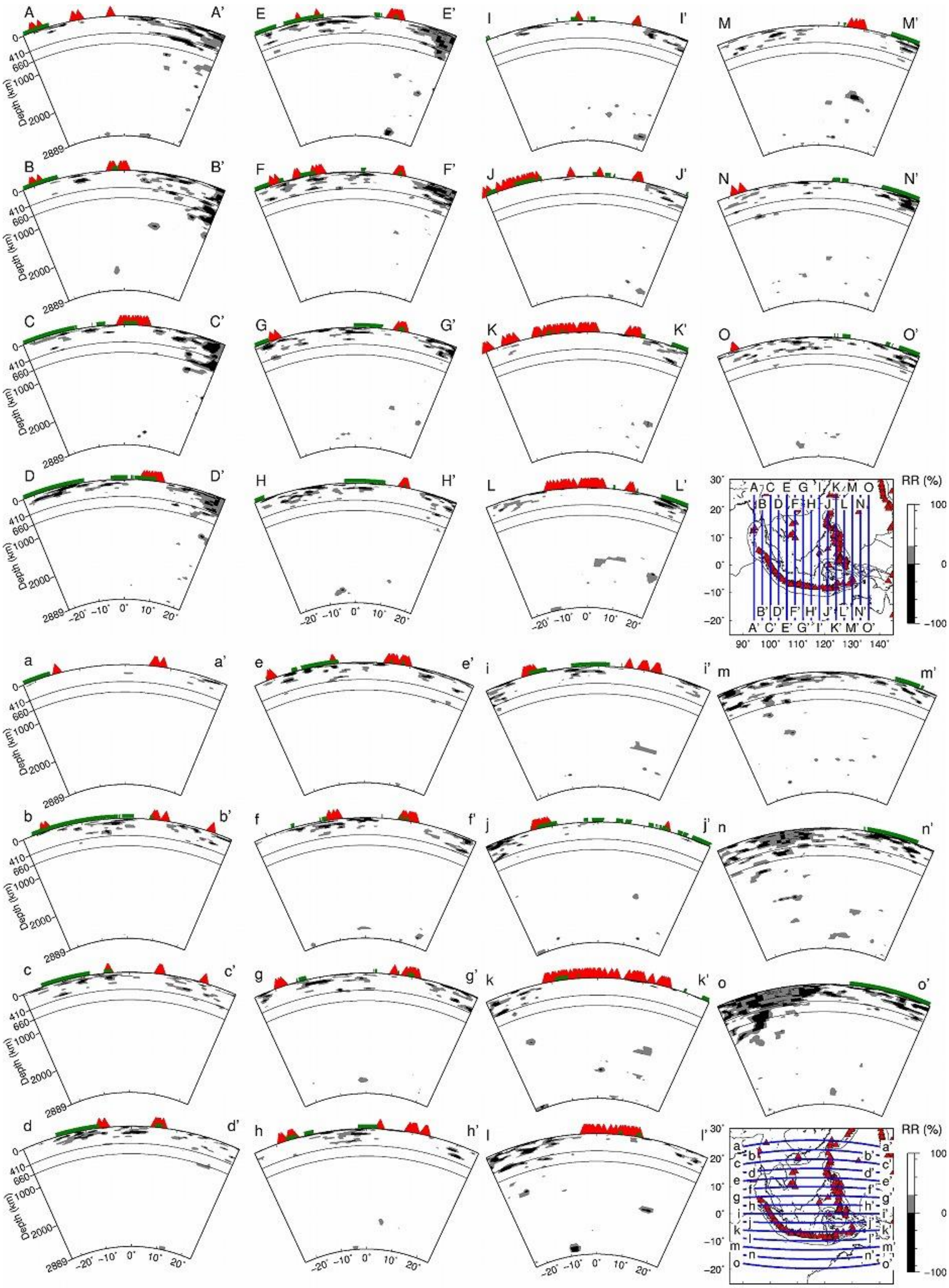

120 **Figure S16.**

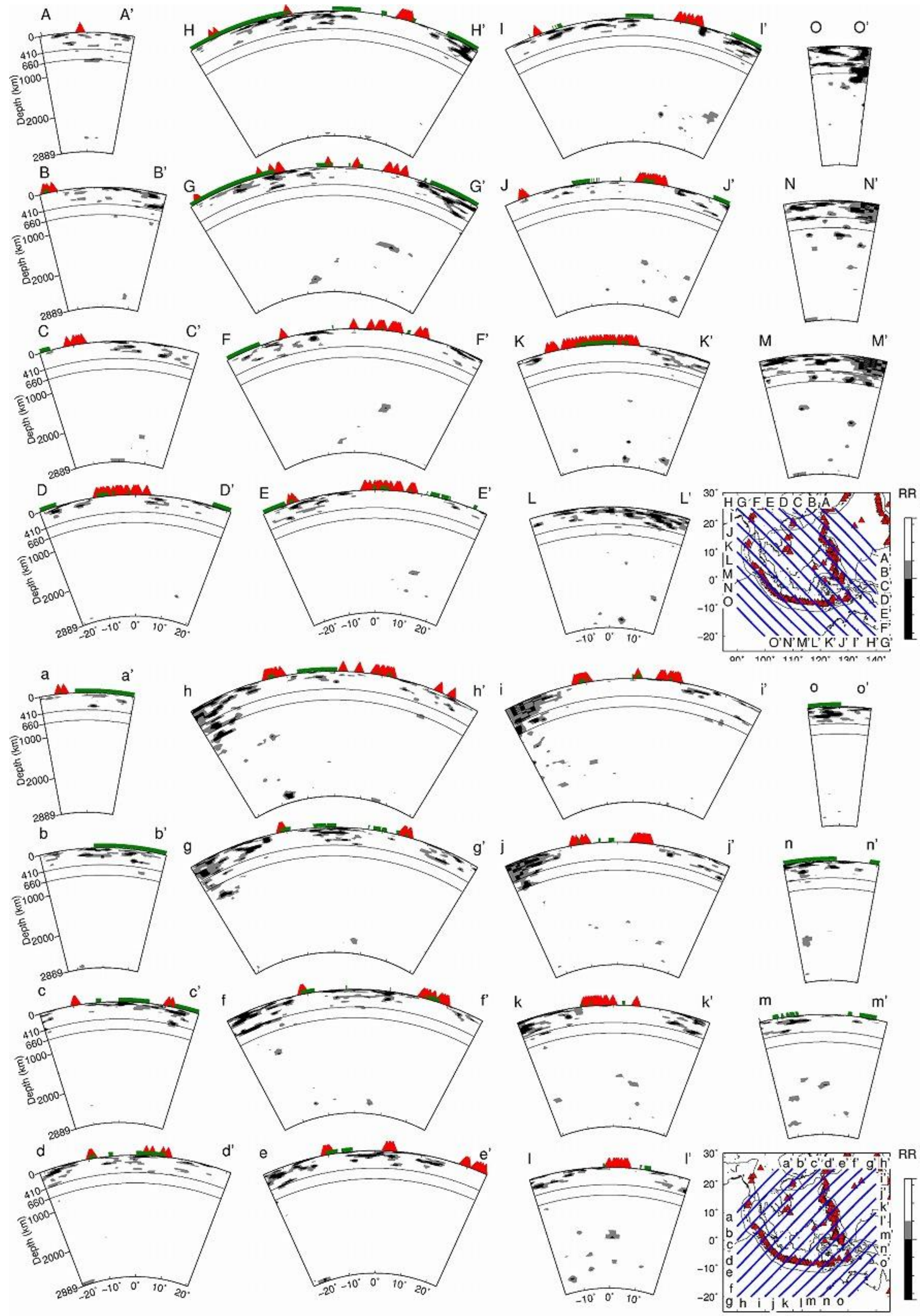
A A'
B B'
C C'
D D'
E E'
F F'
G G'
H H'
I I'
J J'
K K'
L L'
M M'
N N'
O O'
a a'
b b'
c c'
d d'
e e'
f f'
g g'
h h'
i i'
j j'
k k'
l l'
m m'
n n'
o o'
0
410
660
1000
2000
2889
Depth (km)
-20° -10° 0° 10° 20°
-10° 0° 10°
30° 20° 10° 0° -10° -20°
90° 100° 110° 120° 130° 140°
RR (%)
100
0
-100

Figure S17.

Figure S15. The same as Figure S12 but for the checkerboard resolution test with a lateral grid interval of 167 km inside the study region (CRT2).

Figure S16. The same as Figure S13 but for the checkerboard resolution test with a lateral grid interval of 167 km inside the study region (CRT2).

Figure S17. The same as Figure S14 but for the checkerboard resolution test with a lateral grid interval of 167 km inside the study region (CRT2).

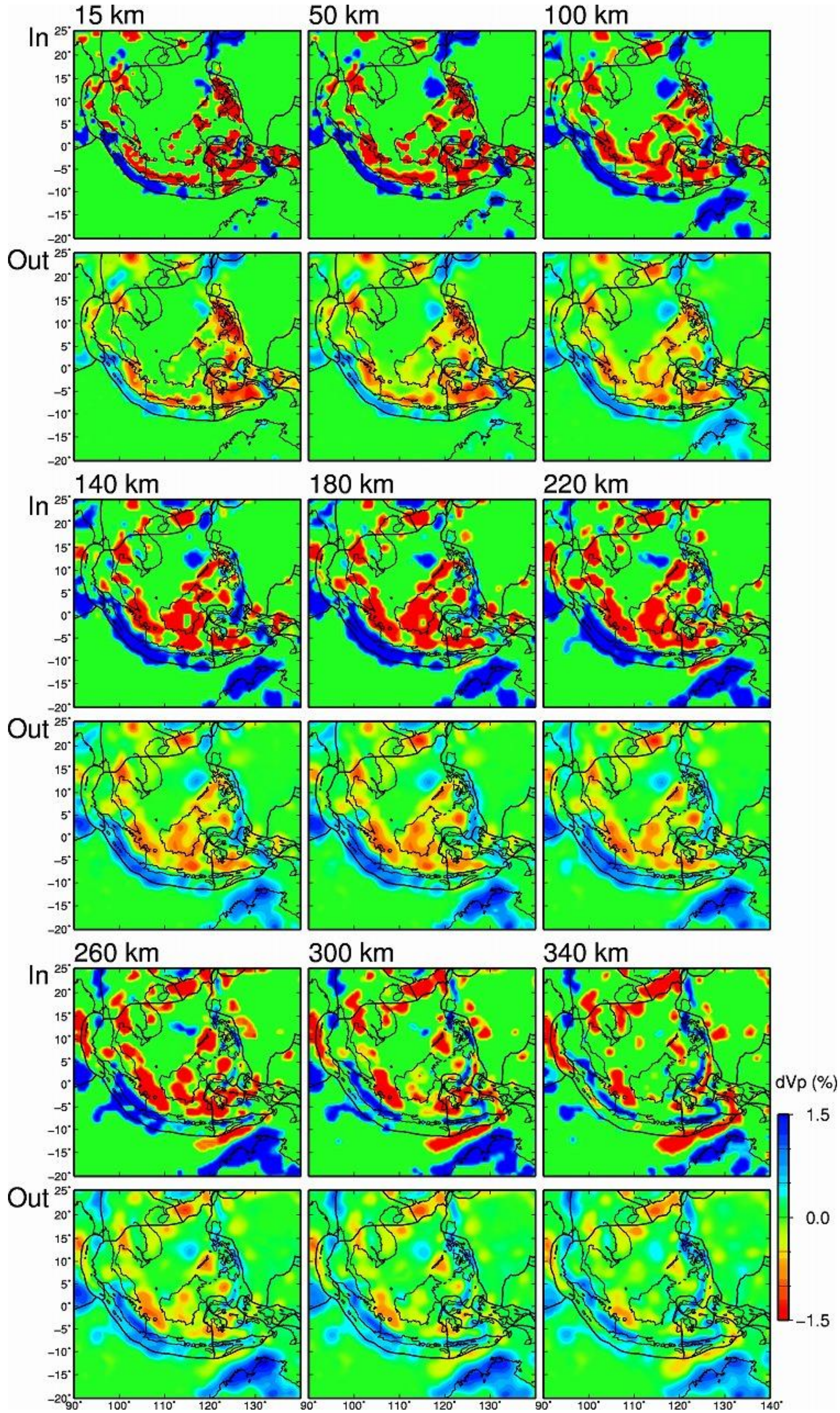

145 **Figure S18.**

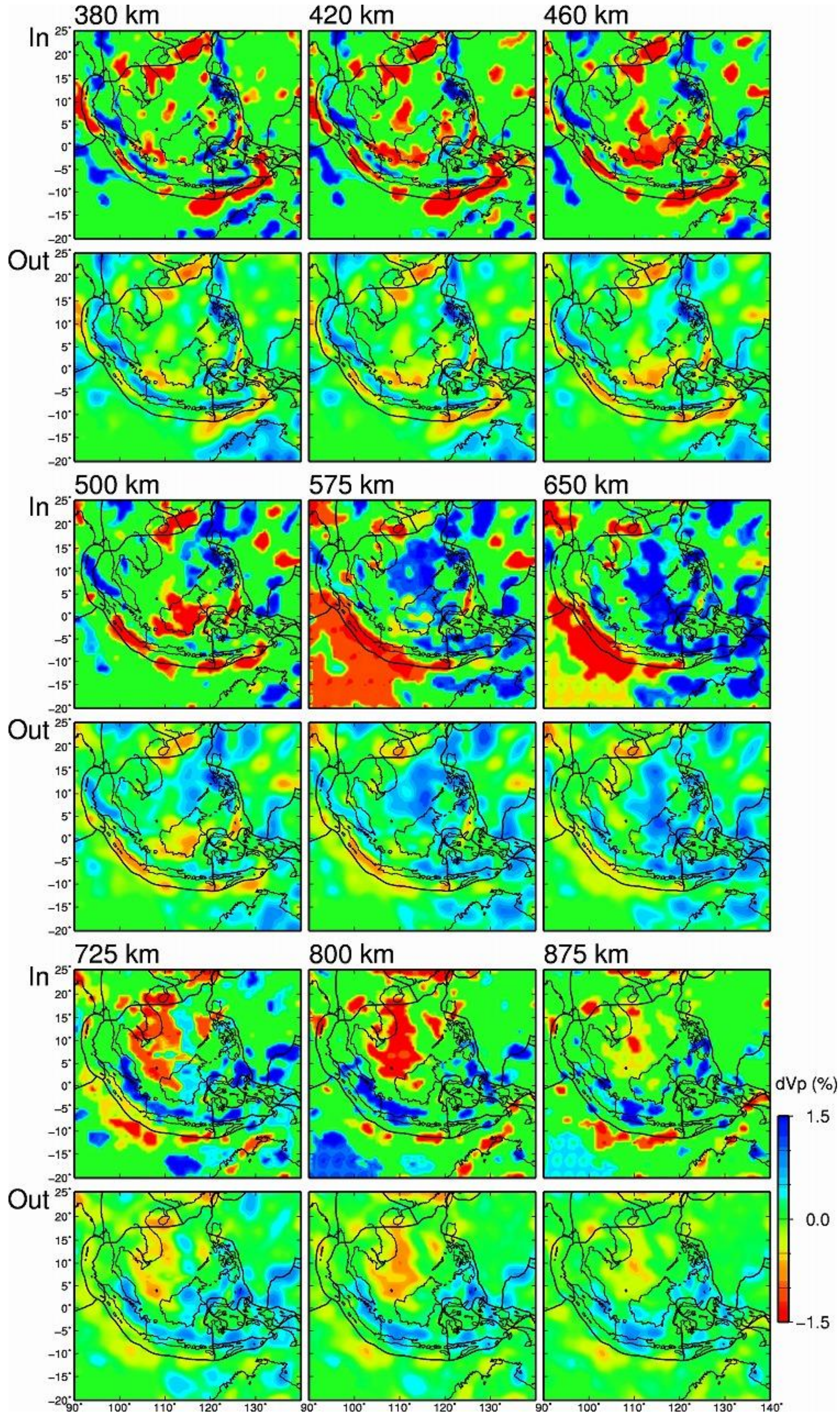

146 **Figure S18.** (continued).

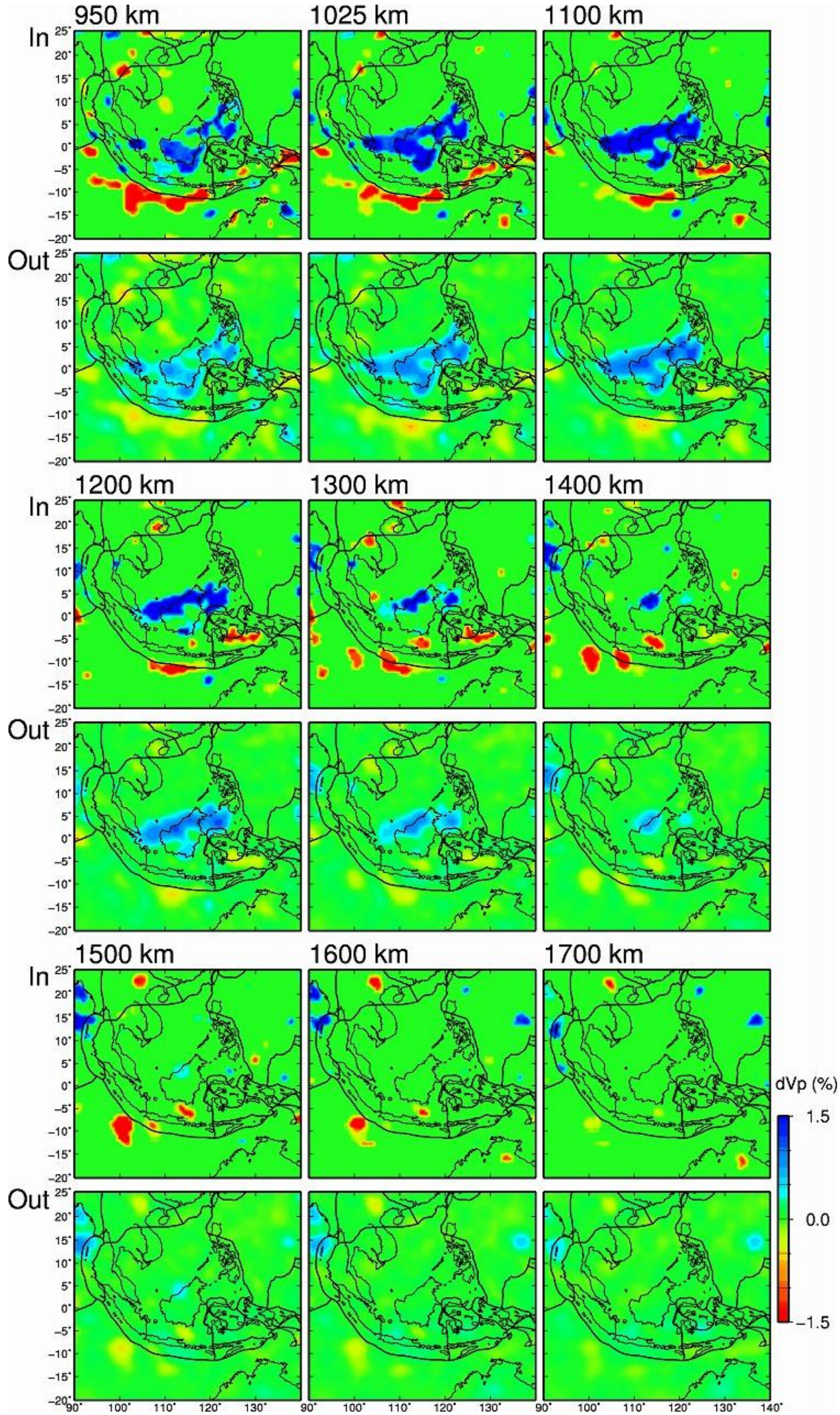

Figure S18. (continued).

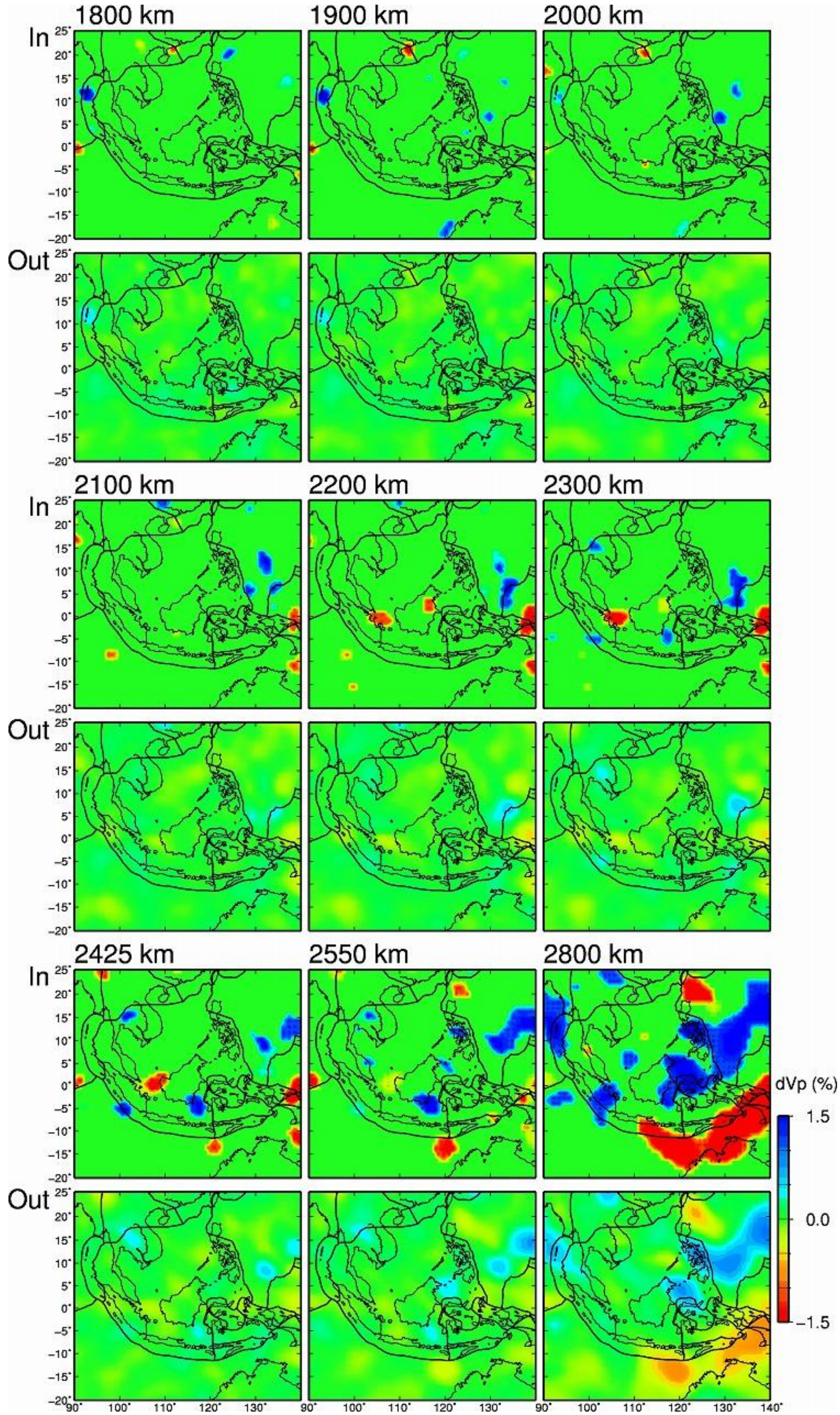

148 **Figure S18.** (continued).

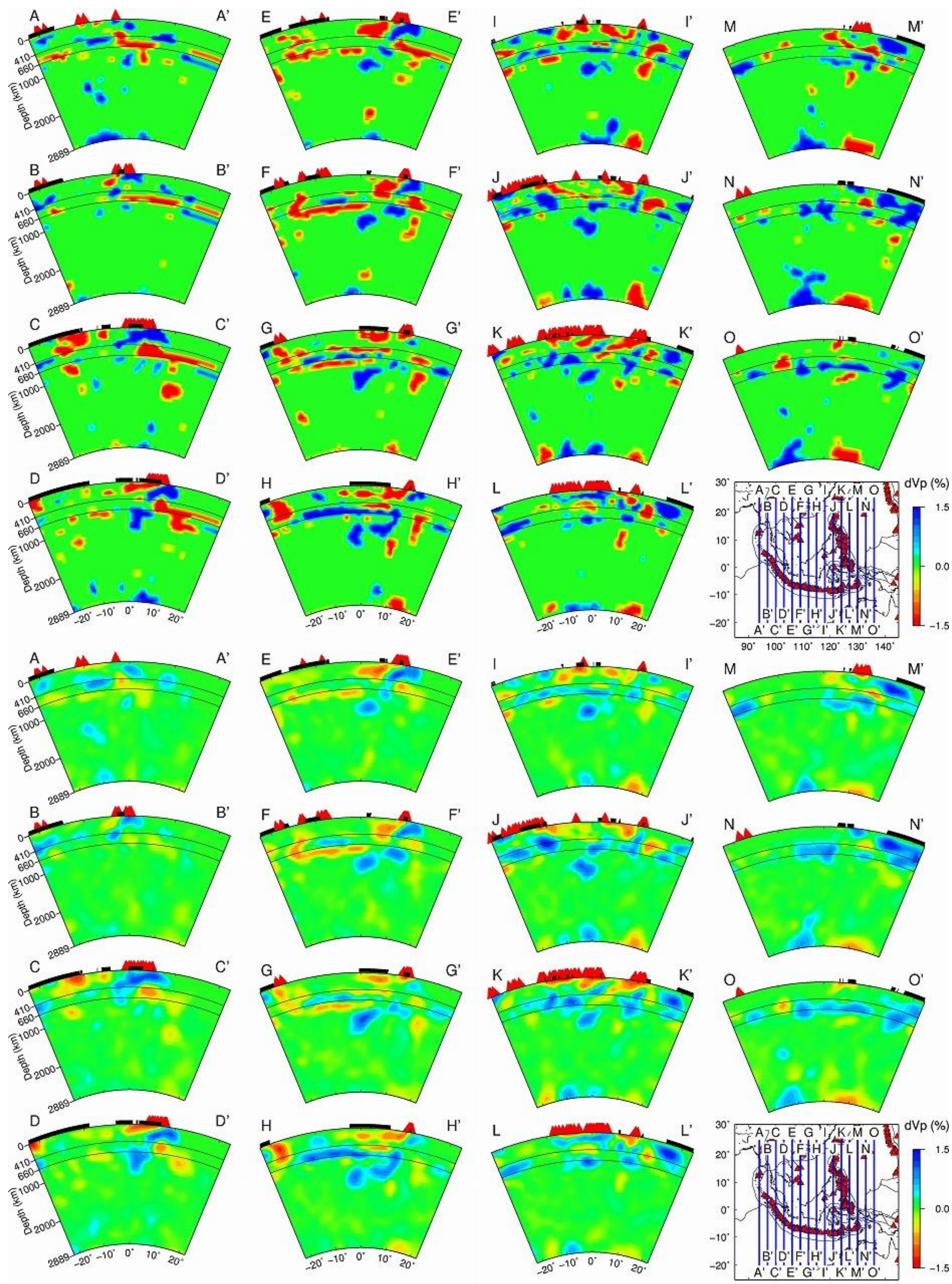

149 **Figure S19.**

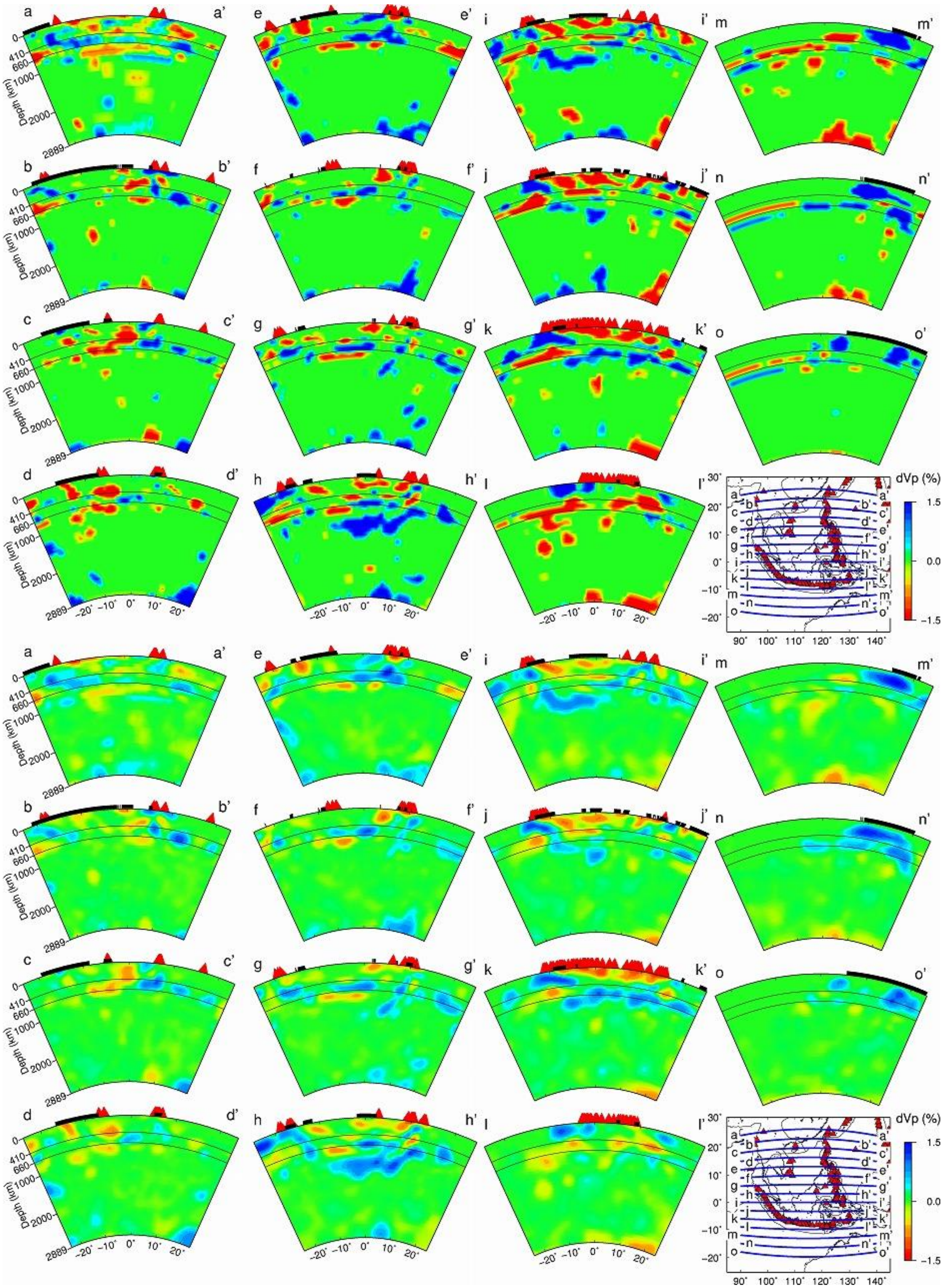

150 **Figure S20.**

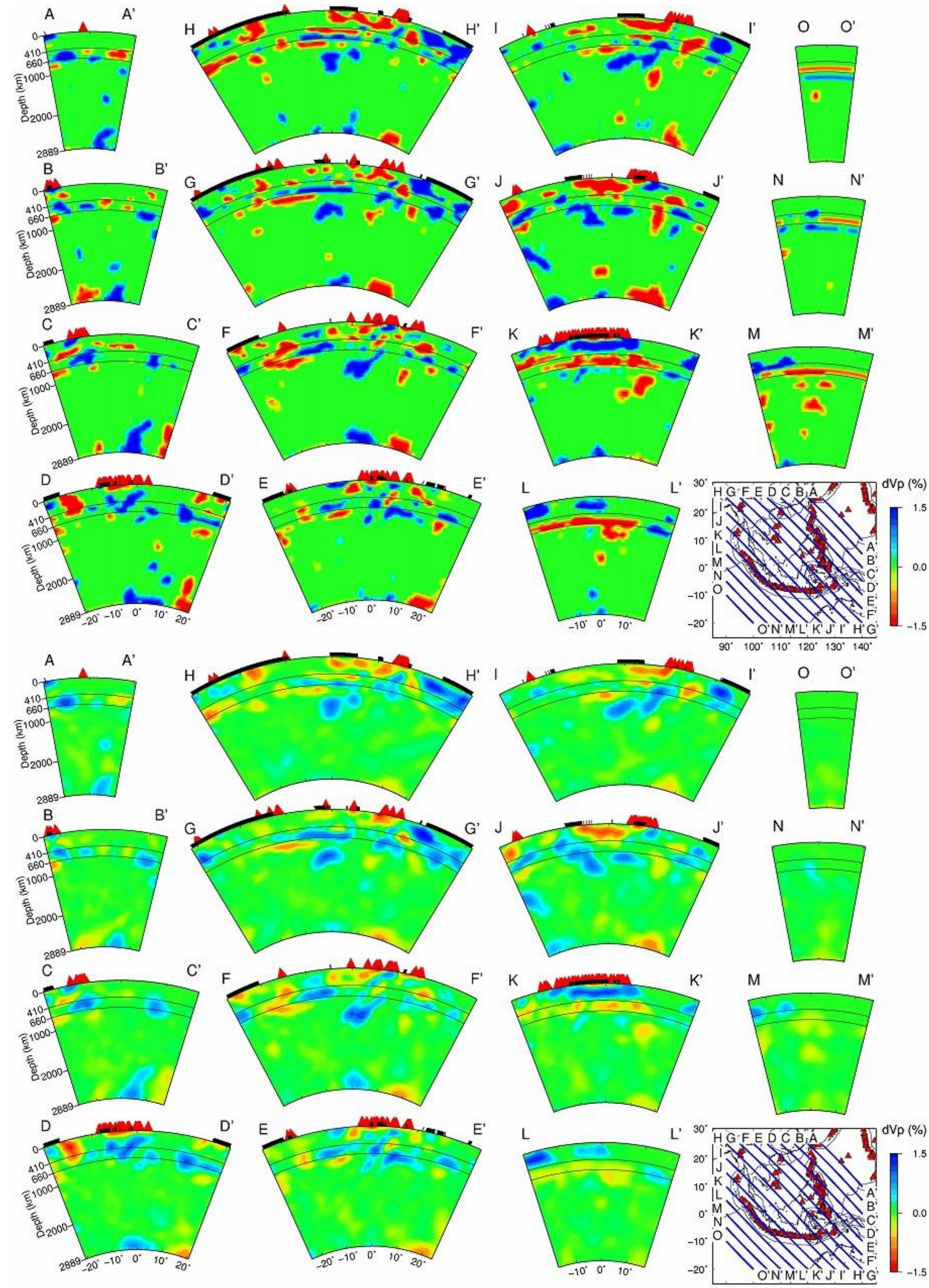

151 **Figure S21.**

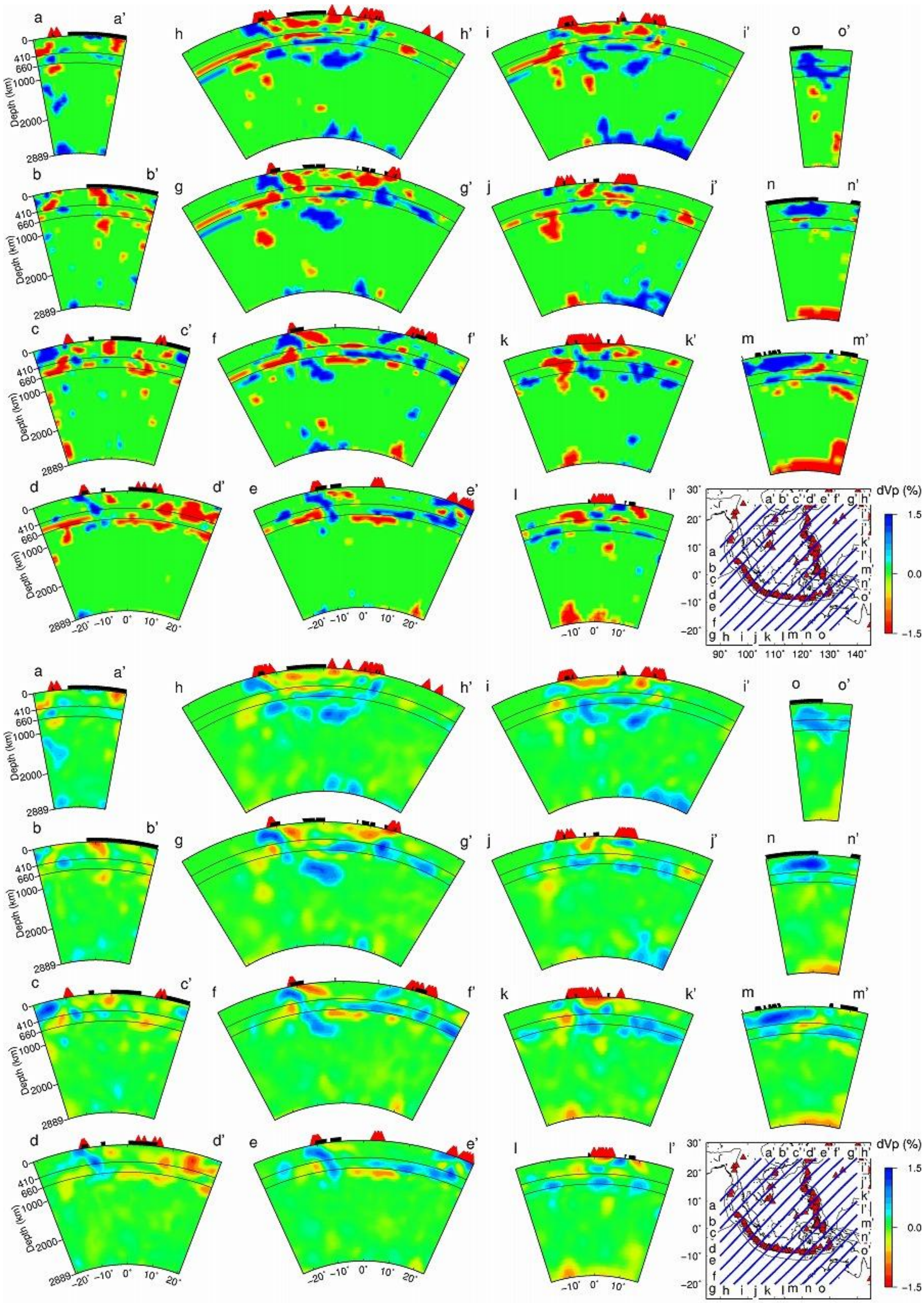

152 **Figure S22.**

Figure S18. Map views showing the input model (upper panels) and output results (lower panels) of the restoring resolution test (RRT). The layer depth is shown above the upper panels. The blue and red colors denote high and low Vp perturbations, respectively, whose scale (in %) is shown on the right.

Figure S19. Vertical cross-sections showing **(top)** the input model and **(bottom)** output results of the restoring resolution test (RRT) along 15 profiles in the N-S direction. Locations of the profiles are shown on the inset map. The 410-km and the 660-km discontinuities are shown in black solid lines. The thick black lines on the surface denote land areas. The red triangles denote active volcanoes. The thin black lines on the inset map denote the plate boundaries.

Figure S20. The same as Figure S19 but along 15 profiles in the E-W direction.

Figure S21. The same as Figure S19 but along 15 profiles in the NW-SE direction.

Figure S22. The same as Figure S19 but along 15 profiles in the NE-SW direction.

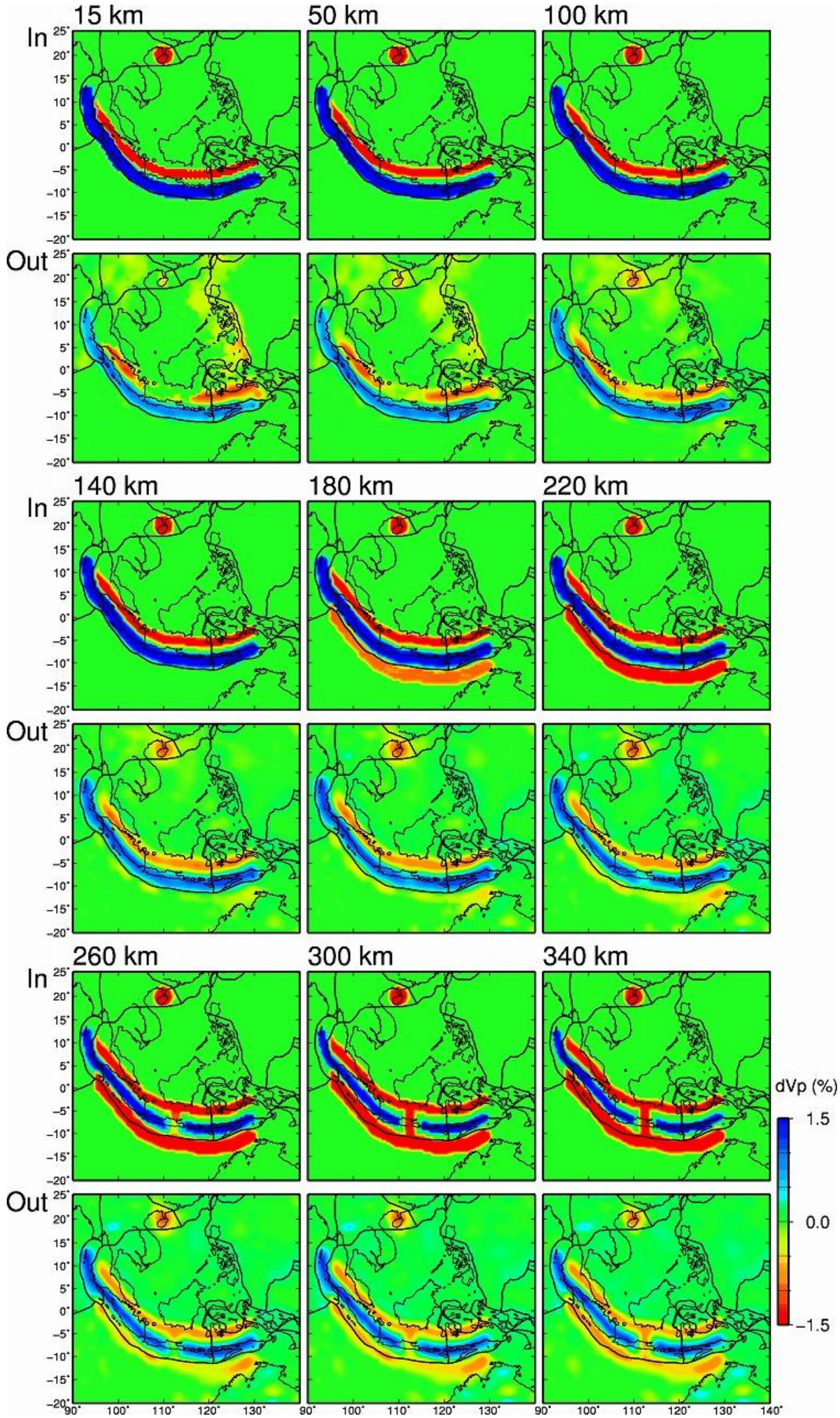

176 **Figure S23.**

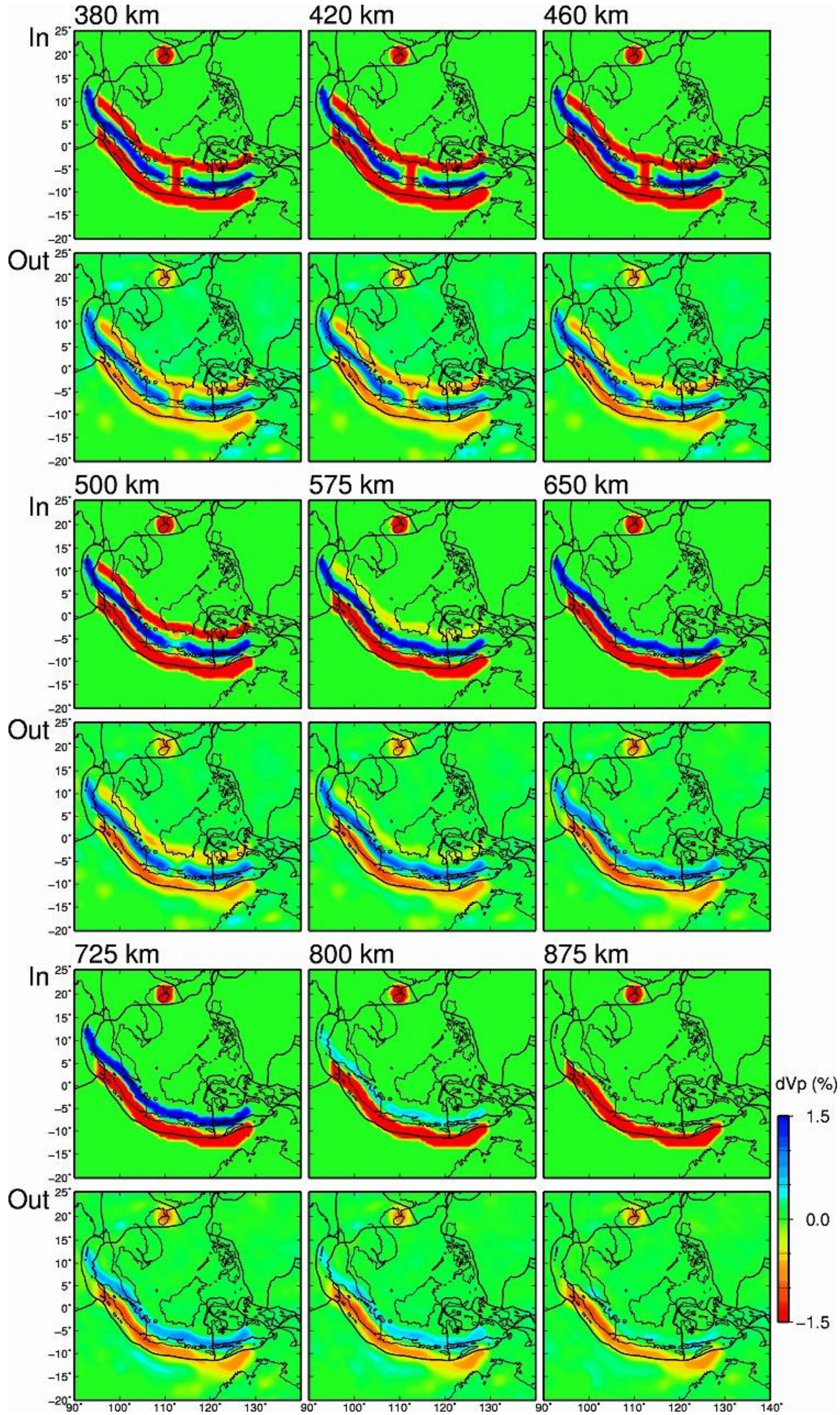

177 **Figure S23.** (continued).

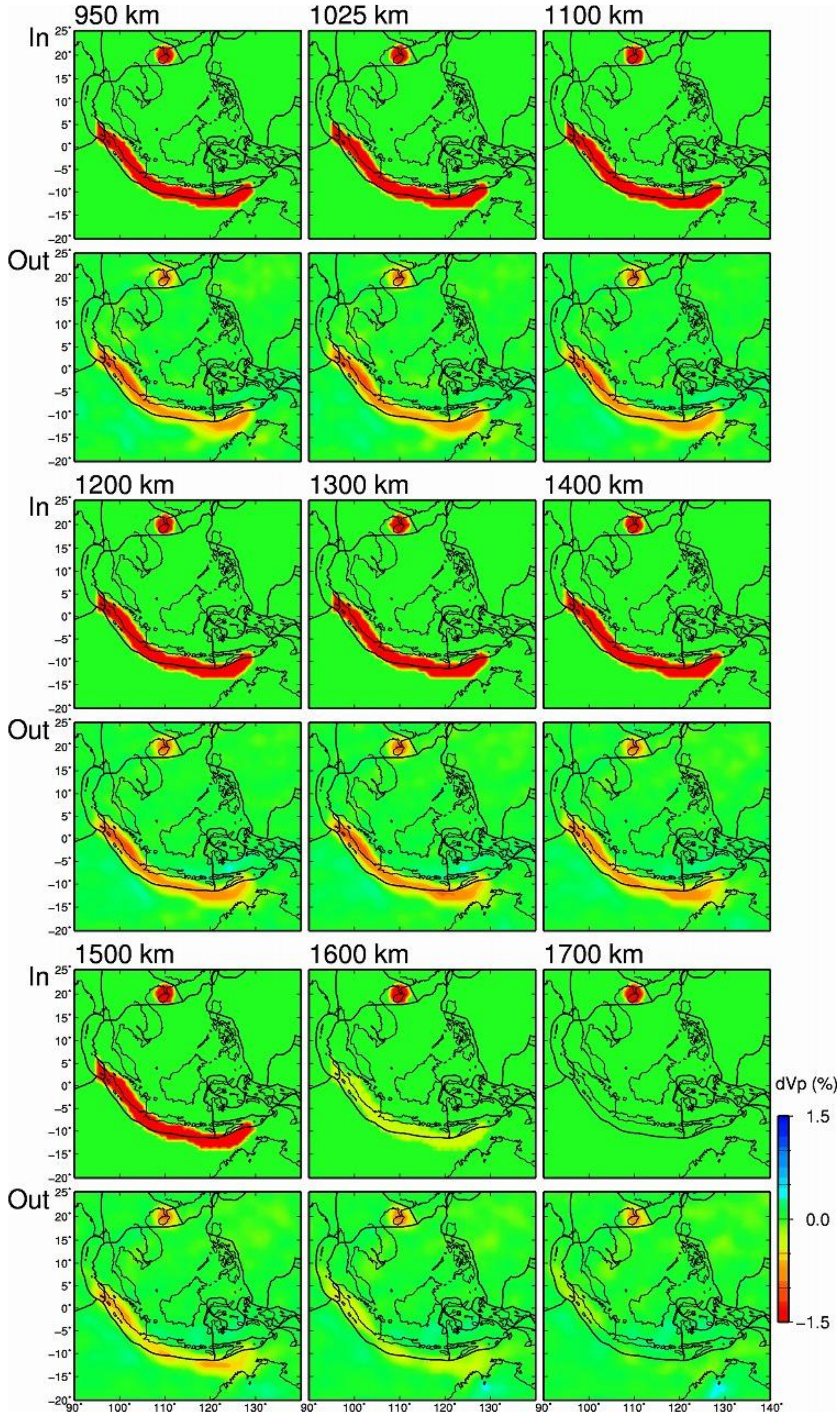

Figure S23. (continued).

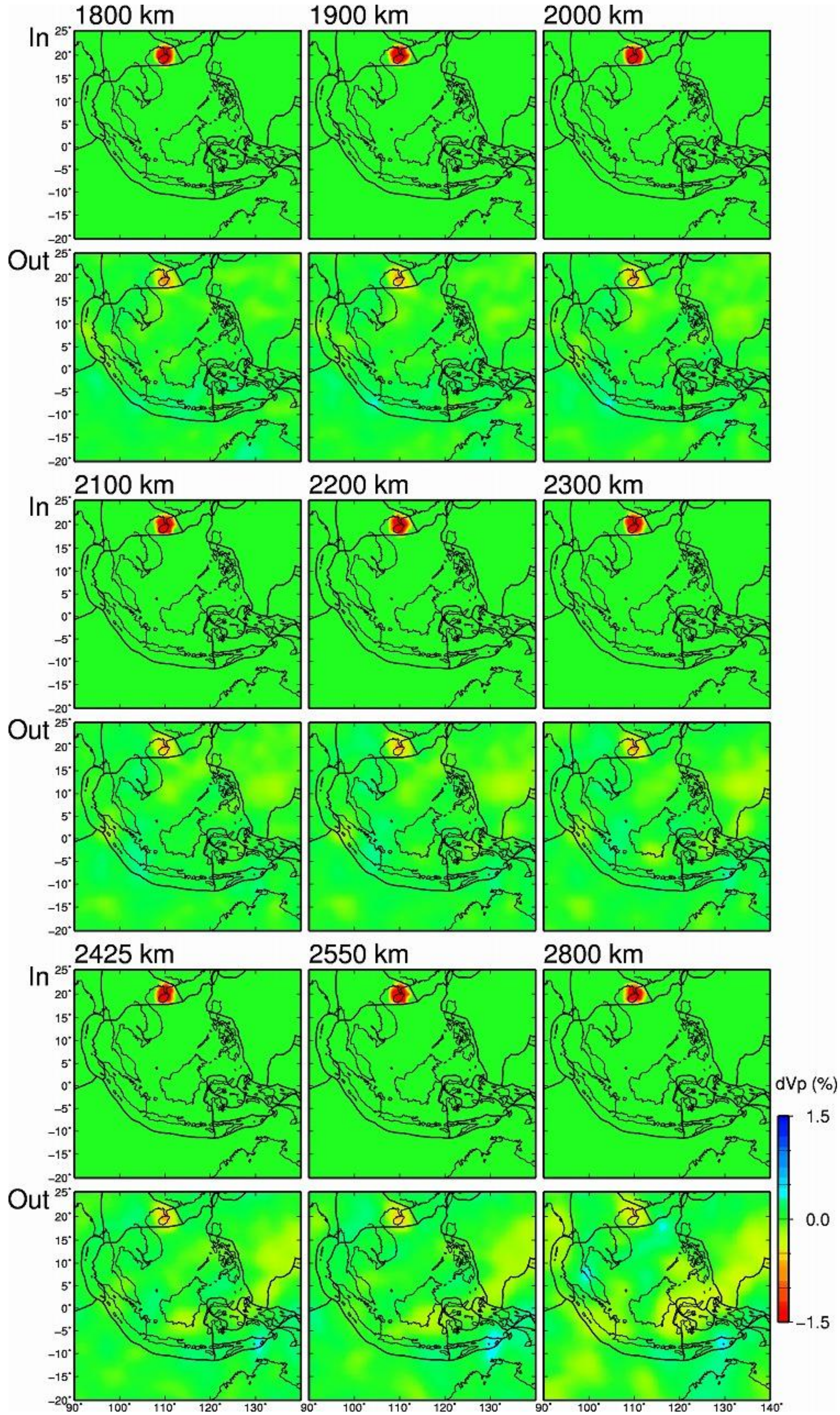

179 **Figure S23.** (continued).

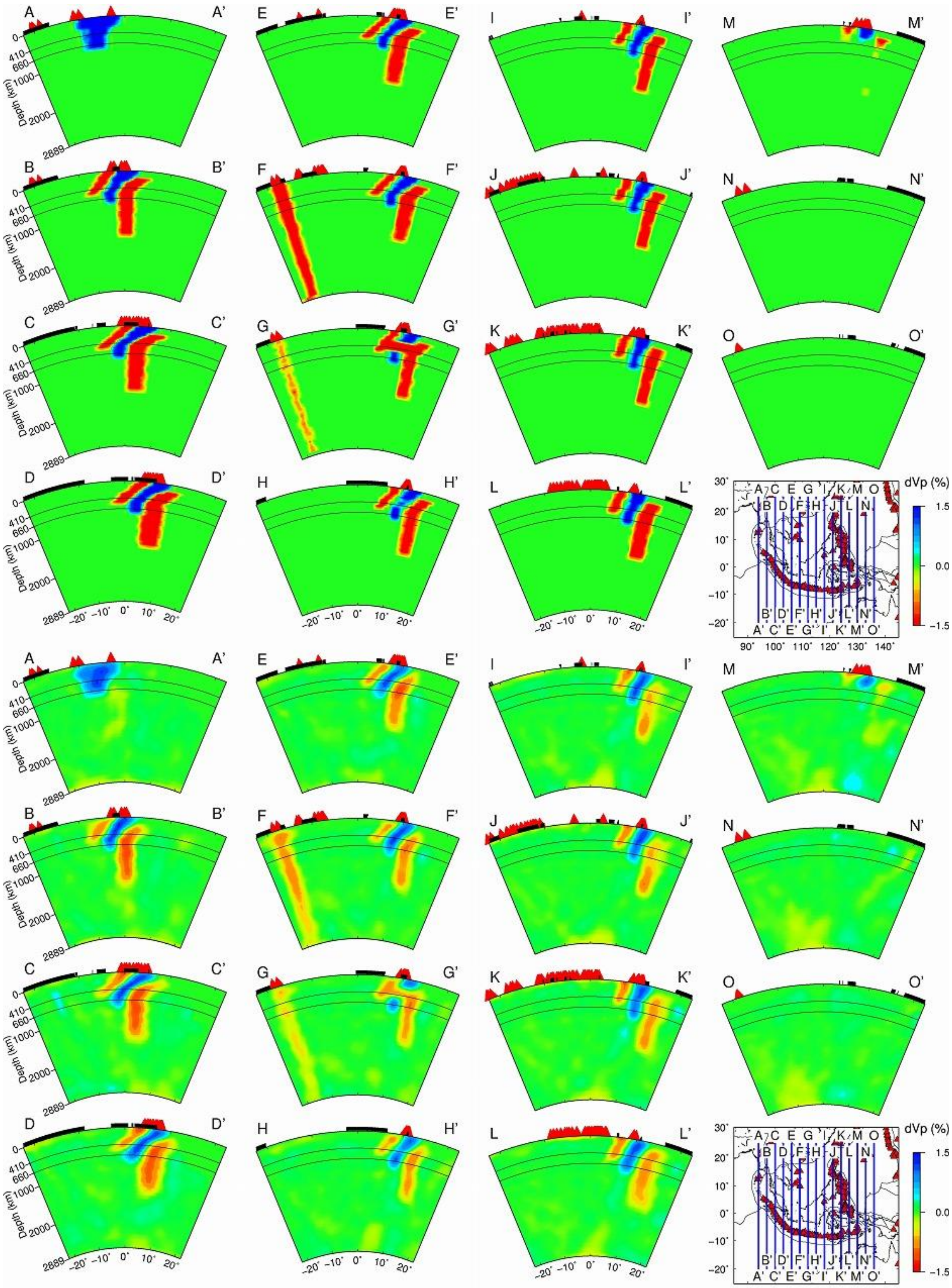
A
A'
B
B'
C
C'
D
D'
E
E'
F
F'
G
G'
H
H'
I
I'
J
J'
K
K'
L
L'
M
M'
N
N'
O
O'
Depth (km)
0
410
660
1000
2000
2889
-20° -10° 0° 10° 20°
dVp (%)
1.5
0.0
-1.5
30°
20°
10°
0°
-10°
-20°
90° 100° 110° 120° 130° 140°

Figure S24.

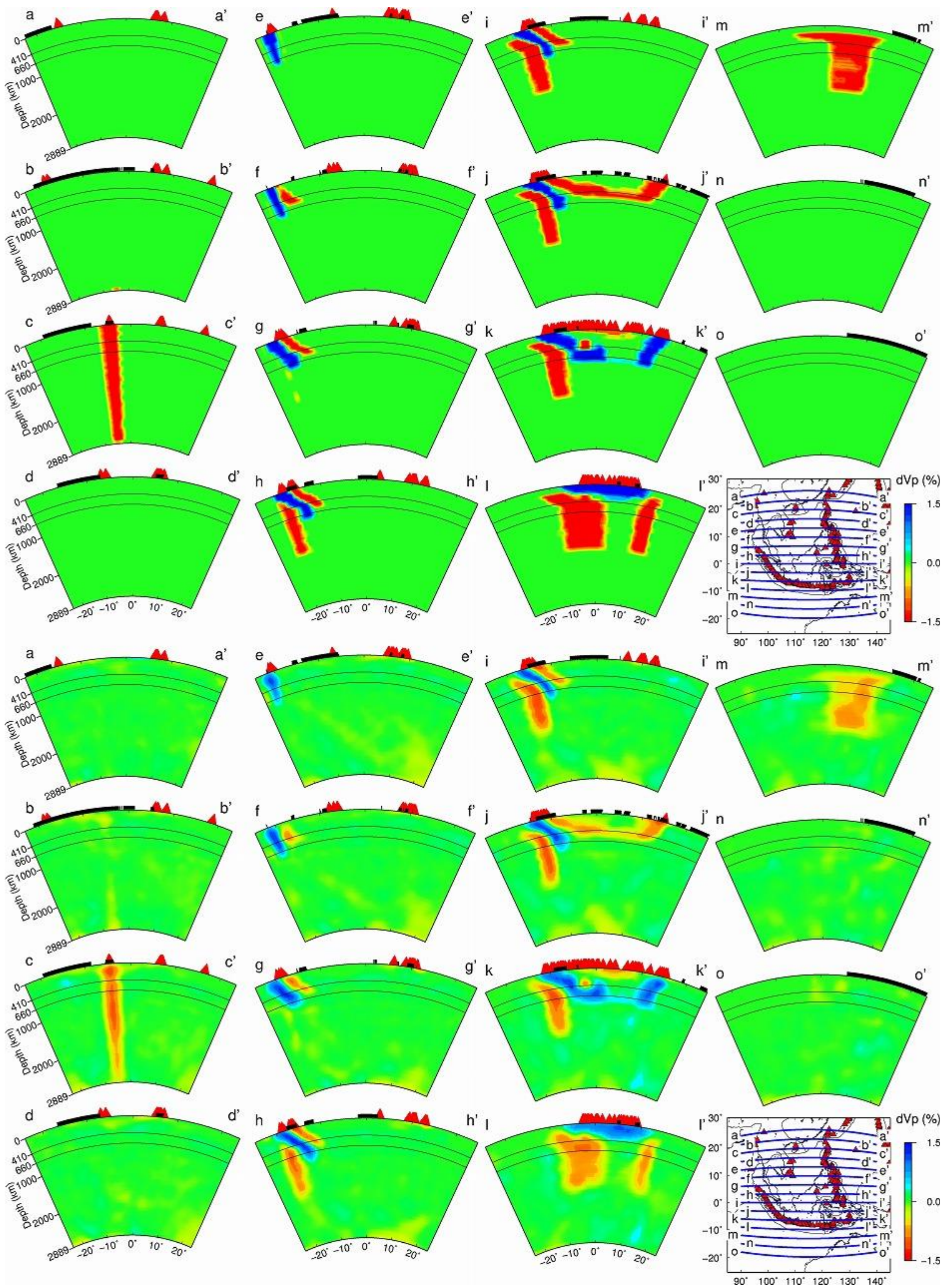

181 **Figure S25.**

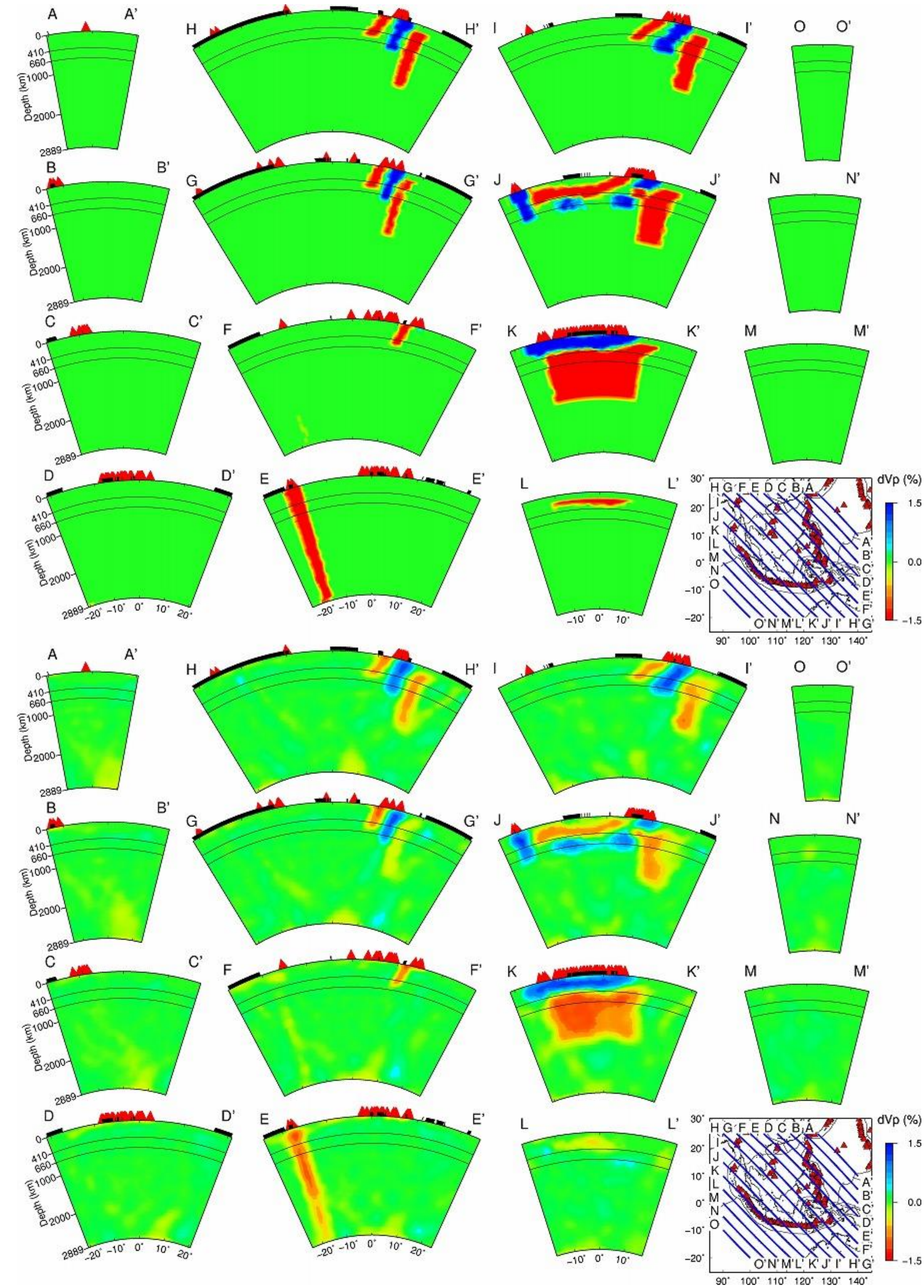

182 **Figure S26.**

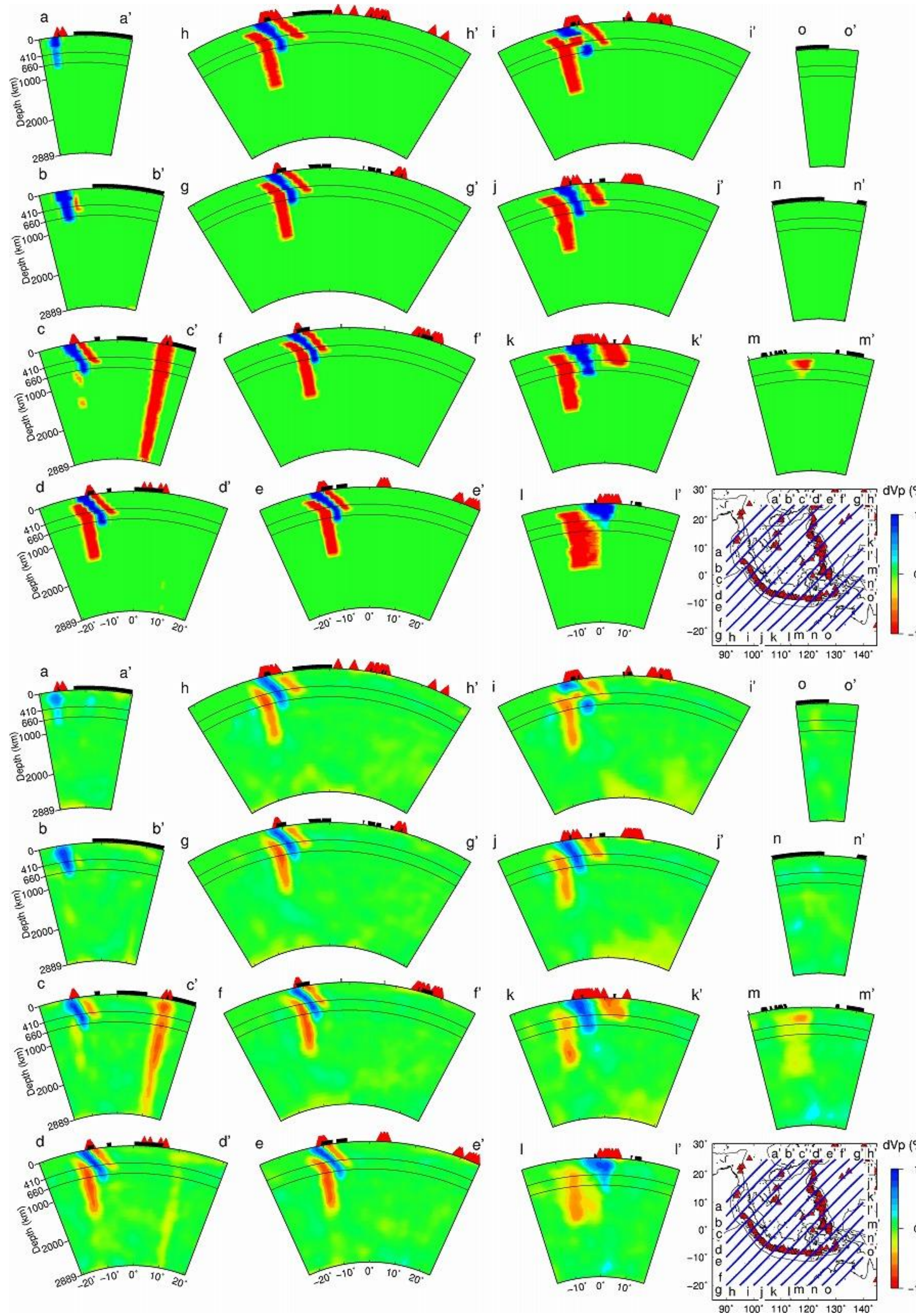

Figure S27.

Figure S23. The same as Figure S18 but for the synthetic resolution test with (1) high-Vp subducting Australian slab, (2) low-Vp hot mantle upwelling in the mantle wedge, (3) low-Vp subslab hot mantle upwelling (SHMU), (4) a hole in the Australian slab at depths of 260−460 km and latitudes 110°−115°, (5) a low-Vp bridge connecting (2) and (3) through the slab hole, and (6) low-Vp whole-mantle Hainan plume (SRT1).

Figure S24. Vertical cross-sections showing **(top)** the input model and **(bottom)** output results of the SRT1 along 15 profiles in the N-S direction. Locations of the profiles are shown on the inset map. The 410-km and the 660-km discontinuities are shown in black solid lines. The thick black lines on the surface denote land areas. The red triangles denote active volcanoes. The thin black lines on the inset map denote the plate boundaries.

Figure S25. The same as Figure S24 but along 15 profiles in the E-W direction.

Figure S26. The same as Figure S24 but along 15 profiles in the NW-SE direction.

Figure S27. The same as Figure S24 but along 15 profiles in the NE-SW direction.

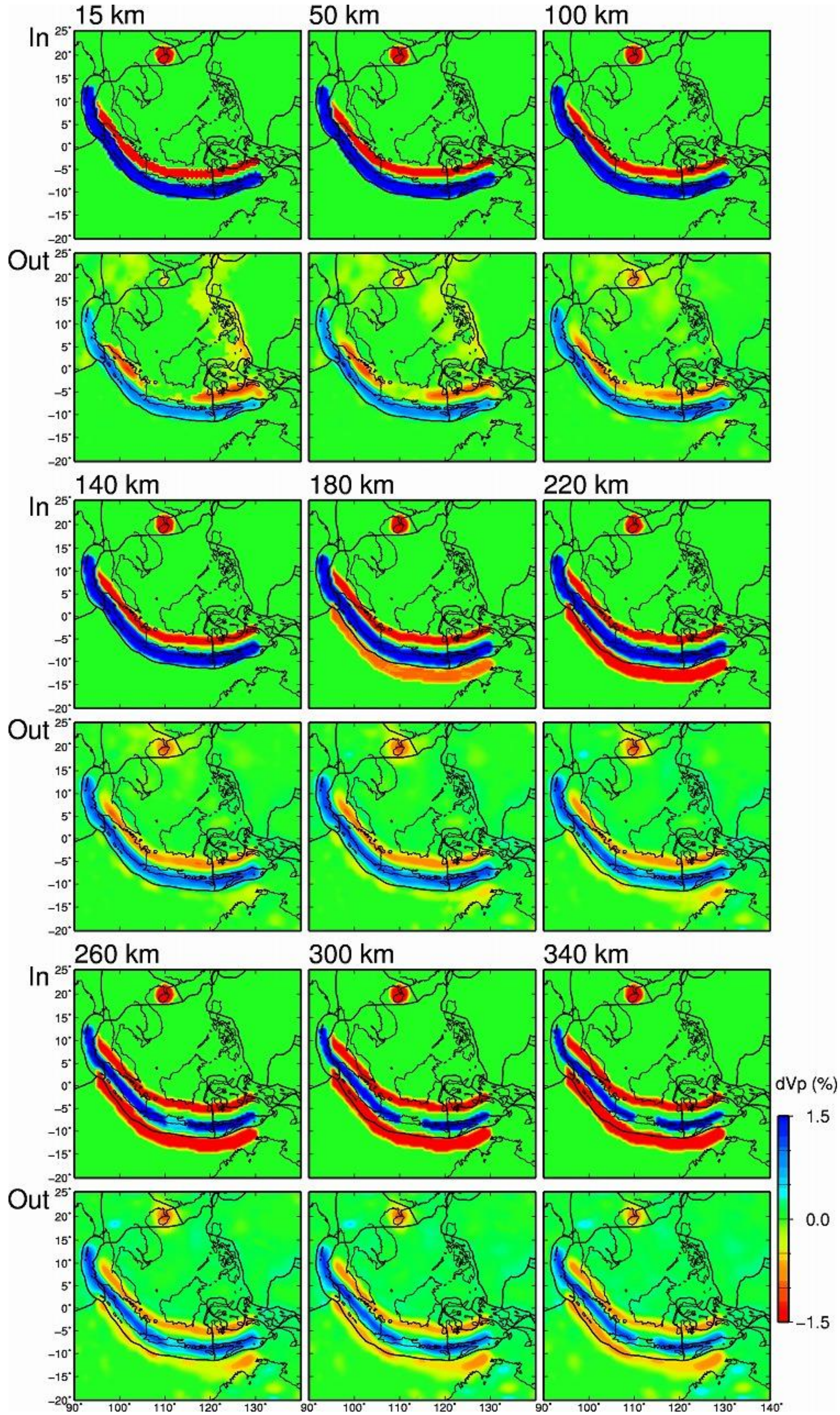

207 **Figure S28.**

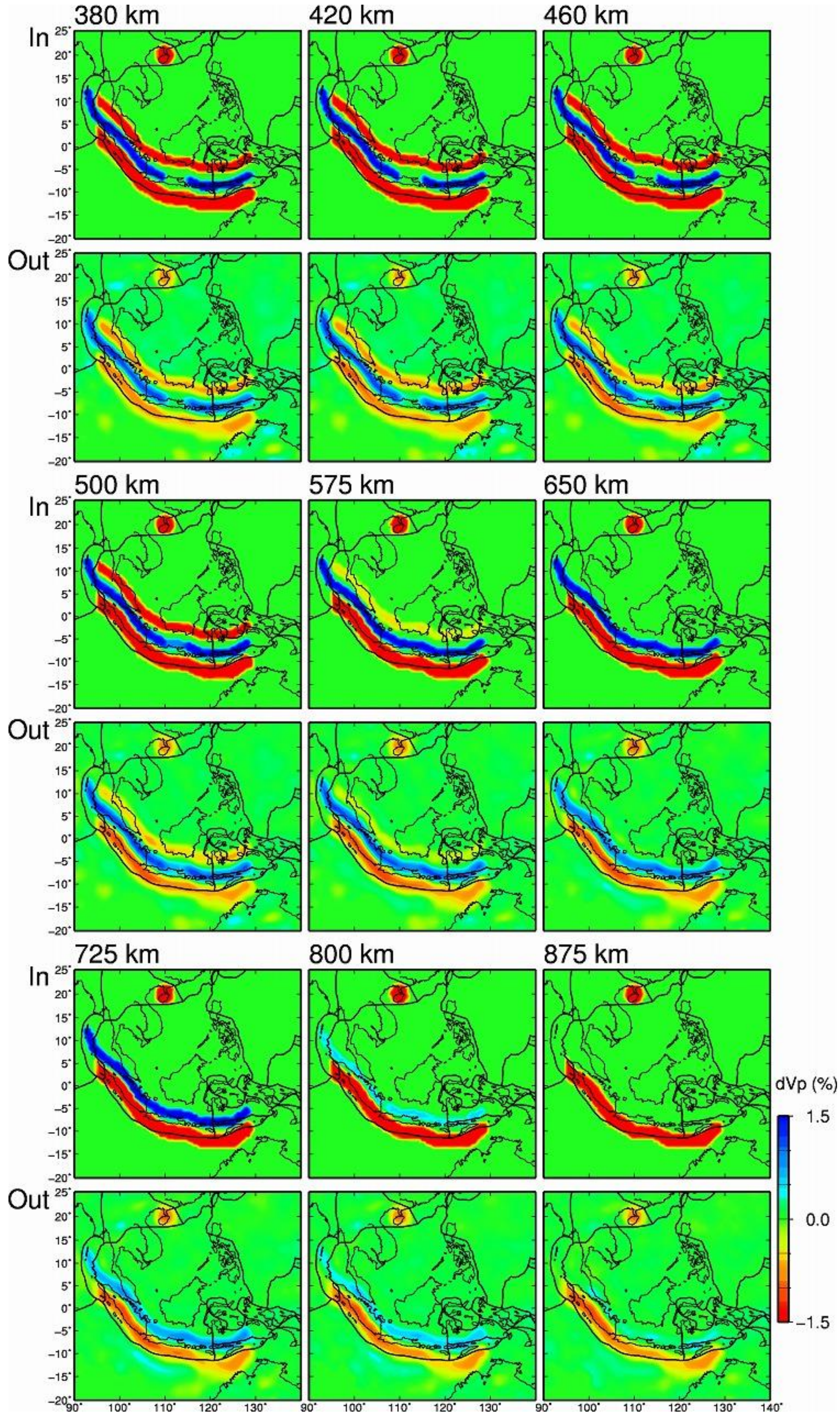

Figure S28. (continued).

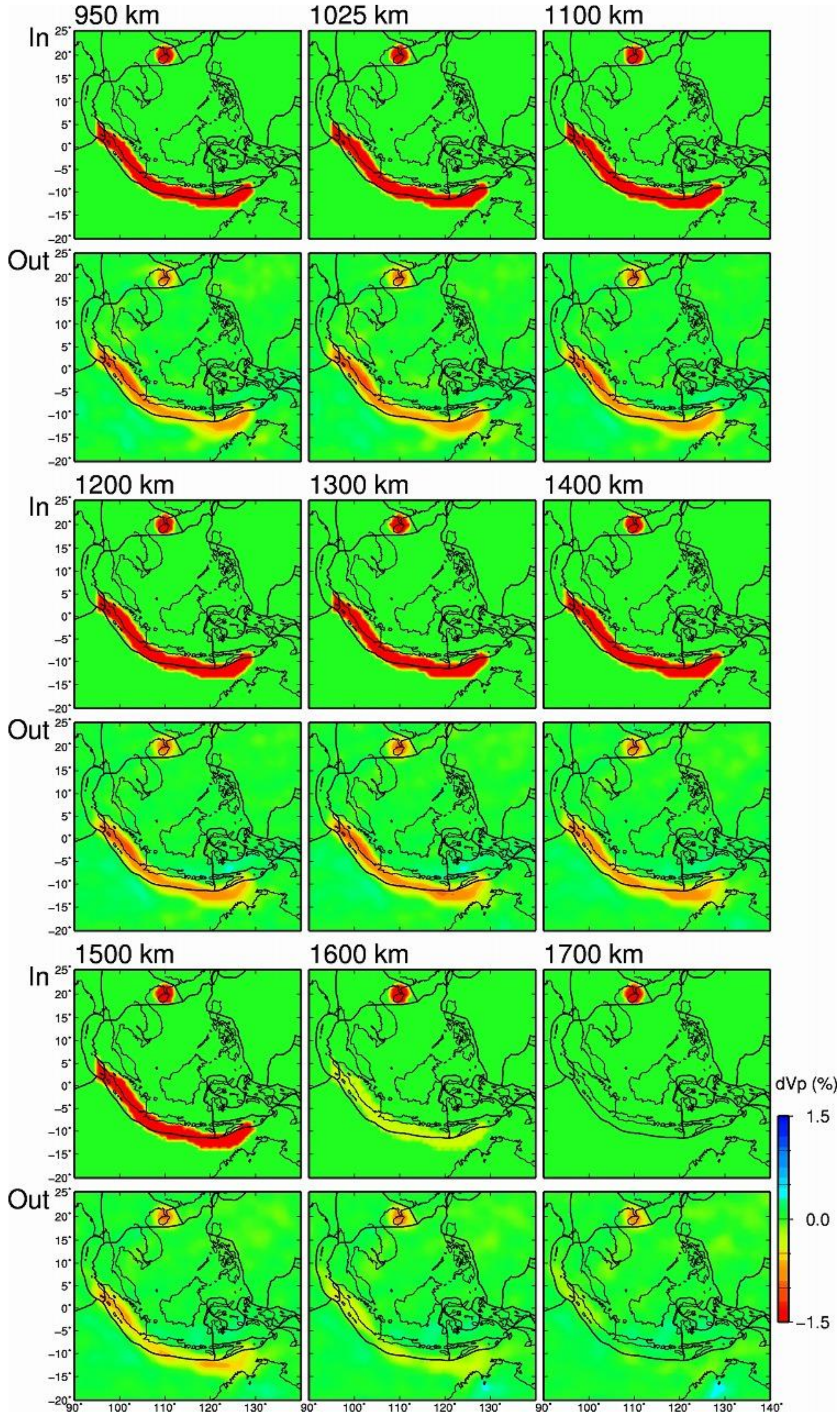

209 **Figure S28.** (continued).

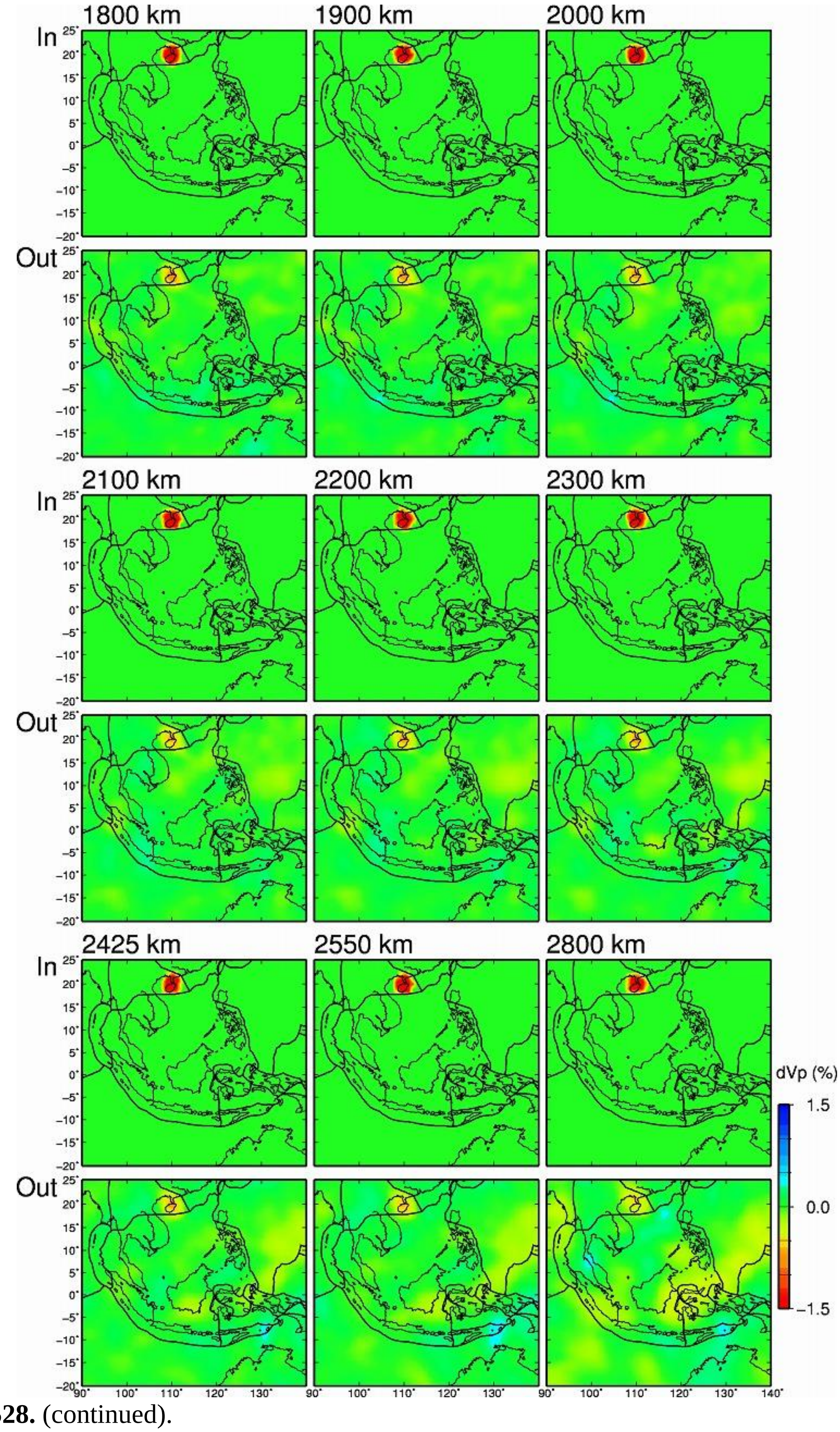

210 **Figure S28.** (continued).

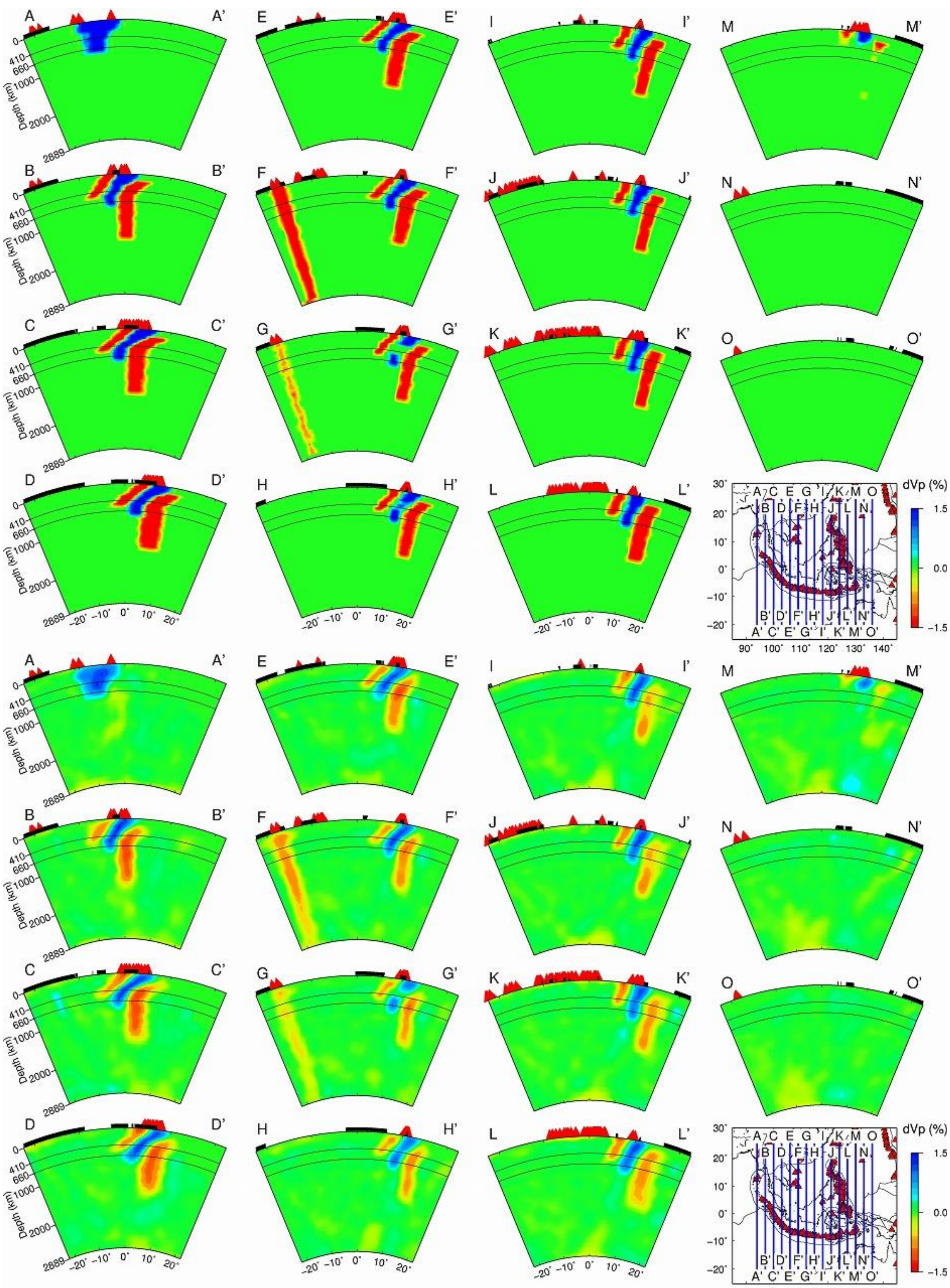

211 **Figure S29.**

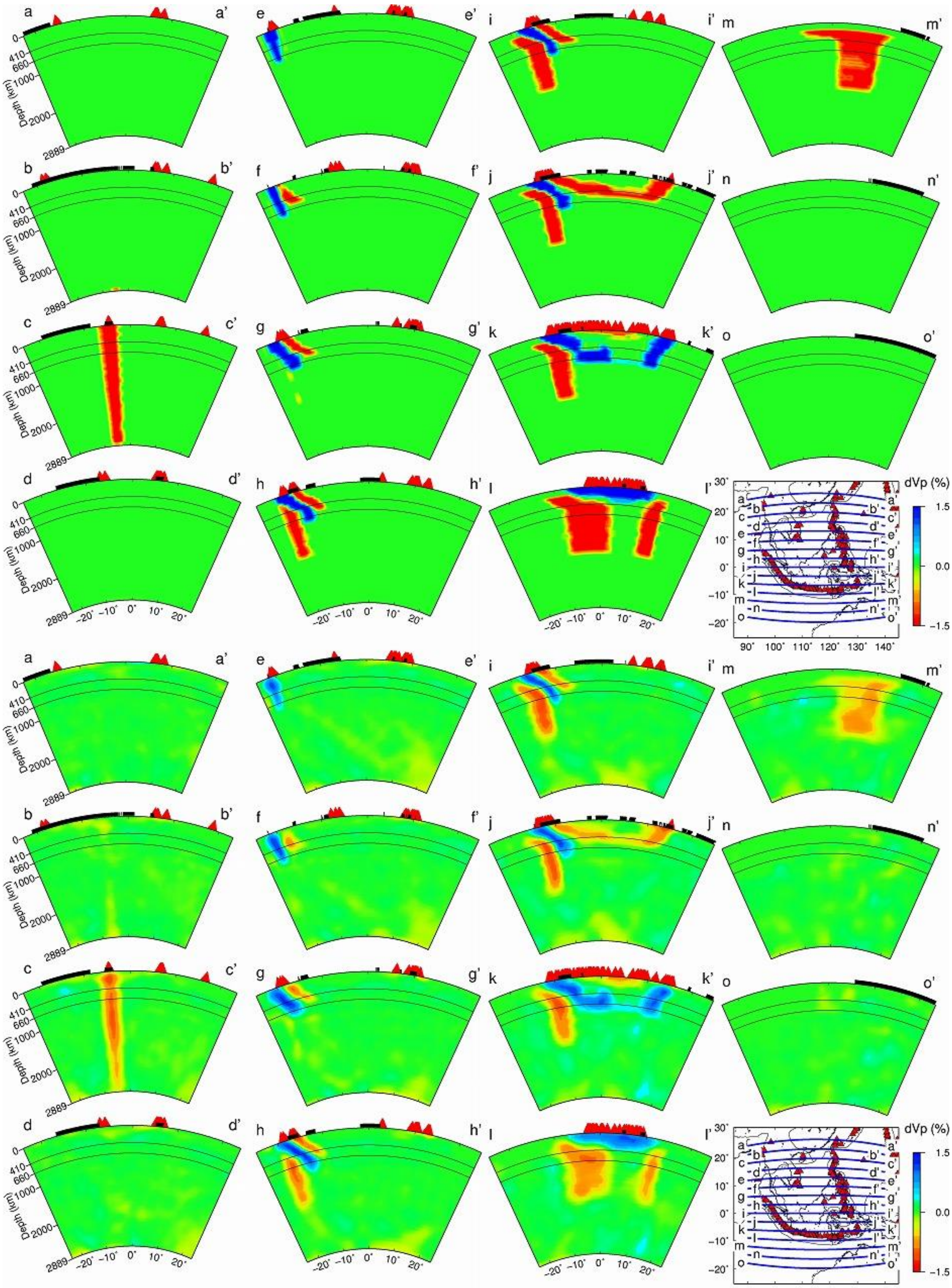
a a' e e' i i' m m'
b b' f f' j j' n n'
c c' g g' k k' o o'
d d' h h' l l'
Depth (km)
0
410
660
1000
2000
2889
-20° -10° 0° 10° 20°
dVp (%)
1.5
0.0
-1.5
30°
20°
10°
0°
-10°
-20°
90° 100° 110° 120° 130° 140°

Figure S30.

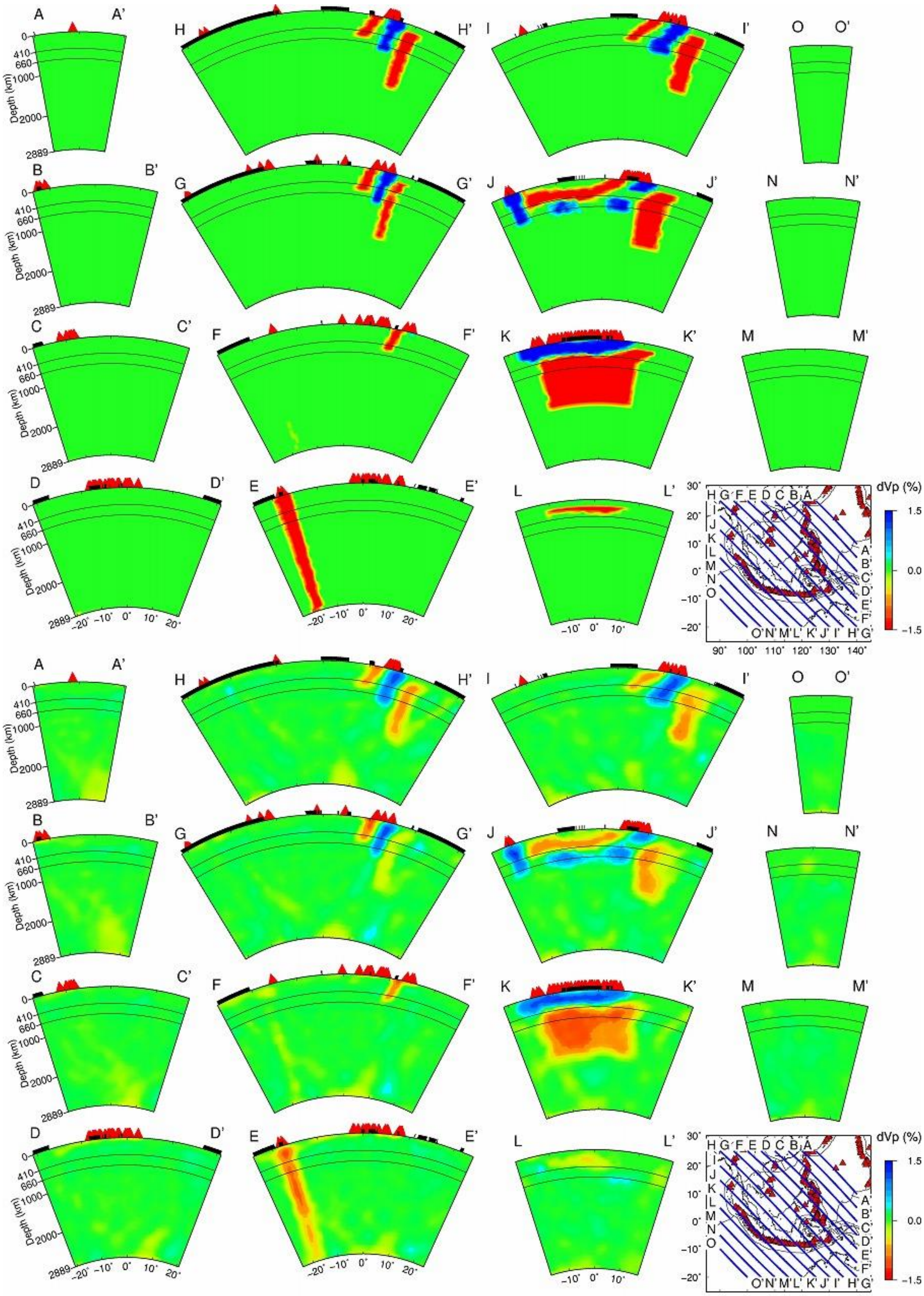

213 **Figure S31.**

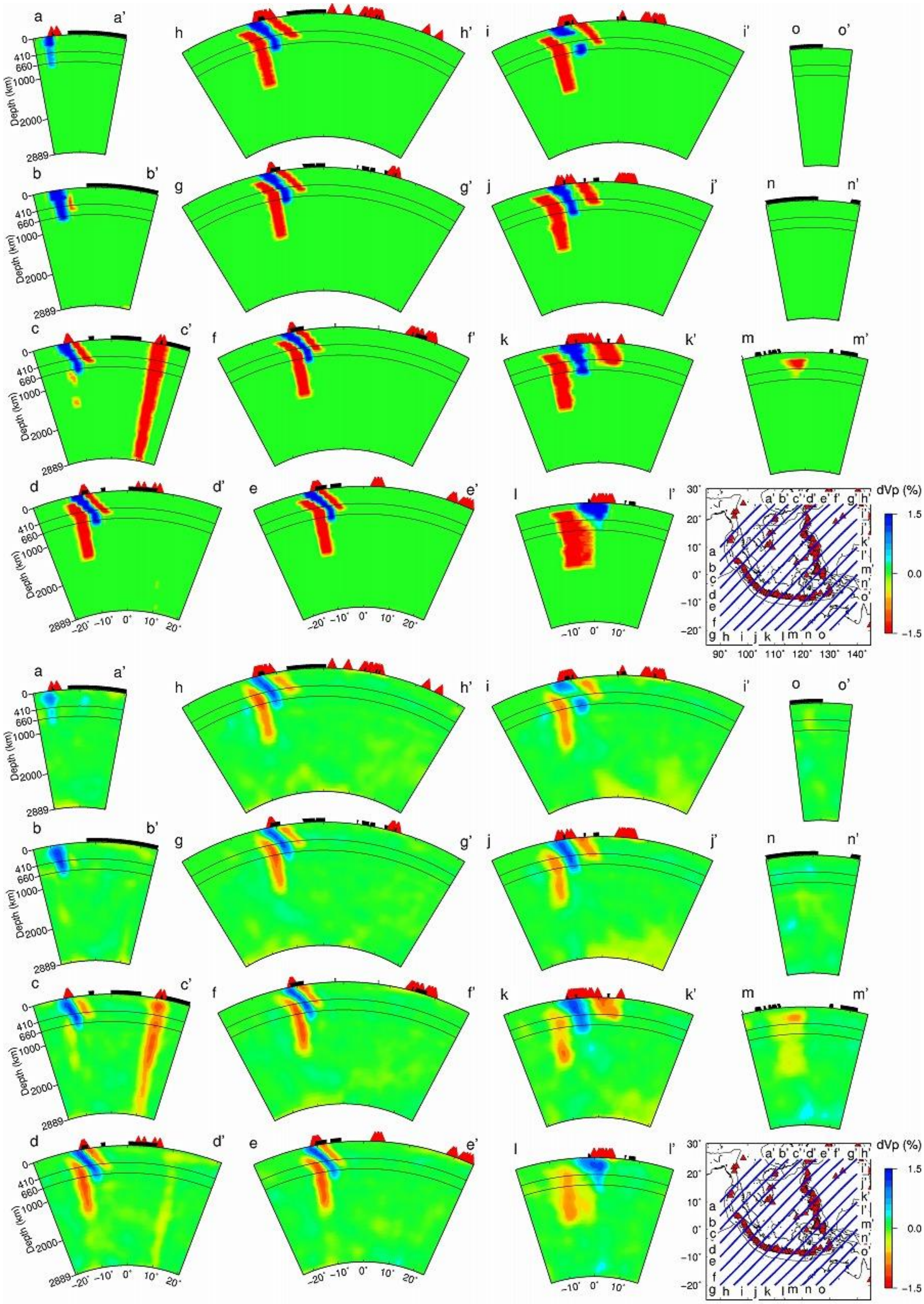

Figure S32.

Figure S28. The same as Figure S23 but for the synthetic resolution test without a low-Vp bridge through the slab hole (SRT2).

Figure S29. Vertical cross-sections showing **(top)** the input model and **(bottom)** output results of the SRT2 along 15 profiles in the N-S direction. Locations of the profiles are shown on the inset map. The 410-km and the 660-km discontinuities are shown in black solid lines. The thick black lines on the surface denote land areas. The red triangles denote active volcanoes. The thin black lines on the inset map denote the plate boundaries.

Figure S30. The same as Figure S29 but along 15 profiles in the E-W direction.

Figure S31. The same as Figure S29 but along 15 profiles in the NW-SE direction.

Figure S32. The same as Figure S29 but along 15 profiles in the NE-SW direction.

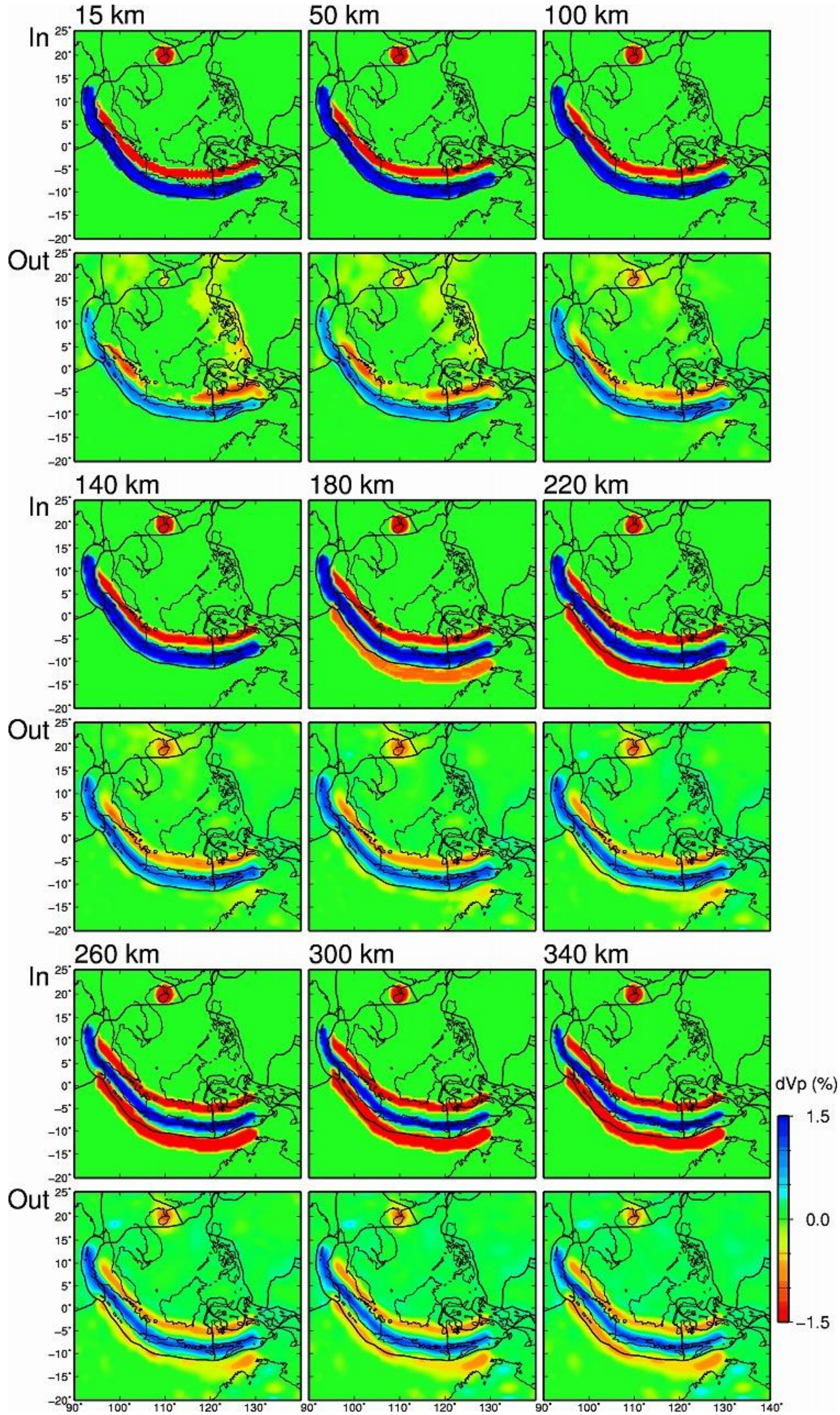

230 **Figure S33.**

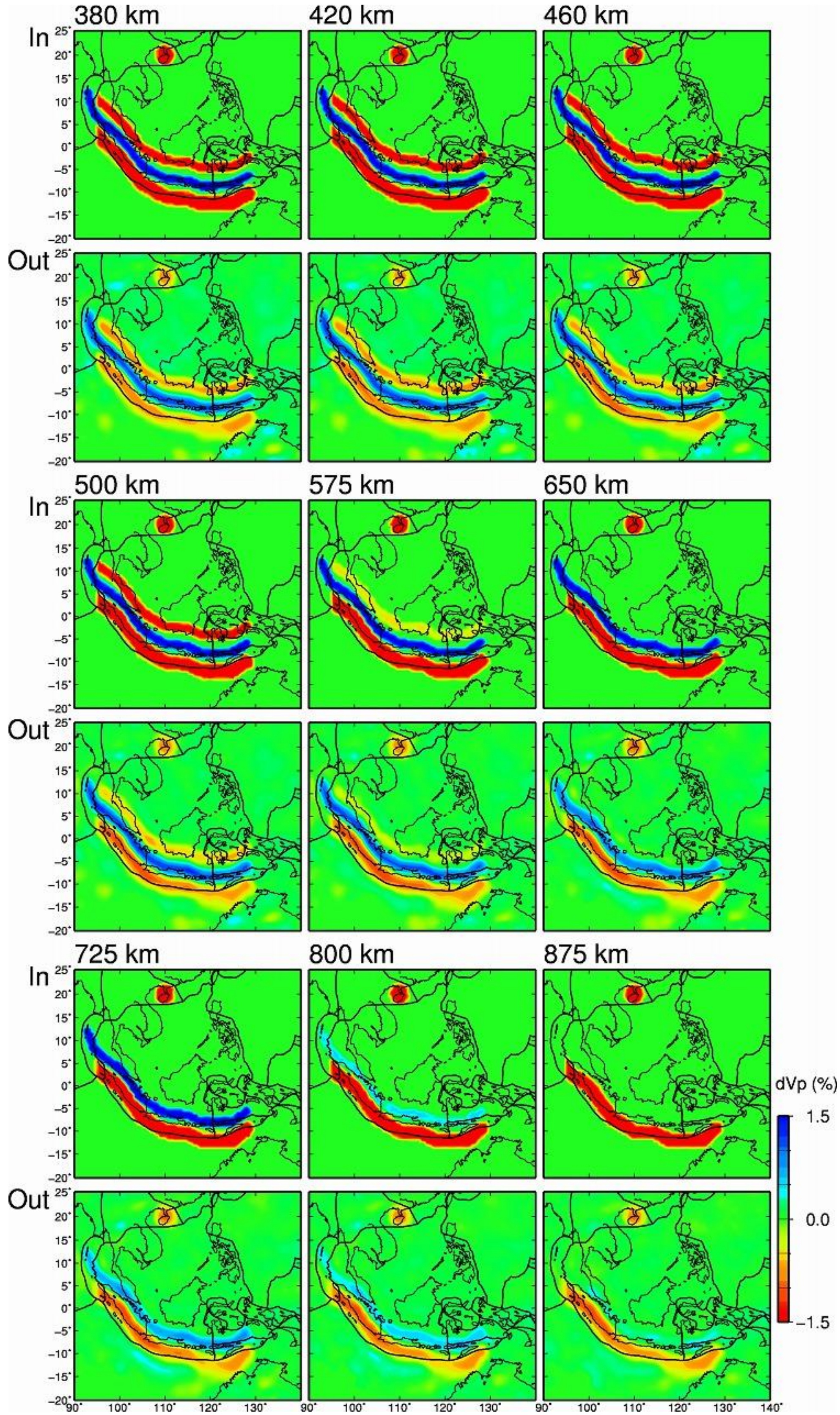

231 **Figure S33.** (continued).

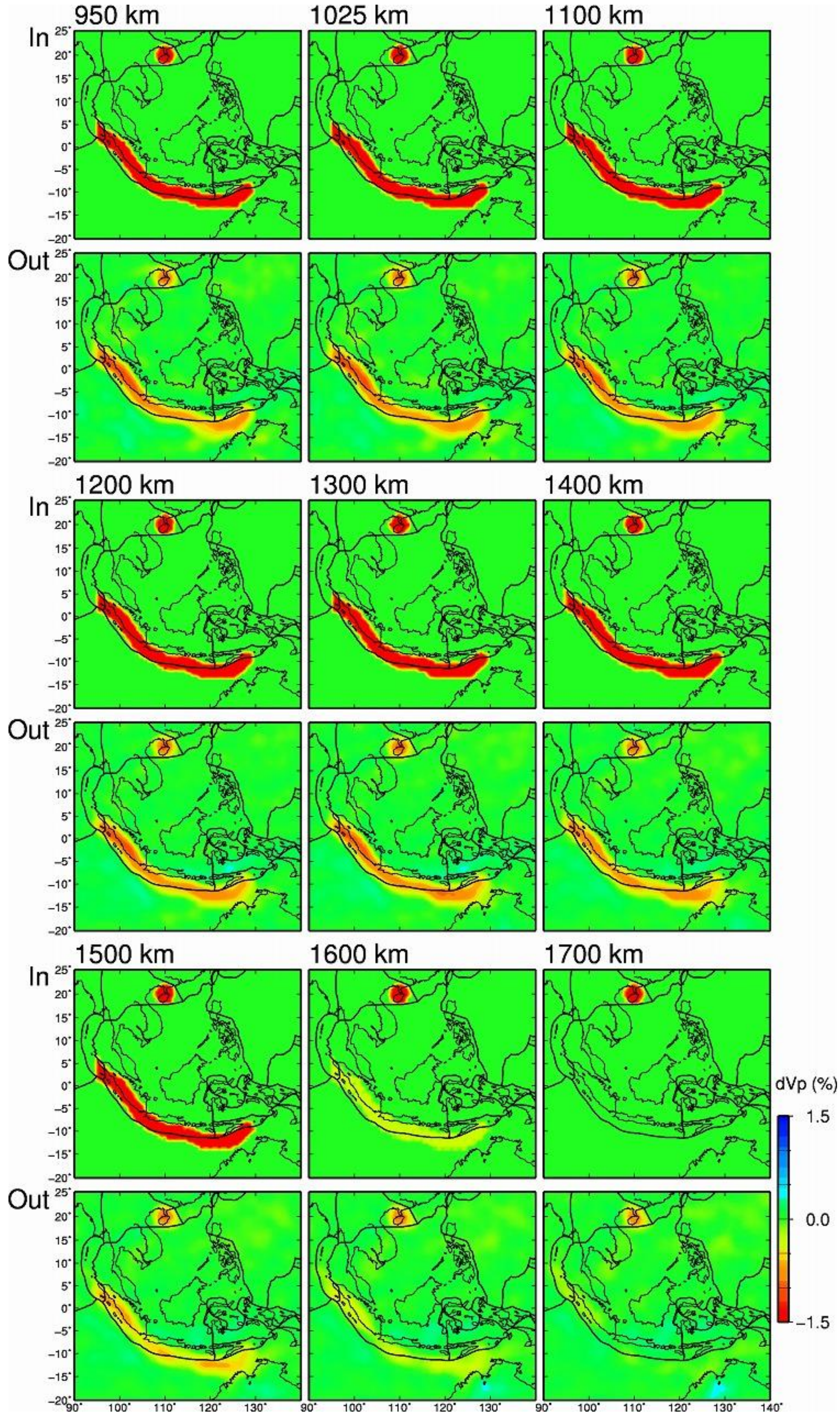

Figure S33. (continued).

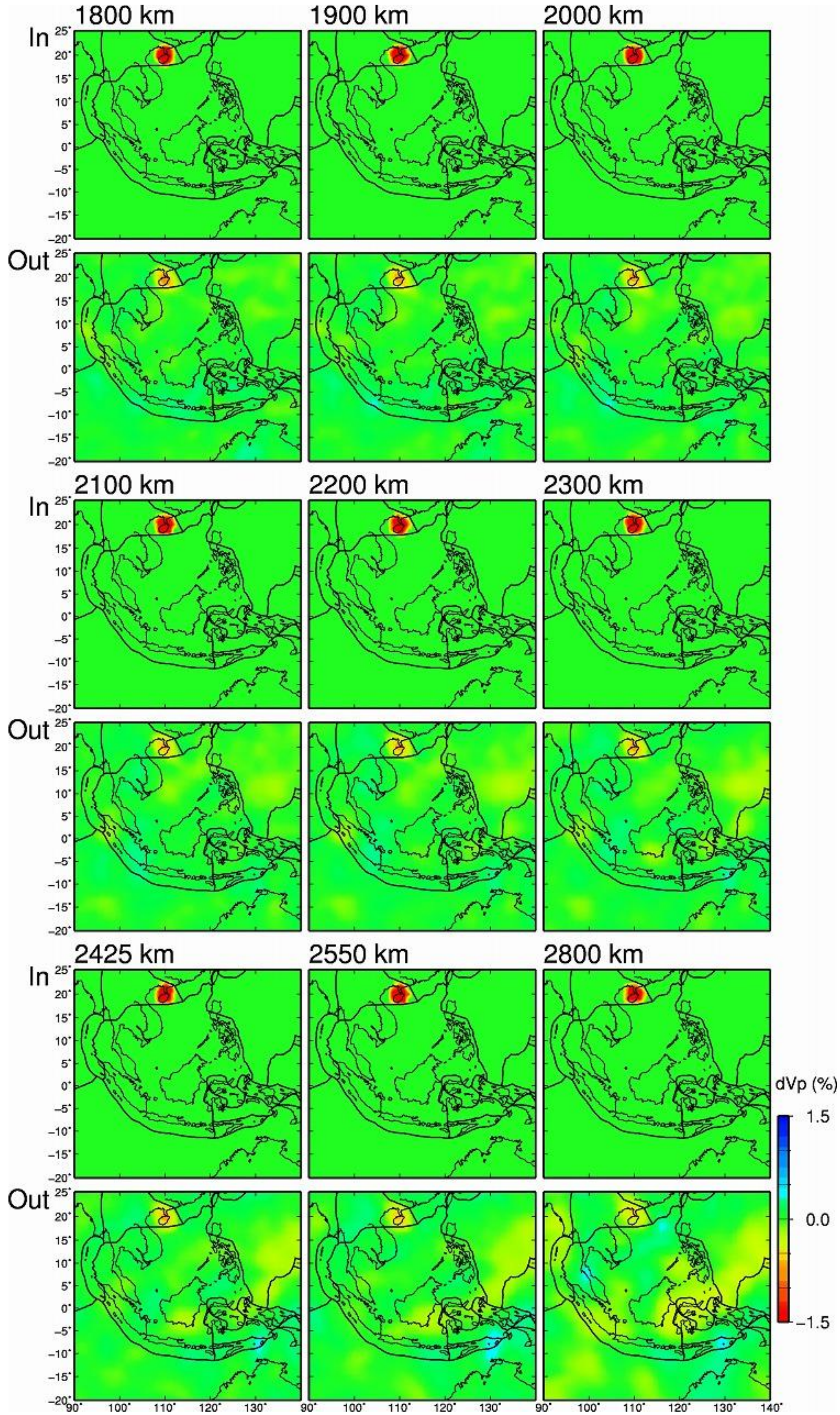

233 **Figure S33.** (continued).

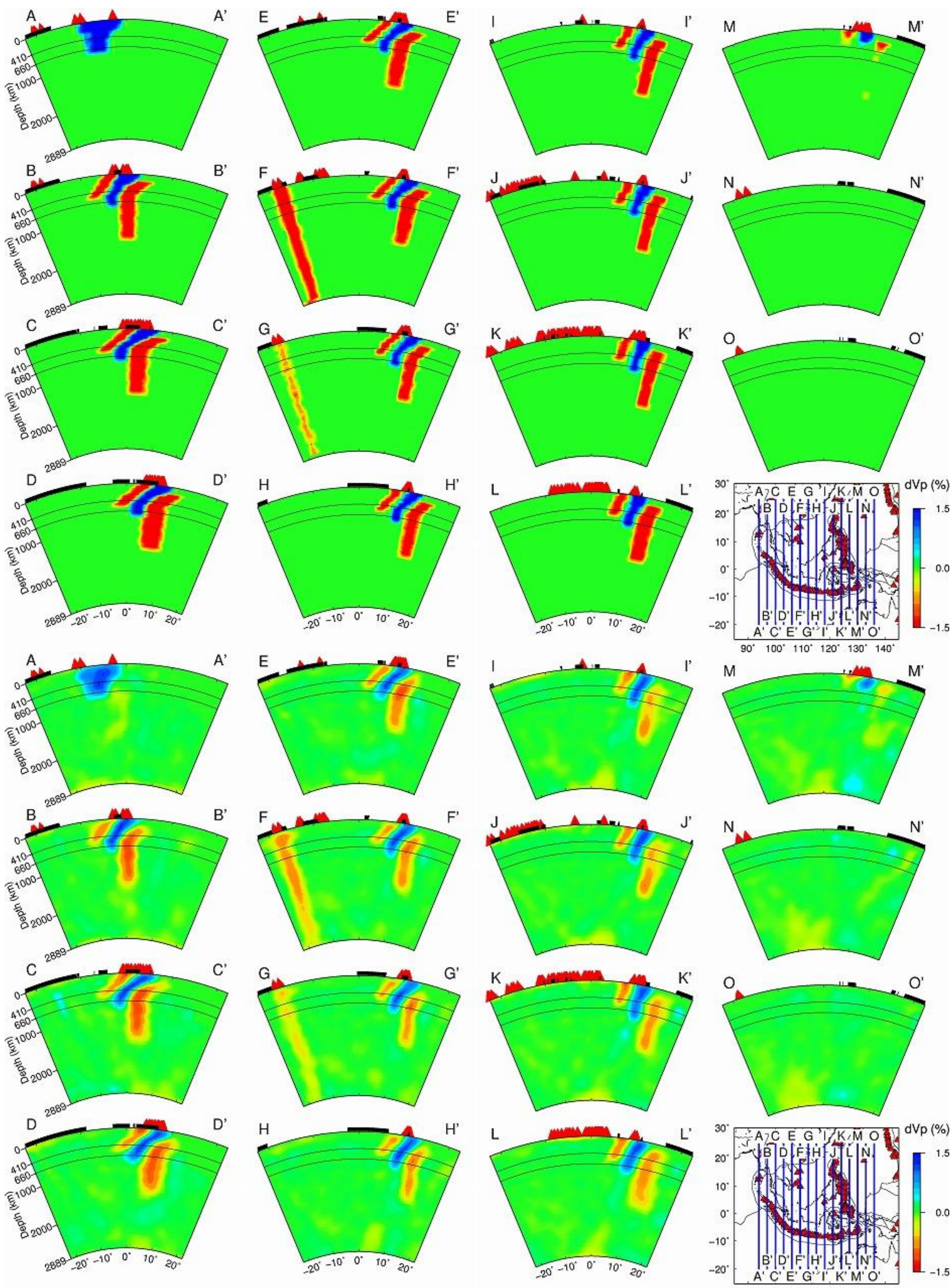

234 **Figure S34.**

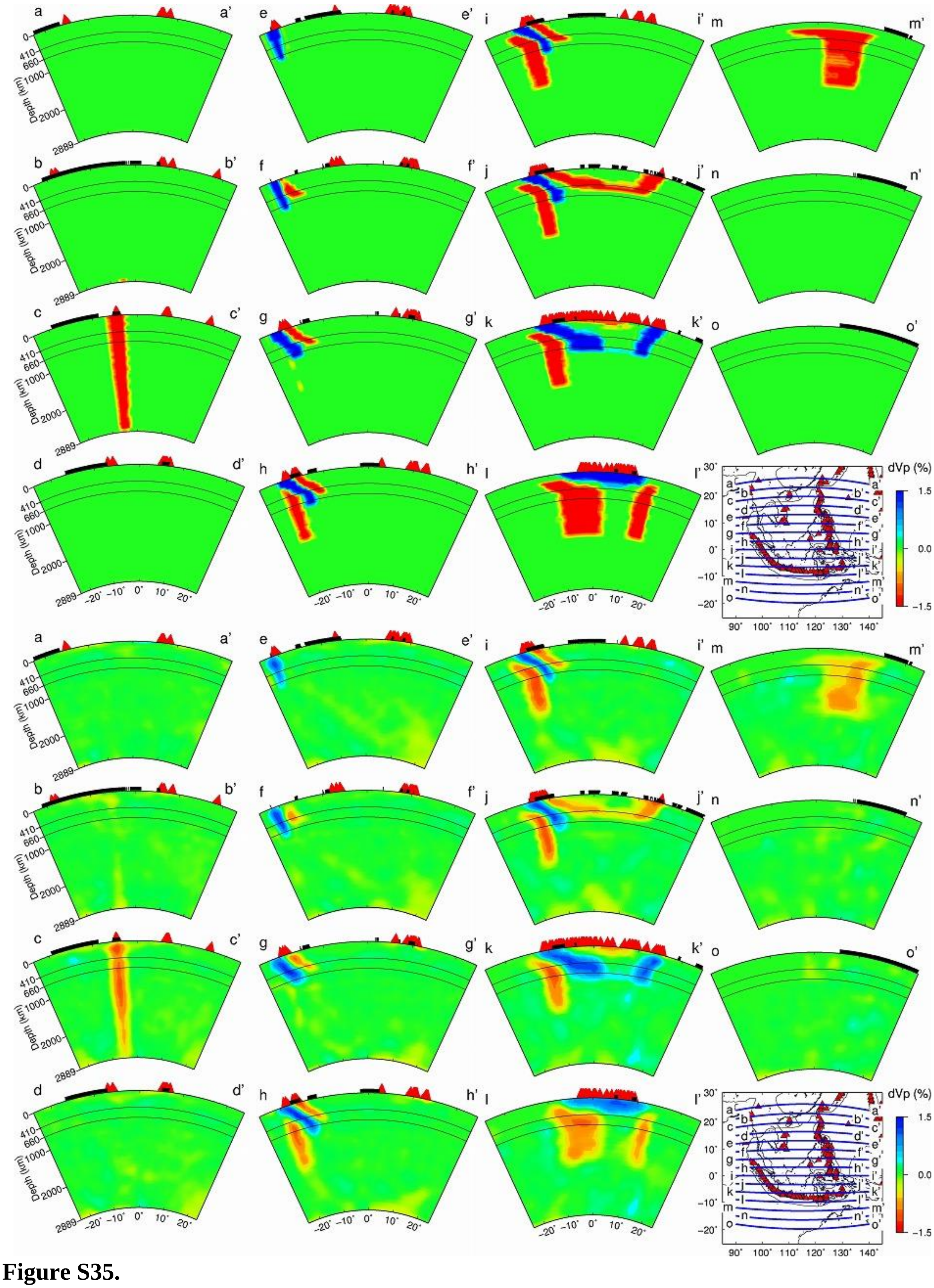

Figure S35.

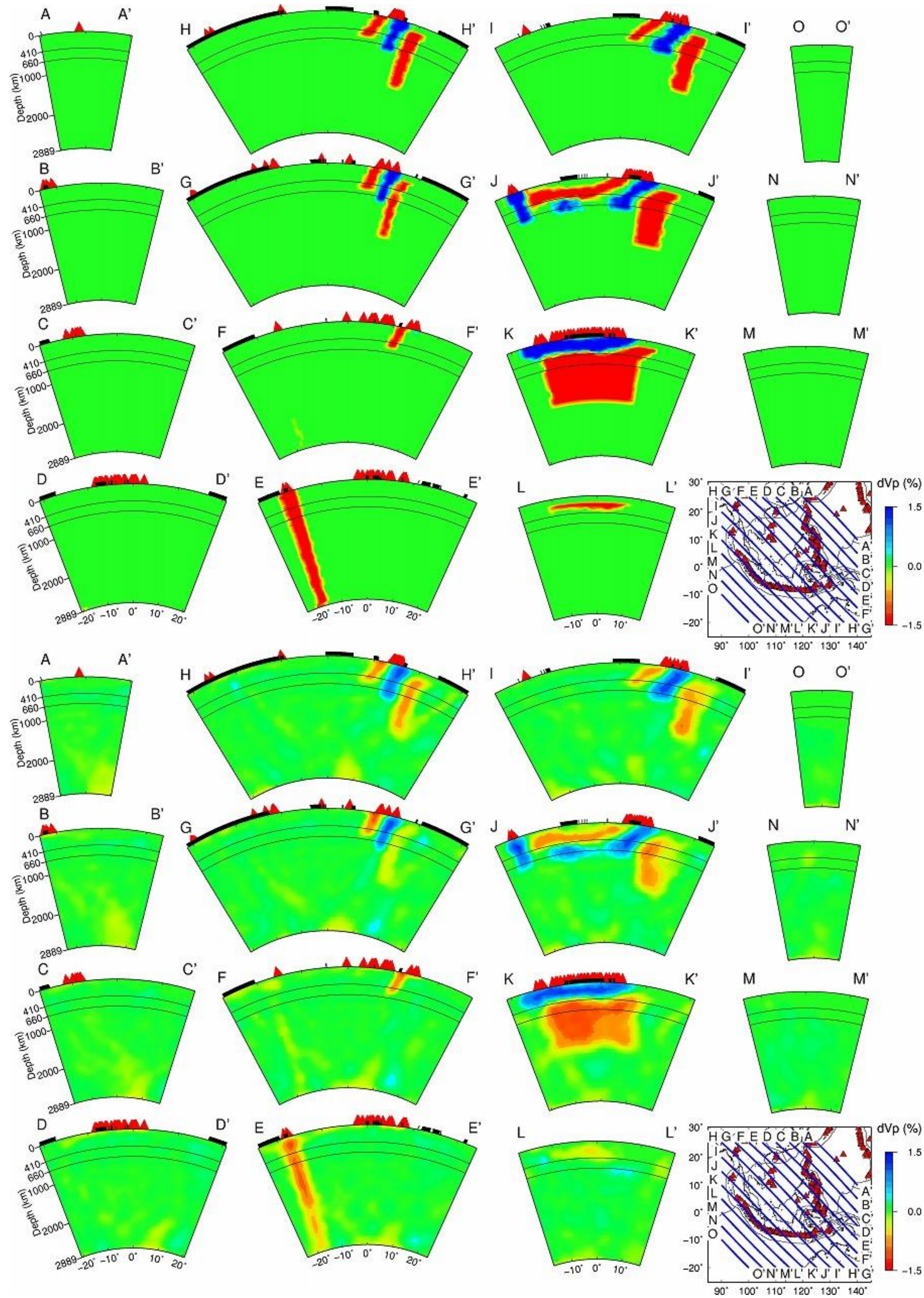

236 **Figure S36.**

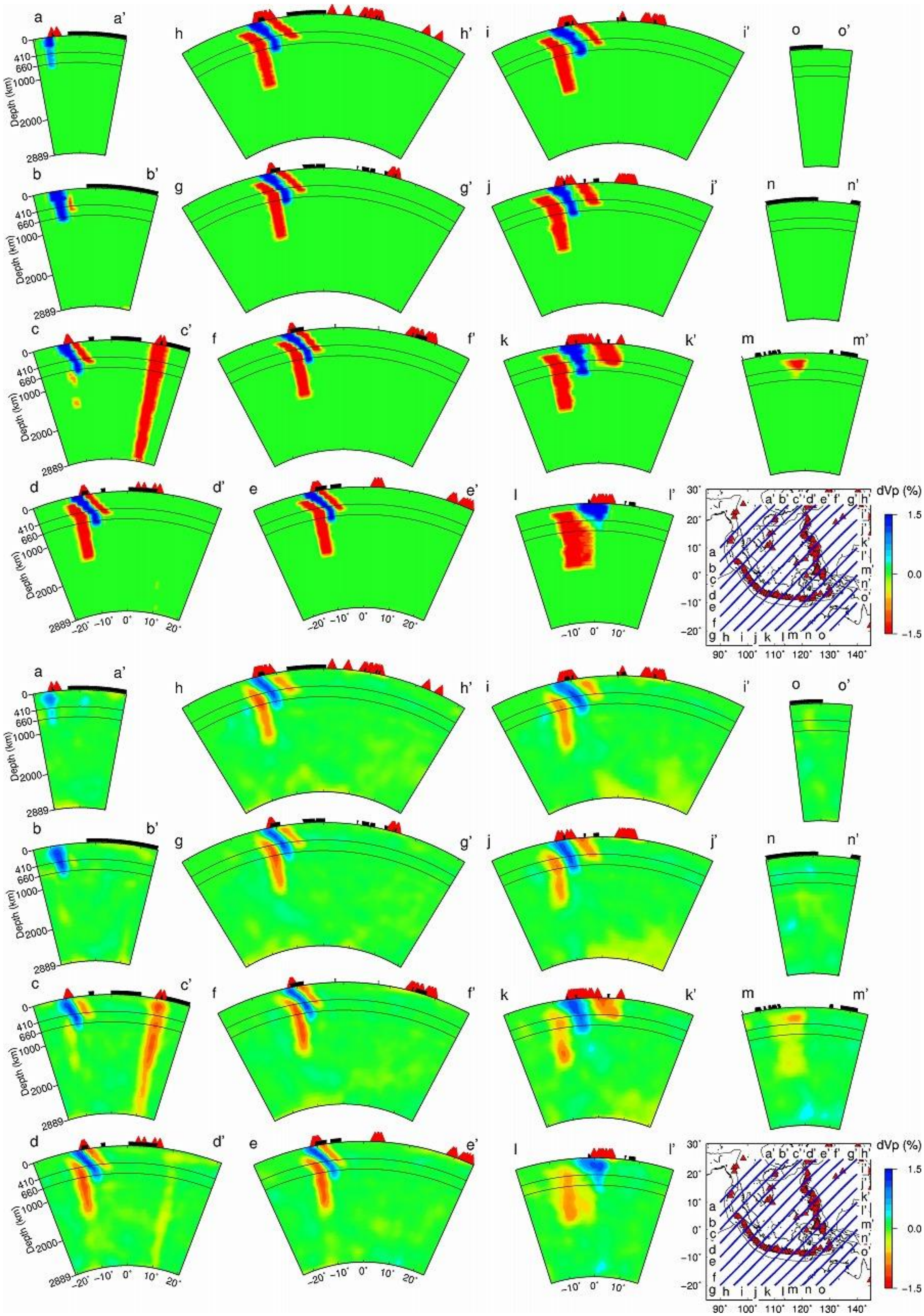

237 **Figure S37.**

Figure S33. The same as Figure S23 but for the synthetic resolution test without a hole in the Australian slab and a low-Vp bridge through the slab hole (SRT3).

Figure S34. Vertical cross-sections showing **(top)** the input model and **(bottom)** output results of the SRT3 along 15 profiles in the N-S direction. Locations of the profiles are shown on the inset map. The 410-km and the 660-km discontinuities are shown in black solid lines. The thick black lines on the surface denote land areas. The red triangles denote active volcanoes. The thin black lines on the inset map denote the plate boundaries.

Figure S35. The same as Figure S34 but along 15 profiles in the E-W direction.

Figure S36. The same as Figure S34 but along 15 profiles in the NW-SE direction.

Figure S37. The same as Figure S34 but along 15 profiles in the NE-SW direction.

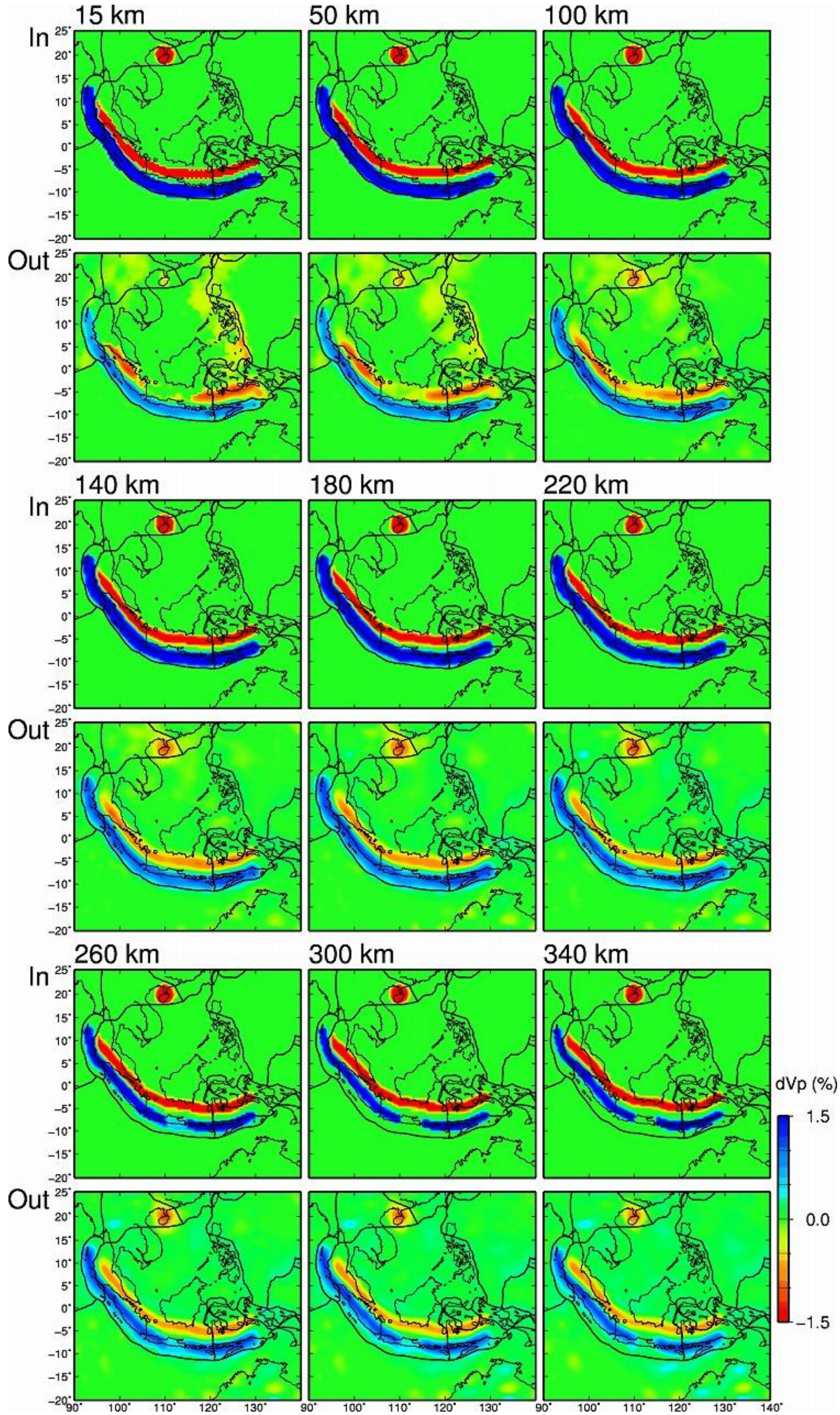
15 km
50 km
100 km
In
Out
140 km
180 km
220 km
In
Out
260 km
300 km
340 km
In
Out
dVp (%)
1.5
0.0
−1.5
25˚
20˚
15˚
10˚
5˚
0˚
−5˚
−10˚
−15˚
−20˚
90˚
100˚
110˚
120˚
130˚
140˚

Figure S38.

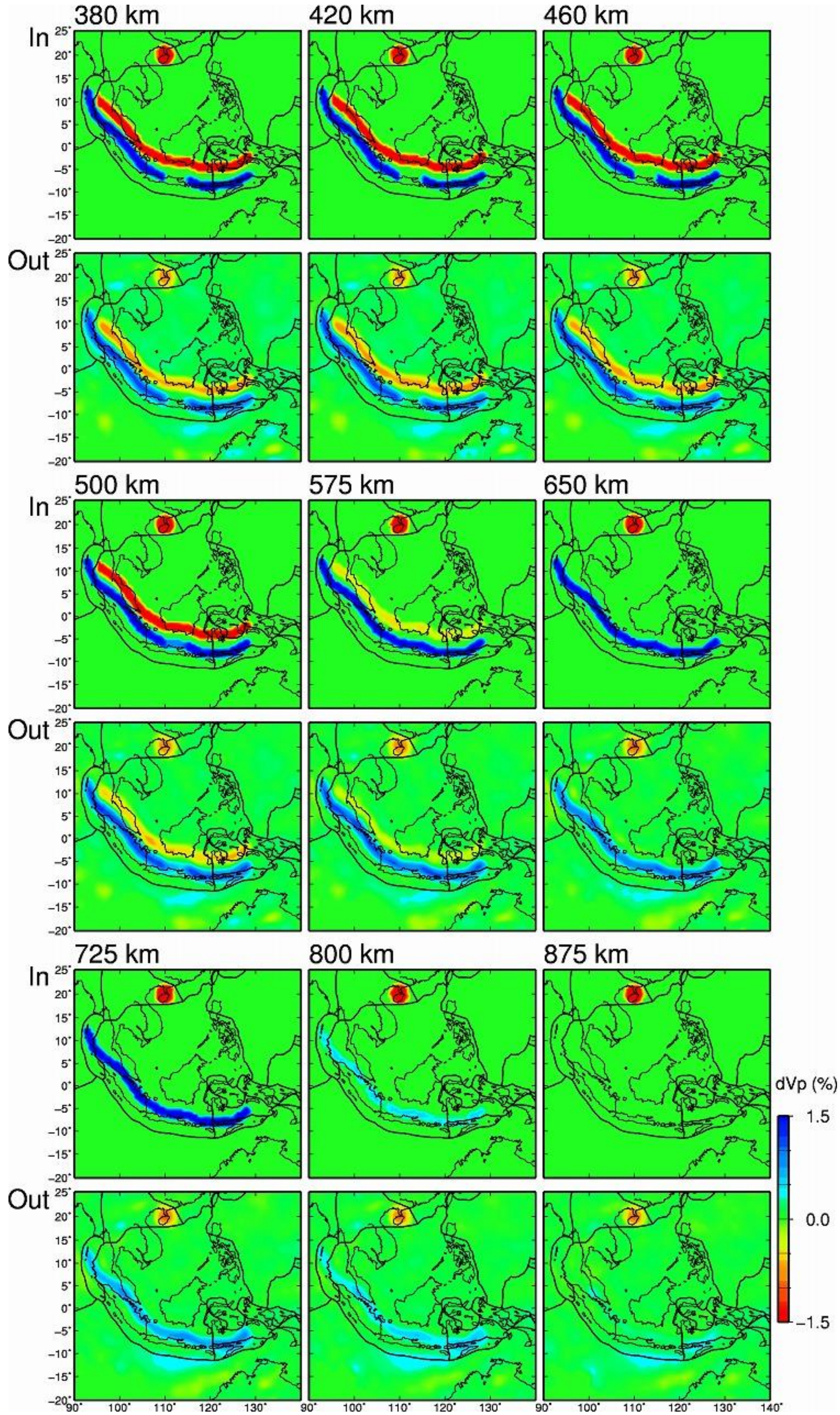

Figure S38. (continued).

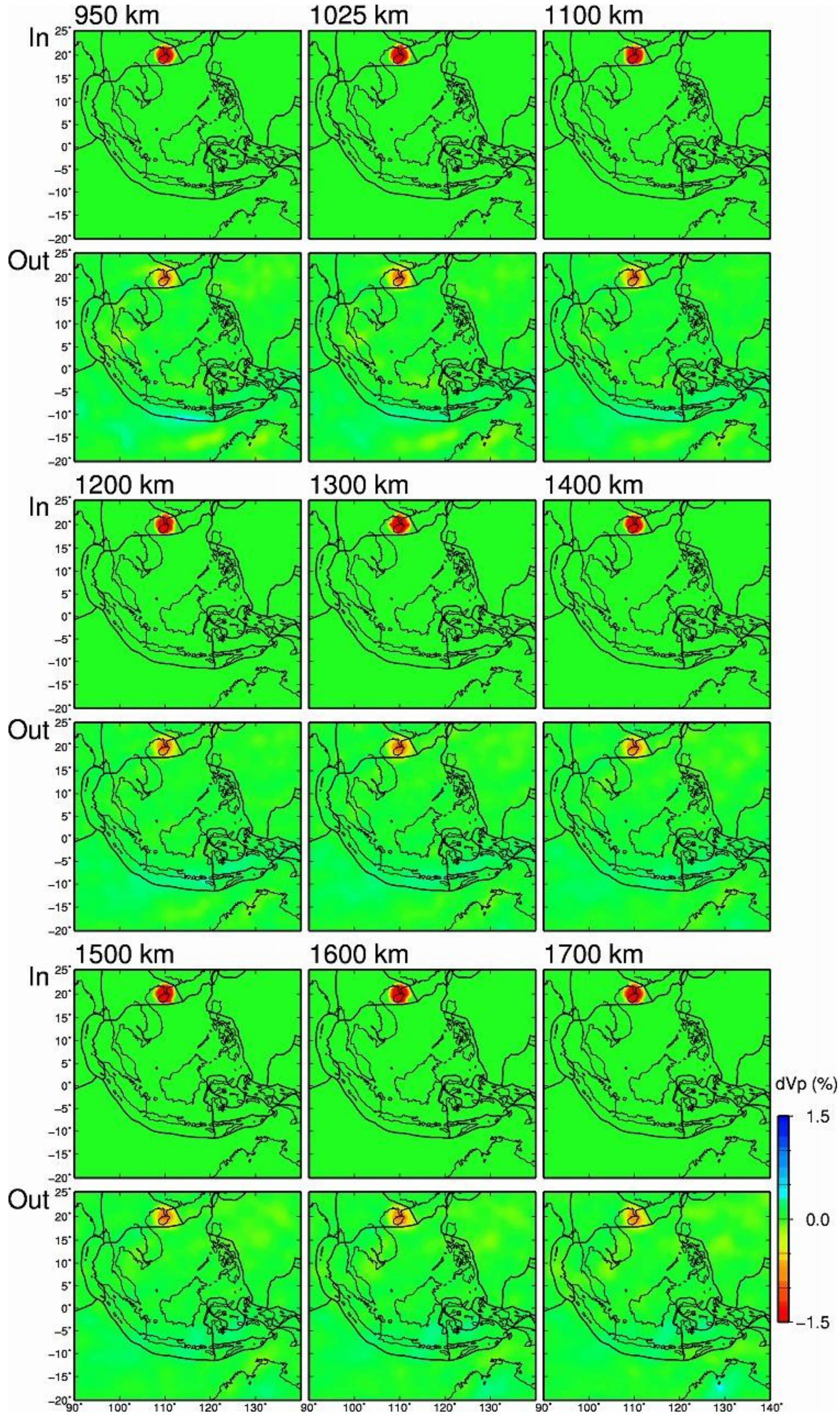

255 **Figure S38.** (continued).

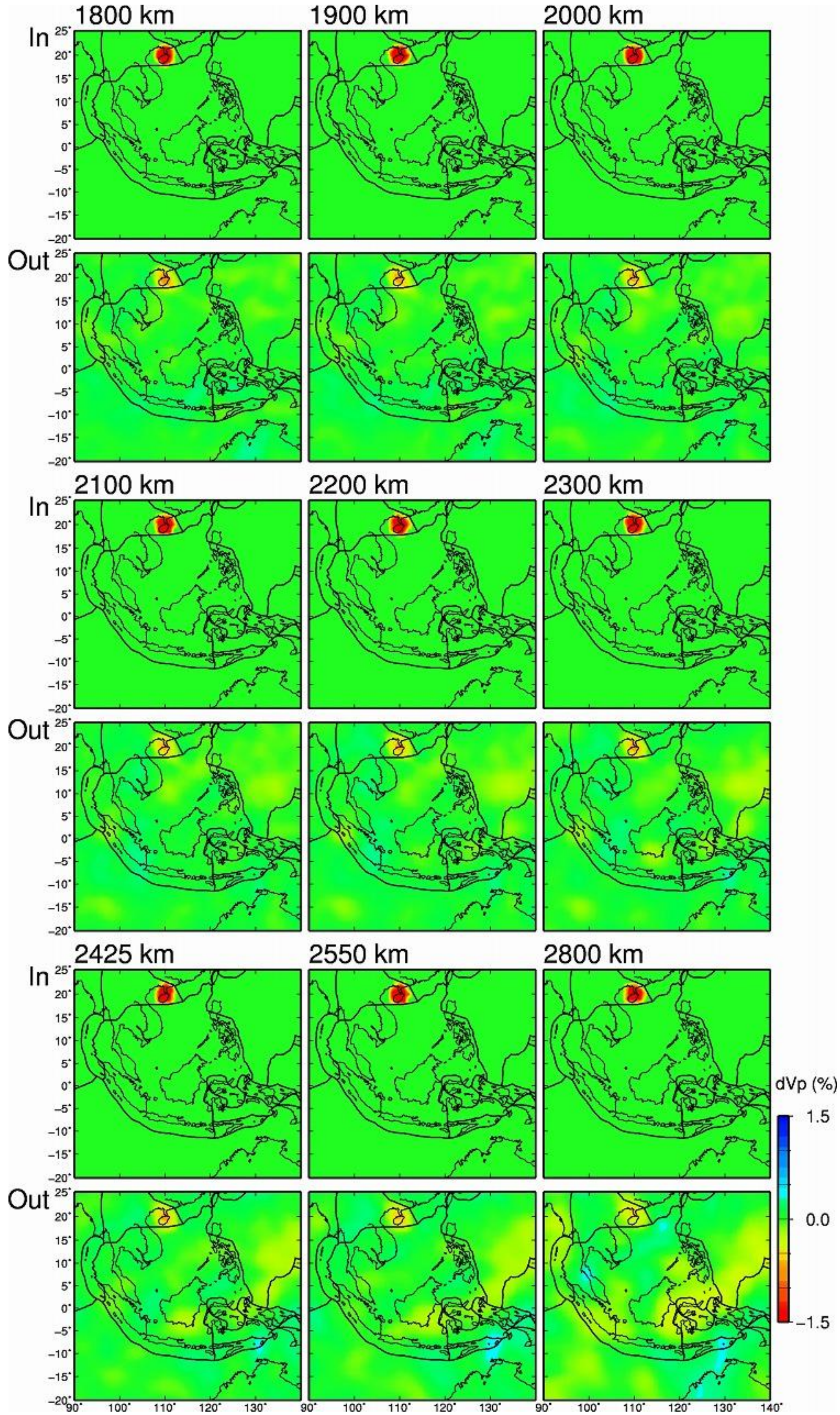

256 **Figure S38.** (continued).

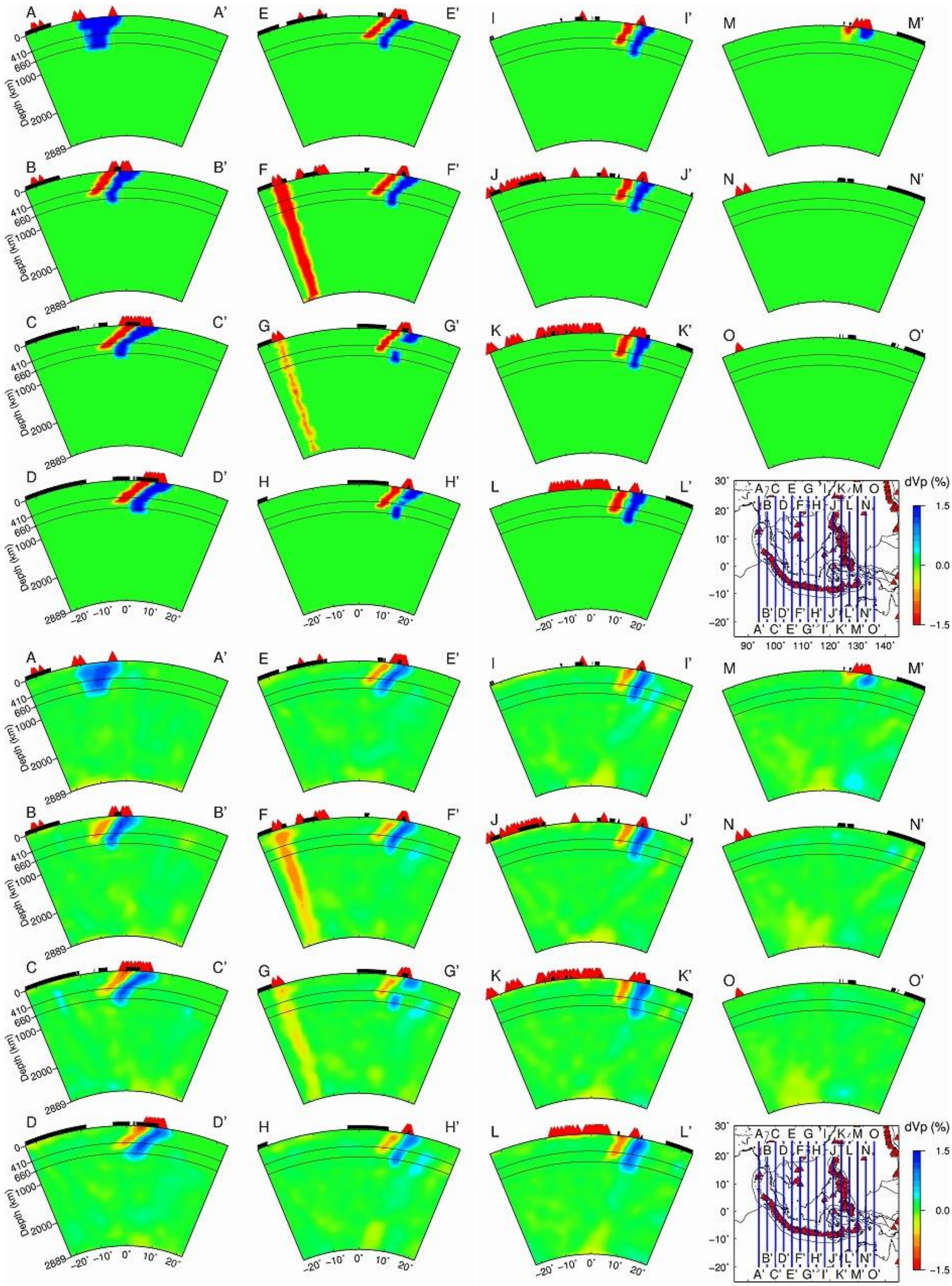
A
A'
B
B'
C
C'
D
D'
E
E'
F
F'
G
G'
H
H'
I
I'
J
J'
K
K'
L
L'
M
M'
N
N'
O
O'
Depth (km)
0
410
660
1000
2000
2889
-20°
-10°
0°
10°
20°
dVp (%)
1.5
0.0
-1.5
30°
20°
10°
0°
-10°
-20°
90°
100°
110°
120°
130°
140°

Figure S39.

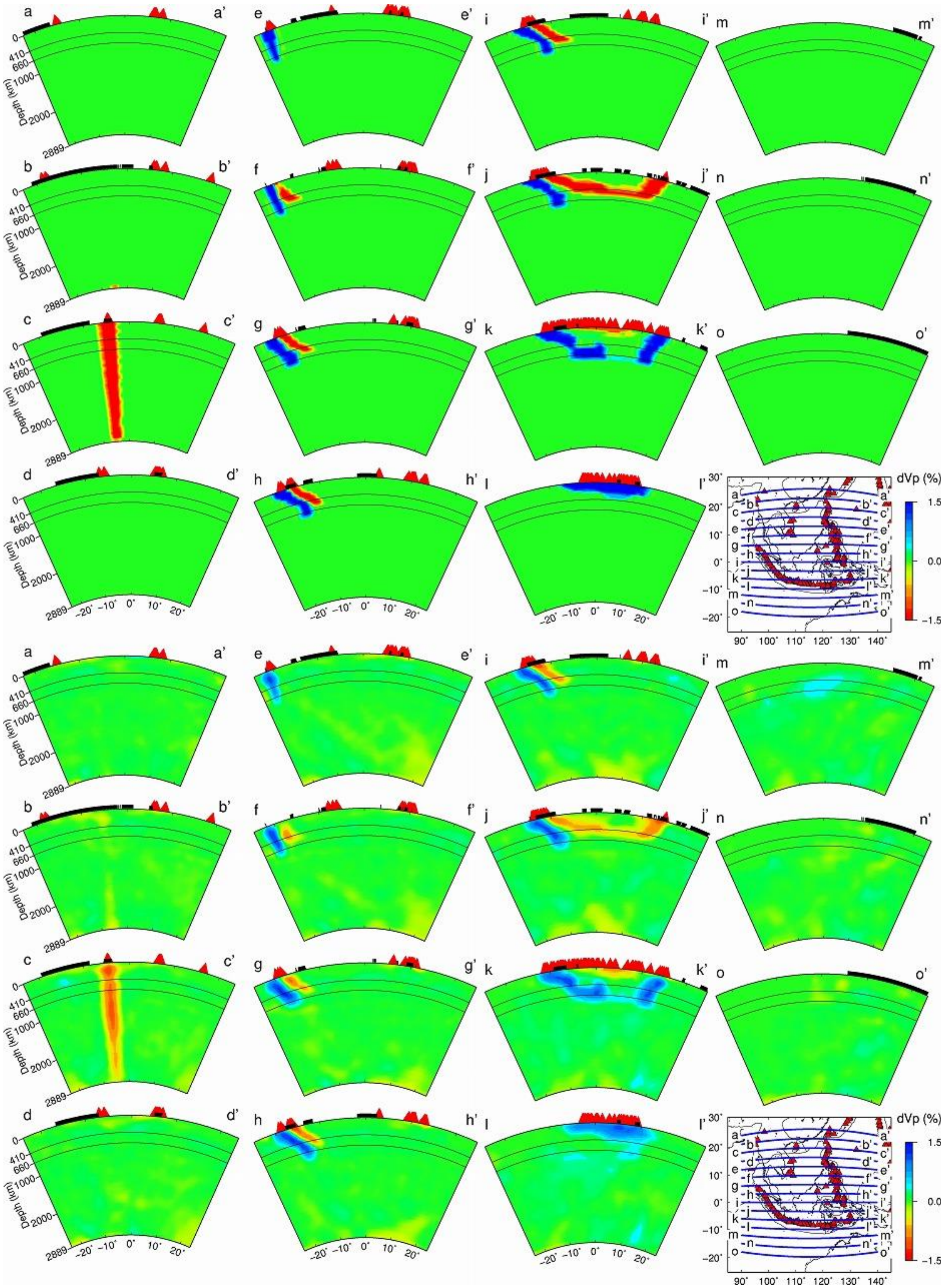

258 **Figure S40.**

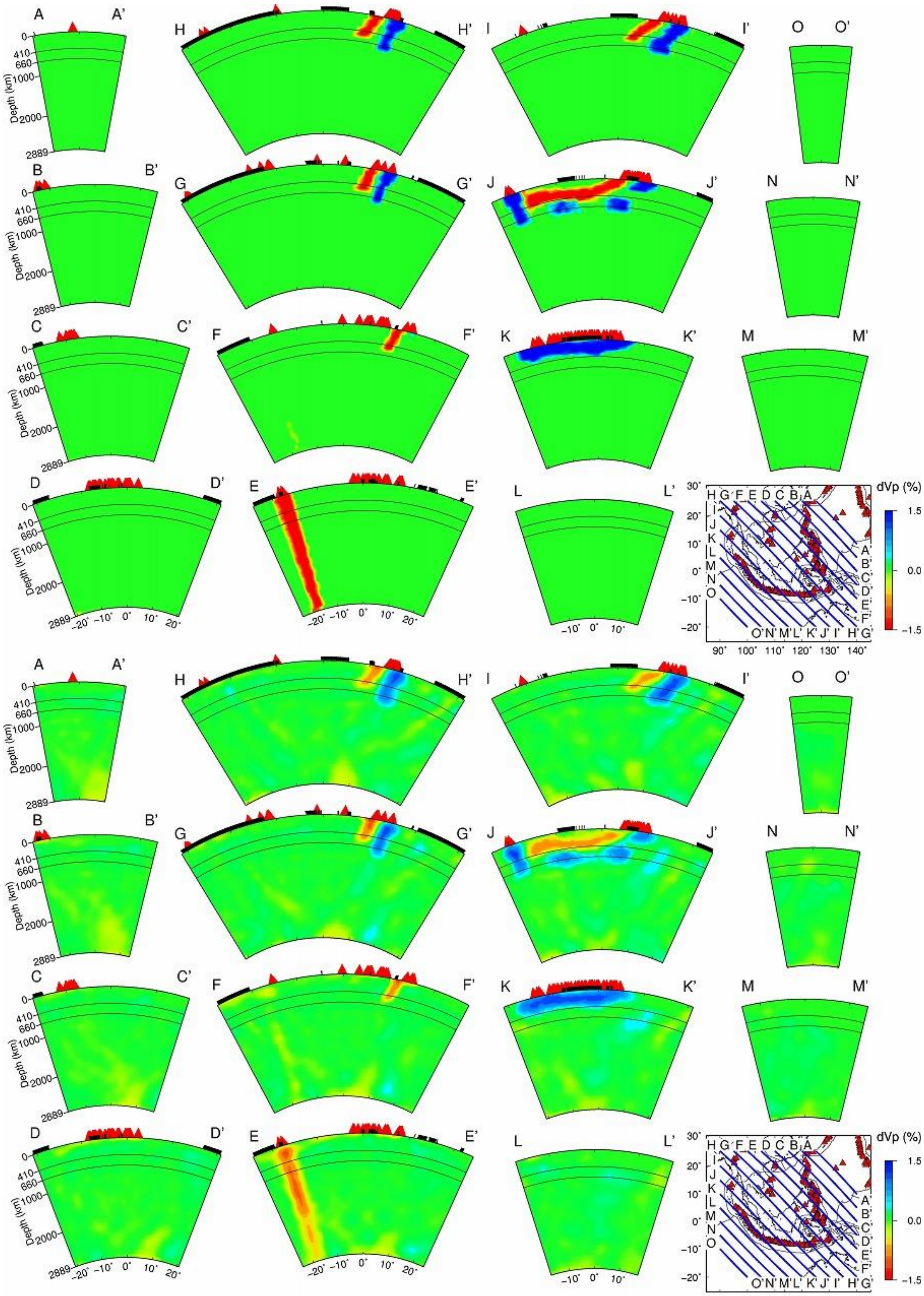
A A'
B B'
C C'
D D'
E E'
F F'
G G'
H H'
I I'
J J'
K K'
L L'
M M'
N N'
O O'
Depth (km)
0
410
660
1000
2000
2889
-20° -10° 0° 10° 20°
dVp (%)
1.5
0.0
-1.5
30°
20°
10°
0°
-10°
-20°
90° 100° 110° 120° 130° 140°

Figure S41.

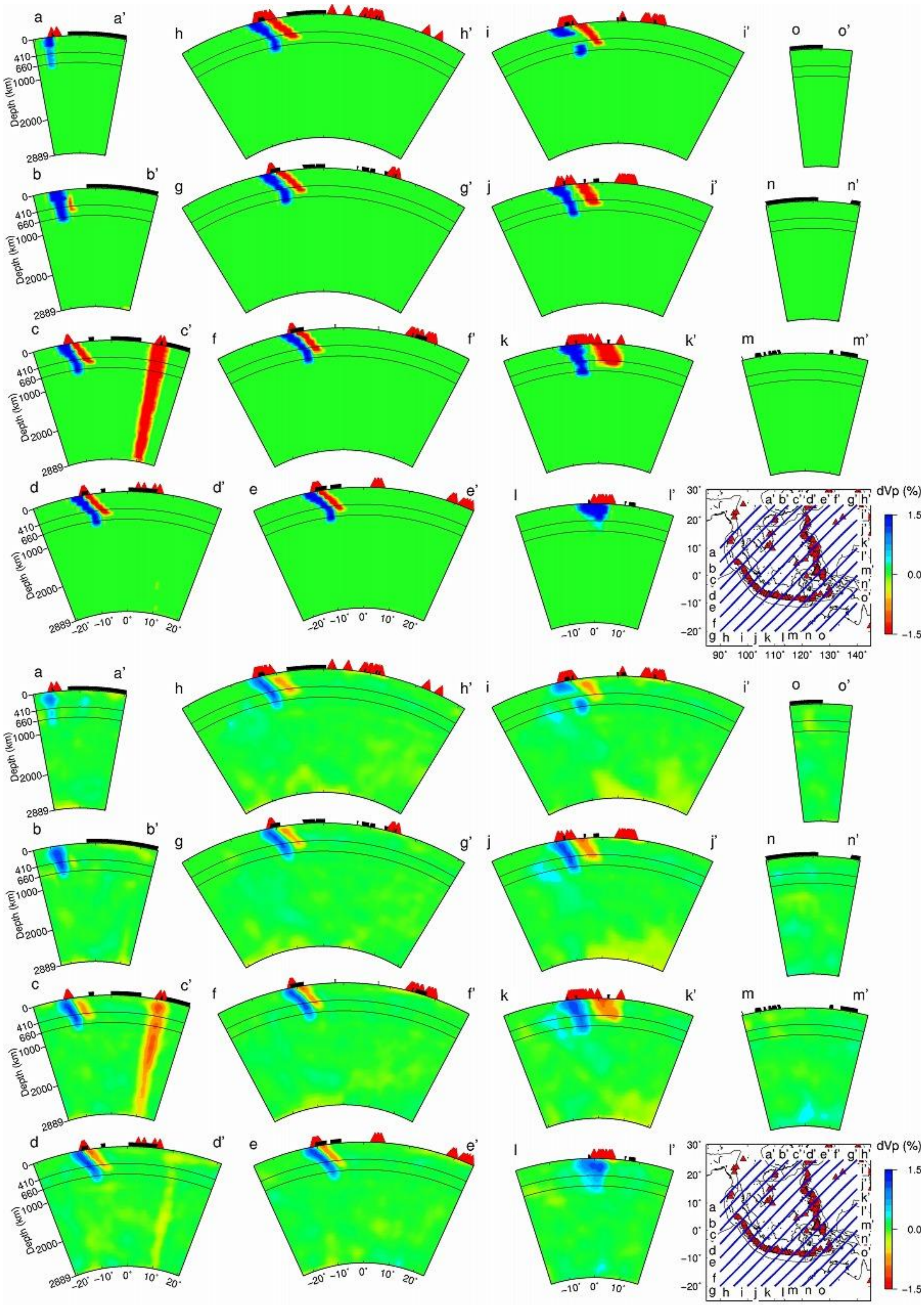

260 **Figure S42.**

Figure S38. The same as Figure S23 but for the synthetic resolution test without a low-Vp subslab hot mantle upwelling (SHMU) and a low-Vp bridge through the slab hole (SRT4).

Figure S39. Vertical cross-sections showing **(top)** the input model and **(bottom)** output results of the SRT4 along 15 profiles in the N-S direction. Locations of the profiles are shown on the inset map. The 410-km and the 660-km discontinuities are shown in black solid lines. The thick black lines on the surface denote land areas. The red triangles denote active volcanoes. The thin black lines on the inset map denote the plate boundaries.

Figure S40. The same as Figure S39 but along 15 profiles in the E-W direction.

Figure S41. The same as Figure S39 but along 15 profiles in the NW-SE direction.

Figure S42. The same as Figure S39 but along 15 profiles in the NE-SW direction.

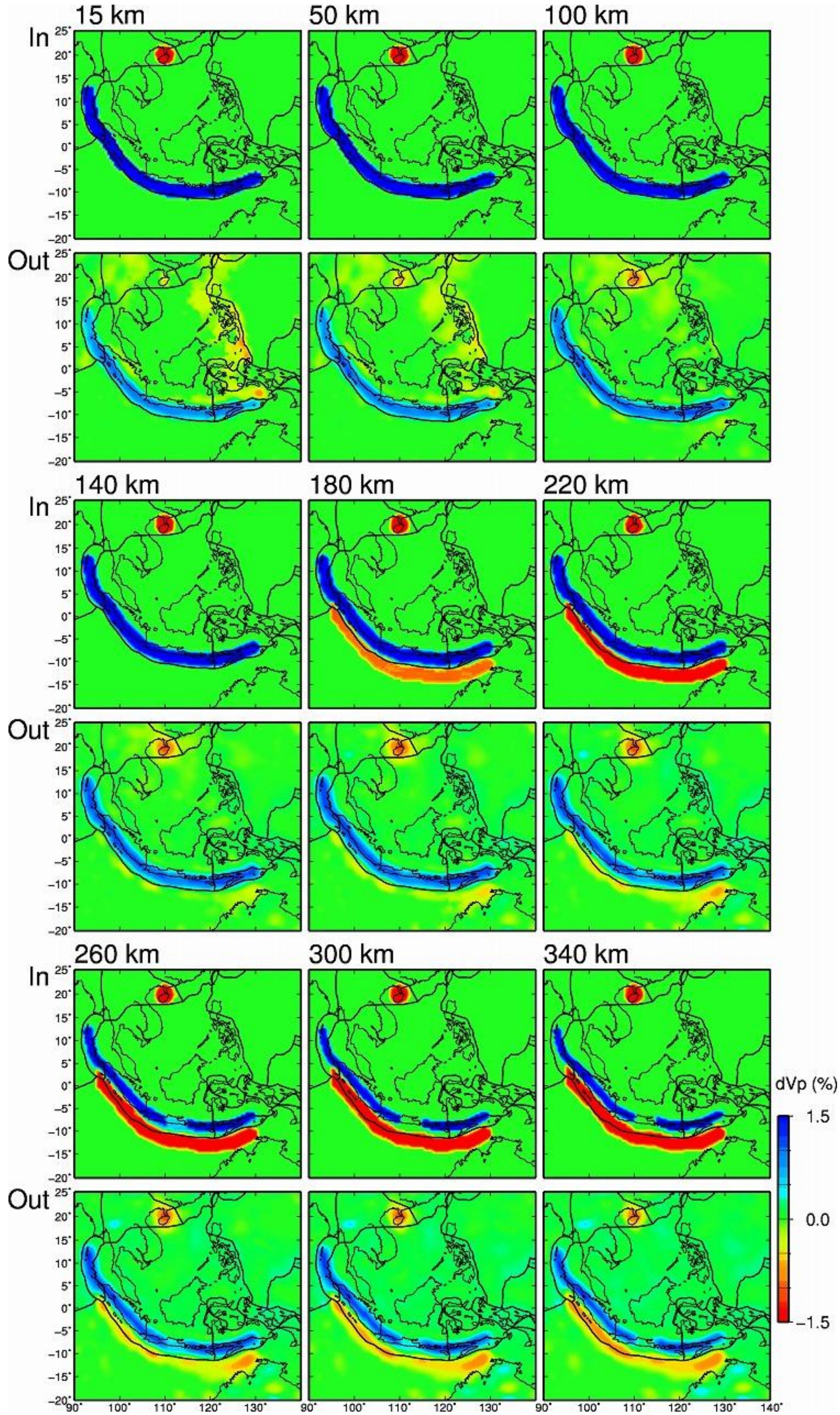

284 **Figure S43.**

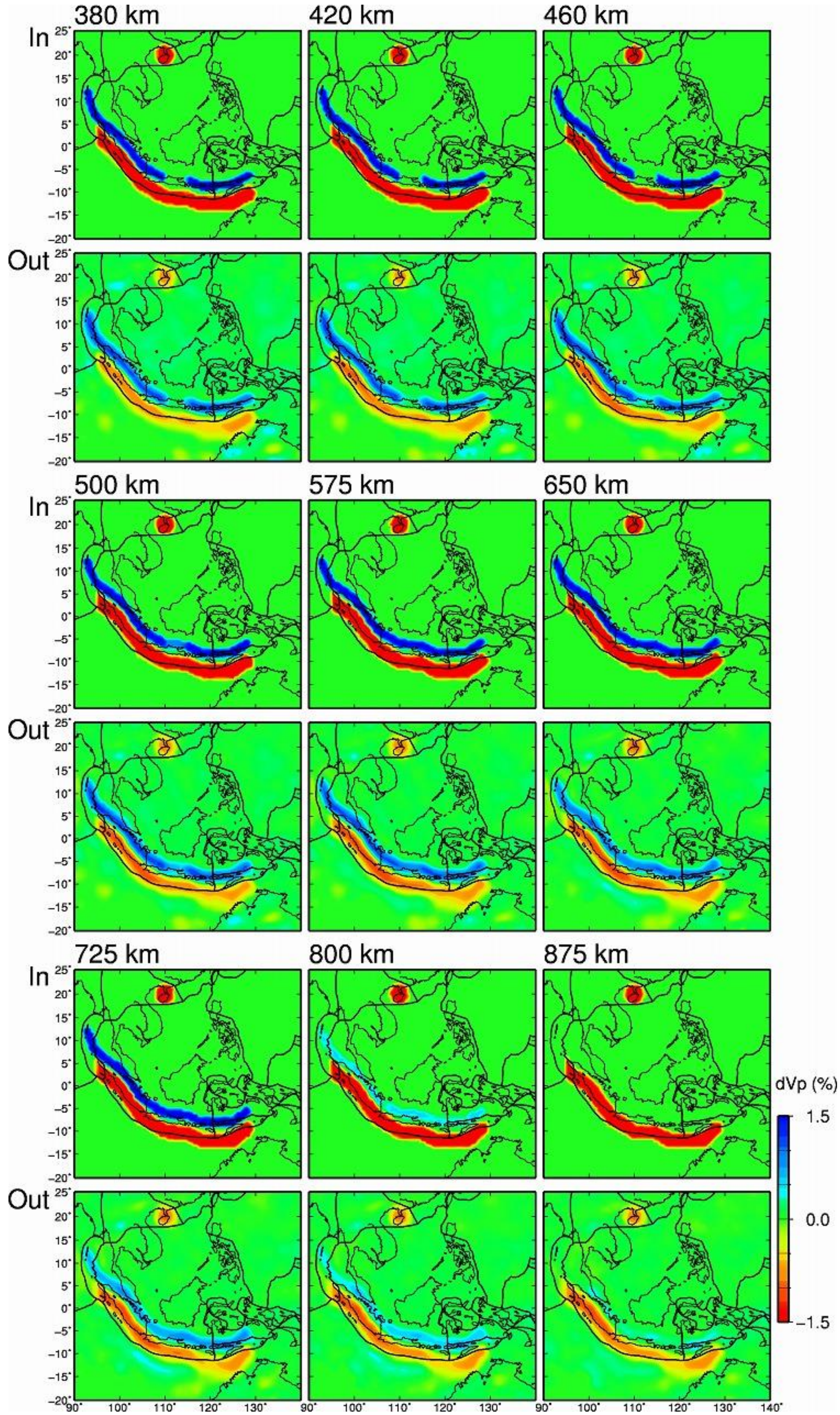

285 **Figure S43.** (continued).

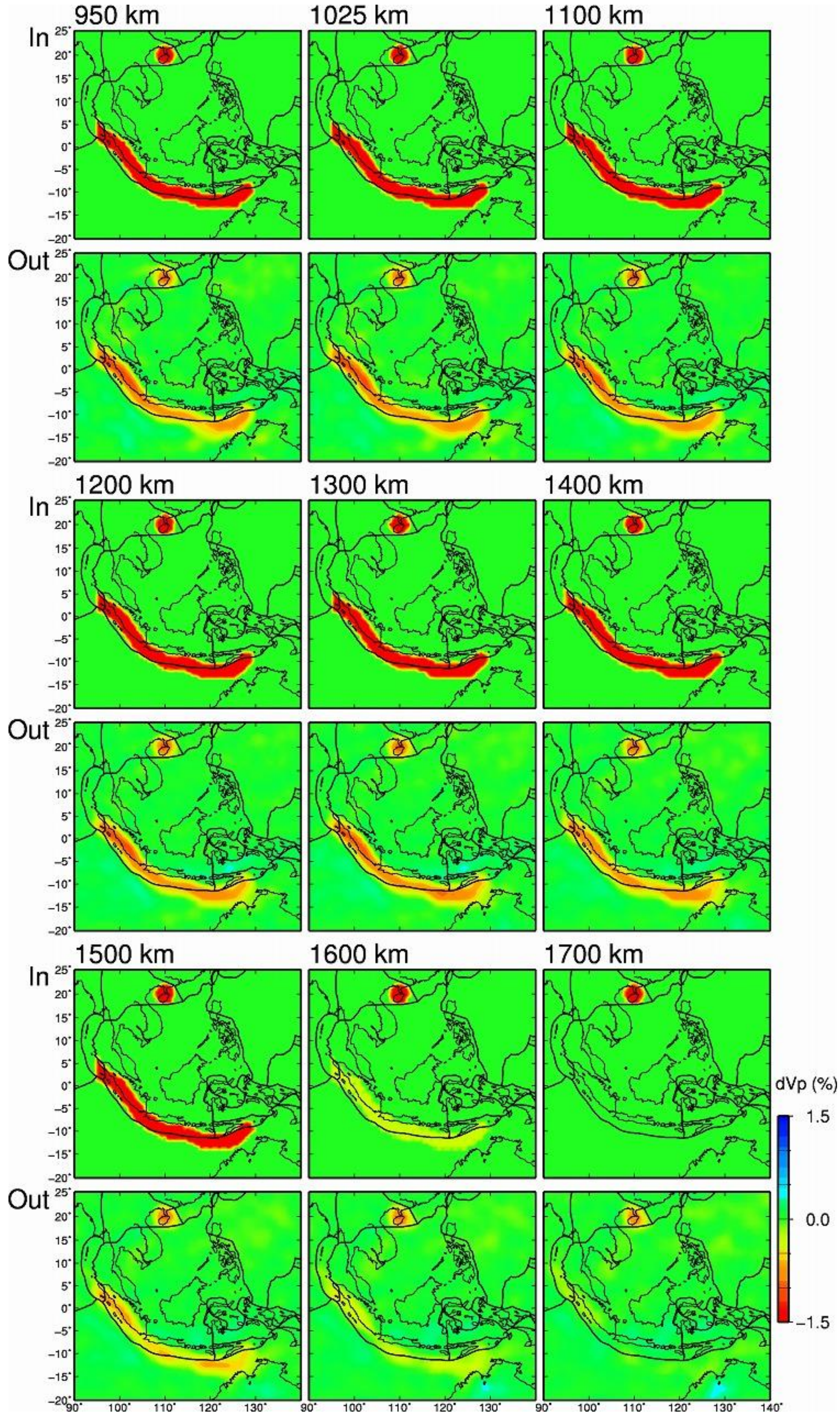

286 **Figure S43.** (continued).

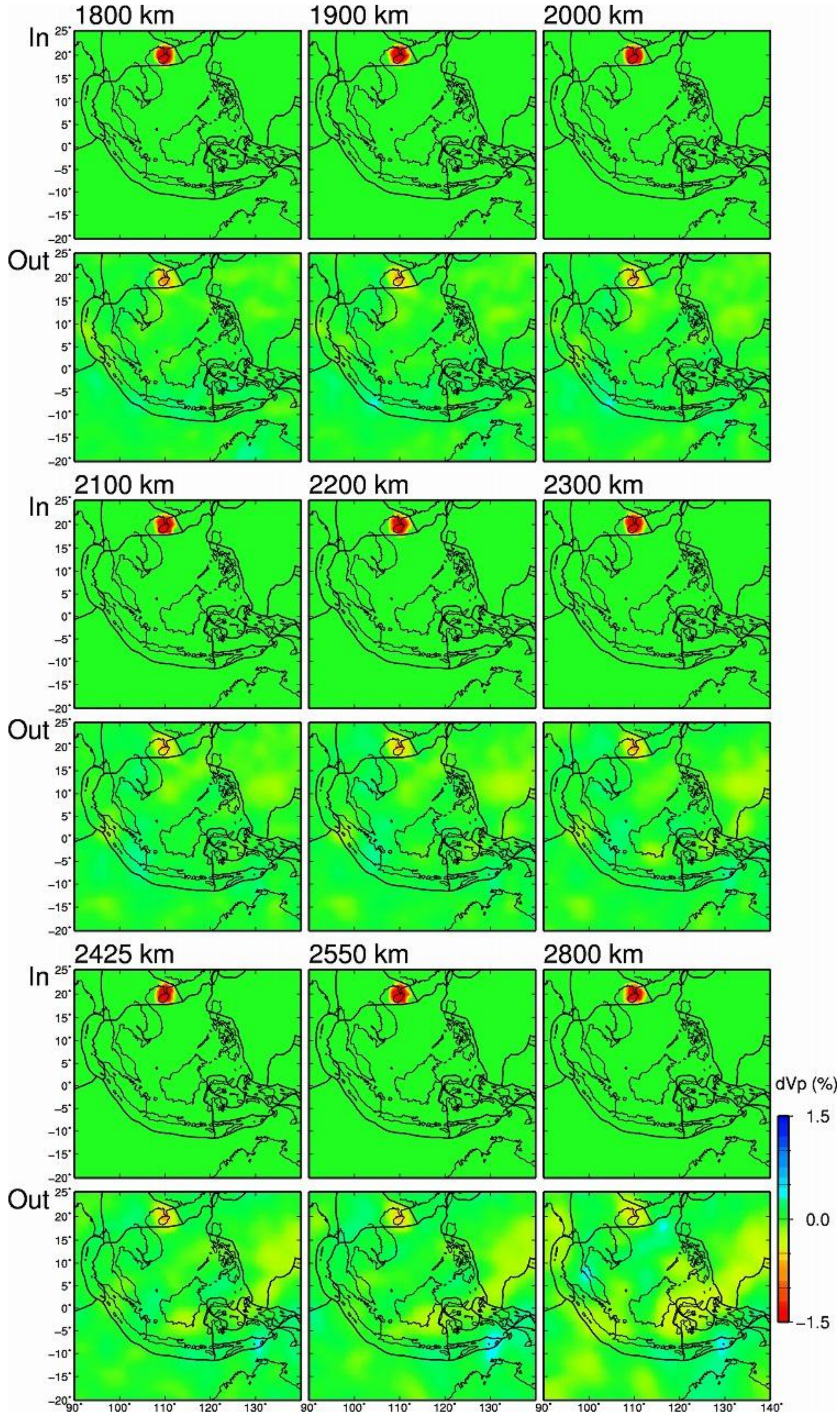

Figure S43. (continued).

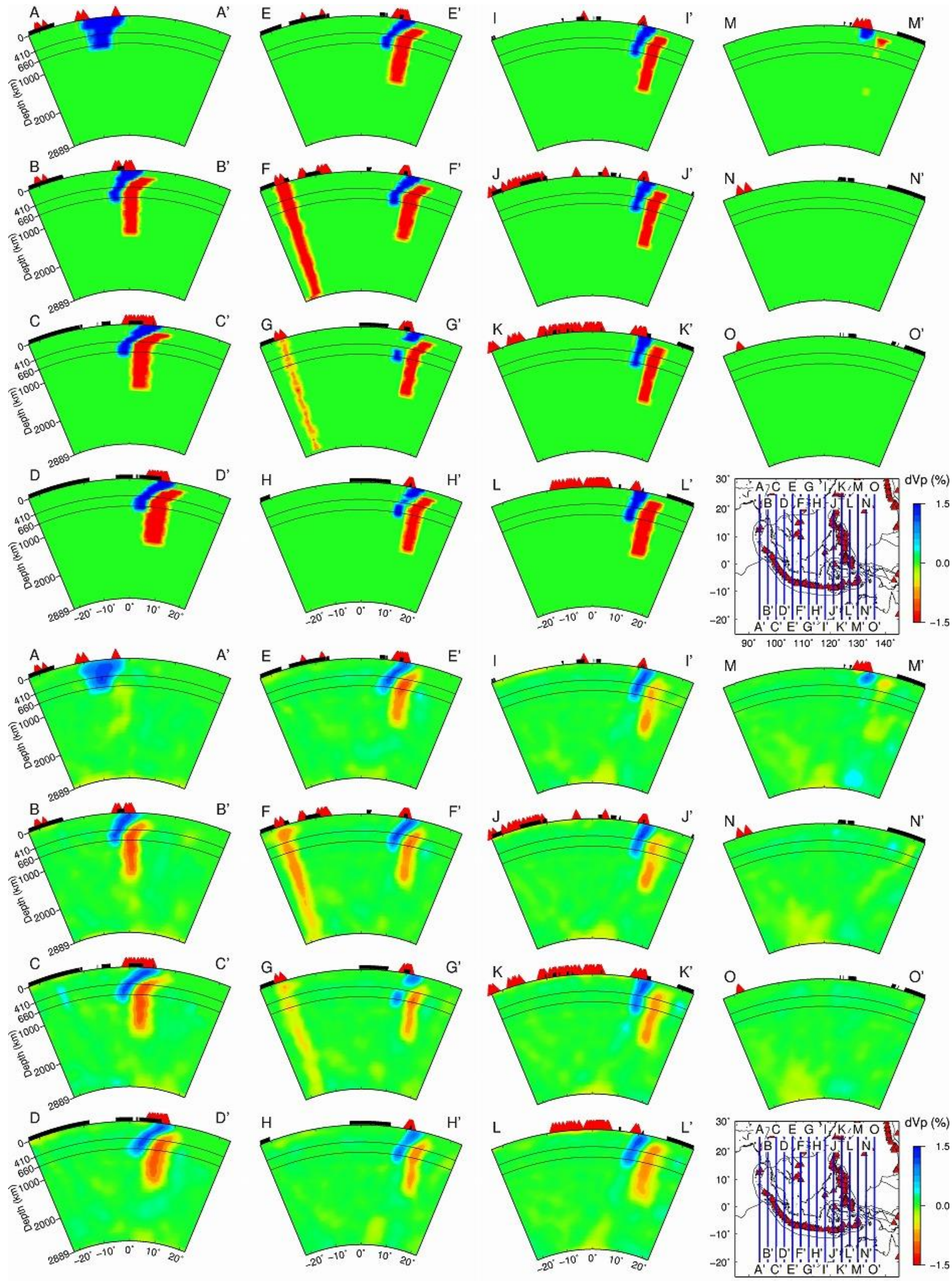
A A'
E E'
I I'
M M'
B B'
F F'
J J'
N N'
C C'
G G'
K K'
O O'
D D'
H H'
L L'
Depth (km)
0
410
660
1000
2000
2889
-20° -10° 0° 10° 20°
dVp (%)
1.5
0.0
-1.5
30°
20°
10°
0°
-10°
-20°
90° 100° 110° 120° 130° 140°

Figure S44.

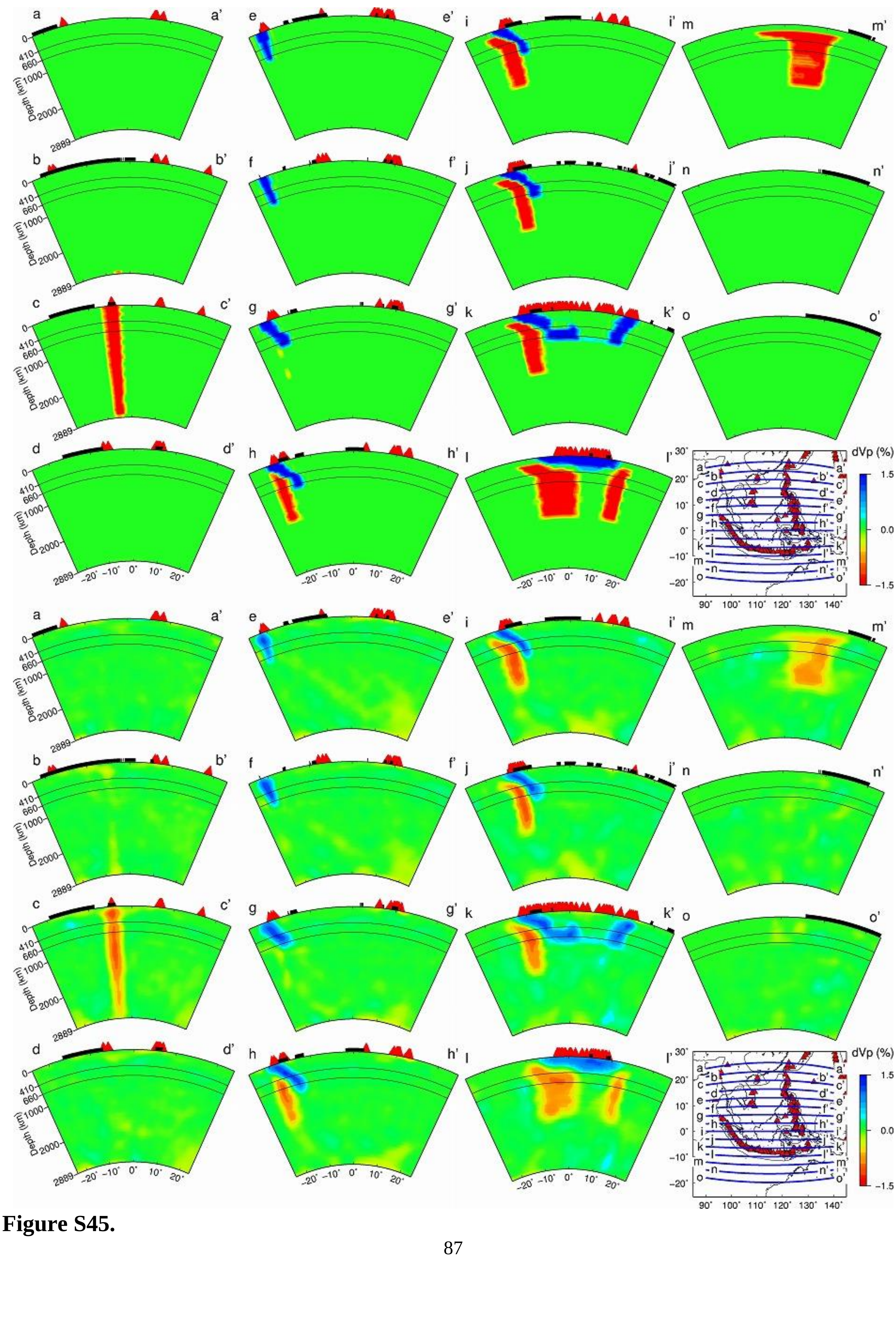

Figure S45.

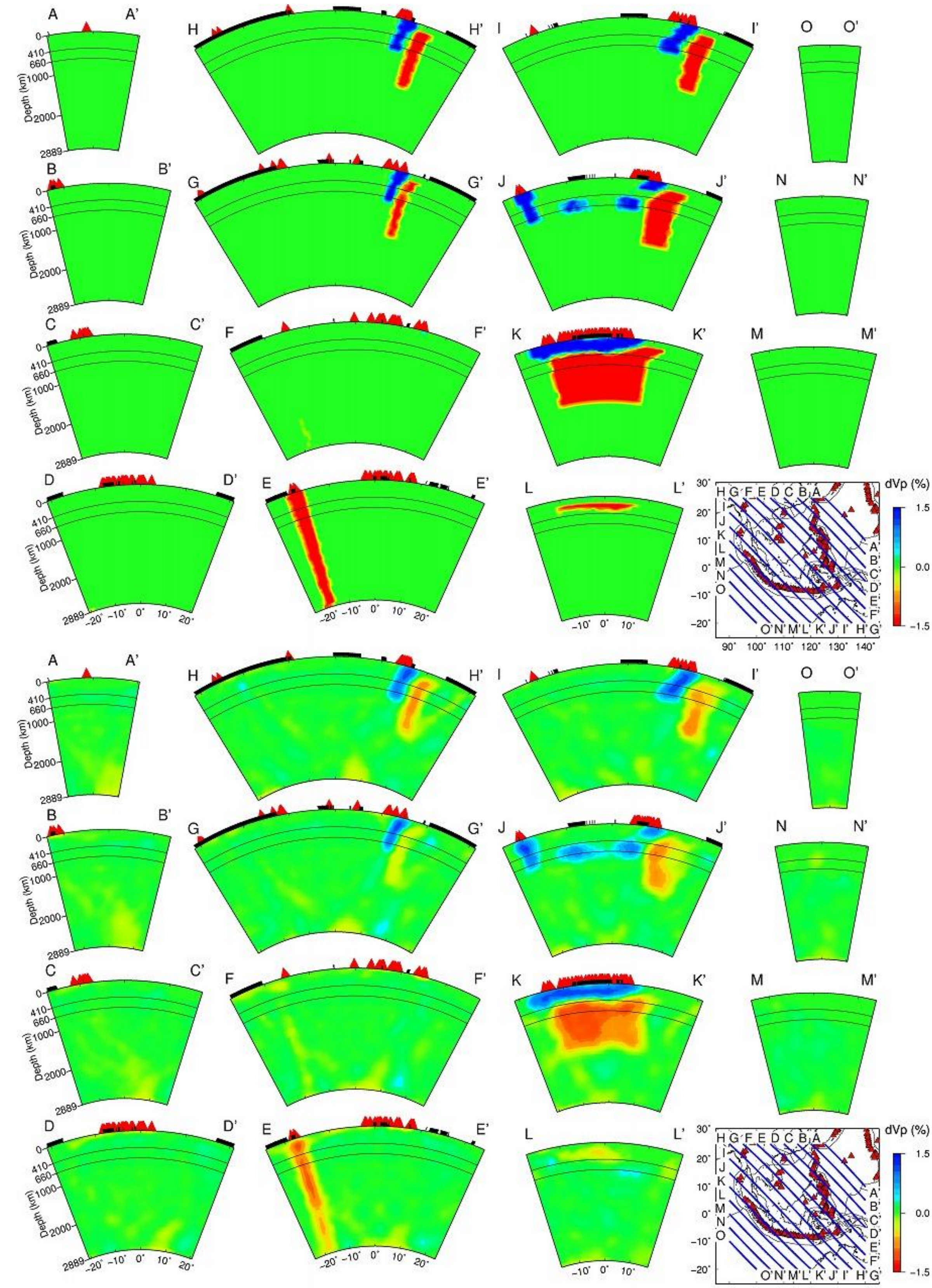
A
A'
H
H'
I
I'
O
O'
B
B'
G
G'
J
J'
N
N'
C
C'
F
F'
K
K'
M
M'
D
D'
E
E'
L
L'
Depth (km)
0
410
660
1000
2000
2889
-20˚ -10˚ 0˚ 10˚ 20˚
dVp (%)
1.5
0.0
-1.5
30˚
20˚
10˚
0˚
-10˚
-20˚
90˚ 100˚ 110˚ 120˚ 130˚ 140˚

Figure S46.

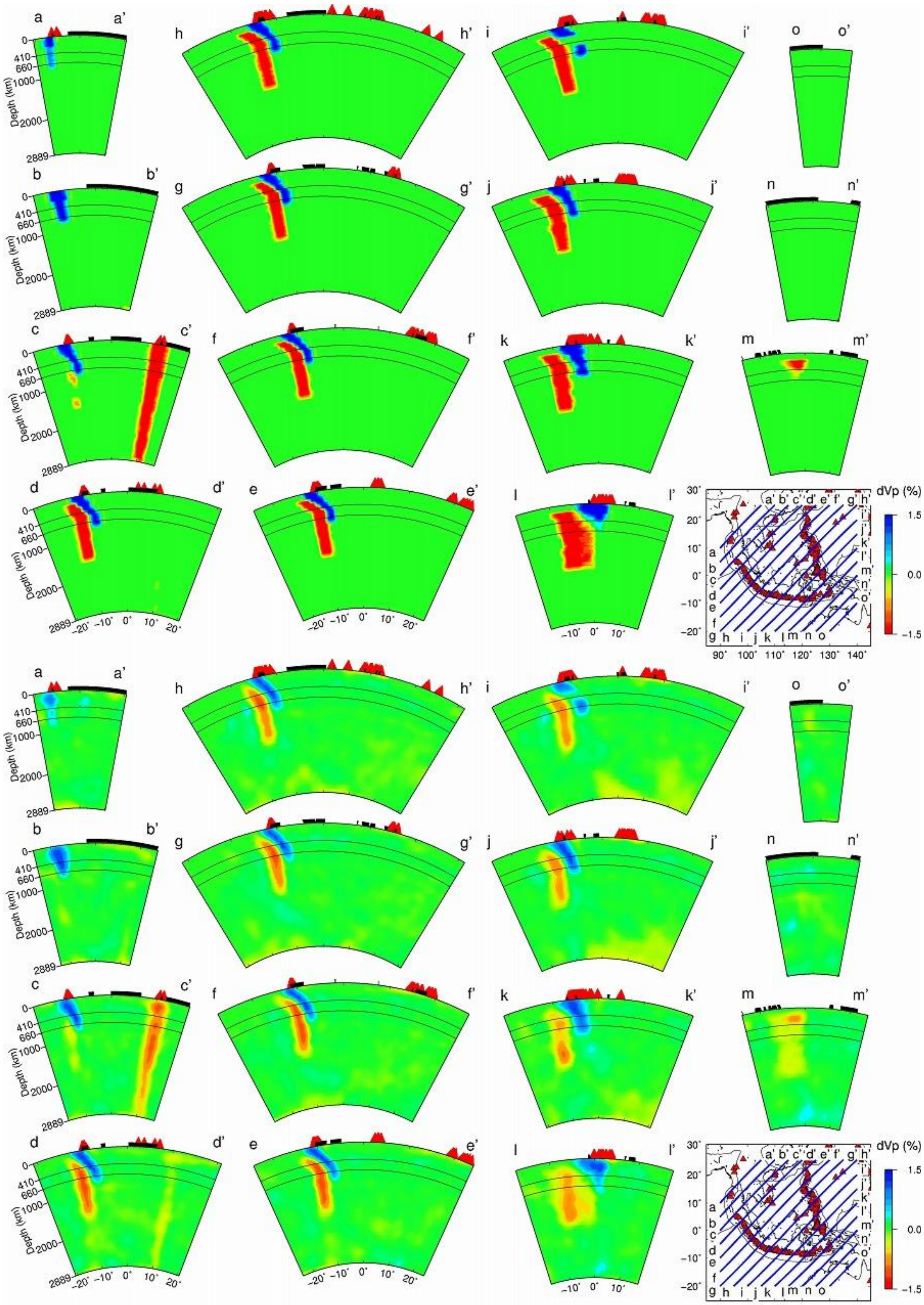
a a'
b b'
c c'
d d'
e e'
f f'
g g'
h h'
i i'
j j'
k k'
l l'
m m'
n n'
o o'
Depth (km)
0
410
660
1000
2000
2889
-20° -10° 0° 10° 20°
30°
20°
10°
0°
-10°
-20°
90° 100° 110° 120° 130° 140°
dVp (%)
1.5
0.0
-1.5

Figure S47.

Figure S43. The same as Figure S23 but for the synthetic resolution test without a low-Vp hot mantle upwelling in the mantle wedge and a low-Vp bridge through the slab hole (SRT5).

Figure S44. Vertical cross-sections showing **(top)** the input model and **(bottom)** output results of the SRT5 along 15 profiles in the N-S direction. Locations of the profiles are shown on the inset map. The 410-km and the 660-km discontinuities are shown in black solid lines. The thick black lines on the surface denote land areas. The red triangles denote active volcanoes. The thin black lines on the inset map denote the plate boundaries.

Figure S45. The same as Figure S44 but along 15 profiles in the E-W direction.

Figure S46. The same as Figure S44 but along 15 profiles in the NW-SE direction.

Figure S47. The same as Figure S44 but along 15 profiles in the NE-SW direction.

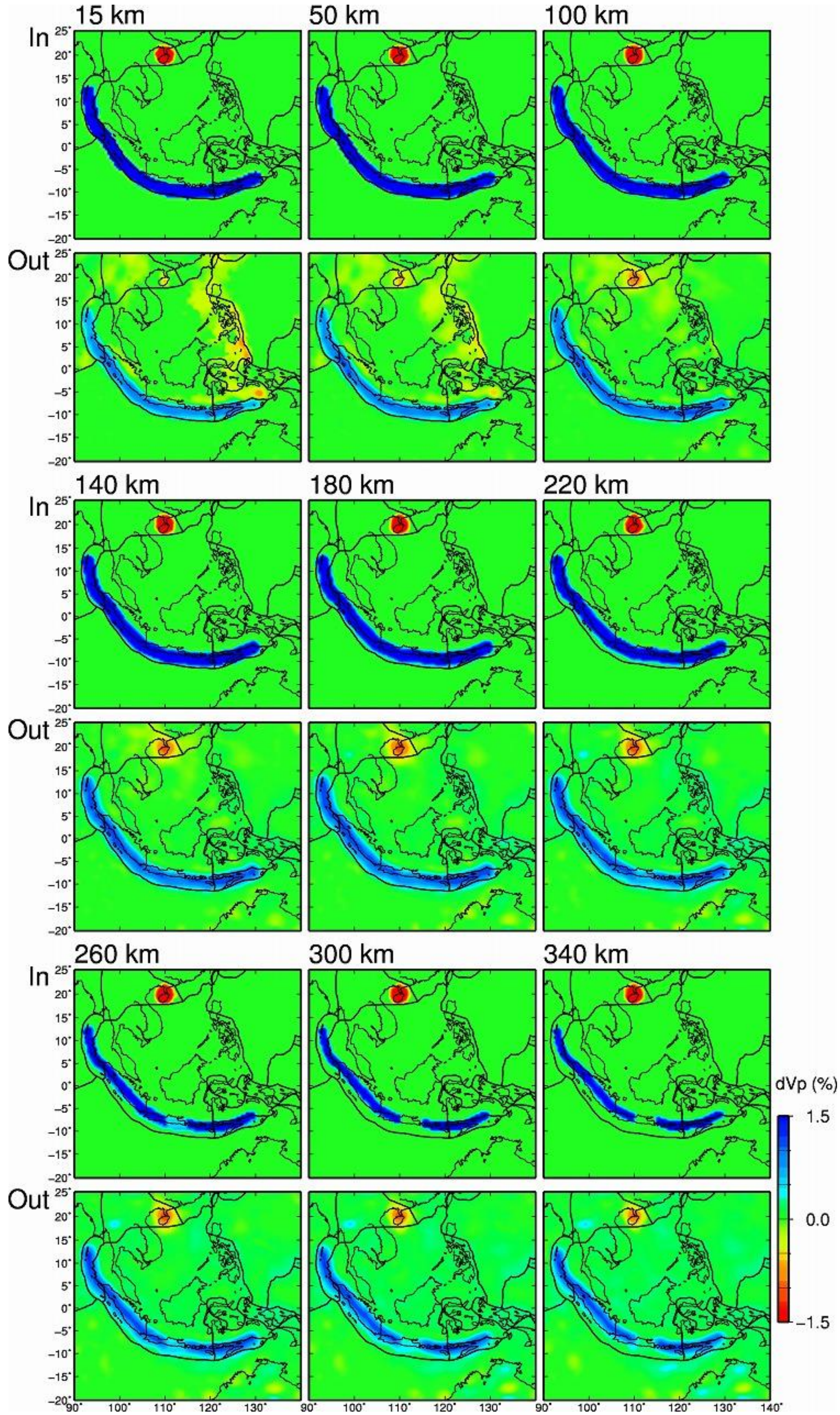

307 **Figure S48.**

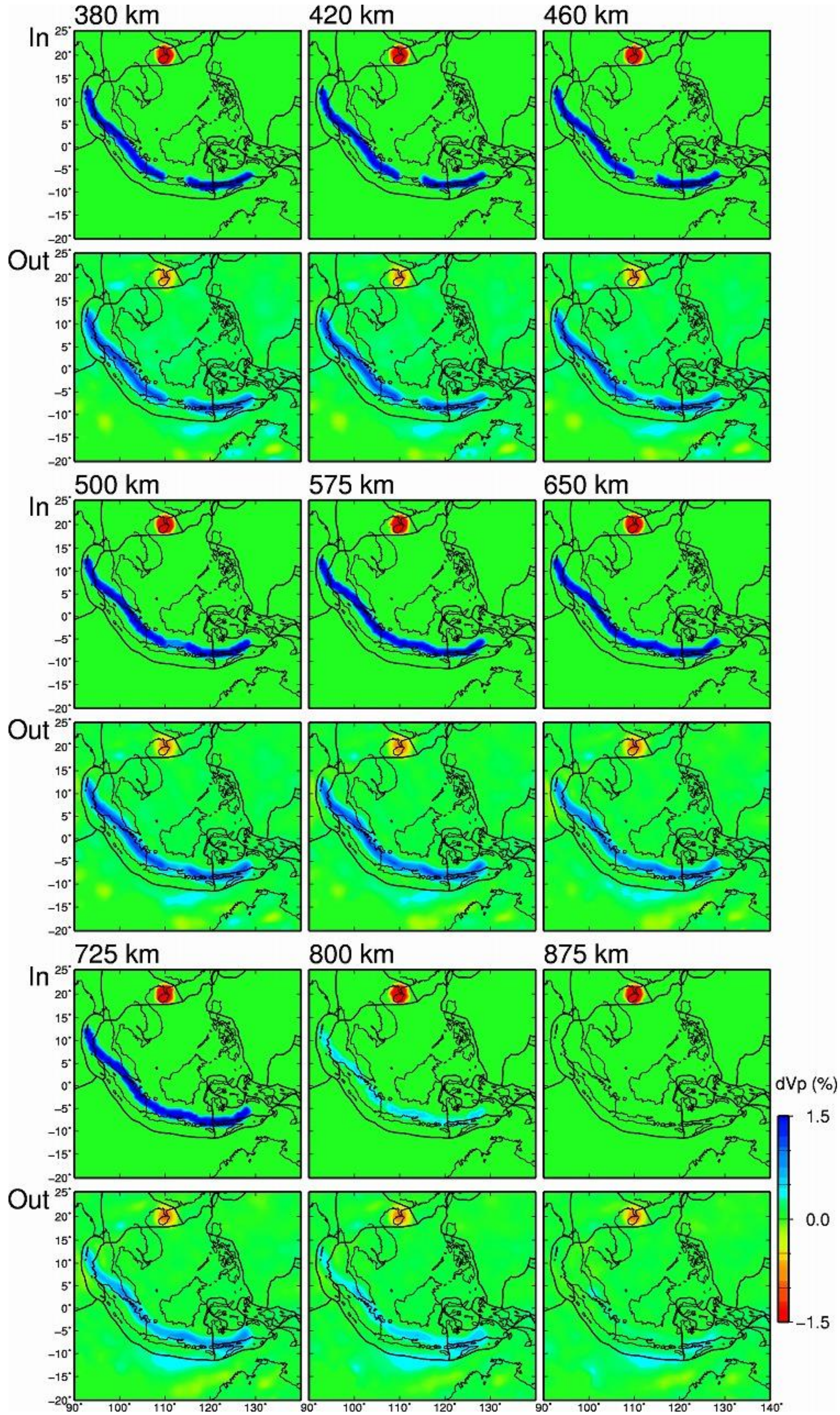

308 **Figure S48.** (continued).

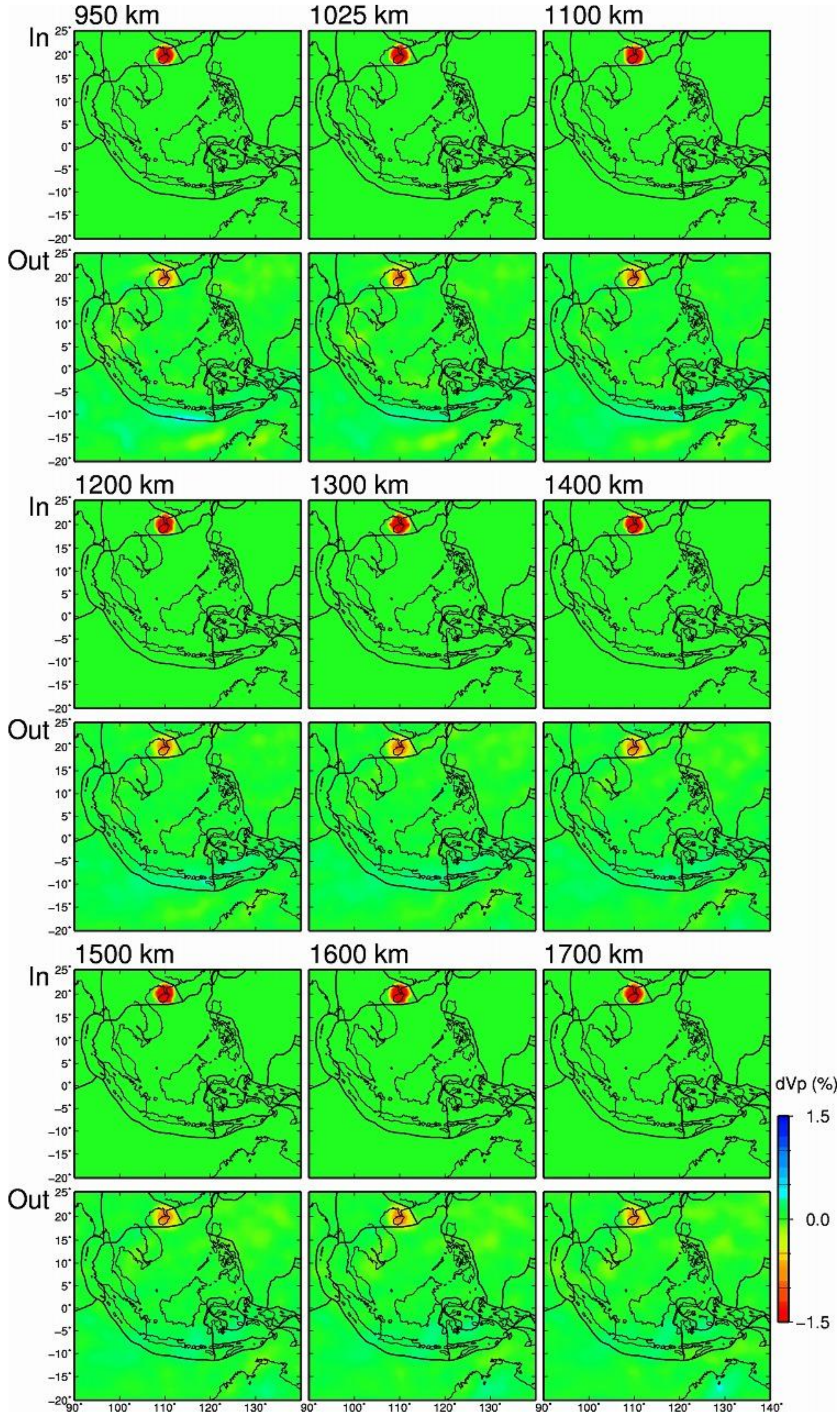

309 **Figure S48.** (continued).

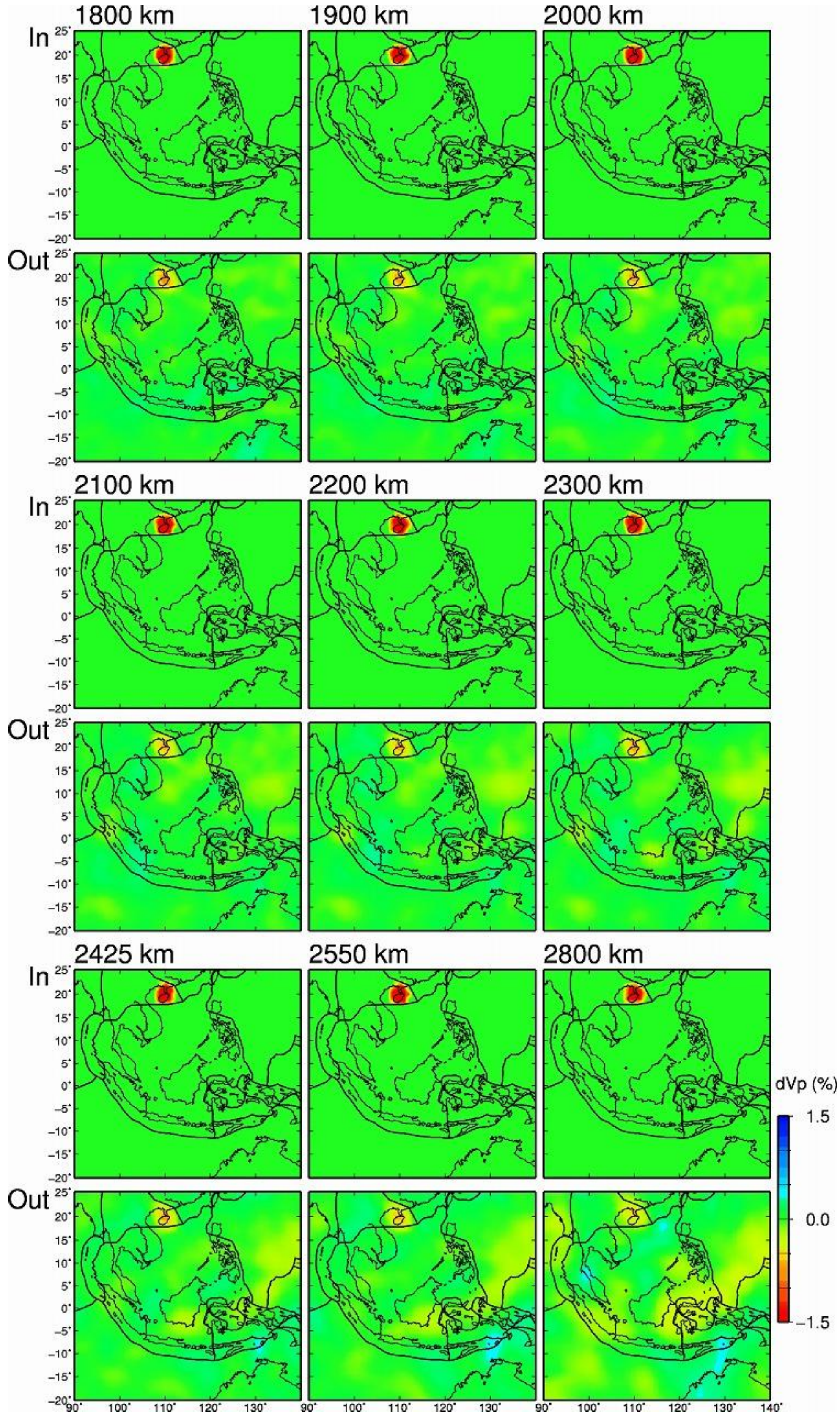

310 **Figure S48.** (continued).

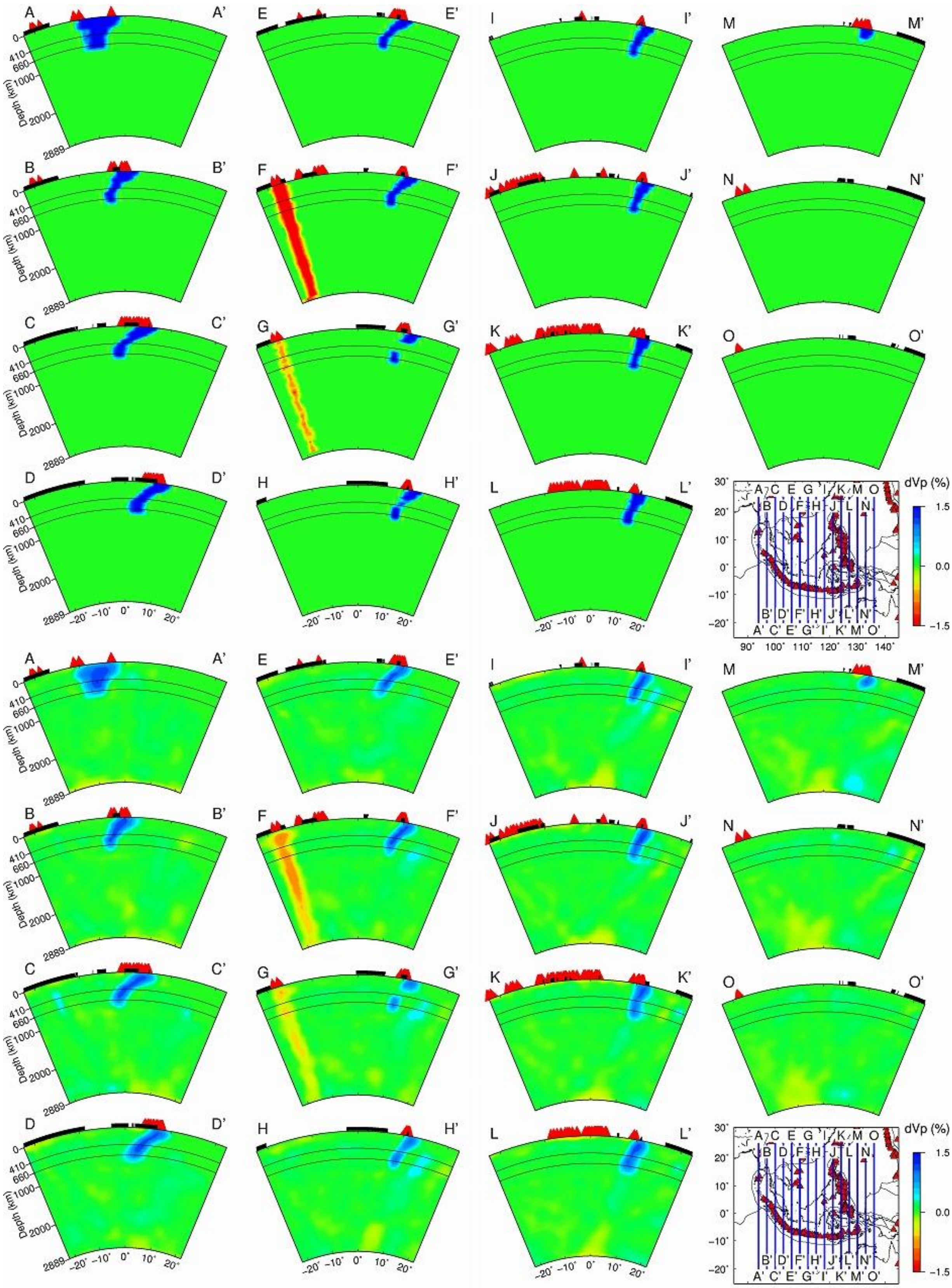

311 **Figure S49.**

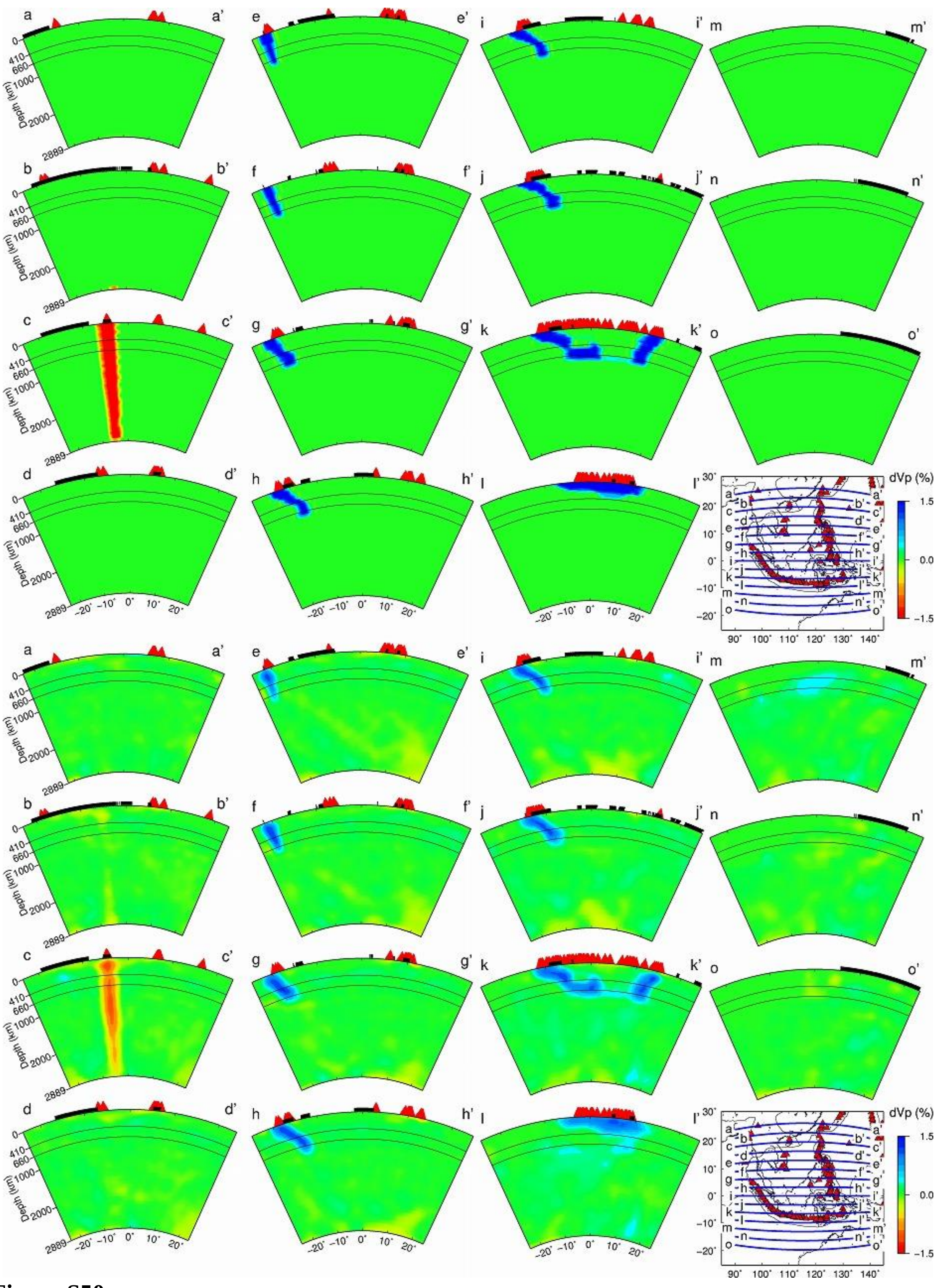

312 **Figure S50.**

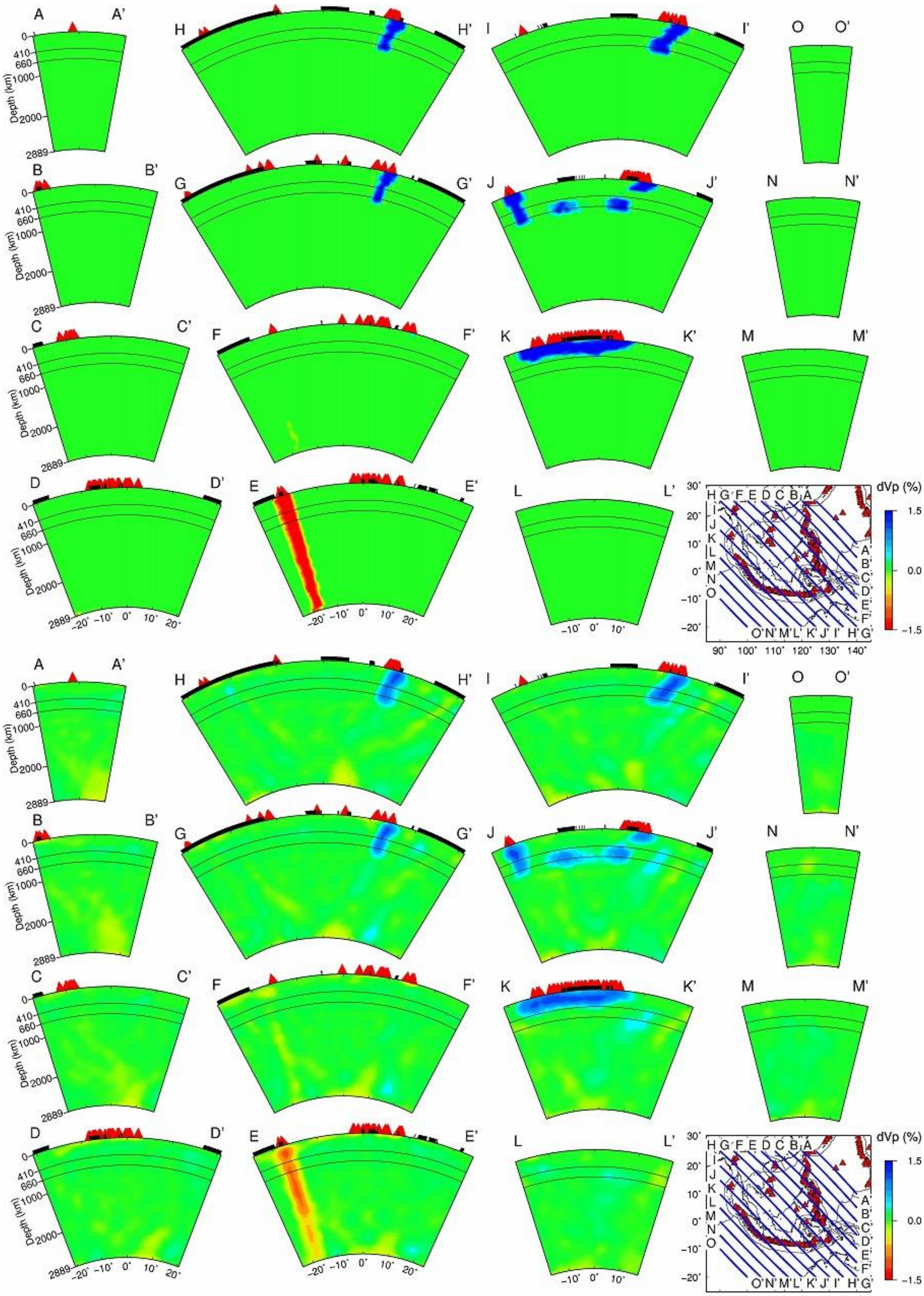
A A'
B B'
C C'
D D'
E E'
F F'
G G'
H H'
I I'
J J'
K K'
L L'
M M'
N N'
O O'
0
410
660
1000
2000
2889
Depth (km)
-20° -10° 0° 10° 20°
dVp (%)
1.5
0.0
-1.5
30°
20°
10°
0°
-10°
-20°
90° 100° 110° 120° 130° 140°

Figure S51.

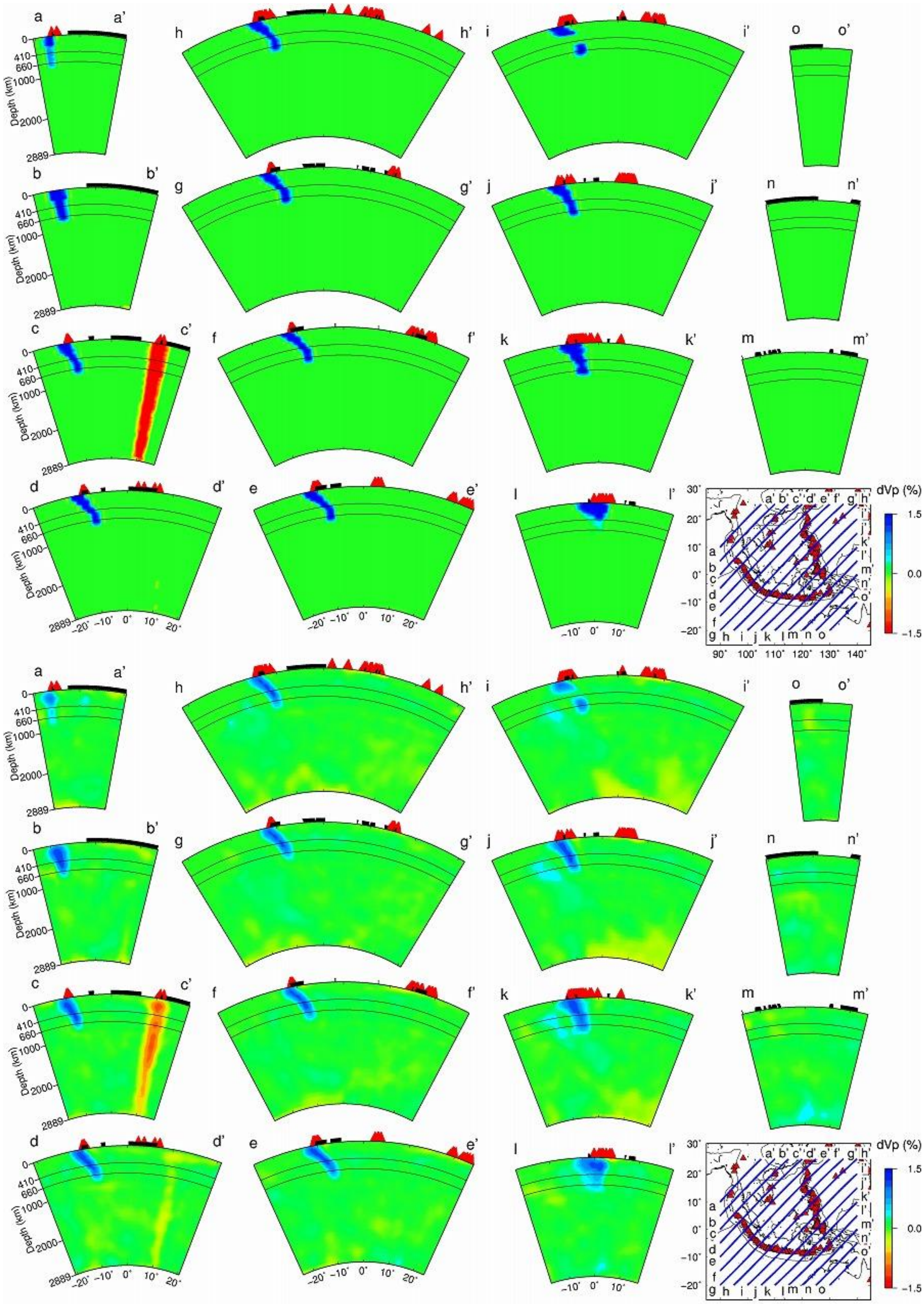

Figure S52.

Figure S48. The same as Figure S23 but for the synthetic resolution test without a low-Vp hot mantle upwelling in the mantle wedge, a low-Vp subslab hot mantle upwelling (SHMU), and a low-Vp bridge through the slab hole (SRT6).

Figure S49. Vertical cross-sections showing **(top)** the input model and **(bottom)** output results of the SRT6 along 15 profiles in the N-S direction. Locations of the profiles are shown on the inset map. The 410-km and the 660-km discontinuities are shown in black solid lines. The thick black lines on the surface denote land areas. The red triangles denote active volcanoes. The thin black lines on the inset map denote the plate boundaries.

Figure S50. The same as Figure S49 but along 15 profiles in the E-W direction.

Figure S51. The same as Figure S49 but along 15 profiles in the NW-SE direction.

Figure S52. The same as Figure S49 but along 15 profiles in the NE-SW direction.

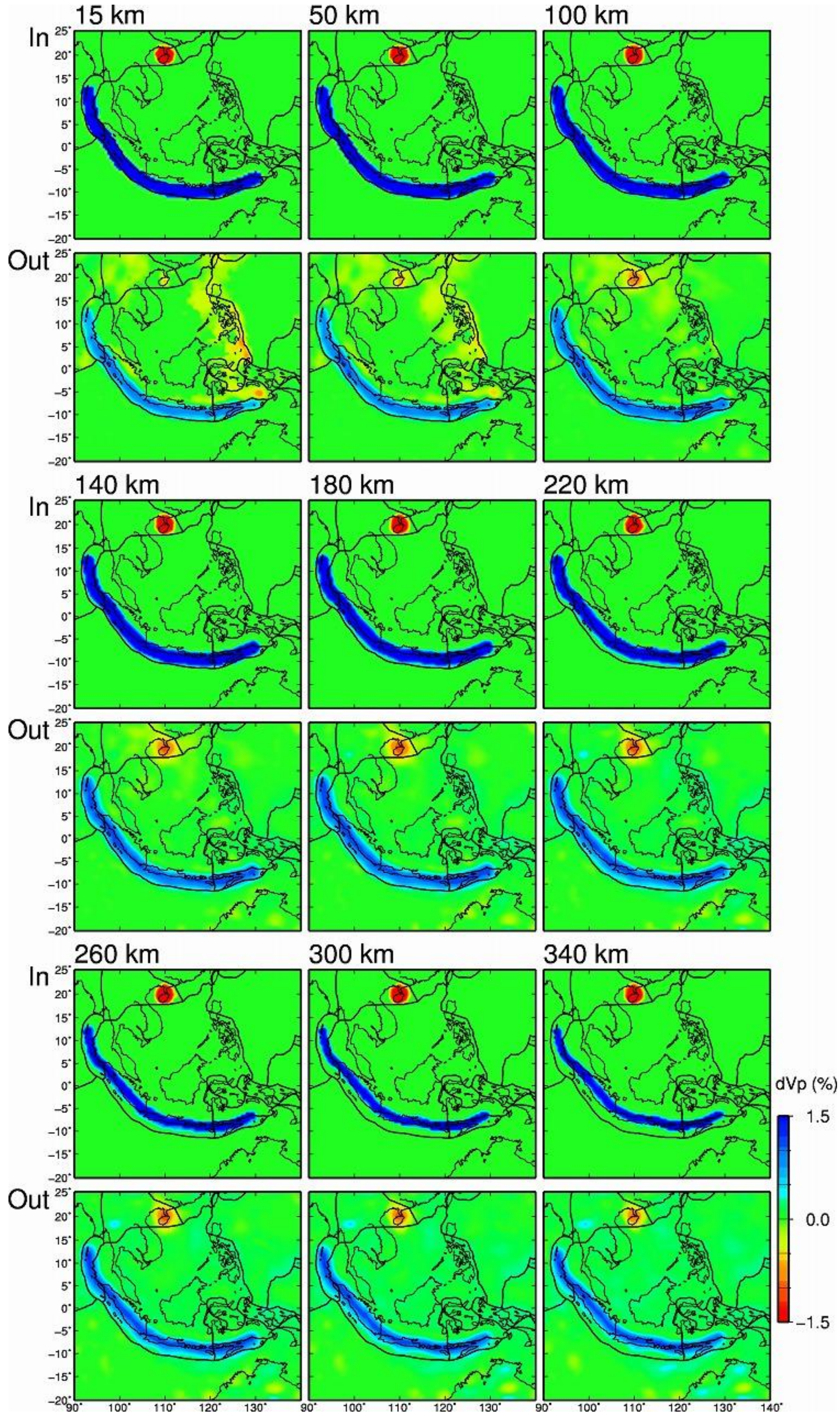

331 **Figure S53.**

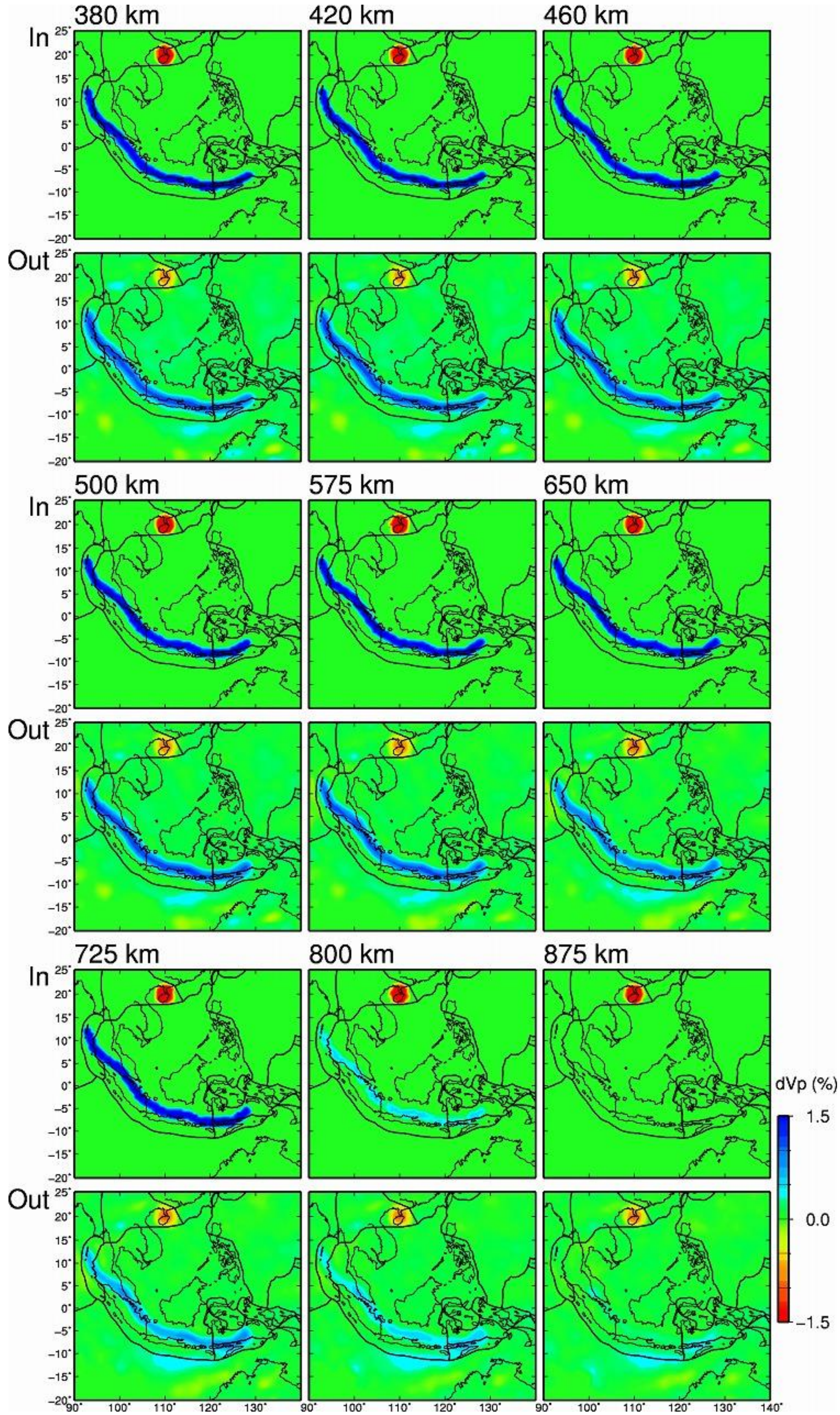

332 **Figure S53.** (continued).

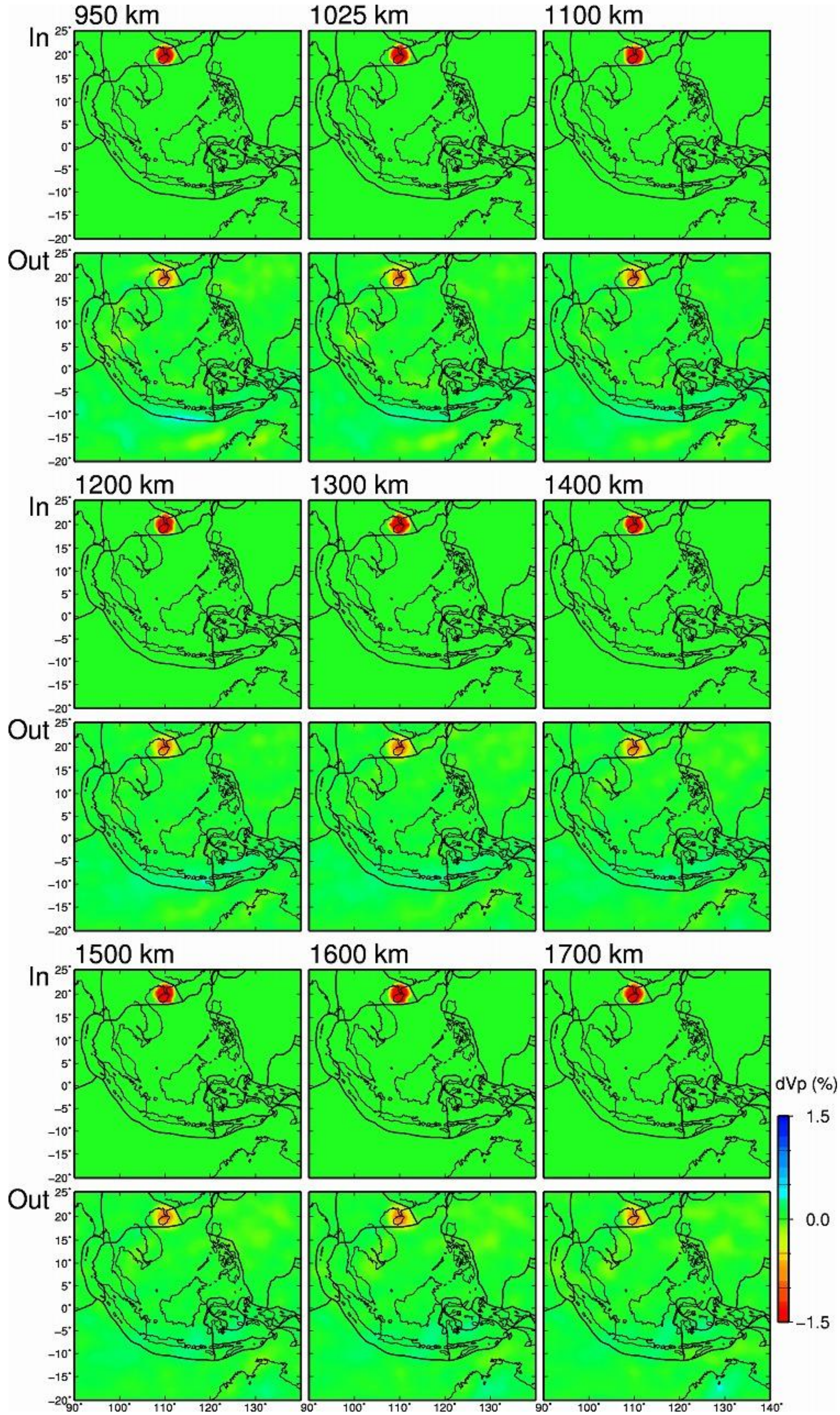

333 **Figure S53.** (continued).

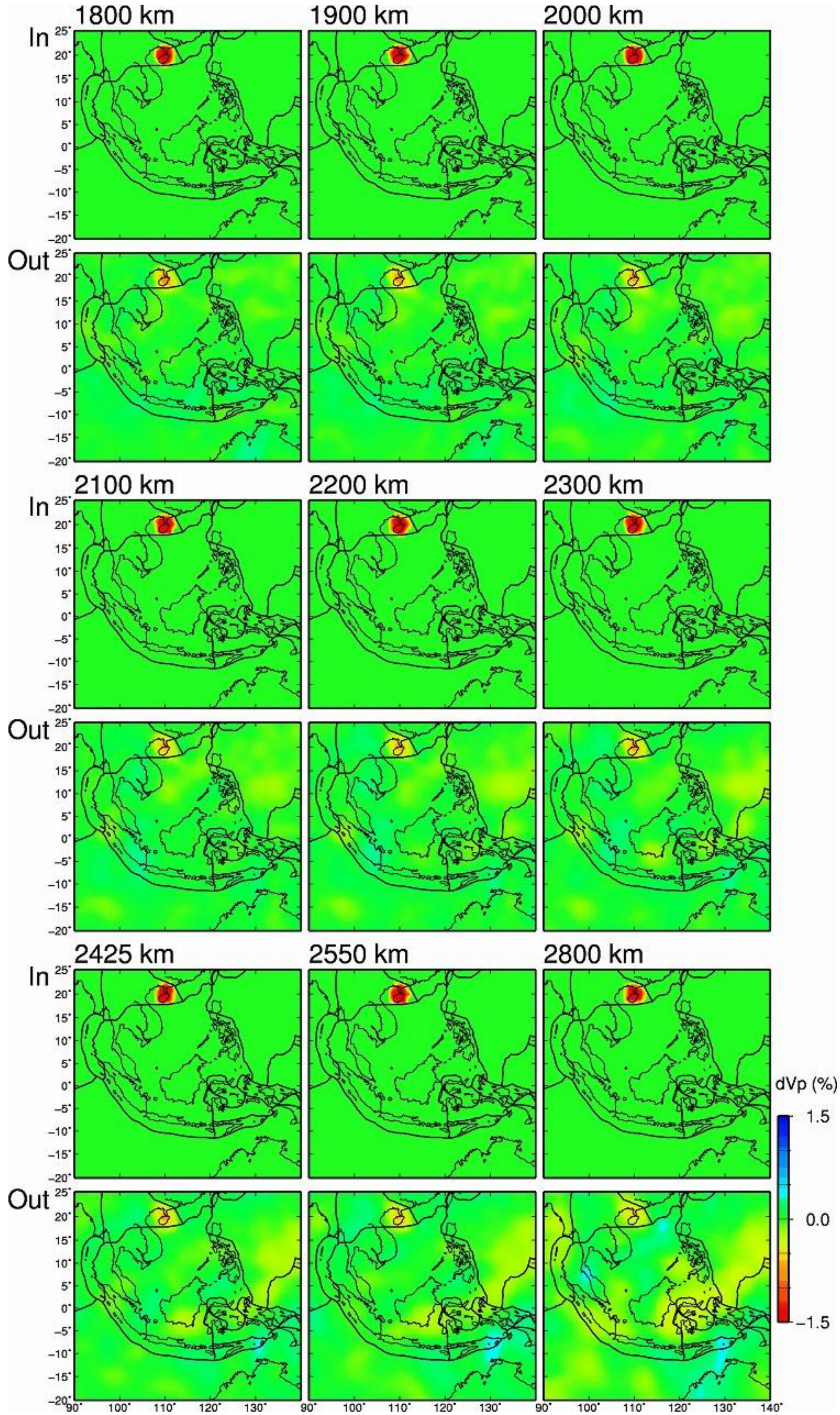

Figure S53. (continued).

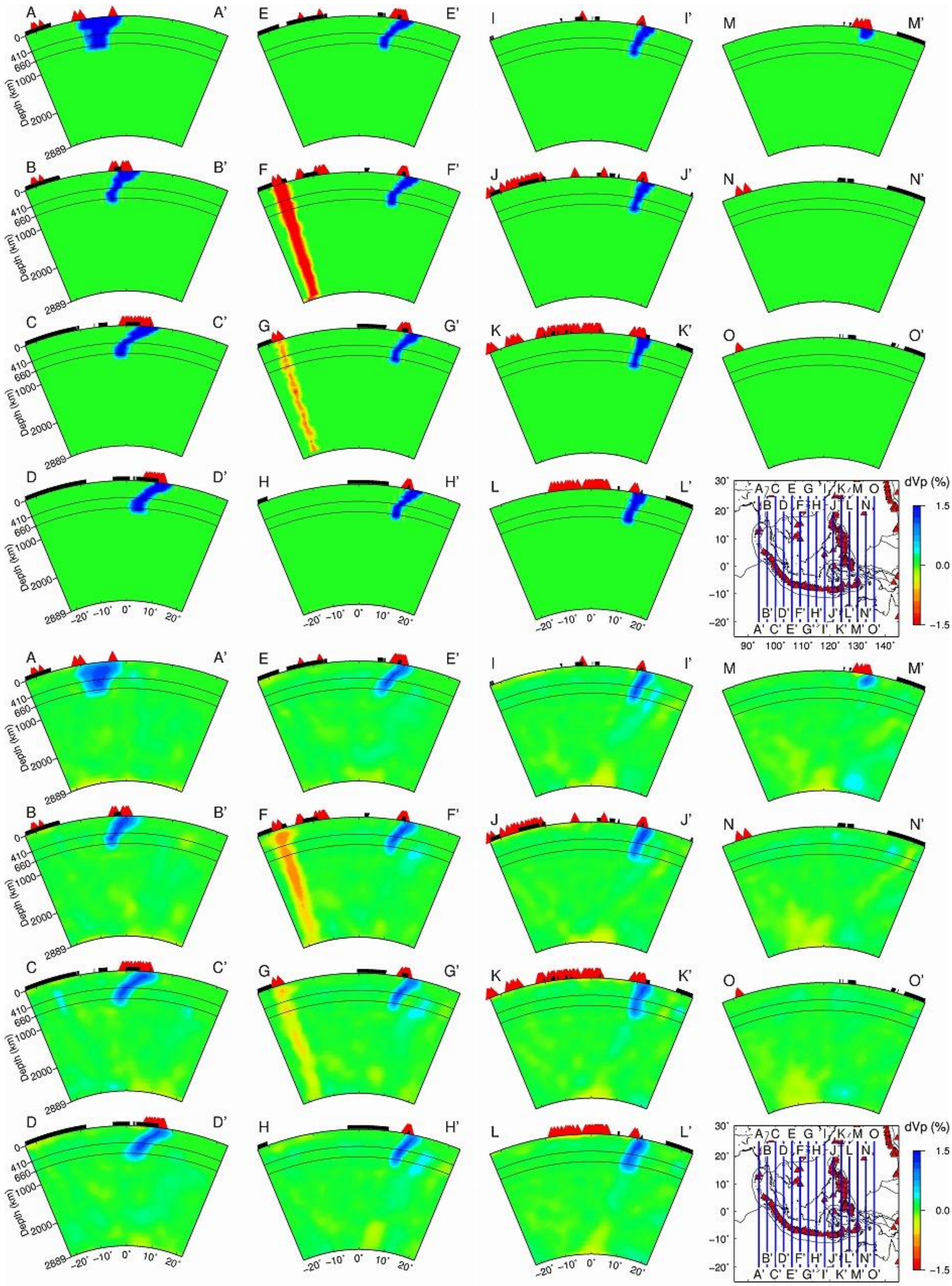

335 **Figure S54.**

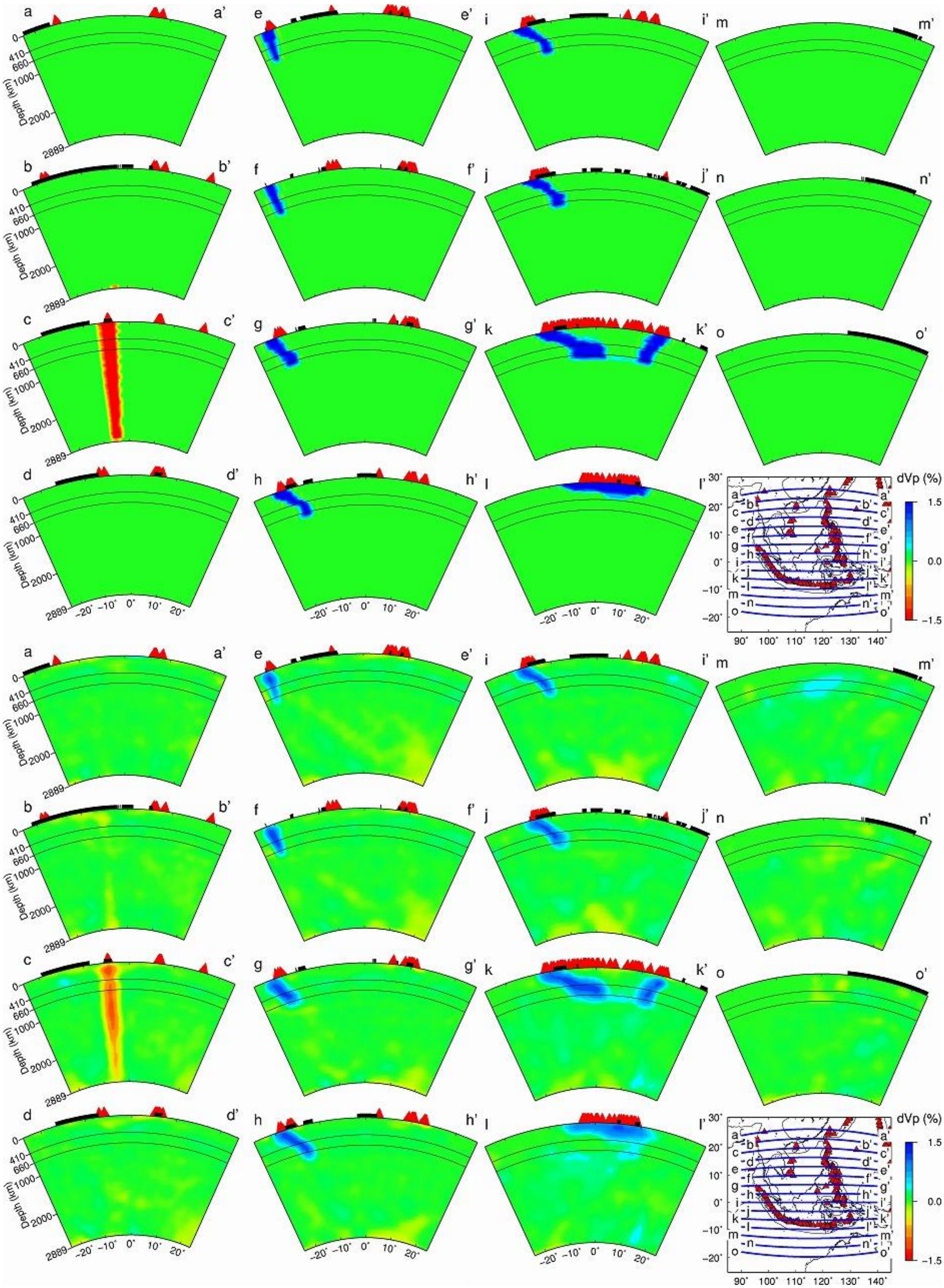

336 **Figure S55.**

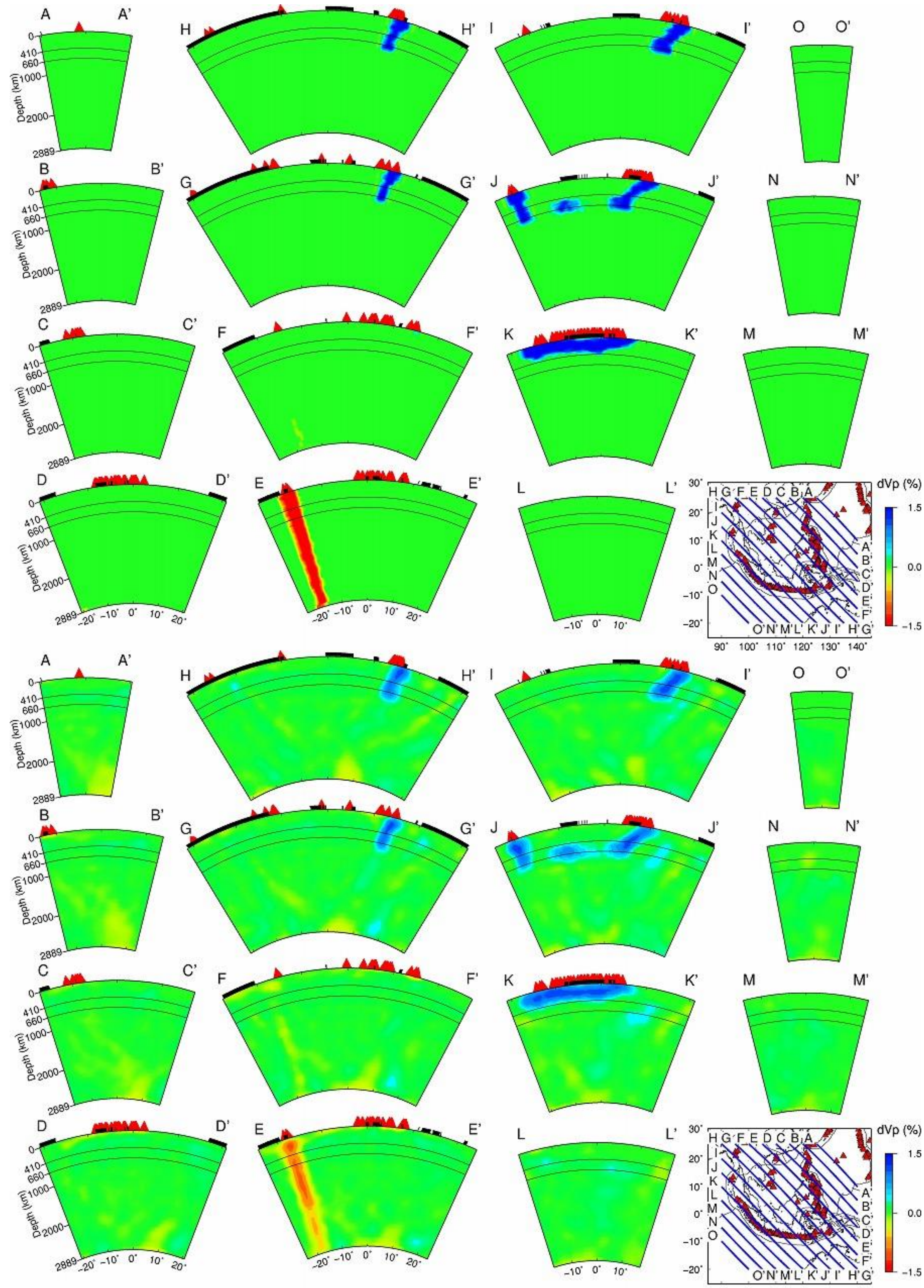

337 **Figure S56.**

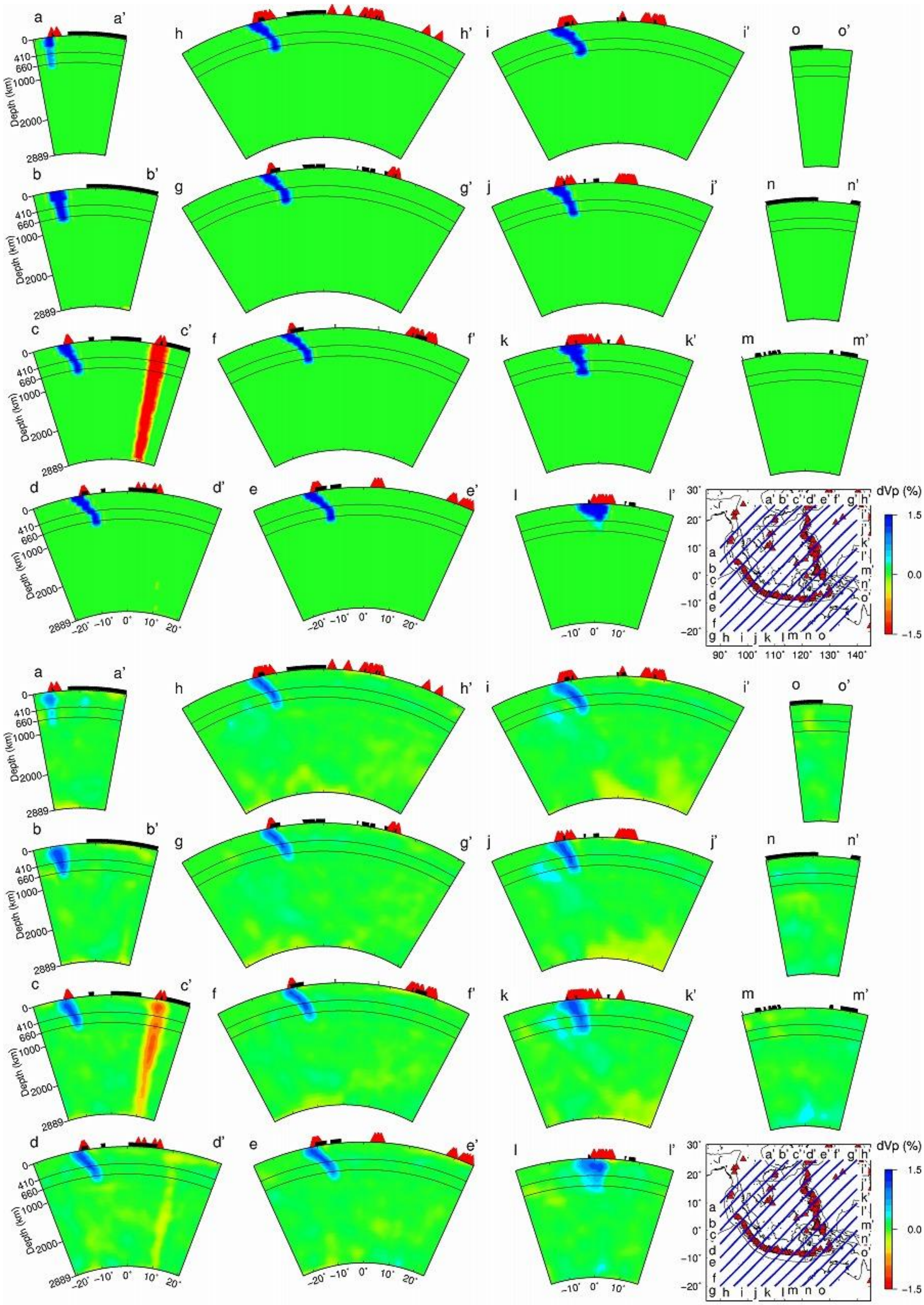

338 **Figure S57.**

Figure S53. The same as Figure S23 but for the synthetic resolution test without a low-Vp hot mantle upwelling in the mantle wedge, a low-Vp subslab hot mantle upwelling (SHMU), a hole in the Australian slab between depths 260−460 km and latitudes 110°−115°, and a low-Vp bridge through the slab hole (SRT7).

Figure S54. Vertical cross-sections showing **(top)** the input model and **(bottom)** output results of the SRT7 along 15 profiles in the N-S direction. Locations of the profiles are shown on the inset map. The 410-km and the 660-km discontinuities are shown in black solid lines. The thick black lines on the surface denote land areas. The red triangles denote active volcanoes. The thin black lines on the inset map denote the plate boundaries.

Figure S55. The same as Figure S54 but along 15 profiles in the E-W direction.

Figure S56. The same as Figure S54 but along 15 profiles in the NW-SE direction.

Figure S57. The same as Figure S54 but along 15 profiles in the NE-SW direction.

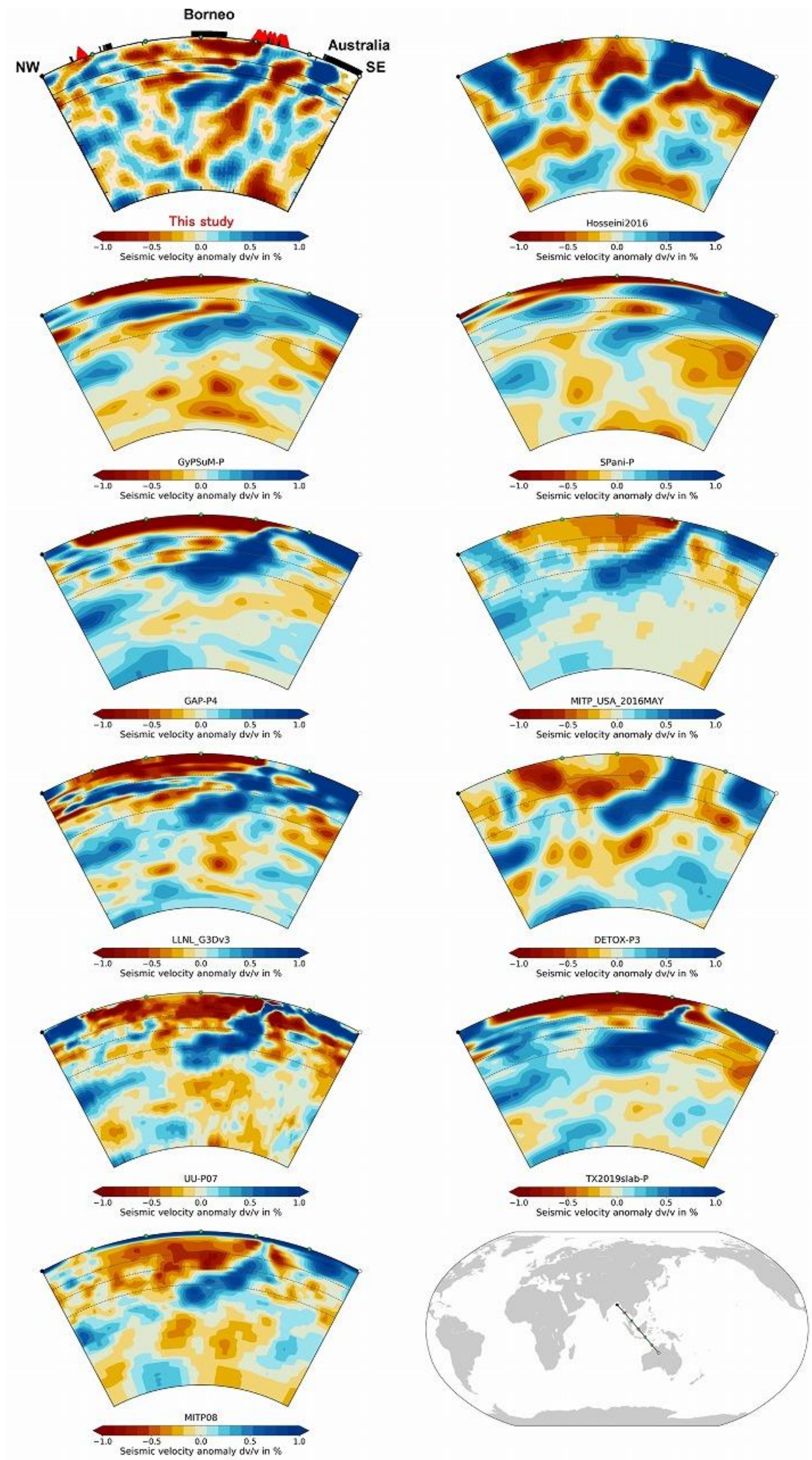

362 **Figure S58**.

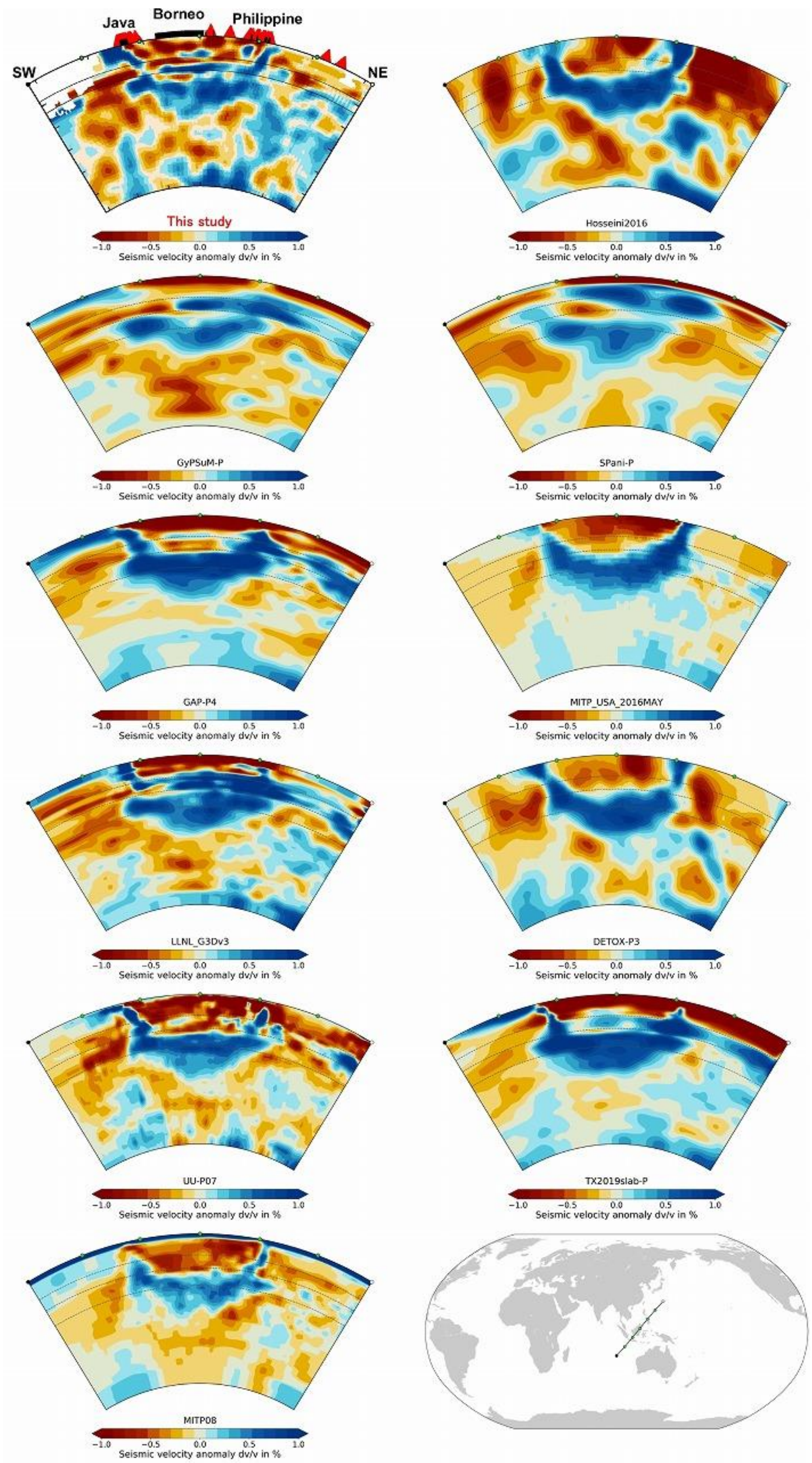

363 **Figure S59**.

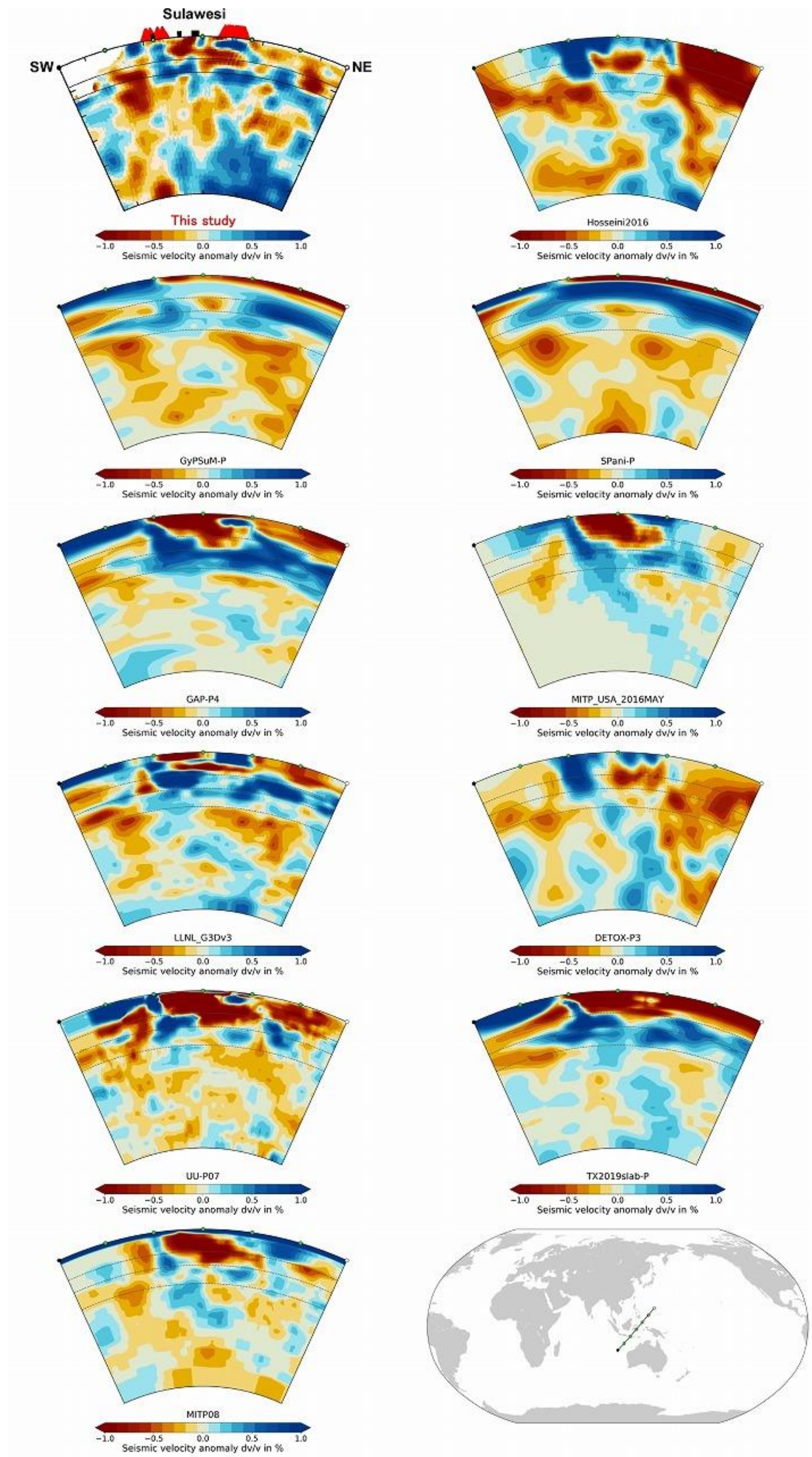

364 **Figure S60**.

Figure S58. Comparison of a Vp cross-section oriented in the NW-SE direction through Borneo and Australia obtained by this study (upper left) with 10 existing models, i.e., UU-P07 (Amaru, 2007), MITP08 (Li et al., 2008), GyPSuM-P (Simmons et al., 2010), LLNL_G3Dv3 (Simmons et al., 2012), GAP-P4 (Fukao & Obayashi, 2013; Obayashi et al., 2013), SPani-P (Tesoniero et al., 2015), Hosseini2016 (Hosseini, 2016), MITP_USA_2016MAY (Burdick et al., 2017), TX2019slab-P (Lu et al., 2019), and DETOX-P3 (Hosseini et al., 2020). All the images are shown with the same color scale. The blue and red colors denote high and low Vp perturbations, respectively, whose scale (in %) is shown below each panel.

Figure S59. The same as Figure S58 but for a Vp cross-section oriented in the NE-SW direction through Java, Borneo, and Philippines.

Figure S60. The same as Figure S58 but for a Vp cross-section oriented in the NE-SW direction through Sulawesi.

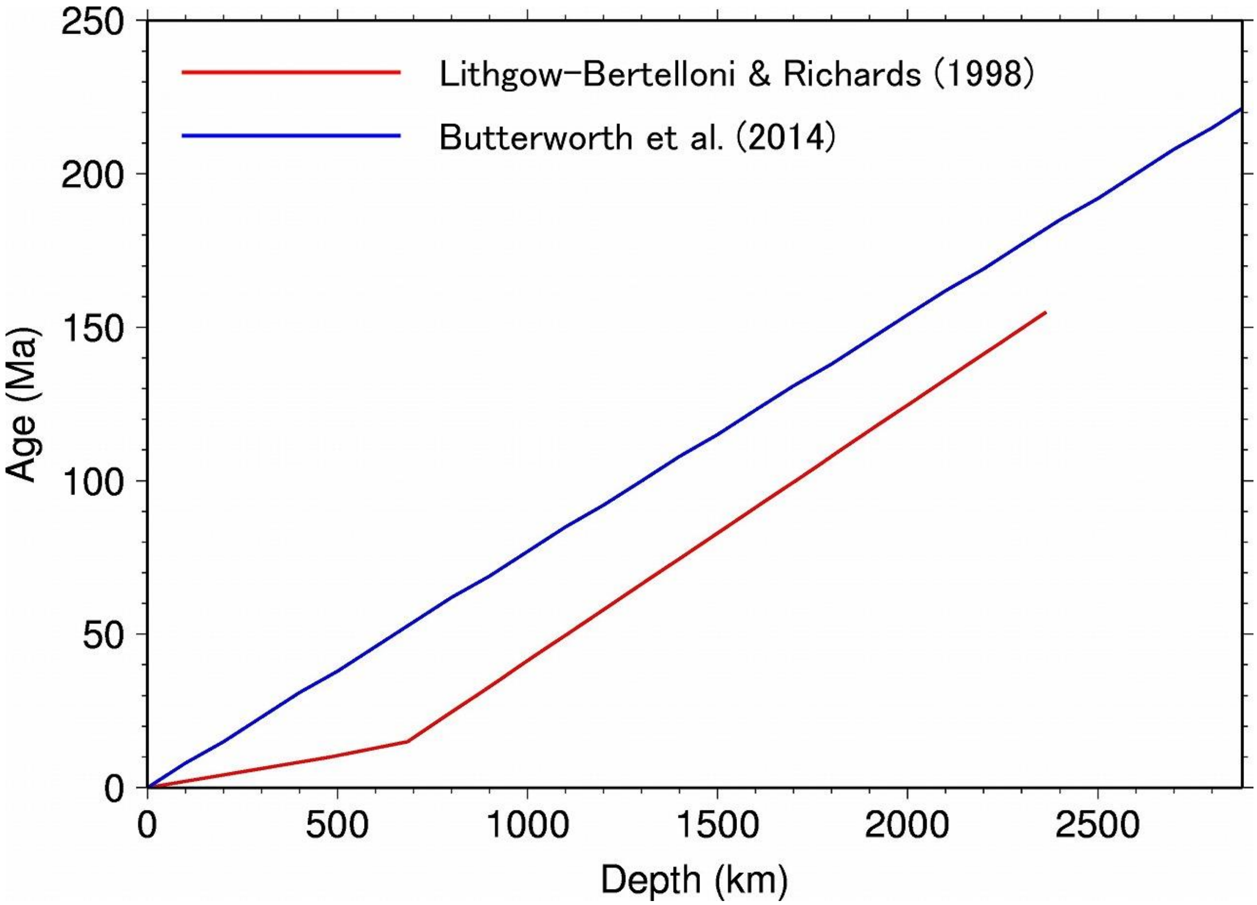

Figure S61. The age-depth relationships of a subducted slab obtained by (red) Lithgow-Bertelloni & Richards (1998) and (blue) Butterworth et al. (2014). We note that the relationship by Butterworth et al. (2014) only holds for the lower mantle.

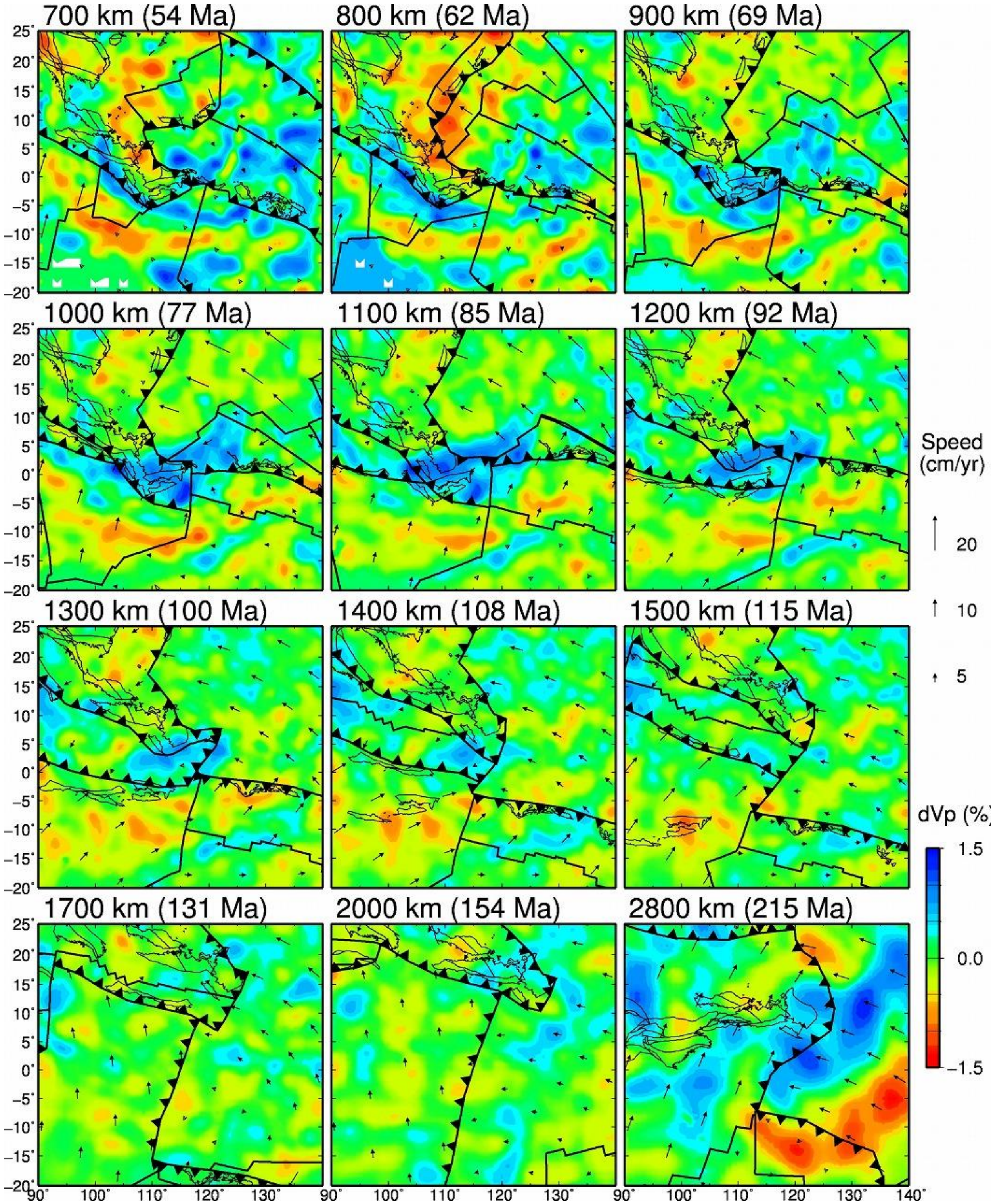

Figure S62. The same as Figure 14 but for the age-depth relationship by Butterworth et al. (2014).

402 **Table S1**. Number of grid nodes at each depth, which are arranged for conducting the
403 tomographic inversion.

Depth (km)	The number of grids
15.0	18,717
32.5	8,929
50.0	18,612
75.0	8,751
100.0	18,284
140.0	8,679
180.0	17,848
220.0	8,370
260.0	17,388
300.0	8,185
340.0	16,992
380.0	7,976
420.0	16,580
460.0	7,786
500.0	15,961
575.0	7,451
650.0	15,101
725.0	7,093
800.0	14,425
875.0	6,741
950.0	13,711
1025.0	6,389
1100.0	12,989
1200.0	6,015
1300.0	12,001
1400.0	5,570
1500.0	11,055
1600.0	5,124
1700.0	10,158
1800.0	4,700
1900.0	9,434
2000.0	4,300
2100.0	8,597
2200.0	3,913
2300.0	7,796
2425.0	3,509
2550.0	6,794
2675.0	3,117
2800.0	6,018
Total	391,059

404

405

Table S2. Number of grid nodes at each depth for the checkerboard resolution test with a lateral grid interval of 278 km inside the target region (CRT1).

Depth (km)	The number of grids
15.0	1,964
32.5	393
50.0	1,954
75.0	391
100.0	1,946
140.0	389
180.0	1,887
220.0	383
260.0	1,866
300.0	376
340.0	1,841
380.0	351
420.0	1,724
460.0	346
500.0	1,703
575.0	339
650.0	1,642
725.0	313
800.0	1,533
875.0	306
950.0	1,466
1025.0	300
1100.0	1,366
1200.0	272
1300.0	1,300
1400.0	265
1500.0	1,183
1600.0	231
1700.0	1,107
1800.0	214
1900.0	1,003
2000.0	203
2100.0	948
2200.0	185
2300.0	853
2425.0	175
2550.0	732
2675.0	148
2800.0	666
Total	34,264

Table S3. Number of grid nodes at each depth for the checkerboard resolution test with a lateral grid interval of 167 km inside the target region (CRT2).

Depth (km)	The number of grids
15.0	5,404
32.5	1,048
50.0	5,373
75.0	1,035
100.0	5,328
140.0	1,029
180.0	5,217
220.0	982
260.0	5,013
300.0	969
340.0	4,883
380.0	959
420.0	4,822
460.0	908
500.0	4,659
575.0	897
650.0	4,366
725.0	839
800.0	4,224
875.0	794
950.0	3,976
1025.0	770
1100.0	3,745
1200.0	722
1300.0	3,466
1400.0	667
1500.0	3,185
1600.0	614
1700.0	2,921
1800.0	566
1900.0	2,774
2000.0	520
2100.0	2,527
2200.0	475
2300.0	2,288
2425.0	431
2550.0	1,968
2675.0	385
2800.0	1,724
Total	92,473